Developing Proteomimetic Inhibitors of Large Surface Area, Low Affinity Protein-Protein Interactions

by

Paul Anthony Bruno

A dissertation submitted in partial fulfillment of
the requirements for the degree of
Doctor of Philosophy
(Chemistry)
in the University of Michigan
2015

Doctoral Committee:

Professor Anna K. Mapp, Chair
Professor Neil E. Marsh
Assistant Professor Corinna S. Schindler
Assistant Professor Matthew B. Soellner

Acknowledgements

First off, I would like to thank Professor Amelia Fuller. She played an important role in my development as a scientist and provided me with my first research experience during my undergraduate education at Santa Clara University. It was there that she cultivated my interest in the development of proteomimetics and encouraged me to pursue this field in my graduate studies. I am truly grateful for the experience and opportunities that she provided me as a young scientist.

I would also like to thank Professor Anna Mapp. My interest in developing proteomimetics spurred my curiosity in her research and she allowed me to pursue these interests to the fullest extent during my five years here. She is a fantastic mentor and truly shaped my development as both a scientist and a researcher. She taught me not only how to approach problems, but how to address problems in the face of tremendous adversity. Without these lessons, the work presented herein would not have been possible. Not only did these lessons help me in graduate school, but I know they will continue to shape my future as both a scientist and a mentor.

I would also like to thank Professor Neil Marsh, Professor Matt Soellner, and Professor Corinna Schindler for serving as committee members. You have all provided helpful advice throughout the course of my dissertation. I feel that my work has benefitted tremendously from your input and allowed me to greatly refine the body of work that I have put forward. I am fortunate to have you met all of you and you have all served as great role models for my own development as a researcher.

I will cherish both the memories and experiences that I have had in the Mapp lab and none of this would have been possible without the people that I have had the pleasure of interacting with on an everyday basis. I am truly grateful for the guidance and mentorship that I received when I joined the lab. Chinmay, Jonas, Chris, Amy, James, Ningkun, and Amanda all served as tremendous role models during my early years in graduate school. In particular, I have to thank Chris for serving as my graduate student mentor when I joined the lab. He was particularly helpful at the beginning stages of all of my dissertation projects and I continue to benefit from the things that he taught me. His unwavering support even when things did not work was both refreshing and encouraging to me as a new graduate student, an attitude that I continue to emulate today. He was a fantastic mentor. When I joined the Mapp lab, I started with two other graduate students, JP and Steve. Upon joining the Mapp lab, we were donned the nickname "the young guns" and as we finish up our dissertations and move on to new things, we leave the lab as "the old guard". Having the opportunity to go through graduate school with JP and Steve was a truly special experience that has provided me with several cherished memories. Both JP and Steve have provided levity throughout my time in graduate school and were immensely supportive, especially when times were tough. I have to give special thanks to Steve Sturlis, who helped me start the VP16-ACID project. At the time of starting this project, I joked that together Steve and I made one fully functional graduate student that I named Saul Stuno, a name that stuck throughout working on this project, and continues to live on today. I would also like to give special thanks to the younger students in lab. Jean, Matt, Andy, Rachel, Cassie, and Laura are all great friends and promising scientists. Coming into lab everyday was a much more enjoyable experience with all of you around and I wish you the best of luck in your future endeavors.

Lastly, I would like to thank my friends and family for all of the support that you have provided me throughout this experience. My dad, mom, Ari, and Gaby have been incredibly encouraging throughout graduate school and have been willing to listen to both my successes and the struggles with nothing but encouraging and supportive things to say. Although you may not have known what I was talking about all the time, your patience and your unwavering belief that I was capable of completing this endeavor did not go

unnoticed. I am truly grateful for all of your support and I hope that one day I might be able to provide you with this same sort of love and unwavering support in your own endeavors. I would also like to thank Bridgette, who has been on this journey with me every step of the way. She is one of the most intelligent people I know and, although she does not consider herself a scientist, she has provided me with fresh perspective and provided solutions for several of the problems that I have encountered in graduate school. You understand me better than anyone else and you believe that I am capable of things that I do not. All of these experiences were made easier with you by my side and for that, I will be forever grateful. I love you all and I am truly blessed for all your support during graduate school as well as in my future endeavors.

TABLE OF CONTENTS

List of Figures

List of Tables

List of Abbreviations

AD	Activation Domain
ATF6α	Activation transcription factor 6 α
CBP	CREB binding protein
coIP	co-immunopreciptation
DBD	DNA-binding domain
DMEM	Dulbecco's modified eagle medium
DMSO	dimethylsulfoxide
DNA	deoxyribonucleic acid
FBS	fetal bovine serum
FP	fluorescence polarization
HPLC	high performance liquid chromatography
HTS	high-throughput screen
IC_{50}	half maximal inhibitory concentration
IKK	inhibitor of kappa b kinase
Med	Mediator complex
mRNA	messenger rna

MsCl	methanesulfonyl chloride
NEMO	NF-kappaB essential modifier
NMR	nuclear magnetic resonance
NosCl	nitrobenzene sulfonyl chloride
NR	nuclear receptor
PolII	RNA polymerase II
RNA	ribonucleic acid
RT-qPCR	reverse transcription quantitative polymerase chain reaction
siRNA	silencing RNA
TAD	transriptional activation domain
TBS	tert-butyldimethylsilyl
tBu	tert-butyl
TFIIB	ultraviolet
UV	visible
Vis	visible
VP16	herpes simplex virion protein 16
Å	angstrom

Abstract

The majority of cellular processes are governed by the activity of multimeric protein complexes assembled through specific protein-protein interactions (PPIs). With more than 650,000 estimated PPIs, less than 0.01% of these interactions have been successfully targeted with small molecules. One processes, transcription, allows for the regulation and expression of relevant genes in both a cell specific and tissue specific manner. Dysregulation of the transcription process is implicated in the vast majority of human diseases, either as a cause or consequence of this dysregulation. Given the significant role that transcriptional dysregulation plays in human disease, it is evident that there is immense therapeutic potential for finding strategies to restore proper transcriptional regulation. There are three general strategies for targeting transcriptional activation pathways in order to restore normal function: regulatory/masking proteins, transcriptional activator dimerization, and specific contacts made with coactivators to recruit the transcriptional machinery. PPIs have traditionally been defined as "undruggable" due to the fact that many protein-protein interactions lack surface topology and occur over large surface areas. These characterizations make PPIs difficult to target with small molecules, particularly large surface area, low affinity PPIs, a subclass of PPI often used by transcriptional activator pathways. Herein, we discuss strategies for targeting this subclass of PPIs by using small molecule combination strategies, high-throughput screening of natural products, and peptide stabilization methods to target this difficult class of PPIs.

In one example, we demonstrated how **i1**, an inhibitor of the ESX transcriptional activator, could be used in combination with other ESX signaling pathway inhibitors to obtain synergistic inhibition against ESX-driven Head and Neck Squamous Cell Carcinoma

(HNSCC). We also demonstrated the utility of natural products belonging to the depsidone and depside molecule subclass as inhibitors of the VP16-ACID interaction. Specifically, we demonstrated the utility of norstictic acid and psoromic acid as the first inhibitors of the VP16-ACID interaction and inhibitors of ACID-mediated transcriptional processes. Lastly, we demonstrate the use of constrained peptides to mimic a non-regular structural motif utilized in the NF-κB signaling pathway, resulting in the development of an inhibitor with 10-fold greater potency than an unmodified peptide inhibitor.

Chapter 1

Features of Protein-Protein Interactions and Strategies for Modulating Them

1.1 Abstract

The majority of cellular processes are governed by the activity of multimeric protein complexes assembled through specific protein-protein interactions (PPIs). One of these cellular processes, transcription, allows for the regulation and expression of relevant genes in both a cell-specific and tissue-specific manner. Dysregulation of the transcription process is implicated in the vast majority of human diseases, either as a cause or consequence of this dysregulation. Given the significant role that transcriptional dysregulation plays in human diseases, it is evident that there is immense therapeutic potential for finding strategies to restore proper transcriptional regulation. This introductory chapter defines the characteristics of protein-protein interactions and the challenges traditionally associated with targeting these "undruggable" interactions. With these challenges in mind, new technical methods and targeting strategies will be presented to expand the number of druggable targets at our disposal using combination therapy, natural product compound libraries, and novel peptide stabilization methods.

1.2 Introduction

All living things contain the genetic information needed to carry out basic, everyday life functions such as metabolism, digestion, and movement.[1] These functions are accomplished by specialized tissues composed of differentiated cells that are capable of carrying out cell-specific processes. [2,3] Upon encountering external or internal stimuli, specific activation pathways will be engaged, causing the expression or repression of target

genes needed to respond to these stimuli.[4] Although all cells contain the same common DNA template, certain cells are capable of carrying out cell-specific processes, whereas other cells are not. This is possible due to master regulator proteins known as transcription factors, which allow cells to activate or repress specific target genes using the common DNA template shared among all cells.[5] The ability of transcription factors to either activate or repress target gene expression occurs through a process known as transcription.[6] Dysregulation of the transcription process is implicated in the majority of human diseases, with transcriptional dysregulation arising as either a cause or consequence of disease. [7-9] Given the importance of transcription as it pertains to cell-specific responses and its role in disease, there is immense therapeutic potential for finding small molecules capable of mitigating or restoring the process of transcription as seen in healthy cells. Small molecules capable of specifically inhibiting a cell signaling pathway would allow modulation of transcription factor protein levels in the cell, whereas small molecules targeting the coactivators used by transcription factors would allow for modulation by inhibiting the ability of transcription factors to initiate transcription.

1.3 Transcriptional activators and the process of transcription

Cellular processes are often mediated by the signaling events that result from specific activation pathways. One of these downstream cellular processes resulting from signaling events, transcription, is mediated by proteins known as transcription factors and more specifically, transcriptional activators. [10-12] These transcriptional activator proteins are minimally composed of a DNA-binding domain (DBD) and a transcriptional activation domain (TAD). [13-15] The DBD subunit is used to recognize and bind to a specific promoter sequence located upstream of the target gene, whereas the TAD is used to make specific contacts with coactivators needed to assemble the transcriptional machinery at the target gene (Figure 1.1). Assembly of the transcriptional machinery at the target gene results in upregulation of that specific target gene and subsequent protein expression (Figure 1.2). In human disease, it is common to observe dysregulation of the transcription process. For example, the herpes simplex virus causes dysregulation of transcription through expression of herpes simplex virus protein vmw65 (VP16), a transcriptional activator that recruits coactivator Med25, a specific subunit of the transcriptional machinery. [16-18] This

ultimately causes overexpression of VP16 target genes and downregulation of other transcription factor target genes that rely on Med25 for expression. A similar mode of transcription dysregulation has been documented in breast cancer such as overexpression of the transcriptional activator epithelial-restricted with serine box (ESX) recruits Med23, a subunit of the transcriptional machinery. This leads to overexpression of Human Epidermal growth factor Receptor 2 (Her2), a biomarker and oncogene responsible for the development and progression of breast cancer.[19] Dysregulation of transcription can also occur through constitutive activation of a specific signaling pathway. This occurs in rheumatoid arthritis, an autoimmune disease that cause constitutive activation of the nuclear factor kappa-light-chain enhancer of activated B cells (NF-κB), resulting in upregulation of NF- κB target genes that cause chronic inflammation and tissue injury. [20,21]

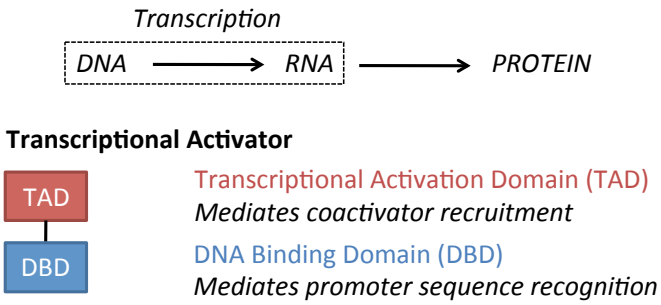

Figure 1.1 Transcription and transcriptional activator proteins The central dogma of molecular biology outlines the conversion from DNA to RNA to protein. The conversion of DNA to RNA is completed through a process known as transcription, whereas the conversion of RNA to protein is completed through a process known as translation.

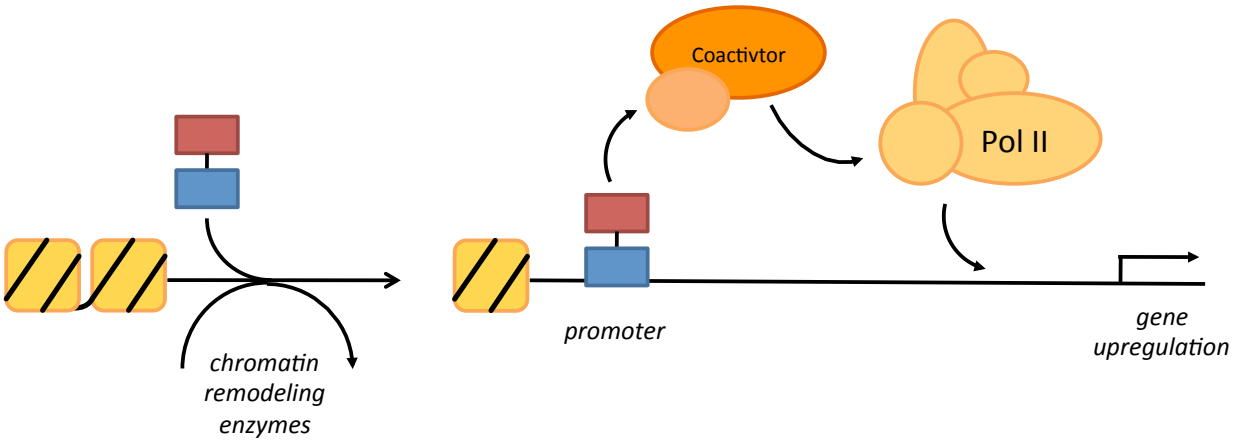

Figure 1.2 Localization of a transcriptional activator to a target gene and subsequent gene upregulation During a cell signaling event, a transcriptional activator with localize to the cell nucleus where the DNA-binding domain will bind to a specific DNA promoter sequence located upstream of the target gene. The transcriptional activation domain will then make specific protein-protein interactions with coactivators that will in turn, recruit the transcriptional machinery and upregulate target gene expression.

1.4 Methods for targeting transcriptional activators

With basic knowledge of how the process of transcription is dysregulated in human diseases, there are strategies can be utilized to modulate and restore normal activity to the transcription process. By targeting protein-protein interactions required for transcriptional activator function, there exists three general ways to directly inhibit transcriptional activator function: targeting masking or regulatory proteins, inhibiting homo/heterodimerization, and inhibiting binding to coactivators (Figure 1.3). [13,22] Alternatively, inhibiting protein-DNA interactions exist as a viable alternative, but remains challenging. [23-25]

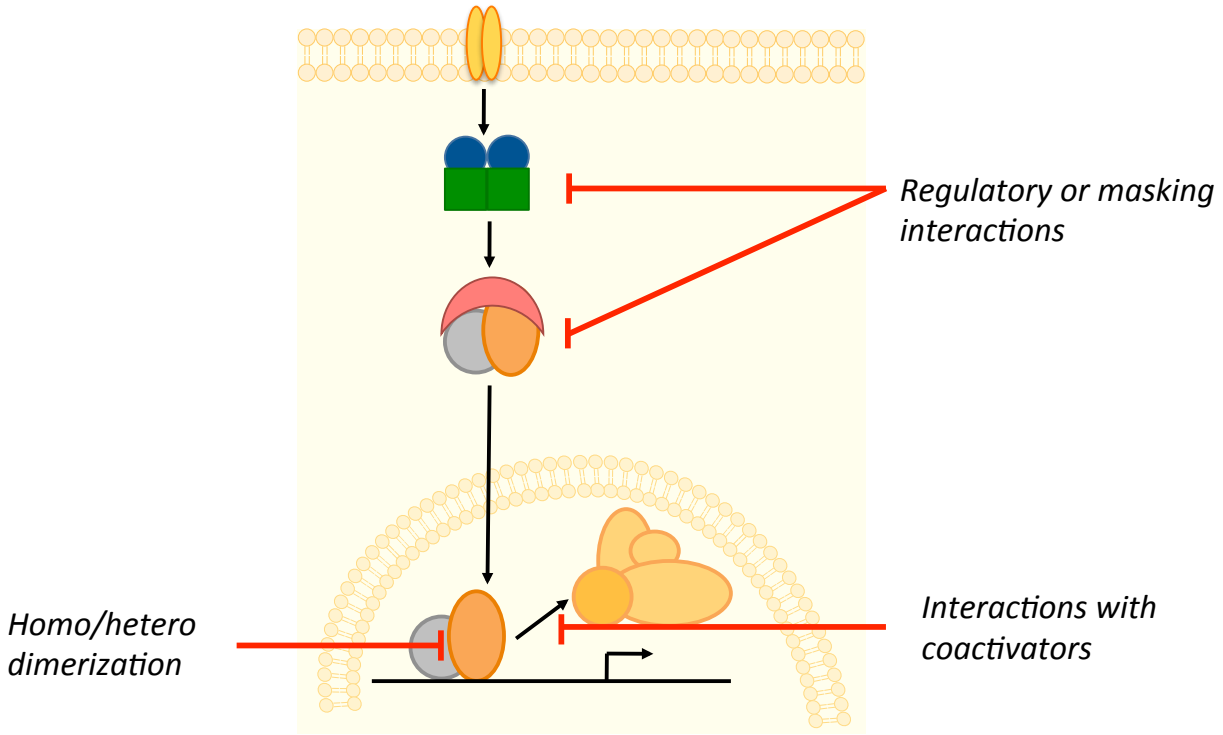

Figure 1.3 Inhibition strategies for transcriptional activators Upon activation of a signaling pathway, there are a series of actions that take place including: activation of regulatory proteins, degradation of masking proteins, homo/heterodimerization of transcriptional activators, interaction with specific coactivators, and upregulation of target genes. These processes are all mediated by protein-protein interactions and represent possible sites of small molecule intervention.

Regulatory and masking proteins

The majority of transcriptional activator signaling pathways utilize either regulatory proteins, masking proteins, or a combination of the two when encountered by specific external or internal stimuli. In the MAPK/ERK pathway (mitogen-activated protein kinase/extracellular signal-regulated kinase), the epidermal growth factor receptor serves as a regulatory protein for the signaling cascade leading to activation of transcriptional activators CREB and c-Myc. [26-28] Activation of MAPK/ERK pathway is accomplished through the epidermal growth factor receptor (EGFR) binding the extracellular ligand epidermal growth factor (EGF). [29,30] This external stimulus causes the tyrosine kinase domain of EGFR to be activated, leading to autophosphorylation of several C-terminal tyrosine residues, a common post-translational modification used to activate signaling pathways. This

phosphorylated domain of EGFR causes an activation cascade of several other proteins including RAS, RAF, MEK, and MAPK.[31] This signaling cascade ultimately results in activation of transcriptional activators CREB and c-Myc and upregulation of their respective target genes. The above example highlights the importance of EGFR as a regulator protein in the MAPK/ERK signaling pathway. In the absence of the EGF ligand, EGFR inhibits the rest of the pathway from being activated.

Whereas regulator proteins tend to function as the "master switch" for signaling pathways, masking proteins serve as protein inhibitors, sequestering transcriptional activators until needed. The canonical example when discussing masking proteins in signaling pathways is the p53-Mdm2 protein-protein interaction. The tumor protein 53 (p53) pathway is important in humans due to the role of the p53 transcriptional activator as a tumor suppressor.[32] When cells experience stressors such as genotoxic stress or DNA damage, p53 is phosphorylated, causing the masking protein Mdm2 to release p53, allowing localization to the nucleus and upregulation of target genes for survival.[33] In the absence of genotoxic stress, Mdm2 binds to p53, causing p53 to localize to the cytosol and remain inactive by sequestering the TAD of p53.[34] Interestingly, some pathways use a combination of regulatory and masking proteins in order to regulate activity of transcriptional activators. NF-κB can respond to numerous stimuli such as DNA damage, chemokines, as well as chemokines.[35] In the presence of any of these stimuli, the NF-κB essential modulator (NEMO) serves as a regulatory protein, promoting assembly of the activation complex required for NF-κB activation.[36] Upon assembly of the activation complex, the complex will go on to phosphorylate the inhibitor of κB (IκB), a masking protein of the NF-κB transcriptional activator. Phosphorylation of IκB promotes the release of the transcriptional activator NF-κB, localization to the nucleus, and upregulation of NF-κB target genes (Figure 1.4).[37]

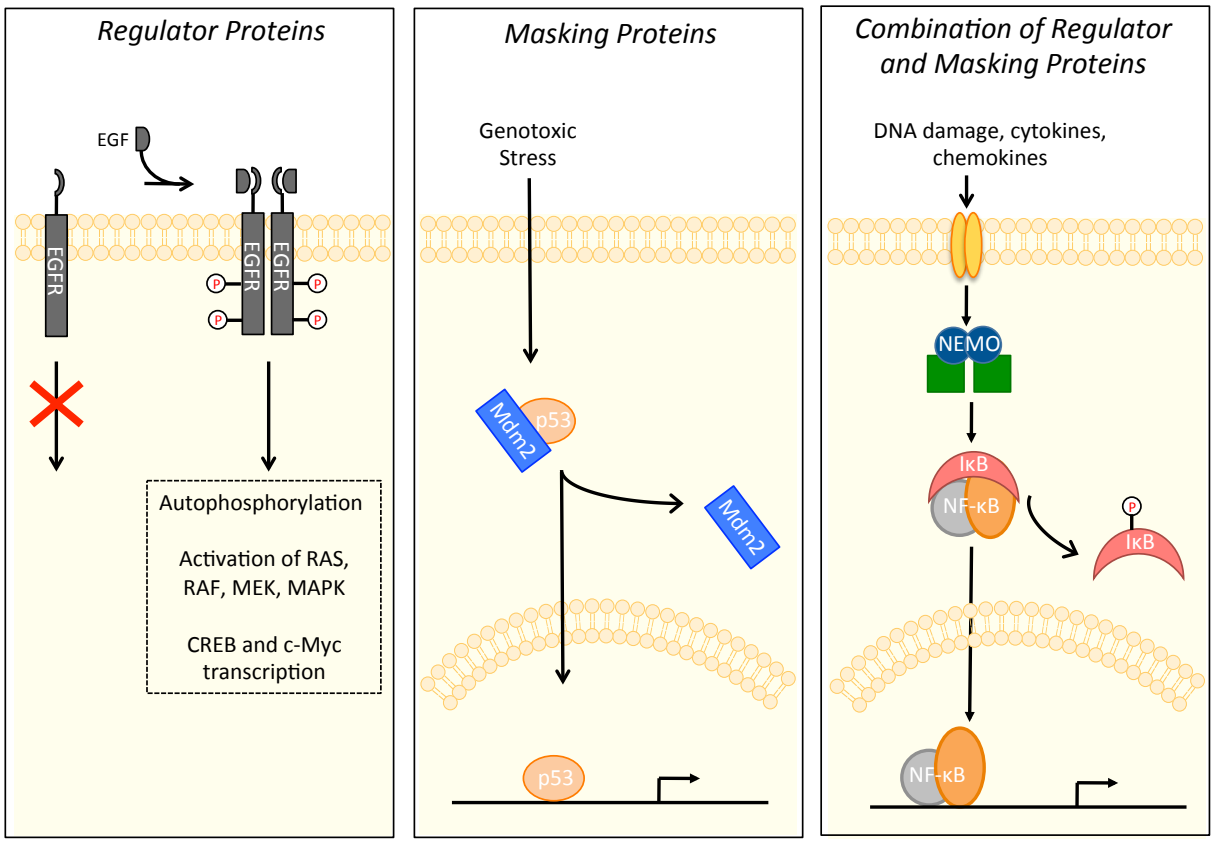

Figure 1.4 Representation of regulatory and masking proteins in transcriptional activator signaling pathways *Left panel:* In the MAPK/ERK pathway, the EGFR protein serves a regulatory protein that serves as the "master switch" for activation of the pathway. Only upon binding EGF will EGFR be activated, causing a signal cascade and activation of several downstream proteins. *Middle panel*: Mdm2 is the canonical example used to illustrate the role of masking proteins in transcriptional activator signaling pathways. In an inactive state, the p53 transcriptional activator is bound by the masking protein Mdm2 causing it to be sequestered it in the cytosol. The presence of external stimuli such as genotoxic stress causes release of p53 from the Mdm2 masking protein and upregulation of p53 target genes. *Right panel:* In the NF-κB transcriptional activator signaling pathway both regulatory and masking proteins are used to regulate activation. The NEMO protein serves as the regulatory protein needed to assembly of the activation complex. This activation complex goes on to phosphorylate IκB, the masking protein. This causes release of the NF-κB transcriptional activator and upregulation of NF-κB target genes.

Homo/heterodimerization of transcriptional activators

Through the use of regulatory and masking proteins, cells have adapted efficient mechanisms for activating transcriptional activator pathways in order to respond to the various stimuli encountered. However, evolutionarily, it would not have been beneficial for cells to only adapt methods for simple activation or inactivation of transcriptional activator

pathways. This would cause every target gene of the respective transcriptional activator to be upregulated, a crude mechanism for regulating responses to stimuli. In order to tighten regulation of the mechanism for activation, transcriptional activator signaling pathways have evolved to add an additional layer of regulation through the use of transcriptional activator homo/heterodimerization.[38] Subtle differences in the promoter sequence of a target gene can select for one specific dimer while another gene promoter site can select for a completely different dimer. Homo/heterodimers of transcriptional activators will have different inherent activities associated with them in addition to the fact that different target genes will prefer different dimers, providing transcriptional activator pathways additional control over the expression of target genes. One example of homo-/heterodimerization regulation of target gene expression is NF-κB, which is composed of five transcriptional activators that can homo/heterodimerize to regulate various processes. The NF-κB transcriptional activator consists of: RelA/p65, RelB, c-Rel, p50, and p52. All of the proteins can homodimerize with the exception of RelB, but numerous different heterodimers can be formed. The combinatorial control that NF- κB utilizes to form various homo/heterodimers can be used to express completely different sets of target genes as depicted in Table 1.1.[39]

Table 1.1 NF-κB proteins and the role of various homo/heterodimers

NF-κB Protein	Proposed dimerization partners	Selected target genes
p65/RelA	p65-p65 homodimer p65-p50 p65-c-Rel	IL-8, type-VII collagen, ICAM1 IκBα, IL-8, IL-6, TNFα, GM-CSF, HIV1 uPA, IL2Rα, MCP-1
RelB	no homodimer RelB-p50 RelB-p52	 MDC SLC, ELC, MDC
c-Rel	c-Rel—c-Rel homodimer c-Rel-p50	IL-8 IL-12/p40, IL-12/p35, IL2Rα
p50	p50-p50 homodimer p50-BCL3	TNFα, IL-6, MHCII BCL2
p52	p52-p52 homodimer P52-BCL3	MHCII Cyclin D1, BCL2

Transcriptional activator interactions with coactivators

Current models suggest that transcriptional activators must recruit multiple protein complexes in order to carry out the process of transcription. DNA is organized as chromatin, a compacted form in which the DNA is wound around histones. Early in transcription initiation, transcriptional activators recruit chromatin remodeling complexes such as Swi/Snf and SAGA in order to alter chromatin structure, causing the target gene to be more accessible.[40] Once chromatin remodeling has taken place, transcriptional activators recruit coactivators to the target gene promoter site.[41] These coactivators serve as a "bridge" between the transcriptional activator and the transcriptional machinery that includes RNA Pol II, the protein that carries out synthesis of the target gene mRNA (Figure 1.5).

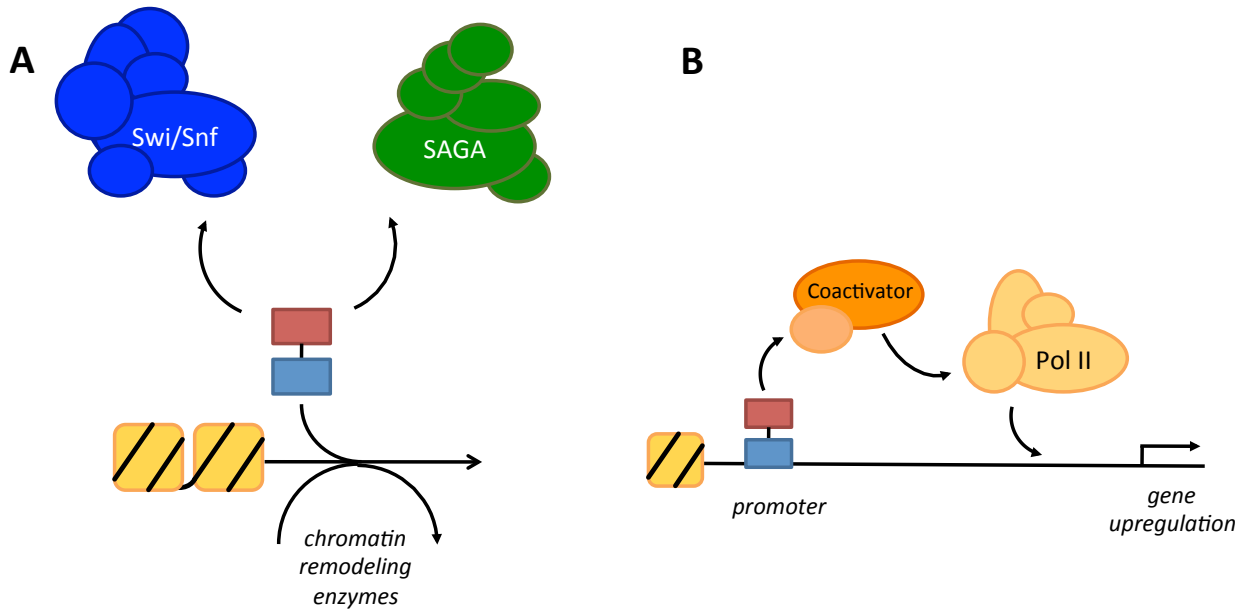

Figure 1.5 Protein complexes recruited by transcriptional activators A. Transcriptional activators will initially recruit complexes such as Swi/Snf and SAGA in order to reorganize chromatin structure at the target gene more accessible. B. After chromatin remodeling enzymes act on the target gene promoter site, coactivators will be recruited resulting in assembling the transcriptional machinery and target gene upregulation.

As demonstrated in the previous sections, transcriptional activation is a multi-layered process with multiple sites of regulation including: regulatory and masking proteins, homo-/heterodimerization of transcriptional activators, and specific contacts with coactivators

and other subunits of the transcriptional machinery. The common thread between all of these processes is that they utilize many different PPIs in order to accomplish the aforementioned processes. In order to externally modulate the transcriptional process, then targeting these different PPI functional classes with small molecules is required and as outlined, in the subsequent section, there are unique challenges associated with each type of PPIs.

1.5 Protein-protein interactions (PPIs)

Cellular functions are carried out by a myriad of protein complexes. These protein complexes are traditionally made up of at least one enzyme protein and several non-enzyme proteins.[42] The proteins involved in these protein complexes are often assembled in a combinatorial manner with the specific combination of proteins in the complex dictating the location, duration, and manner that the enzymatic activity is performed. Historically, efforts have focused on targeting the enzymatic activity of these complexes; however, with more than 650,000 estimated PPIs, less than 0.01% of these interactions have been successfully targeted with small molecules.[43] This presents an incredible opportunity and immense therapeutic potential to find additional inhibitors. Although the idea of targeting protein-protein interactions has been around for several years, these interactions have largely been classified as "undruggable" due to the challenges associated with targeting them.[44]

In contrast with protein-ligand interactions, protein-protein interactions are much larger and lack surface topology. Protein-protein interactions occur over an average surface area of 1940 $\pm$ 760 Å^2 and these interactions can use a small number of residues or a large number of residues to facilitate binding.[45] Consistent with the range of residues facilitating binding, the affinities of these interactions can span from picomolar to millimolar affinities.[46] The visual representation of the ranges and affinities that protein-protein interactions use can be seen in Figure 1.6. Unsurprisingly, the high-affinity, low surface area interactions have been the most successfully targeted PPIs. This is largely due to the fact that these interactions most closely resemble protein-ligand interactions, with very few molecules targeting large surface area protein-protein interactions. This is mostly

due to the fact that large surface areas tend to use several residues to facilitate binding to its target protein. Additionally, deciphering which residues contribute most to the binding free energy of two proteins, more commonly known as "hot spots", is not a easy task, making small molecule discovery and design efforts immensely challenging. [47,48]

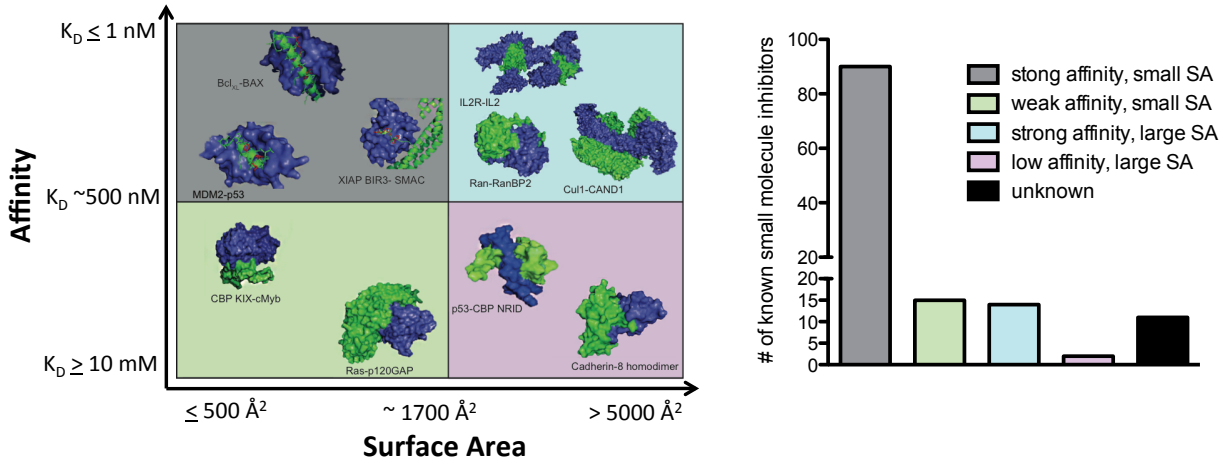

Figure 1.6 Scope of protein-protein interactions The left panel is a visual representation of the affinity and surface area of various characterized protein-protein interactions. The right panel illustrates the number of small molecule inhibitors that have been developed for the various classes of protein-protein interactions.

1.6 Targeting protein-protein interactions

Using small molecules to target PPIs

Small molecule inhibitors have tremendous potential as both tools to study cellular signaling pathways as well as potential therapeutics. Having the ability to develop highly specific inhibitors has the potential to provide a tool molecule for further functional studies of cellular signaling pathways.[49,50] During the nascent period of drug discovery and development, strategies for identifying new drugs involved using anecdotal evidence to identify potential sources. It was not until the late 20th century, with greater implementation of molecular biology, that we were able to gain a better understanding of the molecular mechanism associated with different diseases and conditions. This provided us with greater knowledge of the signaling pathways involved in various diseases and conditions, but more importantly, this knowledge provided scientists with target proteins that could be used for rational design of inhibitors. [51,52] By targeting a specific protein that is dysregulated in the disease state, side effects can be mitigated. This is in comparison to earlier chemotherapeutics that simply targeted the fastest growing cells.[53] Unfortunately,

there are often a great number of proteins that are dysregulated in a disease, making it difficult to initially target the necessary protein for the desired biological effect.

Due to both the costly and timely endeavor associated with developing a drug, it would be beneficial to have methods of speeding up the drug discovery process. By developing chemical probes targeted at a specific protein of interest, we can afford ourselves the ability to investigate the cellular effects of inhibiting a targeted protein.[54] Although chemical probes are not drugs, we can use these probes to give us new insights into the molecular mechanism of a disease on a cellular level and in some cases, even in animals.[55] These probes are not drugs, but they can give us a good idea of the therapeutic potential of developing a drug for the targeted protein. This is due to the ability of chemical probes to effectively mimic the function of a drug. There are a number of diseases that lack targeted drugs including some types cancers and most neurological diseases such as Alzheimer's and Parkinson's disease. Using chemical probes in combination with molecular biology will aid in speeding up the process of future drug discovery efforts as well as identifying potential target proteins associated with the disease state.

Challenges of targeting PPIs

Protein-protein interactions have traditionally been defined as "undruggable", this is largely due to the fact that many protein-protein interactions lack well-defined surface topology and occur over large areas. [56,57] This is problematic because classic drug discovery efforts have focused on protein-ligand interactions, which occur over small areas and are often associated with well-defined binding sites. The features of protein-ligand interactions make them well suited for small molecule screening efforts. The compound libraries used to carry out these screens are largely guided by Lipinski's rules, which are based on the observation that most orally administered drugs are relatively small and moderately lipophilic molecules. Unfortunately, only a small subclass of protein-protein interactions is amenable to screening with these types of small molecules, specifically the small surface area, tight affinity protein-protein interactions.[58] This is further evidenced by figure 1.6, which highlights the fact that over 70% of known inhibitors of protein-protein interactions target this specific subclass.

Strategies used to target PPIs

Protein-protein interactions that occur within protein complexes are mediated by specific contacts that are spatially arranged by the tertiary structure of the individual proteins. Tertiary structure of proteins is facilitated by both "regular" and "non-regular" structures at the interfaces of these PPIs.[59] "Regular" structures are classified as helical and strand residues, while "non-regular" structures include coils, turns, and loops. Although the design of inhibitors can be quite convoluted, peptides and other peptiomimetics are promising due to their ability to directly mimic specific secondary structure. β-turns and β-strands have been successfully mimicked using diverse libraries of small-molecule and peptide libraries.[60] Several strategies have been developed to mimic α-helices such as amphipathic chemical scaffolds,[61] as well as several peptidomimetic strategies such as side chain-to-side chain crosslinks,[62] back bone-to-side chain crosslinks,[63] and back bone-to-back bone crosslinks.[64] Other non-peptidic scaffolds have been used as well, including terphenyls and macrocycles.[65] These strategies have had varying degrees of success, but a recent study on PPI interface structure using the Protein Data Bank (PDB) demonstrated that 26% of interface residues have α-helical structure, 24% have β-strand secondary structure, and the remaining 50% have non-regular secondary structure, with this last category representing a tremendous opportunity to develop new inhibitors.[59]

Strategies used to target β-strand structure

Secondary structures containing β-turns and β-strands have been targeted using a combination of chemical and peptidomimetic strategies over the years. β-sheets consist of β-strands that interact with at least two or three backbone hydrogen bonds in either a parallel or anti-parallel orientation and are connected by β-turns. Nowick and coworkers pioneered several of the chemical strategies use to target β-sheet structure and interactions.[60] Their early efforts consisted of synthesis of a diurea turn, which they termed "molecular scaffold". This allowed for assembly of a hydrogen-bonded 10-membered ring, the same as seen in traditional β-turns. This led to further studies that indicated that this molecular scaffold could be used to make artificial β-sheets. This concept was further improved by the addition of 5-amino-2-methoxybenzoic acid amide into the peptide chain, allowing for enhanced folding and reduced uncontrolled intermolecular interactions. This

also allowed for synthesis of a template that better mimicked the pattern of hydrogen bonding observed in β-strands. In addition to these peptidomimetic strategies, other chemical scaffolds have been developed to mimic these β-sheet structures.[66] The work pioneered by the Nowick lab was later expanded on by Cheng and coworkers who used these methods to develop **ABSM 1a**, an inhibitor of Aβ aggregation with an EC_{50} < 1 μM.[67] Given the success of these peptidomimetic strategies to target β-sheets, Webb and coworkers later developed a chemical scaffold to mimic β-sheets. Webb and coworkers developed a chemical scaffold based on the Garland-Dean triangles, the connections of atoms that mimic the C-α atom positions in peptide β-turns. They were able to accomplish this through the use of a spirocycle chemical scaffold that contained four substituents, the same number of substituents in a β-turn. This strategy was used to develop new agonists of melanocortin type-4 receptor (MC4R), a G-coupled receptor, which has an IC_{50} of 5.6 μM.[68]

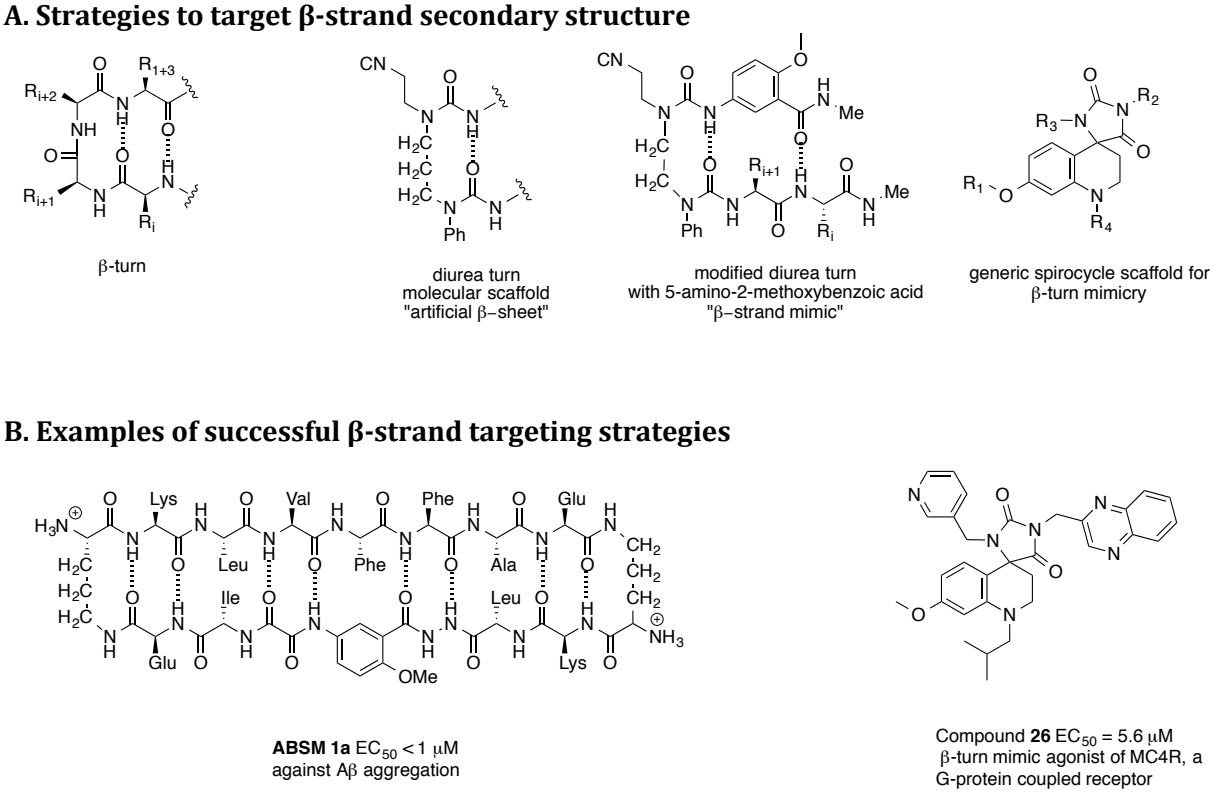

Figure 1.7 Targeting strategies for mimicking β-sheets A. A representation of the β-turn structure in a β-sheet with hydrogen bonding indicated. Peptidomimetic and chemical scaffolds developed to mimic β-turn and β-strand secondary structure. B. Examples of inhibitors developed using both peptidomimetic and chemical scaffolds.

Chemical strategies used to target α-helices

In addition to the development of peptidomimetic and chemical strategies used to target β-sheets, there has also been significant work done to target α-helices. These include both chemical and peptidomimetic strategies. Hamilton and coworkers have made significant contributions to targeting α-helices with chemical scaffolds through their development of terphenyl-based inhibitors. Hamilton demonstrated that regularly spaced terphenyls with substituents located in the ortho position of the aryl ring mimicked the spacing seen in α-helices, specifically the spacing of the i, i+4, and i+7 amino acid side groups in an α-helix. [65,69] This allowed for effective mimicking of the hydrophobic face of amphipathic helices and although effective for in-vitro applications, concerns about their solubility have limited their use for in-cellulo and other in-vivo applications. Mapp and coworkers demonstrated that isoxazolidines could also be used as mimics of amphipathic helices. Isoxazolidine **i1** was developed as a mimic of ESX and had a K_i of 620 nM for the target protein Med23.[70] More recently, other chemical scaffolds have been discovered as α-helix mimics. In one example, Majmudar and coworkers discovered sekikaic acid in a high-throughput screen of the MLL-KIX interaction using natural product extracts.[71] Deconvolution of the natural product extracts resulted in the discovery of sekikaic acid, a natural product derived from lichens. Computational modeling of sekikaic acid demonstrated that the lowest energy conformation of the molecule resembles an amphipathic helix, providing a possible mode of action for the inhibitor. The discovery of sekikaic acid suggests that other chemical scaffolds may exist in natural products that could later be developed as inhibitors of α-helices.

Peptidomimetic strategies used to α-helices

In addition to the development of α-helix chemical scaffolds, there has been considerable research and development devoted to peptidomimetic inhibitors of α-helices. Peptoids have had moderate success in mimicking α-helices, but the sterics-driven approach to inducing α-helicity has limited their use. [72,73] Other methods utilizing peptidomimetics with side-chain to side-chain, side-chain to backbone, and backbone-to-backbone crosslinks have yielded more promising results. Although some of the above strategies have employed using both lactams and disulfides, these functionalities are still susceptible to proteolysis through lysozymes and proteases. Verdine pioneered a new

method of peptide stabilization utilizing olefin metathesis to stabilize α-helix secondary structure, which he termed "peptide stapling".[74] Verdine and coworkers accomplished this "peptide stapling" strategy through the incorporation of unnatural olefin-containing amino acids that were incorporated during solid phase peptide synthesis.[75] Once the sequence was finished, olefin cross metathesis was performed to yield a "stapled peptide", trapping the peptide in an α-helical conformation. Verdine and coworkers demonstrated that these "staples" could be incorporated in a variety of ways, but the constructs that utilized a "staple" between the i and i+4 or i and i+7 position of a peptide yielded the most helical constructs, which also led to higher affinity for its target protein and enhanced protection from proteolysis.[76] This strategy was utilized to develop a peptidomimetic inhibitor based on the p53 sequence responsible for binding to the masking protein MDM2.[77] Incorporation of a "staple" on the solvent exposed face of the helix at the i and i+7 position resulted in a peptidomimetic inhibitor that was more proteolytically stable and had 8x greater affinity for MDM2 compared to the unmodified, wild-type p53 sequence. This "peptide stapling" strategy was also applied to other biological systems including BCL-2,[78] NOTCH,[79] and even resulted in the formation of the company Aileron Therapeutics, which now has one drug based on "stapled peptide" technology in phase II clinical trials. Although "stapled peptide" technology works well for amphipathic α-helices with well-defined hydrophilic and hydrophobic faces, it can cause problems for interfaces that rely on amino acid side chains located on the solvent exposed face for recognition and specificity.[80] In order to circumvent this problem, Arora and coworkers have developed hydrogen bond surrogates (HBS).[81] These HBS peptides utilize a side chain-to-backbone crosslink also utilizing olefin metathesis. The additional benefit afforded by HBS peptides is that they utilize only one amino acid side chain to stabilize α-helical formation. This is particular advantageous for systems that do not allow for modification or substitution of solvent exposed residues. This strategy was utilized to develop an inhibitor of the p300 CH1 domain using an HBS of HIF 1α.[63] The HIF 1α HBS was based on the portion of the sequence required for binding to CH1 and resulted in an inhibitor with 2x greater affinity for the CH1 domain compared to the unmodified sequence. HIF 1α HBS was also demonstrated to have an IC_{50} of 1 μM against HIF 1α-mediated transcription, whereas the unmodified sequence had no inhibitory effects presumably due to proteolytic degradation. To a lesser extent,

cyclic peptides containing a backbone-to-backbone cyclization have also been identified as inhibitors of α-helices. The natural product chlorofusin was identified as an inhibitor of the p53-HDM2 interaction,[82] however, development of cyclic peptides as inhibitors of α-helices has been limited due to the fact that the spacing of the amino acid side chains are not oriented in in the correct 3-dimensional space to inhibit α-helices.

A. Chemical strategies for targeting α-helical secondary structure

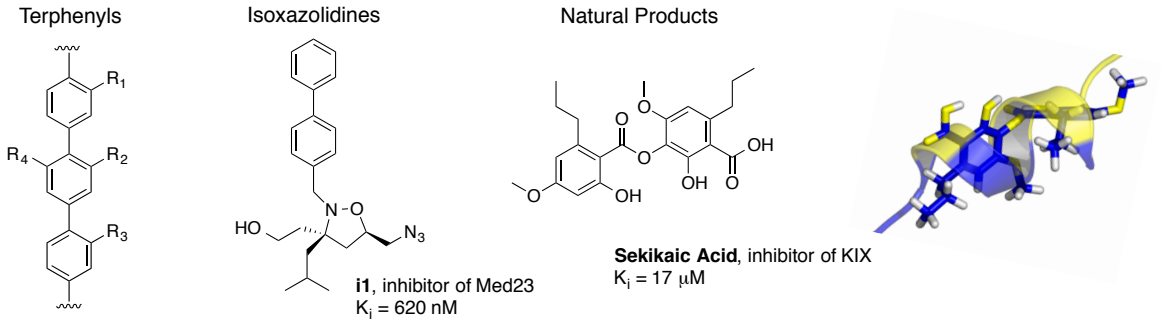

B. Peptidomimetic strategies for targeting α-helical secondary structure

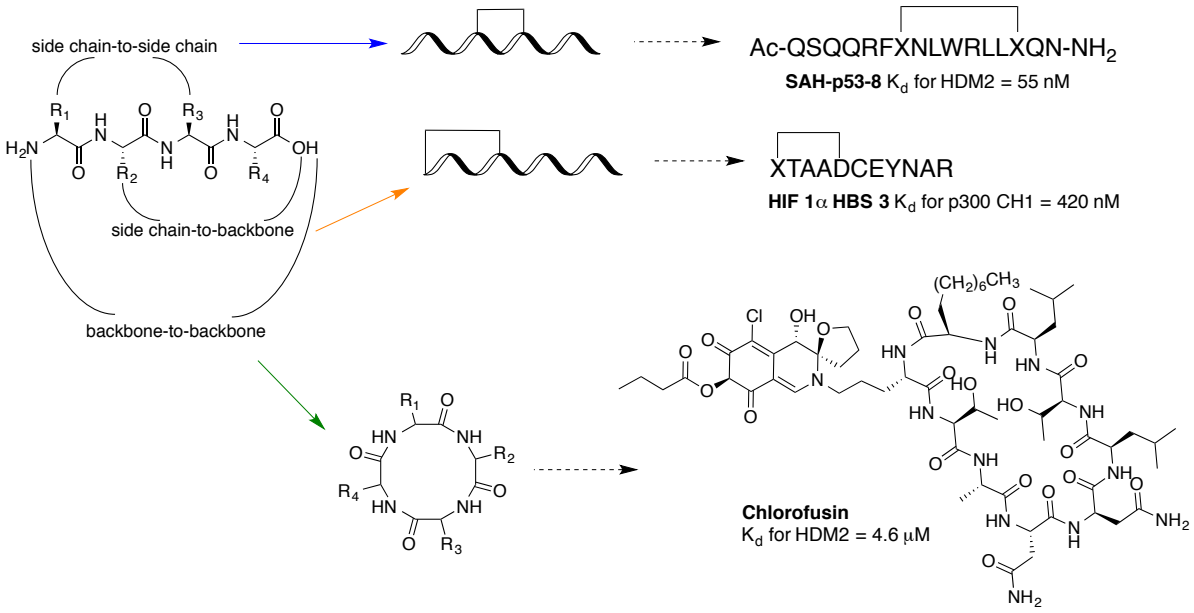

Figure 1.8 Targeting strategies for mimicking α-helices A. Examples of chemical scaffolds that have been utilized to target α-helices. B. Peptidomimetic strategies developed to target α-helices.

Strategies for targeting non-regular secondary structure

Although there has been considerable success mimicking the β-sheet and α-helix secondary structure, this secondary structure only accounts for half of the types of structure found at protein-protein interfaces.[59] The Kritzer group has recently highlighted the vast number of "non-regular" structure involved at the interface of protein-protein interactions.[83] This non-regular structure consists of turns, coils and loops. Furthermore, Kritzer et al. have demonstrated that several of these non-regular secondary structures exist within the structures submitted to the PDB. A systematic screen of the PDB yielded 25,005 non-redundant loops, representing a large number of possible sites for mimicking with chemical or peptidomimetic strategies. These interface loops were then sorted by the presence and location of hot spot residues, with hot spots defined as $\Delta\Delta G_{residue} \geq 1$ kcal mol^{-1}. To further refine this data, Kritzer et al identified "hot loops", which were determined by identification of loops with two consecutive hot spots, loops with at least three hot spots, and loops for which the average $\Delta\Delta G_{residue}$ was greater than 1 kcal mol^{-1}. This further refinement, resulted in identification of 1,407 hot loops. Additionally, the total predicted binding energy associated with the hot loop was compared to the total predicted binding energy of the corresponding interface. This examination revealed that 36% of hot loops are responsible for over half of the predicted binding energy associated with an interface and 67% of hot loops are responsible for more than a quarter of the predicted binding energy associated with an interface. Given the substantial percentage of binding energy contributed by hot loops, these hot loops serve as ideal starting points for identifying new inhibitors.

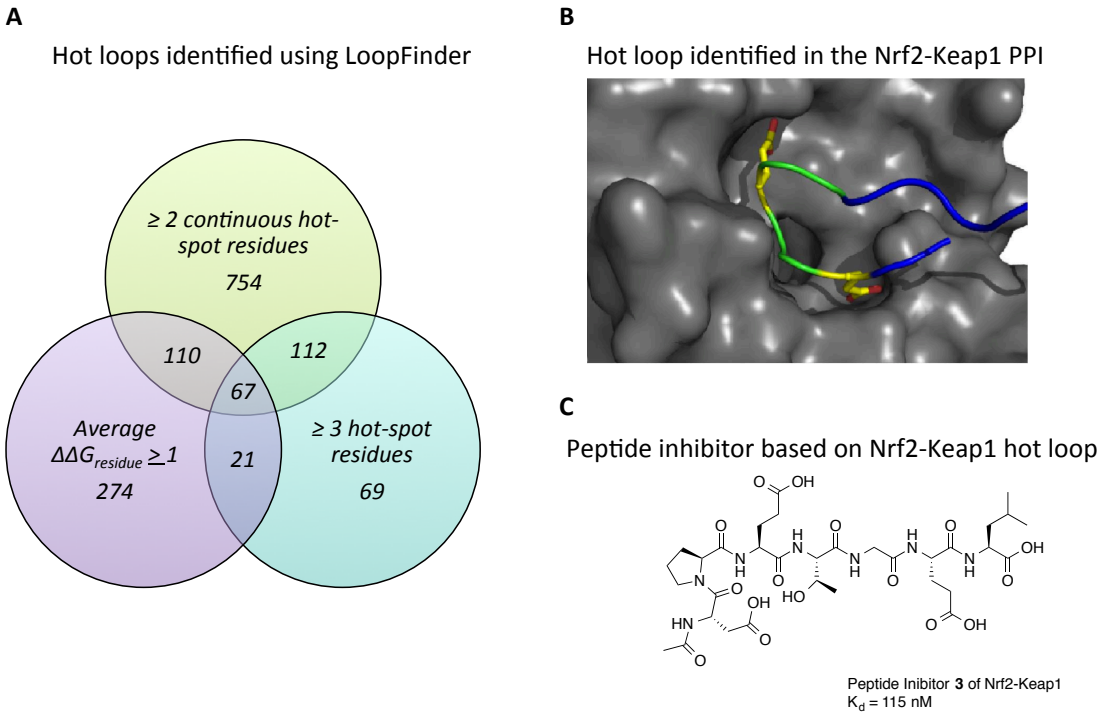

Figure 1.9 Overview of PPI hot loop identification A. Overview of analysis performed using LoopFinder B. Example of hot loop identified by LoopFinder analysis C. Peptide inhibitor developed based on Nrf2-Keap1 hot loop.

One of the loops that LoopFinder was able to identify was a β-hairpin loop in the Nrf2-Keap1 PPI. The full length interaction between Nrf2-Keap1 has a K_d of 5-9 nM[84] and peptides developed based on this hot loop possessed a K_d of 115 nM, similar to the full length interaction. More recently, development of macrocyclic peptides derived from this loop have been able to attain IC_{50} values in the 15 nM range.[85] In the Nrf2-Keap1 example, LoopFinder was able to identify a hot loop that has resulted in inhibitory peptides with low nanomolar affinities and validates other potential hot loops for inhibitor development.

1.7 Strategies for targeting low affinity, large surface area PPIs

Highlighted above are strategies that have been developed for targeting PPIs, as well as how several of these strategies are tailored to low surface area, high affinity PPIs. One of the challenges of using these strategies for targeting low affinity, large surface area interactions is developing selective inhibitors. In the case of helix mimetic **i1** (Figure 1.8 A), only modest selectivity can be achieved. There is only 1.5 fold selectivity in IC_{50} for erbB2+ SkBr3 breast cancer cells compared to non-tumorigenic IMR90 cells.[70] This is not entirely

surprising since transcriptional activators initiate transcription through a complex series of low affinity PPIs with domains of coactivators that are designed to accommodate a variety of non-homologous activation domains. This suggests that there may be a limit to the affinity and biological activity that can be achieved using small molecules or short peptidomimetics. Although this selectivity is modest and prohibits further development of **i1** as drug to be used as a single agent, **i1** can be utilized in combination therapy. Taylor et al demonstrated how **i1**, an inhibitor of ESX-mediated erbB2 protein expression, and other existing therapeutic inhibitors of erbB2 activity lead to dose reductions of greater than 15-fold for both agents and increased selectivity for erbB2+ cells up to 30-fold.[86] This strategy is readily applicable to other systems and will be highlighted in chapter 2.

The aberrant function of transcriptional activators is associated with human diseases such as cancer. Developing small molecules that can inhibit that ability of transcriptional activators to control target gene expression have immense potential as both biochemical tools and therapeutics. One of the challenges of targeting the interactions between transcriptional activators and the transcriptional machinery proteins is that these interactions are transient, their affinities are modest (high nanomolar to low micromolar), and often bind over large surface areas. Traditional small molecules are not well suited for screening against these interactions due to their development for small surface area, high affinity PPIs. One strategy that has had some success for targeting these types of interactions has been screening against natural product extracts. A screen against the MLL-KIX interaction identified sekikaic acid and lobaric acid, a depside and depsidone isolated from lichens. Molecular dynamics modeling of these molecules demonstrated that the lowest energy conformation resembled an amphipathic α-helix, providing a possible mode of action for these depside and depsidone inhibitors. In chapter 3 we will show how a high-throughput screen of the Med25-VP16 interaction using natural product extracts can yield additional amphipathic molecules capable of inhibiting this PPI.

Given the importance of "non-regular" secondary structure at the interface of protein-protein interactions, macrocycles and cyclic peptides have garnered renewed interest as potential therapeutics. There are several efforts ongoing in both industry and academia for identifying new macrocycles and cyclic peptides; however, these two scaffolds are unlikely to be able to target all possible hot loop types at PPIs. Given the need

for additional strategies, new peptidomimetic and chemical strategies need to be developed to target other types of hot loops. In chapter 4, we will present a unique, novel constrained peptide strategy developed based on a hot loop identified in the IKK-NEMO interface.

1.8 References

(1) Lockhart, D. J.; Winzeler, E. A. Genomics, Gene Expression and DNA Arrays. *Nature* **2000**, *405*, 827–836.

(2) Lenardo, M. J.; Baltimore, D. NF-κB: a Pleiotropic Mediator of Inducible and Tissue-Specific Gene Control. *Cell* **1989**, *58*, 227–229.

(3) Greene, C. S.; Krishnan, A.; Wong, A. K.; Ricciotti, E.; Zelaya, R. A.; Himmelstein, D. S.; Zhang, R.; Hartmann, B. M.; Zaslavsky, E.; Sealfon, S. C.; Chasman, D. I.; FitzGerald, G. A.; Dolinski, K.; Grosser, T.; Troyanskaya, O. G. Understanding Multicellular Function and Disease with Human Tissue-Specific Networks. *Nat. Genet.* **2015**. Advance online publication. doi:10.1038/ng.3259

(4) Lukas, J.; Lukas, C.; Bartek, J. Mammalian Cell Cycle Checkpoints: Signalling Pathways and Their Organization in Space and Time. *DNA Repair* **2004**, *3*, 997–1007.

(5) Tworkowski, K. A.; Salghetti, S. E.; Tansey, W. P. Stable and Unstable Pools of Myc Protein Exist in Human Cells. *Oncogene* **2002**, *21*, 8515–8520.

(6) Ptashne, M. Gene Regulation by Proteins Acting Nearby and at a Distance. *Nature* **1985**, *322*, 697-701.

(7) Giudici, M.; Goni, S.; Fan, R.; Treuter, E. Nuclear Receptor Coregulators in Metabolism and Disease. *Handb Exp Pharmacol* **2015**, 1–41.

(8) Cha, J.-H. J. Transcriptional Dysregulation in Huntington's Disease. *Trends in Neurosciences* **2000**, *23*, 387–392.

(9) Baldwin, A. S., Jr. Series Introduction: the Transcription Factor NF-κB and Human Disease. *Journal of Clinical Investigation* **2001**, *107*, 3-6.

(10) Ptashne, M.; Gann, A. *Genes and Signals*; CSHL Press, 2002.

(11) Chen, X.; Xu, H.; Yuan, P.; Fang, F.; Huss, M.; Vega, V. B.; Wong, E.; Orlov, Y. L.; Zhang, W.; Jiang, J.; Loh, Y.-H.; Yeo, H. C.; Yeo, Z. X.; Narang, V.; Govindarajan, K. R.; Leong, B.; Shahab, A.; Ruan, Y.; Bourque, G.; Sung, W.-K.; Clarke, N. D.; Wei, C.-L.; Ng, H.-H. Integration of External Signaling Pathways with the Core Transcriptional Network in Embryonic Stem Cells. *Cell* **2008**, *133*, 1106–1117.

(12) Göttgens, B. Regulatory Network Control of Blood Stem Cells. *Blood* **2015**, *125*, 2614–2620.

(13) Lee, L. W.; Mapp, A. K. Transcriptional switches: chemical approaches to gene regulation. *J. Biol. Chem.* **2010**, *285*, 11033-11038.

(14) Højfeldt, J. W.; Van Dyke, A. R.; Mapp, A. K. Transforming Ligands Into Transcriptional Regulators: Building Blocks for Bifunctional Molecules. *Chemical Society Reviews* **2011**, *40*, 4286–4294.

(15) Mapp, A. K.; Ansari, A. Z. A TAD Further: Exogenous Control of Gene Activation. *ACS Chem. Biol.* **2007**, *2*, 62–75.

(16) Yang, F.; DeBeaumont, R.; Zhou, S.; Näär, A. M. The Activator-Recruited Cofactor/Mediator Coactivator Subunit ARC92 Is a Functionally Important Target of the VP16 Transcriptional Activator. *Proc Natl Acad Sci USA* **2004**, *101*, 2339–2344.

(17) Vojnic, E.; Mourão, A.; Seizl, M.; Simon, B.; Wenzeck, L.; Larivière, L.; Baumli, S.; Baumgart, K.; Meisterernst, M.; Satler, M.; Cramer, P. Structure and VP16 Binding of the Mediator Med25 Activator Interaction Domain. *Nat Struct Mol Biol* **2011**, *18*, 404-409.

(18) Milbradt, A. G.; Kulkarni, M.; Yi, T.; Takeuchi, K.; Sun, Z. Y.; Luna, R. E.; Selenko, P.; Näär, A. M.; Wagner, G. Structure of the VP16 Transactivator Target in the Mediator. *Nat Struct Mol Biol* **2011**, *18*, 410-415.

(19) Asada, S.; Choi, Y.; Yamada, M.; Wang, S.-C.; Hung, M.-C.; Qin, J.; Uesugi, M. External Control of Her2 Expression and Cancer Cell Growth by Targeting a Ras-Linked Coactivator. *Proc Natl Acad Sci USA* **2002**, *99*, 12747–12752.

(20) Makarov, S. S. NF-kappaB in Rheumatoid Arthritis: a Pivotal Regulator of Inflammation, Hyperplasia, and Tissue Destruction. *Arthritis Res.* **2001**, *3*, 200-206.

(21) Strickland, I.; Ghosh, S. Use of Cell Permeable NBD Peptides for Suppression of Inflammation. *Ann. Rheum. Dis.* **2006**, *65*, 75–82.

(22) Akira, S.; Gossen, M.; Kaufmer, J.; Triezenberg, S. J. *Transcription Factors*; Springer Science & Business Media, 2004.

(23) Li, S.; Huang, L. Nonviral Gene Therapy: Promises and Challenges. *Gene Therapy* **2000**, *7*, 31-34.

(24) Ferrari, M. Cancer Nanotechnology: Opportunities and Challenges. *Nature Reviews Cancer* **2005**, *5*, 161-171.

(25) Donnelly, J. J.; Wahren, B.; Liu, M. A. DNA Vaccines: Progress and Challenges. *J Immunol* **2005**, *175*, 633-639.

(26) Lee, H. Y.; Crawley, S.; Hokari, R.; Kwon, S.; Kim, Y. S. Bile Acid Regulates MUC2 Transcription in Colon Cancer Cells via Positive EGFR/PKC/Ras/ERK/CREB, PI3K/Akt/IκB/NF-κB and P38/MSK1/CREB Pathways and Negative JNK/C-Jun/AP-1 Pathway. *International Journal of Oncology* **2010**, *36*, 941–953.

(27) Iguchi, H.; Mitsui, T.; Ishida, M.; Kanba, S.; Arita, J. cAMP Response Element-Binding Protein (CREB) Is Required for Epidermal Growth Factor (EGF)-Induced Cell Proliferation and Serum Response Element Activation in Neural Stem Cells Isolated from the Forebrain Subventricular Zone of Adult Mice. *Endocrine Journal* **2011**, *58*, 747-759.

(28) Jorissen, R. N.; Walker, F.; Pouliot, N.; Garrett, T. Epidermal Growth Factor Receptor: Mechanisms of Activation and Signalling. *Experimental Cell Research* **2003**, *284*, 31-53.

(29) Yoshida, K.; Kyo, E.; Tsuda, T.; Tsujino, T. EGF and TGF-A, the Ligands of Hyperproduced EGFR in Human Esophageal Carcinoma Cells, Act as Autocrine Growth Factors. *International Journal of Cancer* **1990**, *45*, 131-135.

(30) Mendelsohn, J.; Baselga, J. The EGF Receptor Family as Targets for Cancer Therapy. *Oncogene* **2000**.

(31) Santarpia, L.; Lippman, S. M. Targeting the MAPK-RAS-RAF Signaling Pathway in Cancer Therapy. *Expert opinion on ...* **2012**.

(32) Ryan, K. M.; Phillips, A. C.; Vousden, K. H. Regulation and Function of the P53 Tumor Suppressor Protein. *Current opinion in cell biology* **2001**.

(33) Kruse, J.-P.; Gu, W. Modes of P53 Regulation. *Cell* **2009**, *137*, 609–622.

(34) Lee, C. W.; Ferreon, J. C.; Ferreon, A. C. M.; Arai, M.; Wright, P. E. Graded Enhancement of P53 Binding to CREB-Binding Protein (CBP) by Multisite Phosphorylation. *Proc Natl Acad Sci USA* **2010**, *107*, 19290–19295.

(35) Hoesel, B.; Schmid, J. A. The Complexity of NF-κB Signaling in Inflammation and Cancer. *Mol. Cancer* **2013**, *12*, 86.

(36) Makris, C.; Godfrey, V. L.; Krähn-Senftleben, G.; Takahashi, T.; Roberts, J. L.; Schwarz, T.; Feng, L.; Johnson, R. S.; Karin, M. Female Mice Heterozygous for IKK Gamma/NEMO Deficiencies Develop a Dermatopathy Similar to the Human X-Linked Disorder Incontinentia Pigmenti. *Mol Cell* **2000**, *5*, 969–979.

(37) Rothwarf, D. M.; Zandi, E.; Natoli, G.; Karin, M. IKK-Gamma Is an Essential Regulatory Subunit of the IkappaB Kinase Complex. *Nature* **1998**, *395*, 297–300.

(38) Calkhoven, C.; Ab, G. Multiple Steps in the Regulation of Transcription-Factor Level and Activity. *Biochem J* **1996**, *317*, 329-342.

(39) Chen, L.-F.; Greene, W. C. Shaping the Nuclear Action of NF-κB. *Nat Rev Mol Cell Biol* **2004**, *5*, 392–401.

(40) Peterson, C. L.; Workman, J. L. Promoter Targeting and Chromatin Remodeling by the SWI/SNF Complex. *Current Opinion in Genetics & Development* **2000**, *10*, 187-192.

(41) Yudkovsky, N.; Logie, C.; Hahn, S. Recruitment of the SWI/SNF Chromatin Remodeling Complex by Transcriptional Activators. *Genes & Development* **1999**, *13*, 2369-2374.

(42) Thompson, A. D.; Dugan, A.; Gestwicki, J. E.; Mapp, A. K. Fine-Tuning Multiprotein Complexes Using Small Molecules. *ACS Chem. Biol.* **2012**, *7*, 1311–1320.

(43) Overington, J. P.; Al-Lazikani, B.; Hopkins, A. L. How Many Drug Targets Are There? *Nature Reviews Drug Discovery* **2006**, *5*, 993-996.

(44) Verdine, G. L.; Walensky, L. D. The Challenge of Drugging Undruggable Targets in Cancer: Lessons Learned From Targeting BCL-2 Family Members. *Clinical Cancer Research* **2007**, *13*, 7264–7270.

(45) Fuller, J. C.; Burgoyne, N. J.; Jackson, R. M. Predicting Druggable Binding Sites at the Protein–Protein Interface. *Drug Discovery Today* **2009**, *14*, 155-161.

(46) Nooren, I.; Thornton, J. M. Diversity of Protein–Protein Interactions. *EMBO J* **2003**, *22*, 3486-3492.

(47) Bogan, A. A.; Thorn, K. S. Anatomy of Hot Spots in Protein Interfaces. *J. Mol. Biol.* **1998**, *208*, 1-9.

(48) Arkin, M. R.; Wells, J. A. Small-Molecule Inhibitors of Protein-Protein Interactions: Progressing Towards the Dream. *Nat Rev Drug Discov* **2004**, *3*, 301–317.

(49) Lamb, J.; Crawford, E. D.; Peck, D.; Modell, J. W.; Blat, I. C. The Connectivity Map: Using Gene-Expression Signatures to Connect Small Molecules, Genes, and Disease. *Science* **2006**, *313*, 1929-1935.

(50) Schreiber, S. L. The Small-Molecule Approach to Biology. *Chem Eng News,* **2003**.

(51) Hopkins, A. L.; Groom, C. R. The Druggable Genome. *Nat Rev Drug Discov* **2002**, *1*, 727–730.

(52) Dobson, C. M. Chemical Space and Biology. *Nature* **2004**, *432*, 824–828.

(53) Kerr, J. F. R.; Winterford, C. M.; Harmon, B. V. Apoptosis. Its Significance in Cancer and Cancer Therapy. *Cancer* **1994**, *73*, 2013–2026.

(54) Heal, W. P.; Dang, T. H. T.; Tate, E. W. Activity-Based Probes : Discovering New Biology and New Drug Targets. *Chemical Society Reviews* **2011**, *40*, 246–257.

(55) Frye, S. V. The Art of the Chemical Probe. *Nat. Chem. Biol.* **2010**, *6*, 159–161.

(56) Betzi, S.; Guerlesquin, F.; Morelli, X. Protein-Protein Interaction Inhibition (2P2I): Fewer and Fewer Undruggable Targets. *CCHTS* **2009**, *12*, 968–983.

(57) Makley, L. N.; Gestwicki, J. E. Expanding the Number of "Druggable" Targets: Non-Enzymes and Protein–Protein Interactions. *Chem Biol Drug Des* **2013**, *81*, 22–32.

(58) Zinzalla, G.; Thurston, D. E. Targeting Protein–Protein Interactions for Therapeutic Intervention: a Challenge for the Future. *Future Medicinal Chemistry* **2009**, *1*, 65–93.

(59) Guharoy, M.; Chakrabarti, P. Secondary Structure Based Analysis and Classification of Biological Interfaces: Identification of Binding Motifs in Protein-Protein Interactions. *Bioinformatics* **2007**, *23*, 1909–1918.

(60) Nowick, J. S. Exploring Beta-Sheet Structure and Interactions with Chemical Model Systems. *Acc. Chem. Res.* **2008**, *41*, 1319–1330.

(61) Lee, L. W.; Mapp, A. K. Transcriptional Switches: Chemical Approaches to Gene Regulation. *Journal of Biological Chemistry* **2010**, *285*, 11033–11038.

(62) Walensky, L. D.; Pitter, K.; Morash, J.; Oh, K. J.; Barbuto, S.; Fisher, J.; Smith, E.; Verdine, G. L.; Korsmeyer, S. J. A Stapled BID BH3 Helix Directly Binds and Activates BAX. *Mol Cell* **2006**, *24*, 199–210.

(63) Henchey, L. K.; Kushal, S.; Dubey, R.; Chapman, R. N.; Olenyuk, B. Z.; Arora, P. S. Inhibition of Hypoxia Inducible Factor 1-Transcription Coactivator Interaction by a Hydrogen Bond Surrogate Alpha-Helix. *J. Am. Chem. Soc.* **2010**, *132*, 941–943.

(64) Illesinghe, J.; Guo, C. X.; Garland, R.; Ahmed, A. Metathesis Assisted Synthesis of Cyclic Peptides. *Chem Comm.* **2009**. *0*, 295-297.

(65) Hang Yin; Gui-in Lee; Kristine A Sedey; Olaf Kutzki; Hyung Soon Park; Brendan P Orner; Justin T Ernst; Hong-Gang Wang; Said M Sebti, A.; Andrew D Hamilton. Terphenyl-Based Bak BH3 A-Helical Proteomimetics as Low-Molecular-Weight Antagonists of Bcl-xL. *J. Am. Chem. Soc.* **2005**, *127*, 10191–10196.

(66) Liu, C.; Sawaya, M. R.; Cheng, P.-N.; Zheng, J.; Nowick, J. S.; Eisenberg, D. Characteristics of Amyloid-Related Oligomers Revealed by Crystal Structures of Macrocyclic B-Sheet Mimics. *J. Am. Chem. Soc.* **2011**, *133*, 6736–6744.

(67) Cheng, P.-N.; Liu, C.; Zhao, M.; Eisenberg, D.; Nowick, J. S. Amyloid B-Sheet Mimics That Antagonize Protein Aggregation and Reduce Amyloid Toxicity. *Nat Chem* **2012**, *4*, 927–933.

(68) Webb, T. R.; Jiang, L.; Sviridov, S.; Venegas, R. E.; Vlaskina, A. V.; McGrath, D.; Tucker, J.; Wang, J.; Deschenes, A.; Li, R. Application of a Novel Design Paradigm to Generate General Nonpeptide Combinatorial Templates Mimicking Beta-Turns: Synthesis of Ligands for Melanocortin Receptors. *J Comb Chem* **2007**, *9*, 704–710.

(69) Ross, N. T.; Katt, W. P.; Hamilton, A. D. Synthetic Mimetics of Protein Secondary Structure Domains. *Philos Trans A Math Phys Eng Sci* **2010**, *368*, 989–1008.

(70) Lee, L. W.; Taylor, C. E. C.; Desaulniers, J.-P.; Zhang, M.; Højfeldt, J. W.; Pan, Q.; Mapp, A. K. Inhibition of ErbB2(Her2) Expression with Small Molecule Transcription Factor Mimics. *Bioorganic & Medicinal Chemistry Letters* **2009**, *19*, 6233–6236.

(71) Majmudar, C. Y. Sekikaic Acid and Lobaric Acid Target a Dynamic Interface of the Coactivator CBP/P300. *Angewandte Chemie International Edition* **2012**, *51*, 11258–11262.

(72) Cindy W Wu; Tracy J Sanborn; Kai Huang; Ronald N Zuckermann, A.; Annelise E Barron. Peptoid Oligomers with A-Chiral, Aromatic Side Chains: Sequence Requirements for the Formation of Stable Peptoid Helices. *J. Am. Chem. Soc* **2001**, *123*, 6778–6784.

(73) Armand, P.; Kirshenbaum, K.; Falicov, A.; Dunbrack, R. L., Jr; Dill, K. A.; Zuckermann, R. N.; Cohen, F. E. Chiral N-Substituted Glycines Can Form Stable Helical Conformations. *Folding and Design* **1997**, *2*, 369–375.

(74) Henchey, L. K.; Jochim, A. L.; Arora, P. S. Contemporary Strategies for the Stabilization of Peptides in the Alpha-Helical Conformation. *Curr Opin Chem Biol* **2008**, *12*, 692–697.

(75) Bird, G. H.; Bernal, F.; Pitter, K.; Walensky, L. D. Synthesis and Biophysical Characterization of Stabilized Alpha-Helices of BCL-2 Domains. *Meth Enzymol* **2008**, *446*, 369–386.

(76) Schafmeister, C. E.; Po, J.; Verdine, G. L. An All-Hydrocarbon Cross-Linking System for Enhancing the Helicity and Metabolic Stability of Peptides. *J. Am. Chem. Soc.* **2000**, *122*, 5891–5892.

(77) Bernal, F.; Tyler, A. F.; Korsmeyer, S. J.; Walensky, L. D.; Verdine, G. L. Reactivation of the P53 Tumor Suppressor Pathway by a Stapled P53 Peptide. *J. Am. Chem. Soc.* **2007**, *129*, 2456–2457.

(78) Lee, S.; Braun, C. R.; Bird, G. H.; Walensky, L. D. Photoreactive Stapled Peptides to Identify and Characterize BCL-2 Family Interaction Sites by Mass Spectrometry. *Meth Enzymol* **2014**, *544*, 25–48.

(79) Moellering, R. E.; Cornejo, M.; Davis, T. N.; Bianco, C. D.; Aster, J. C.; Blacklow, S. C.; Kung, A. L.; Gilliland, D. G.; Verdine, G. L.; Bradner, J. E. Direct Inhibition of the NOTCH Transcription Factor Complex. *Nature* **2009**, *462*, 182–188.

(80) Jochim, A. L.; Arora, P. S. Assessment of Helical Interfaces in Protein-Protein Interactions. *Mol Biosyst* **2009**, *5*, 924–926.

(81) Chapman, R. N.; Dimartino, G.; Arora, P. S. A Highly Stable Short Alpha-Helix Constrained by a Main-Chain Hydrogen-Bond Surrogate. *J. Am. Chem. Soc.* **2004**, *126*, 12252–12253.

(82) Clark, R. C.; Lee, S. Y.; Searcey, M.; Boger, D. L. The Isolation, Total Synthesis and Structure Elucidation of Chlorofusin, a Natural Product Inhibitor of the P53-mDM2 Protein-Protein Interaction. *Nat Prod Rep* **2009**, *26*, 465–477.

(83) Gavenonis, J.; Sheneman, B. A.; Siegert, T. R.; Eshelman, M. R.; Kritzer, J. A. Comprehensive Analysis of Loops at Protein-Protein Interfaces for Macrocycle Design. *Nat. Chem. Biol.* **2014**, *10*, 716–722.

(84) Chen, Y.; Inoyama, D.; Kong, A.-N. T.; Beamer, L. J.; Hu, L. Kinetic Analyses of Keap1-Nrf2 Interaction and Determination of the Minimal Nrf2 Peptide Sequence Required for Keap1 Binding Using Surface Plasmon Resonance. *Chem Biol Drug Des* **2011**, *78*, 1014–1021.

(85) Hancock, R.; Schaap, M.; Pfister, H.; Wells, G. Peptide Inhibitors of the Keap1-Nrf2 Protein-Protein Interaction with Improved Binding and Cellular Activity. *Org. Biomol. Chem.* **2013**, *11*, 3553–3557.

(86) Taylor, C. E.; Pan, Q.; Mapp, A. K. Synergistic Enhancement of the Potency and Selectivity of Small Molecule Transcriptional Inhibitors. *ACS Med. Chem. Lett.* **2011**, *3*, 30–34.

Chapter 2

Using Combination Approaches to Target Head and Neck Squamous Cell Carcinoma (HNSCC)*

2.1 Abstract

The epithelial growth factor receptor (EGFR) is elevated in 90% of head and neck squamous cell carcinoma (HNSCC), yet the majority of patients do not respond to anti-EGFR therapeutics. The possible modes of mechanism for this insensitivity to EGFR inhibitors could be due to kinase-independent actions of EGFR and/or activation of Her2. Therapies that utilize strategies capable of reducing levels of EGFR and Her2 in combination with anti-EGFR therapeutics could enhance the efficacy of the current therapeutics. In this chapter, we show that knockdown of the transcription factor epithelial-restricted with serine box (ESX) decreased EGFR and Her2 promoter activity, expression and protein levels. Additionally, ESX levels were elevated in primary HNSCC tumors and associated with the increased EGFR and Her2 levels seen in these primary tumors. Knockdown of ESX using shRNA enhanced the effects of EGFR/Her2 tyrosine kinase inhibitors (TKI) lapatinib and afatanib. Biphenyl isoxazolidine (**i1**), a small molecule inhibitor of ESX transcription, was able to reduce EGFR and Her2 levels and enhanced the

* The research described in chapter 2 is a collaborative effect. P.A. Bruno performed synthesis, purification, characterization, and validation of inhibitor of **i1**. M. Zhang, L. Piao, J. Datta, S. Bhave, T. Su, J.C. Lang, X. Xi, and T.N. Teknos performed cellular assays, immunohistochemical analysis, gene expression analysis, and murine *in vivo* studies. Parts of this chapter are reproduce in Zhang, M.; Taylor, C. E.; Longzhou, P.; Datta, J.; Bruno, P. A.; Bhave, S.; Tizhi, S.; Lang, J. C.; Xie, X.; Teknos, T. N.; Mapp, A. K.; Pan, Q. Genetic and Chemical Targeting of Epithelial-Restricted with Serine Box Reduces EGF Receptor and Potentiates the Efficacy of Afatinib. *Mol. Cancer Ther.* **2013**, *12*, 1515-1525.

efficacy of afatinib when used in combination. When **i1** was used as a single agent, it was able to reduce tumorigenicity of HNSCC cells, but more importantly, when **i1** was used in combination with afatinib, the combination was superior to the single agents *in vivo* and resulted in a 100% response rate with a 94% reduction in tumor volume.

2.2 Introduction

Over 600,000 cases of head and neck squamous cell carcinoma (HNSCC) are identified globally each year, making HNSCC the sixth most abundant cancer.[1] The predominant phenotype of HNSCC is dysregulation of epithelial growth factor receptor (EGFR), specifically overexpression of EGFR. HNSCC patients with overexpression of EGFR are associated with inferior clinical outcomes. Although the predominant phenotype of HNSCC is overexpression of EGFR, only 5-15% of patients respond to anti-EGFR therapy.[2] This suggests that inhibiting EGFR activity and/or downstream signaling is insufficient for clinical response. One possibility for this low response rate could be due to kinase-independent actions of EGFR.[3] It has been demonstrated that EGFR can translocate to the nucleus to regulate genes associated with cellular proliferation and survival.[4] An alternative mechanism for the lack of response rate from anti-EGFR therapy could be due to a compensatory mechanism where EGFR family members Her2 and Her3 are activated.[5]

The ETS transcription factor family is largely responsible for regulation of genes involved in angiogenesis, invasion, and proliferation.[6] One of the family members of the ETS transcription factor family, epithelial-restricted with serine box (ESX), is exclusively expressed in differentiated epithelial cells, further suggesting the importance of ESX in the control of cellular differentiation.[7] ESX overexpression is a common phenotype seen in breast cancer, specifically the correlation of overexpression of ESX with overexpression of Her2.[8] Furthermore, the association of ESX overexpression with activation and overexpression of Her2 has been demonstrated in several studies.[9] This association was further complicated by the fact that Her2 was found to enhance ESX promoter activity, presenting a two-pronged problem.[10] Therefore, these findings suggest that this positive ESX/Her2 feedback loop may be critical for tumorigenesis.

CHALLENGES ASSOCIATED WITH USING SINGLE AGENT THERAPIES

As noted in Chapter 1, protein-protein interactions in the large surface area, low affinity regime are particularly difficult to target for inhibition.[11] The transient and low affinity interactions between transcriptional activators and the transcriptional machinery often leads to development or discovery of small molecules that have similar affinities. This results in having to use high effective concentrations of the molecule for the desired effect. Additional problems with specificity can also arise when targeting large surface area protein-protein interactions. In the case of small molecule inhibitors, the small surface area associated with some inhibitors cannot completely inhibit the protein-protein interaction of interest, causing an incomplete phenotypic response. Furthermore, the low affinity of these inhibitors can make them promiscuous, causing off-target effects with other protein-protein interactions necessary for cellular function. Furthermore, these inhibitors are designed to mimic a peptide motif that itself is a promiscuous binder and therefore, we cannot expect a TAD mimic to have a more selective binding profile that the TAD itself.[12]

Selectivity is not the only concern for developing single agent therapies for the protein of interest. Whereas inhibitors developed for large surface area, low affinity protein-protein interactions can lack affinity and specificity; kinase inhibitors can be developed with high affinity and good selectivity. [13,14] Kinases possess enzymatic activity and are traditionally defined by a binding interface with a small surface area and high affinity for its substrate. As a result, both industry and academia has had success targeting these proteins and developing drugs against them. One of the issues that can severely affect the affinity of these inhibitors is when mutations occur in the target protein.[15] These mutations can cause misfolding or structural shifts in the protein, causing these inhibitors to no longer bind as well or to lose the ability to bind completely.[16] The combination of the factors noted above ultimately result in drug resistance.

COMBINATION THERAPY

One of the ways to counter the effects of inhibitors with low affinity and modest selectivity or inhibitors that have a tendency to be rendered ineffective due to drug resistance, is to utilize combinations of two or more drugs.[17] These combinations can result in an antagonistic, additive, or synergistic effect with the last being the effect with the most

efficacious clinical outcomes.[18] As a result of identifying a combination with synergistic effects, a lower effective concentration can be used for both single agents and ultimately leads to less off-target effects.[19] These combination therapies have had considerable success, particularly against breast cancer. In one study, the response rate between carboplatin (DNA alkylating agent) as a single agent was compared to carboplatin in combination with trastuzumab (Her2 monoclonal antibody) against Her2+ breast cancer. When using carboplatin as a single agent, the response rate was 32% compared to the carboplatin/trastuzumab combination that yielded a response rate of 50%.[20] Although most combination therapies have focused on DNA alkylating molecules and antibodies, herein chapter 2 we will describe how the protein-protein interaction inhibitor **i1** can be used with kinase inhibitors to develop combination therapies that are more efficacious than either of the inhibitors as single agents.

i1 AS AN INHIBITOR OF HER2+ BREAST CANCER CELLS

Her2 phenotype and upregulation through ESX-Med23 interaction

Her2 (neu/ErbB2) is a member of the epidermal growth factor receptor family of extracellular receptors.[21] Her2 has gained considerable attention due to its use as a biomarker for breast cancer.[22] Amplification or overexpression of Her2 plays a key role in the progression and metastatic potential of breast cancer with overexpression of Her2 found in approximately 30% of breast cancers.[23] Trastuzumab, an antibody developed against the Her2 protein, has had considerable clinical success against Her2+ breast cancer.[24] This clinical success further highlights the importance of Her2 in the progression and metastatic potential of breast cancer. Given the importance of this protein in breast cancer, other strategies that led to down-regulation of Her2 protein levels would have therapeutic potential. One of the possible ways to down-regulate Her2 levels would be directly inhibiting the expression of the Her2 gene. One of the transcriptional activators that has been demonstrated to control Her2 gene expression is the epithelial-restricted with serine box (ESX) transcriptional activator.[9] ESX is expressed solely in differentiated epithelial cells, particularly mammary tissue. Previous studies have demonstrated that ESX strongly activates the Her2 gene and that the ESX promoter site is required for high-level expression of Her2 expression.[25] There also exists a correlation between ESX and Her2

levels in breast cancer, suggesting a positive feedback loop involved between the two proteins.[10] ESX also has a strong transcriptional activation domain that displayed similar potency to the viral transcriptional activator VP16.[26] Asada and coworkers demonstrated a strong affinity for the 130 kDa mediator protein Med23 (CRSP3/DRIP130/Sur2) when performing pull-downs with GST appended with the 17 amino acid ESX transcriptional activation domain and HeLa nuclear extracts.[9] In their studies, Med23 had no affinity in pull-downs using analogous transcriptional activation domains from NF-κB p65, ALL1, and C/EBPβ, suggesting that Med23 binds specifically to the transcriptional activator ESX. Asada and coworkers went on to demonstrate that the subdomain of Med23 responsible for binding to the ESX transcriptional activation domain was the $Med23_{352-625}$ subdomain. Overexpression of $Med23_{352-625}$ inhibited the ability of the ESX transcriptional activation domain to activate transcriptional activity, while it did not inhibit the transcriptional activation domains of NF-κB p65, ALL1, and C/EBPβ. Furthermore, dosing Her2+ breast cancer cells with a cell-penetrating peptide appended to the ESX transcriptional activation domain resulted in downregulation of Her2 protein levels, suggesting that targeting the ESX-Med23 complex could have therapeutic potential.

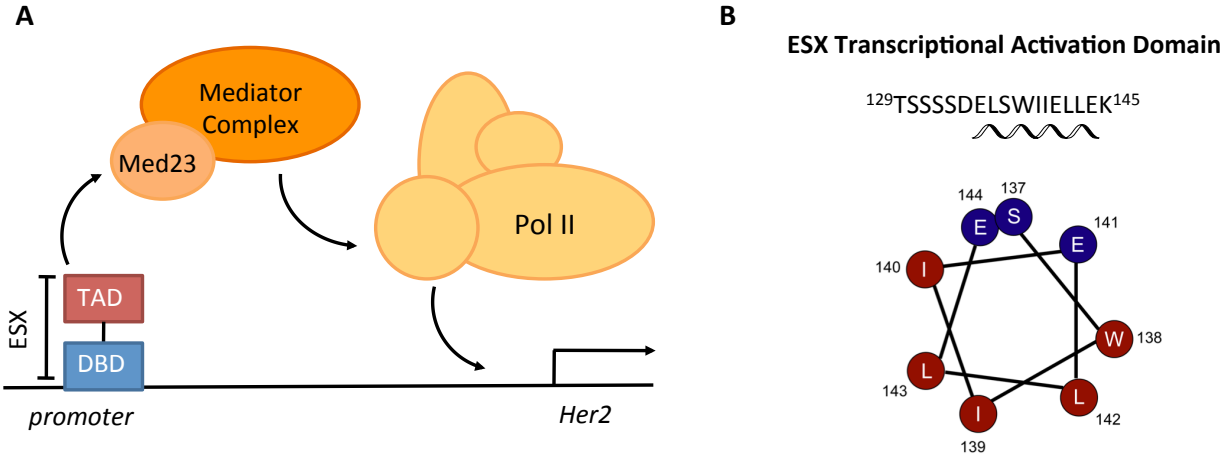

Figure 2.1 ESX transcriptional activation of Her2 mediated by Med23 A. The transcriptional activation domain (TAD) of ESX recruits Med23 and the resulting mediator complex, assembling the transcriptional machinery at the Her2 promoter site, resulting in Her2 upregulation B. The ESX TAD with the α-helical depicted with a helical wheel projection.

i1 *as an amphipathic helix mimetic of ESX*

Asada and coworkers performed mutational analysis on the ESX transcriptional activation subdomain to determine the importance of individual residues on binding to Med23. From these studies, Asada and coworkers were able to determine that the sequence required for Med23 could be localized to residues $ESX_{135\text{-}144}$. Additionally, they demonstrated the critical importance of Trp138 for binding to Med23 since substitutions to Phe, Leu, and Ala resulted in complete loss of ESX binding to Med23. The results of these experiments are summarized in Table 2.1.

Table 2.1 Analysis of the ESX TAD A. Truncation studies on the ESX TAD to determine minimal sequence required for Med23 binding B. Mutational analysis of ESX TAD using alanine scanning to determine important residues

A

Truncation studies on $ESX_{129\text{-}145}$

ESX TAD Sequence	Med23 Binding
^{129}TSSSSDELSWIIELLEK^{145}	+
^{134}DELSWIIELLEK^{145}	+
^{139}IIELLEK^{145}	-
^{135}ELSWIIELLEK^{145}	+
^{136}LSWIIELLEK^{145}	+
^{137}SWIIELLEK^{145}	+
^{138}WIIELLEK^{145}	-
^{137}SWIIELLE^{144}	+
^{137}SWIIELL^{143}	-

B

Mutational studies on $ESX_{129\text{-}145}$

ESX TAD Sequence	Med23 Binding
^{129}TSSSSDELSWIIELLEK^{145}	+
^{129}TSSSSDEL**A**WIIELLEK^{145}	+
^{129}TSSSSDELS**A**IIELLEK^{145}	-
^{129}TSSSSDELSW**A**IELLEK^{145}	-
^{129}TSSSSDELSWI**A**ELLEK^{145}	-
^{129}TSSSSDELSWII**A**LLEK^{145}	+
^{129}TSSSSDELSWIIE**A**LEK^{145}	-
^{129}TSSSSDELSWIIEL**A**EK^{145}	-
^{129}TSSSSDELSWIIELL**A**K^{145}	+
^{129}TSSSSDELS**F**IIELLEK^{145}	-
^{129}TSSSSDELS**L**IIELLEK^{145}	-

Lee and coworkers synthesized several isoxazolidines to investigate the effects that these molecules would have on ESX-Med23 binding.[27] In Figure 2.2 A, the general notation is presented for the isoxazolidine ring. Although the synthesis of these isoxazolidines is not convergent, but rather iterative, many of the same intermediates can be used to develop several other derivatives. Using this synthetic strategy, Lee and coworkers were able to synthesize several analogs using the isoxazolidine scaffold. The general synthetic strategy involves a 1,3-dipolar cycloaddition to generate the isoxazoline ring. The use of different

oximes and alkenes determines the functionality at C3 and C5, respectively. The other substituents are installed in the isoxazolidine ring through nucleophilic addition at C3 followed by substitution at N2 using a reductive amination or direct N alkylation to generate isoxazolidine derivatives (Figure 2.2).

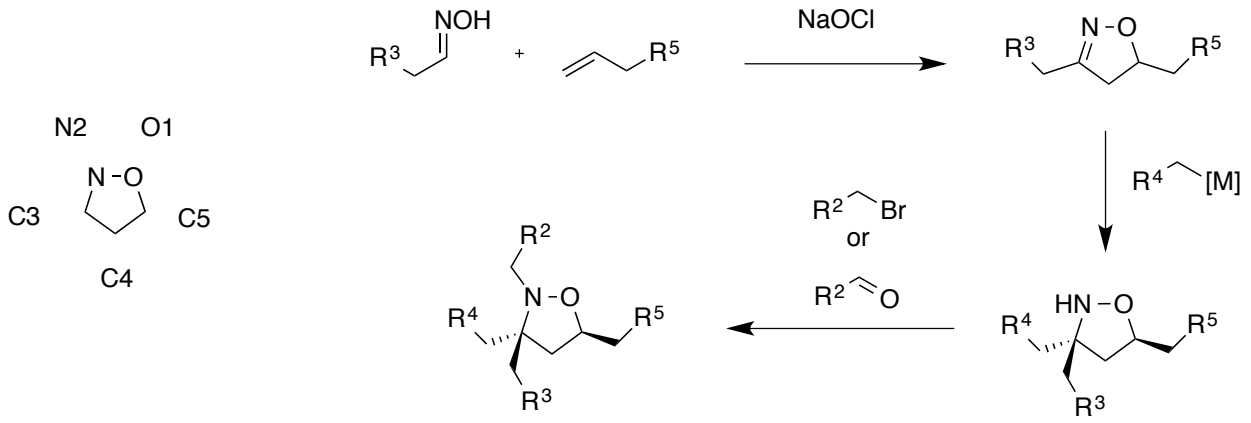

Figure 2.2 Notation of isoxazolidine and general synthetic scheme The general synthetic scheme of isozolidines involves a 1,3-dipolar cycloaddition, followed by nucleophilic addition at C3 and finally substitution at N2.

Lee and coworkers developed a series of tryptophan mimics based on experiments demonstrated by Asada and coworkers that identified tryptophan as a key residue for the ESX-Med23 interaction. The isoxazolidines synthesized by Lee and coworkers were modified at the N2 position with substituents designed to mimic the functionality of Trp 138 in the ESX TAD.

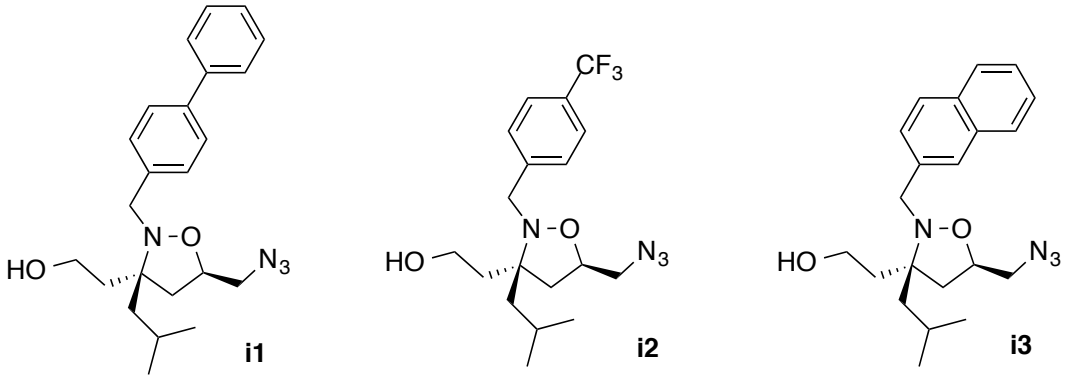

Figure 2.3 Isoxazolidines synthesized as tryptophan mimics against Med23 Several isoxazolidines synthesized by Lee and workers were varied at the N2 position designed to mimic Trp 138 of ESX. Reduction of the azide handle and coupling to fluorescein isothiocyanate was carried out to assess affinity of inhibitors for $Med23_{352-625}$.

From the studies performed by Lee and coworkers, **i1** was the most active isoxazolidine tested. Although substituents substituted with a nitrogen N2 aromatic functional group such as an indole would be more obvious indole mimics, these compounds were less active owing mostly to the reduced stability of the compounds due to the redox sensitive nature of the indole functional group. Work by Lee and coworkers also demonstrated that positional isomers of **i1** were not as effective, suggesting the relative position of the substituents is important for inhibition. This is further demonstrated by a crystal structure of **i1** that demonstrates that the position of the substituents closely mimics the spatial arrangement of side chains in an α-helix. This suggests that **i1** not only acts as a tryptophan mimic, but could also be acting as a helix mimetic as suggested by experiments with the positional isomers and crystal structure of **i1**.

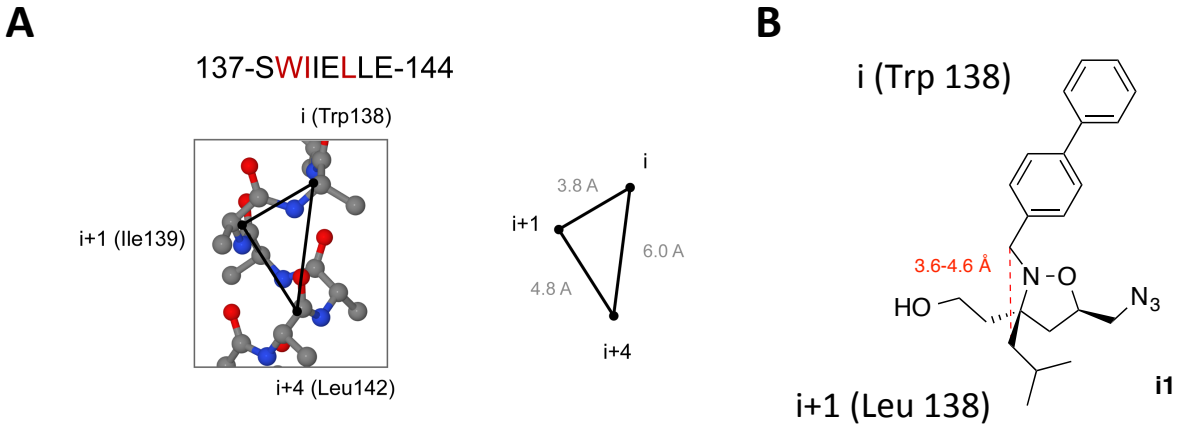

Figure 2.4 Isoxazolidine i1 designed as a tryptophan mimic and helix mimetic A. 3D respresentation of the ESX TAD with the relative distances between i, i+1, and i+4 residues on the ESX TAD hydrophobic face. B. Isoxazolidine **i1** and the distance between the N2 and C3 substituent. The hydroxyl substituent on C3 positions **i1** for binding to Med23.

i1 efficacy against Her2+/Her2- cells

Lee and coworkers tested the efficacy of isoxazoidines **i1-3** for their ability to downregulate Her2 mRNA, protein levels of Her2, as well as the compounds selectivity for Her2+ cells compared to Her2- cells. Isoxazolidine **i1** was able to inhibit mRNA transcript levels of Her2 by ~30%.[27] Isoxazolidine **i1** also exhibited a dose dependent inhibition of Her2 protein levels. This was assessed by western blot analysis of Her2 overexpressing SkBr3 cells dosed with varying concentrations of **i1**. These results were further validated by viability assays performed with **i1** against Her2+ SkBr3 cells and Her2- IMR90 cells. The

IC_{50}s generated from these experiments demonstrated that isoxazolidine **i1** has about 1.5-fold selectivity for Her2+ cells compared to Her2- cells. Together these results suggest that **i1** is and inhibitor of the ESX-Med23 protein-protein interaction. Isoxazolidine **i1** reduced Her2 mRNA and protein levels, indicating that this molecule can inhibit the ability of ESX to activate the target gene Her2. However, **i1** requires micromolar concentrations to exert its cellular effects. This is likely due to a lack of complete inhibition of the ESX-Med23 interaction due to its large surface area and possible off-target effects of **i1** at micromolar concentrations.

Taylor and coworkers followed up on the initial studies of **i1** that investigated the ability of **i1** to be used in a multi-pronged intervention approach against Her2 overexpressing breast cancer cells. This study was carried out in order to investigate the ability of a multi-pronged approach to mitigate the potency and selectivity concerns associated with **i1** as a single agent inhibitor.[17] Isoxazolidine **i1** was used in combination with three other agents (lapatinib, efatinib, and geldanymicin) that target cellular events related to Her2 activity such as protein folding or receptor dimerization required for downstream signaling. Two of these combinations exhibited synergistic increase to potency and selectivity, leading to an overall decrease in the dose of both agents. In one example, **i1** and geldanamycin allowed for dose reductions of greater than 15-fold for both agents and increased selectivity for Her2+ cells by as much as 30-fold compared to the individual agents, suggesting that combination approaches have therapeutic potential.

2.3 Results and Discussion

i1 AND AFATINIB COMBINATION IN HEAD AND NECK SQUAMOUS CELL CARCINOMA (HNSCC)

Several types of breast cancer possess a phenotype characterized by overexpression of one of the EGFR family members.[28] The emergence of targeting EGFR family members through the use of monoclonal antibodies and small molecules inhibitors of these kinases has provided several effective therapeutic strategies for breast cancer patients. These therapies have resulted in high response rates and increased survival rates for patients. It has been demonstrated that HNSCC also displays a similar phenotype characterized by overexpression of EGFR.[2] Given the success that these anti-EGFR family member therapies

have had against several types of breast cancer, it seems intuitive that these effects should also translate to HNSCC; however, this has not been the case. Only 5-15% of HNSCC patients respond to anti-EGFR therapies and this is in contrast to the response rates seen in breast cancer, which tend to be much higher. This lack of response to anti-EGFR therapies could be due to kinase-independent actions of EGFR[3] or due to compensatory mechanisms involving activation of Her2 or Her3.[5]

Investigating the connection between ESX, Her2, and EGFR in HNSCC

In order to assess the relative levels of ESX, Her2, and EGFR in HNSCC, the relative levels of each protein were compared for HNSCC cell lines SCC15, SCC25, and CAL27, using oral epithelial cells (NOEs) as a baseline negative control. This analysis demonstrated that HNSCCs possess increased protein levels of ESX, Her2, and EGFR compared to NOEs (Figure 2.5A). In order to investigate the relationship between ESX expression on EGFR and Her2 protein levels, an ESX-deficient CAL27 cell line was generated using shRNA against ESX. This experiment demonstrated that reduced ESX translated to decreased levels of both Her2 and EGFR (Figure 2.5B). This was further validated at the mRNA level, in which decreased EGFR and Her2 mRNA expression was observed(Figure 2.5C), suggesting that ESX has a direct role in transcriptional control of EGFR and Her2 in HNSCCs. Luciferase driven reporters containing either the Her2 or EGFR promoter site further corroborate these findings. When CAL27/shRNA-control or CAL27/shRNA-ESX cells were transiently transfected with an EGFR or Her2-promoter luciferase reporter, significantly lower Her2 and EGFR promoter activity was observed in ESX deficient cells (Figure 2.5D). Next, we sought to determine whether ESX is associated with increased Her2 and EGFR in primary tumors from previously untreated patients with HNSCC. Using this data, patients were split into two groups: low ESX and high ESX. The high-ESX group had an 11-fold increase in ESX expression compared to the low-ESX HNSCC patients (Figure 2.5E). This also corresponded to a 93% increase in EGFR expression and an 83% increase in Her2 expression for the high-ESX patients. Together, these results suggest that there is a significant correlation with ESX and EGFR in addition to ESX and Her2 (Figure 2.5F).

Given the connection between ESX, EGFR, and Her2 in cells, we next examined the role of ESX on the tumorigenicity of HNSCC cells *in vitro* and *in vivo.* Experiments designed

to look at HNSCC cell proliferation demonstrated the importance of ESX expression, with CAL27/shRNA-ESX cells experiencing a 42% decrease in cell proliferation compared to CAL27/shRNA-control cells (Figure 2.6A). These results also correlate to results from an invasion assay, in which displayed a 67% reduction in cellular invasion (Figure 2.6B). With the observed effects that ESX has on cellular proliferation and invasion, we sought to determine the effect that silenced ESX would have on cellular migration. Wound healing assays performed with CAL27/shRNA-ESX cells compared to CAL27/shRNA-control cells displayed reduced migration (Figure 2.6C).

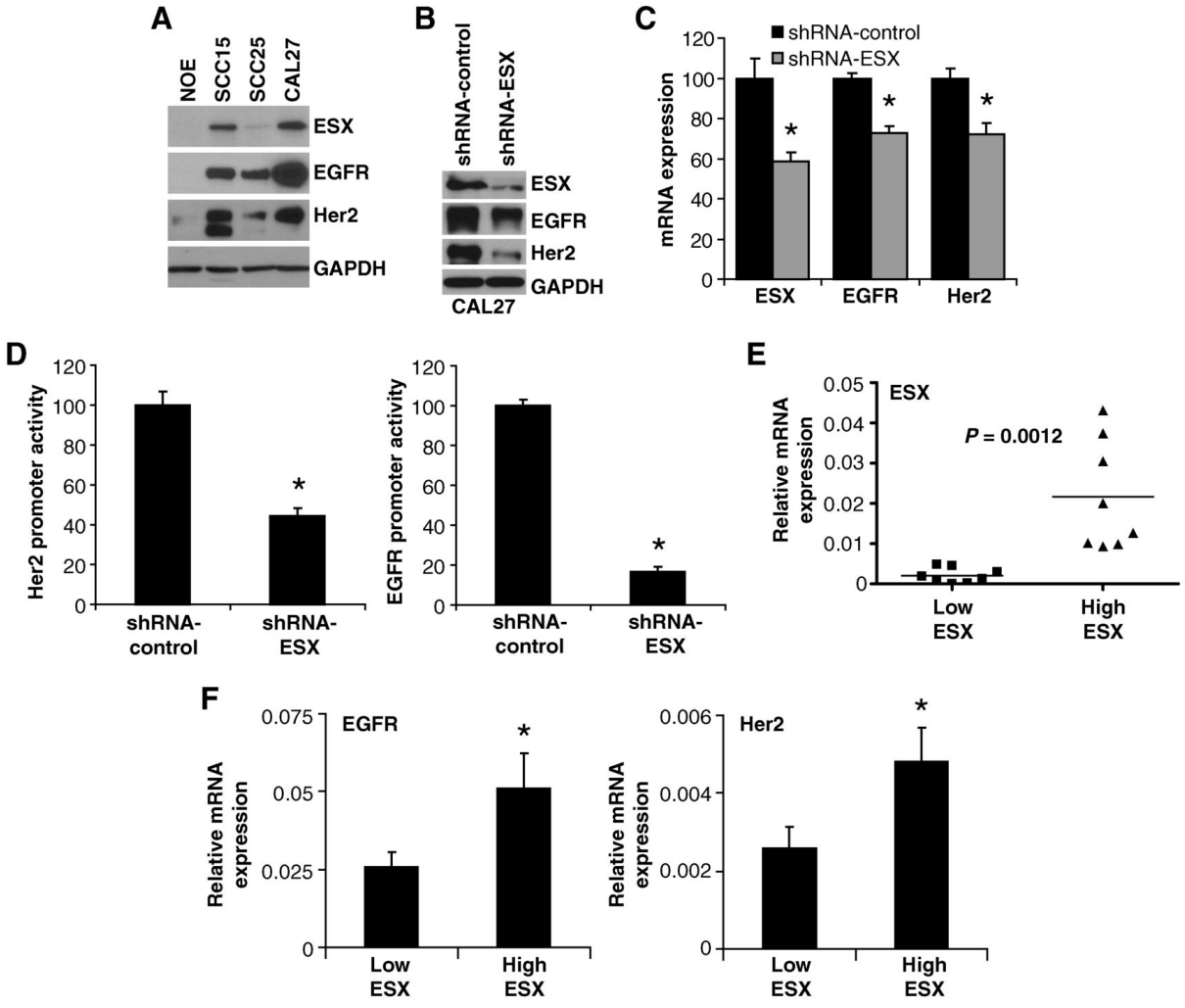

Figure 2.5 ESX regulates EGFR and Her2 in HNSCC Performed by the Pan lab. A, ESX, EGFR, and Her2 levels in HNSCC cells. ESX, EGFR, and Her2 protein levels were determined by immunoblot analyses. B, generation of ESX-deficient CAL27 cells. CAL27 cells were transduced with shRNA-control or shRNA-ESX and selected in antibiotics to generate polyclonal CAL27/shRNA-control and CAL27/shRNA-ESX cells. ESX, EGFR, and Her2

protein levels were determined by immunoblot analyses. C, ESX, EGFR, and Her2 expression. mRNA expression was determined using quantitative PCR with validated TaqMan assays. Data are normalized to CAL27/shRNA-control cells and presented as mean ± SEM. *, $P < 0.01$; n = 3. D, EGFR and Her2 promoter activity. CAL27/shRNA-control and CAL27/shRNA-ESX cells were transiently transfected with an EGFR or Her2 promoter-Firefly luciferase vector and a Renilla luciferase vector. Cell lysates were prepared and measured for Firefly and Renilla luciferase activity. EGFR and Her2 promoter activity was normalized to Renilla luciferase activity to control for transfection efficiency. Data are presented as mean ± SEM. *, $P < 0.001$; n = 9. E, ESX expression in primary HNSCC tumors. ESX mRNA expression was determined using quantitative PCR. Eight patients with the highest ESX expression were binned into the high ESX group and 8 patients with the lowest ESX expression were binned into the low ESX group. $P = 0.0012$; n = 16. F, ESX is associated with EGFR and Her2. ESX, EGFR, and Her2 mRNA expression was determined using quantitative PCR. $P < 0.05$; n = 16**.** Reproduced from Zhang, M et al. *Mol Cancer Ther* **2013**, *12*, 1515-1525.

In vivo tumorigencity of CAL27 cells in mice was retarded (39% inhibition, $P < 0.05$, n = 7) with ESX knockdown (Figure 2.6D and E) and immunohistochemical analyses showed that CAL27/shRNA-ESX tumors had lower ESX, EGFR, and Her2 levels than CAL27/shRNA-control tumors (Figure 2.6F and G). Taken together, these results suggest that ESX is sufficient to decrease the tumorigenicity of HNSCC cells.

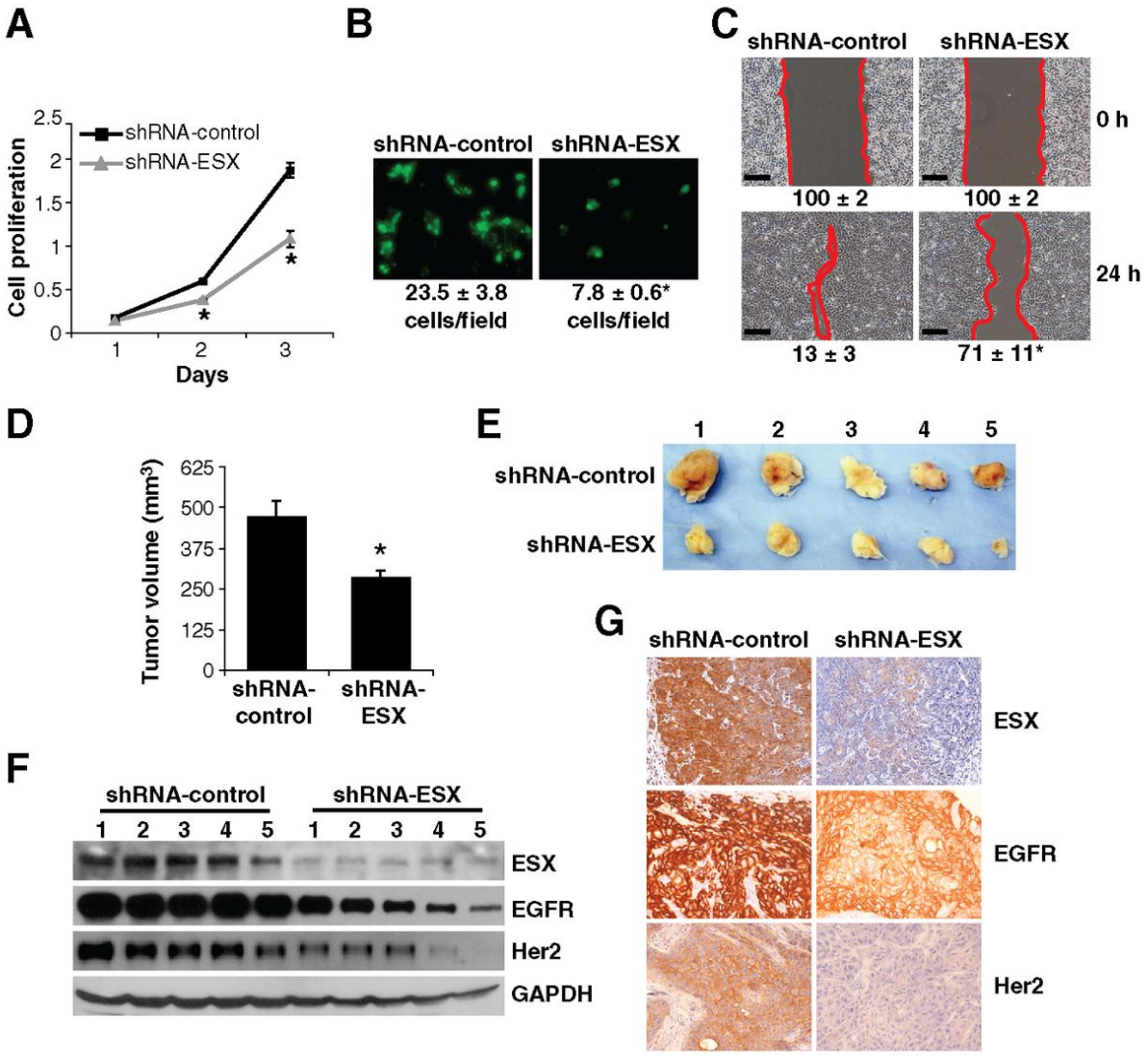

Figure 2.6 Genetic ablation of ESX reduces EGFR and Her2 levels and inhibits tumorigenicity *in vitro* and *in vivo*. Performed by the Pan lab. A, cell proliferation. Cell proliferation was assessed using the CCK-8 reagent to detect metabolically active cells. Data are presented as mean ± SEM. *, $P < 0.005$; n = 3. B, cell invasion. Invasive cells were visualized with fluorescence microscopy. A representative field for each experimental condition is presented. Data are presented as mean ± SEM. *, $P < 0.01$; n = 5. C, cell migration. Cell migration was determined using the wound-healing assay. Confluent monolayers were scratched using a sterile pipette tip, washed, and incubated in complete medium. A representative field for each experimental condition at 0 and 24 hours is presented. Bar, 150 mm. Percentage of cleared area is calculated and presented as mean ± SEM. *, $P < 0.01$; n = 3. D, tumor volume. CAL27/shRNA-control or CAL27/shRNA-ESX cells ($1x10^6$ cells) were implanted into the flanks of athymic nude mice. Tumors were measured using a digital caliper and tumor volumes were calculated. Data are presented as mean ± SEM. * , $P < 0.01$; n = 7. E, representative tumors. Five largest tumors originated from

CAL27/shRNA-control and CAL27-shRNA-ESX cells are shown. F, ESX, EGFR, and Her2 levels. Cell lysates were prepared from the five largest tumors originated from CAL27/ shRNA-control and CAL27-shRNA-ESX cells. ESX, EGFR, and Her2 protein levels were determined by immunoblot analyses. G, immunohistochemical staining. ESX, EGFR, and Her2 staining is shown for a representative shRNA-control and shRNA-ESX tumor. Reproduced from Zhang, M et al. *Mol Cancer Ther* **2013**, *12*, 1515-1525.

It was noted earlier that although EGFR is often elevated in HNSCC, patients often do not respond to anti-EGFR therapies. This lack in response to anti-EGFR therapies is thought to be due to kinase-independent actions of EGFR and activation of other EGFR family members such as Her2. Therefore, strategies that reduce EGFR and Her2 protein levels in concert could prove to be an attractive approach to enhance the efficacy of anti-EGFR therapeutics. This work has demonstrated that EGFR and Her2 levels are decreased with ESX knockdown, suggesting that ESX-deficient HNSCC cells may be more responsive to EGFR/Her2 TKIs, lapatinib and afatinib. As shown in Figure 2.7B, ESX-deficient CAL27 cells were more sensitive to the anti-proliferative effects of lapatinib and afatinib. In CAL27/shRNA-control cells lapatinib had an IC_{50} dose of 11.9 μM and afatinib had an IC_{50} dose of 2.3 μM. In contrast, the IC_{50} was 4.9 μM for lapatinib and 0.7 μM for afatinib in CAL27/shRNA-ESX cells. Knockdown of ESX also reduced clonogenic survival by 73% in CAL27 cells. Clonogenic survival was inhibited by 75% with lapatinib and 89% with afatinib in CAL27/shRNA-control cells. Additionally, CAL27/shRNA-ESX cells were almost more sensitive to EGFR/Her2 TKIs than shRNA-control cells. In the case of afatinib, clonogenic survival was reduced by 98% in CAL27/shRNA-ESX cells. Similar results were also seen in SCC15, another HNSCC cell line. Given the effects observed with knockdown of ESX, a logical next step would be to see if the same effects could be recapitulated with a small molecule inhibitor.

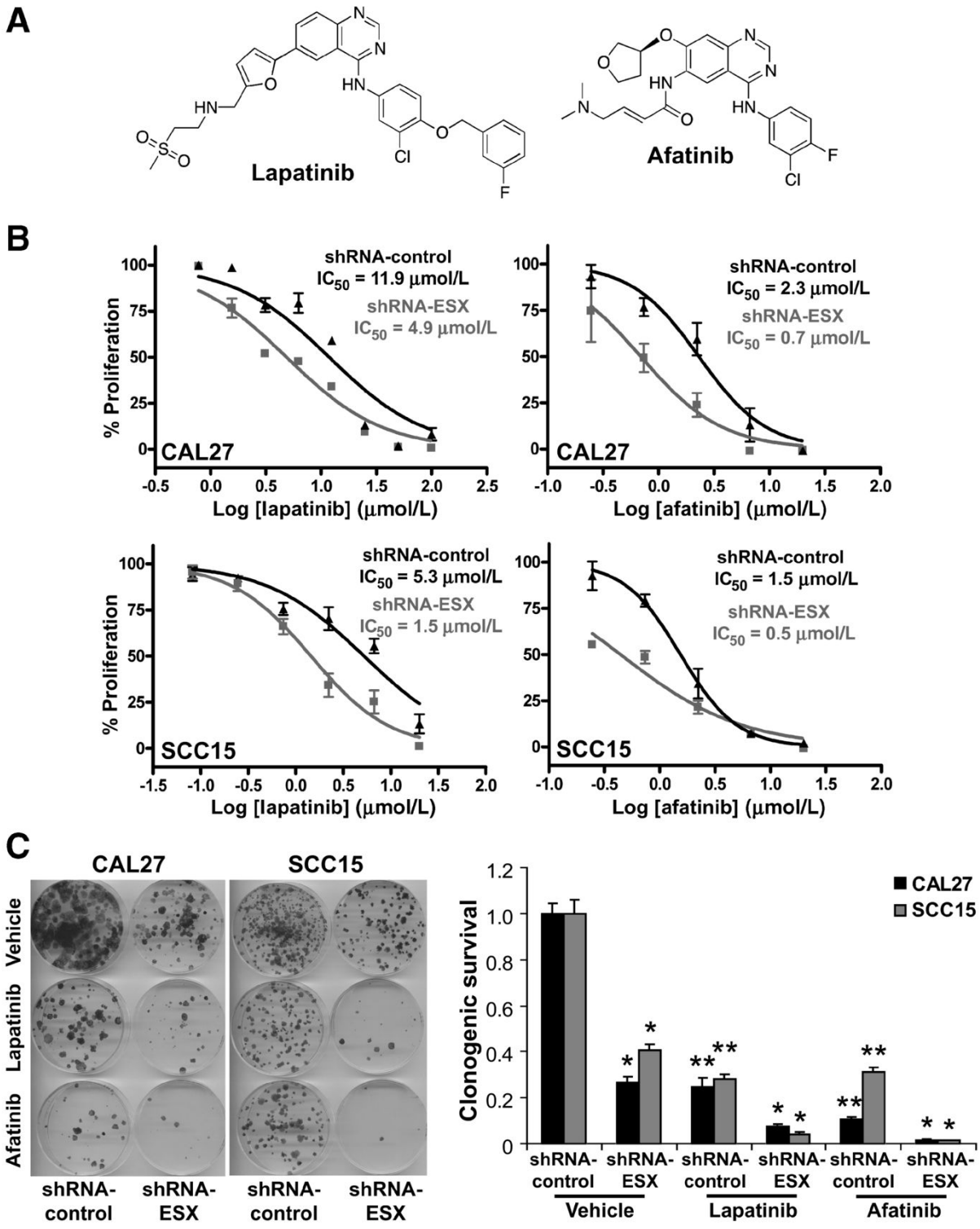

Figure 2.7 Knockdown of ESX potentiates the efficacy of EGFR/Her2 TKIs. Performed by the Pan lab. A, structure of EGFR/ Her2 TKIs, lapatinib, and afatinib. B, cell proliferation. CAL27/shRNA-control, CAL27/shRNA- ESX, SCC15/shRNA-control, and SCC15/shRNA-ESX

cells were treated with lapatinib or afatinib at various concentrations. Cell proliferation was assessed using the CCK-8 reagent to detect metabolically active cells. Dose– response curves and IC50 values were generated using GraphPad Prism 4.0. C, clonogenic survival. CAL27/shRNA-control, CAL27/ shRNA-ESX, SCC15/shRNA- control, and SCC15/shRNA-ESX cells were treated with lapatinib or afatinib at the IC50 dose. Colonies were stained with crystal violet. Data are normalized to shRNA-control/vehicle cells and presented as mean ± SEM. *, P < 0.01, shRNA-control versus shRNA-ESX for vehicle, lapatinib, or afatinib; *, P < 0.01, shRNA-control/vehicle versus shRNA-control/lapatinib or shRNA-control/afatinib, n = 3. Reproduced from Zhang, M et al. *Mol Cancer Ther* **2013**, *12*, 1515-1525.

Modified and optimized synthesis of i1

We decided based on the promising results from the above studies that we would investigate the possible inhibition effects of using chemical targeting of ESX. In order to investigate the possible effects of chemically targeting ESX, we decided to use inhibitor **i1(mESX)**, the molecule that was noted upon earlier. Inhibitor **i1** was previously demonstrated to be an inhibitor of ESX, leading to downregulation of Her2. Taylor and coworkers followed up on this work to demonstrate that combination studies with **i1** and other inhibitors involved in the Her2 activation pathway could enhance potency and selectivity. Based on these observations, we hypothesized that **i1** could have similar effects in HNSCC. This would include both cellular studies and *in vivo* mouse studies requiring scale-up and optimized synthesis of **i1**. The optimized synthetic scheme used to produce gram quantities of **i1** is depicted in Figure 2.8.

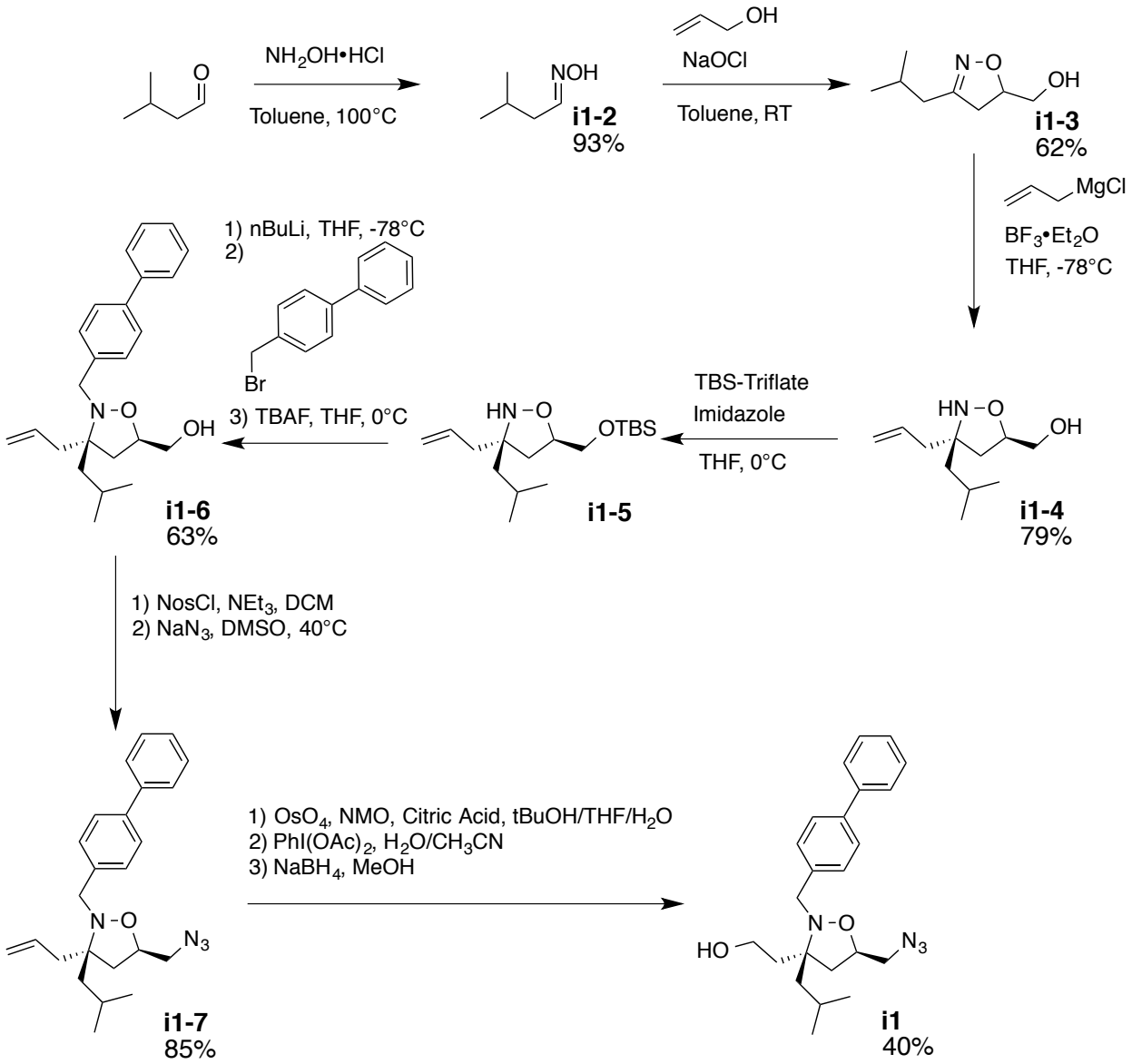

Figure 2.8 Optimized synthesis of i1(mESX) Performed by Paul Bruno. The optimized synthetic scheme used to scale-up synthesis of **i1**. Steps were followed as previously reported, steps were optimized for synthesis of **il-5** to **i1**.

The synthetic route above uses a synthetic route as previously reported,[27] but optimization of the synthesis from **i1-4** to **i1**. The previously published synthetic route from **i1-4** to **i1-6** performed TBS protection of the primary alcohol at C5 using TBS-Cl with greater than 90% yield. In order to optimize this step, TBS-triflate was used for near quantitative conversion in as little time as 30 minutes. For alkylation at the N2 position, the previously published synthesis used microwave irradiation and 5 equivalents of 4-(bromomethyl)biphenyl with 5 equivalents of diisopropylethylamine (DIPEA). This was

followed by deprotection of the TBS protecting group using tetrabutylammonium (TBAF) to yield **i1-6** with a yield of 46%. Optimization of the reaction consisted of trying to perform the N2 functionalization using a reductive amination, but these efforts proved unsuccessful. The reductive amination was sluggish (>24 hours for completion) and a competing reduction of biphenyl-4-carboxaldehyde to biphenyl-4-methanol made it very difficult to separate from the desired product due to similar polarity. Furthermore, after deprotection of the TBS protecting group, the yield of this reaction over these three steps never exceeded 35%. Based on these results, we attempted another alkylation reaction by deprotonating N2 to increase nucleophilicity. This was accomplished by deprotonating the amine using nBuLi, followed by addition of 4-(bromomethyl)biphenyl, and deprotection of the TBS protecting group using TBAF. This route was able to obtain a yield of 63% over three steps and had the added benefit of reducing the equivalents of 4-(bromomethyl)biphenyl from 5 equivalents to 2 equivalents when compared to the original published microwave reaction.

The synthetic step from **i1-6** to **i1-7** involves conversion of the primary alcohol at C5 to an azide. The original published synthesis converted the alcohol to the mesylate and followed by displacement with sodium azide, but these reaction conditions produced a yield of 48%. In the optimized reaction, the primary alcohol was concerted to the nosylate. This was done since the nosylate is a better leaving group compared to the mesylate and is typically more easily displaced by the azide. By converting the alcohol to the nosylate instead of the mesylate, the number of equivalents of sodium azide was reduced from 10 to 2 and the reaction mixture only needed to be heated to 40° C compared to the original synthetic route which required 80° C to drive reaction to completion. This was particularly important since synthesis of this intermediate on gram scale would have required large amount of sodium azide, an explosive material. The optimization of this step resulted in a yield of 85% compared to the original published yield of 48%.

The last synthetic step that was optimized was the dihydroxylation of **i1-7**. The original published synthesis of this molecule performed the dihydroxylation using 10 mol% of osmium tetroxide and required 6-12 hours before reaching completion. In order to optimize this step, we used a citric acid-catalyzed dihydroxylation of **i1-7**. This citric acid catalyzed dihydroxylation is based on methodology developed by the Sharpless lab.[29] This

allowed for a reduction in the osmium tetroxide used to only 1 mol%, Additionally, the reaction was consistently finished after 30 minutes, a significant improvement over the 6-12 hour reaction originally published.

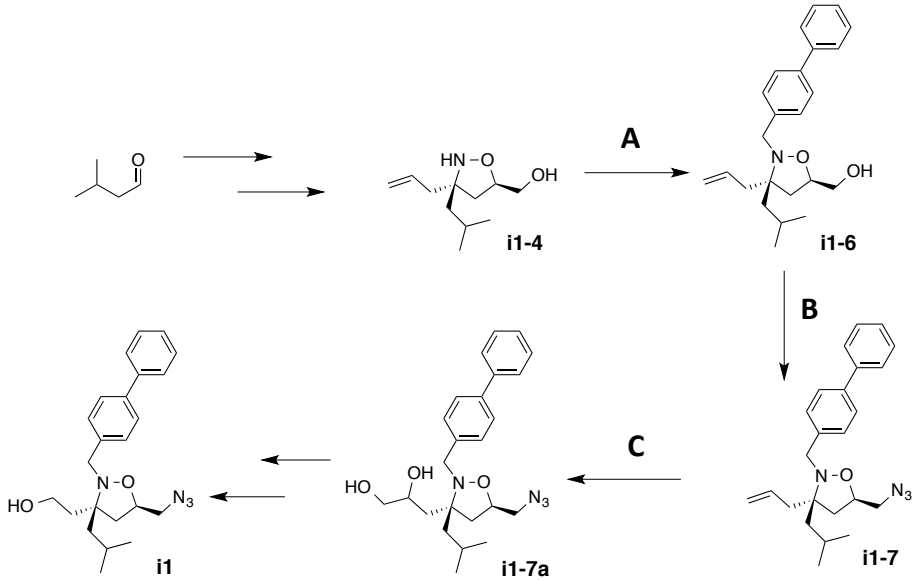

Step	Previous published conditions	Yield	New synthetic conditions	Yield
A	N-alkylation using i) TBS-Cl (1.5 eq), imidazole (1.5 eq), THF, 0°C ii) 4-(bromomethyl)biphenyl (5 eq), DIPEA (5 eq), µwave, DMF iii) TBAF, THF, 0°C	46%	N-alkylation using i) TBS-triflate (1.1 eq), imidazole (1.5 eq), THF, 0°C ii) nBuLi(2eq.), THF, -78°C iii) 4-(bromomethyl)biphenyl (3eq.) iv) TBAF, THF, 0°C	65%
B	i) methane sulfonyl chloride (2eq.), TEA (2eq.), DCM, RT ii) NaN_3(10eq.), DMF, 85°C	48%	i) 2-nitrobenzene sulfonyl chloride(1.5eq.), TEA (2eq.), DCM, RT ii) NaN_3(2eq.), DMF, 40°C	90%
C	Isoxazolidine (1eq.), NMO (1.4eq.), OsO_4(10mol %), H_2O:t-BuOH:THF, 1:1:1, RT ***6-12 hours***	80%	Isoxazolidine (1eq.), NMO (1.5eq.), Citric Acid (1.75eq.) OsO_4(1mol%), H_2O:t-BuOH: THF, 1:1:1, RT 0.5 hours	80%

Figure 2.9 Steps optimized for synthesis of i1 Performed by Paul Bruno. An abbreviated synthetic scheme for **i1** outlining the previous published conditions and yields compared with the new synthetic protocols and optimized yields.

Using this newly optimized synthetic scheme, we were able to synthesize 1.4 g of **i1**, marking the first time that gram quantities of **i1** have ever been produced. Isoxazolidine **i1** was purified by column chromatography, flashmaster chromatography, and the final purity verified by analytical reverse phase HPLC. The biological activity of **i1(mESX)** was initially assessed using a viability assay against SkBr3 and IMR90 cells. The results of the viability assay against both SkBr3 and IMR90 cells produced IC_{50}s in the same range as previously published and also resulted in the same 1.5-fold selectivity as previously observed.[27]

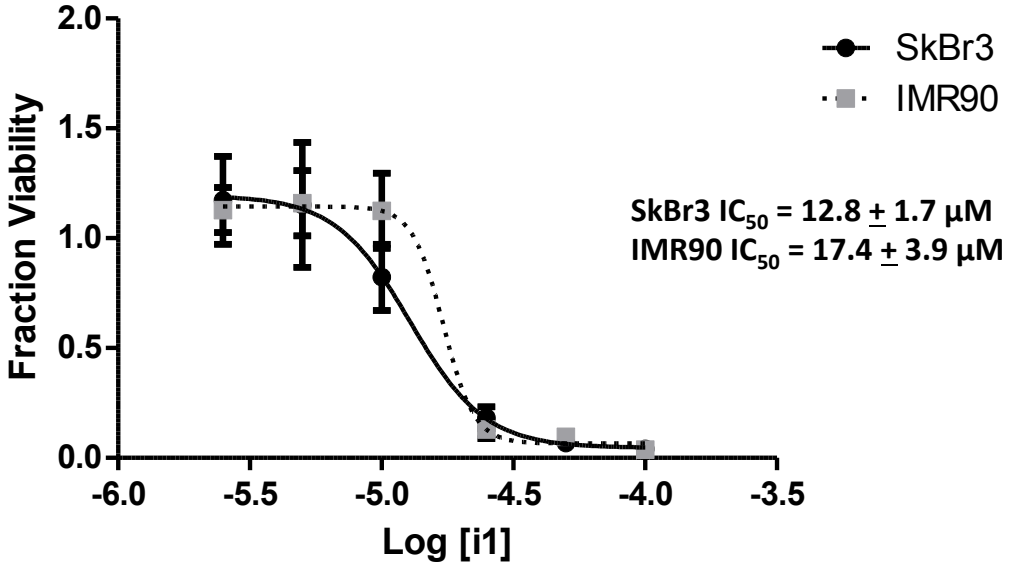

Figure 2.10 Viability assay using i1(mESX) against SkBr3 (Her2+) and IMR90 (Her2-) cells Performed by Paul Bruno. SkBr3 or IMR90 cells were plated at a density of 3 x 10^3 cells per well in a 96-well format. Cells were left to adhere overnight. Media was removed and cells were dosed with varying concentrations of **i1**. Cells were left to incubate in the presence of media containing molecule of vehicle for a total 48 hours. Media was replaced with fresh compound of vehicle after 24 hours. After 48 hours, added WST-1 viability reagent to each well and let incubate for 3 hours before reading the plate at 440 nm using a microplate reader. Data curves were fit using GraphPad 4.0 to determine IC_{50}s.

*Chemical targeting of EGFR and Her2 using **i1(mESX)** in HNSCC*

As mentioned earlier, based on the promising effects we observed with genetic ablation of ESX in HNSCC, we sought to determine if we could chemically target ESX and observe the same effects both in cellular models and an *in* vivo clinical mouse model of HNSCC. In order to carry out the following studies, we had to optimize and scale up the synthesis of **i1** to finished all the required experiments. These efforts produced 1.4 g of the purified compound. When **i1** was used to treat HNSCC cells, similar effects were seen with small molecule inhibition as compared to ESX knockdown in HNSCC cells. Isoxazolidine **i1(mESX)** was able to decrease protein levels of EGFR and Her2 at concentrations lower than the cellular proliferation IC_{50} for CAL27 cells (Figure 2.11B-C). Isoxazolidine **i1(mESX)** also did not show any viability effects against IMR90 cells after incubating with molecule for 24 hours (Figure 2.11D). Furthermore, treating CAL27 cells with **i1(mESX)**

also resulted in decreased invasion and migration of CAL27 cells (Figure 2.11E-F). These results were encouraging since they closely mirrored the effects of ESK knockdown in CAL27 cells, suggesting that ESX activity can be chemically targeted using **i1(mESX)**.

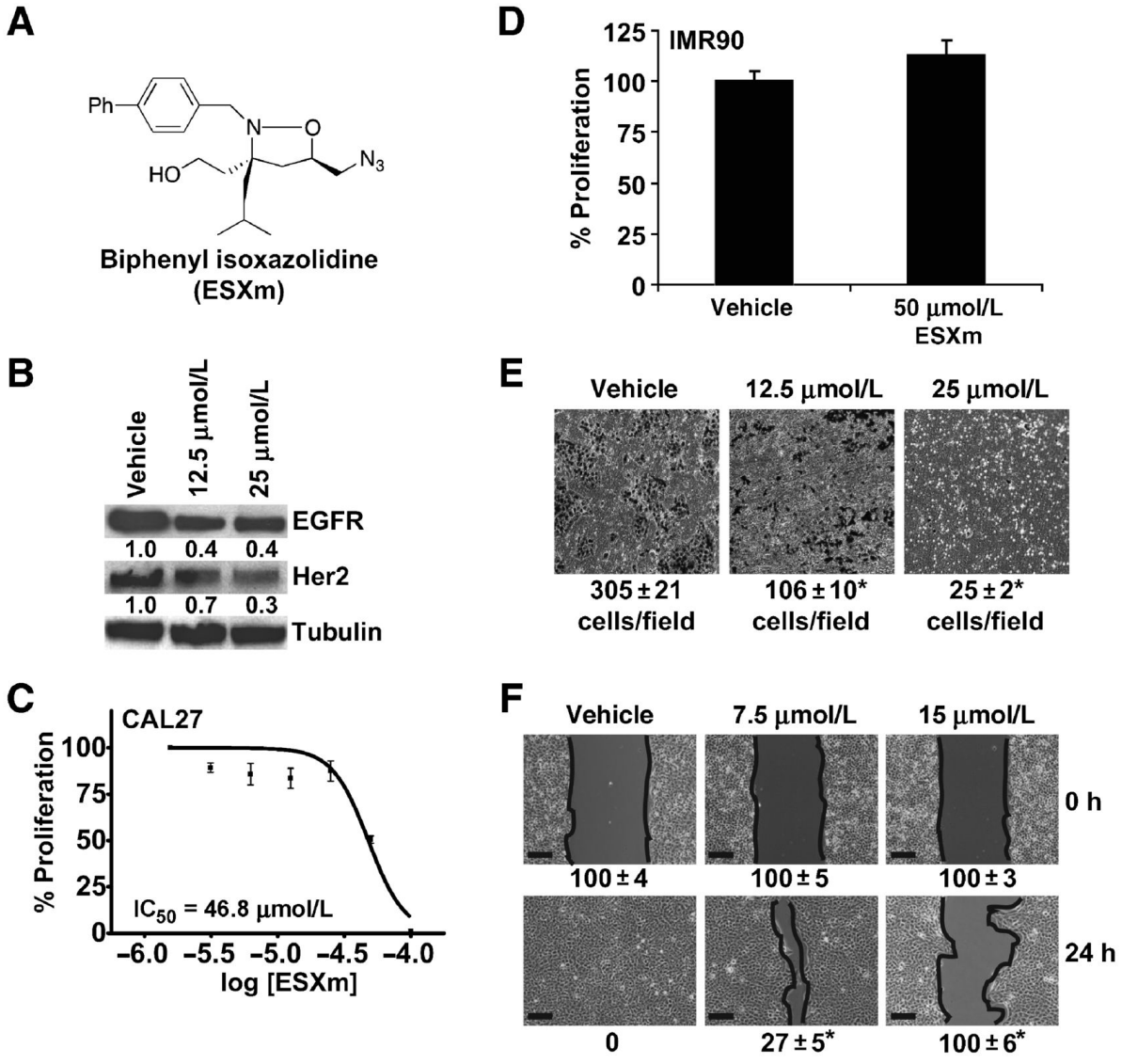

Figure 2.11 i1(mESX) reduces EGFR and Her2 levels and inhibits tumorigenicity *in vitro* Performed by Pan lab. A, structure of i1(mESX). B, EGFR and Her2 levels. CAL27 cells were treated with vehicle or biphenyl isoxazolidine for 24 hours. EGFR and Her2 protein levels by immunoblot analyses. C, cell proliferation of HNSCC cells. CAL27 cells were treated with vehicle or i1 (ESXm) for 24 hours. Cell proliferation was assessed using the CCK-8 reagent to detect metabolically active cells. Dose–response curves and IC50 values were generated using GraphPad Prism 4.0. IC50 was calculated to be 46.8 mmol/L. D, cell proliferation of normal IMR90 fibroblasts. IMR90 cells were treated with vehicle or i1(ESXm) (50 mmol/L) for 24 hours. Cell proliferation was assessed using the CCK-8

reagent to detect metabolically active cells. E, cell invasion. CAL27 cells were treated with vehicle or biphenyl isoxazolidine for 24 hours, harvested, and resuspended in serum-free medium. An aliquot of the prepared cell suspension was added to the top chamber and 10% FBS was added to the bottom chamber. After 24 hours, invasive cells were stained and visualized. A representative field for each experimental condition is presented. Data are presented as mean ± SEM. *, $P < 0.01$; n = 3. F, cell migration. CAL27 cells were seeded and allowed to grow until confluence. Confluent monolayers were treated with biphenyl isoxazolidine for 24 hours, scratched using a sterile pipette tip, washed, and incubated in complete medium. A representative field for each experimental condition at 0 and 24 hours is presented. Bar, 150 mm. Percentage of cleared area is calculated and presented as mean ± SEM. *, $P < 0.01$; n = 3. Reproduced from Zhang, M et al. *Mol Cancer Ther* **2013**, *12*, 1515-1525.

*Enhanced potency from **i1(mESX)**/afatinib combination in HNSCC*

Next, we wanted to determine if **i1(mESX)** could potentiate the effects of TKIs lapatinib and afatatinib in HNSCC cells. In order to investigate whether **i1(mESX)** could potentiate the efficacy of lapatinib or afatinib, CAL27 cells were treated with lapatinib or afatinib at various concentrations with and without an IC_{50} dose of biphenyl isoazoidine (Figure 2.12A). Single agent dosing with lapatinib or afatinib resulted in cell proliferation IC_{50}s of 11.8 μM and 1.3 μM, respectively. Importantly, the combination of **i1(mESX)** with either lapatinib or afatinib decreased cell proliferation by 90% or more in CAL27 cells. These results translated to clonogenic survival assays. Single agent dosing with **i1(mESX)**, lapatinib, and afatinib blocked clonogenic survival by 49%, 45%, and 72%, respectively. In contrast, the clonogenic survival of CAL27 cells was reduced by 89% with combination of **i1(mESX)** and lapatinib and was completely abalted (100%) with the combination of **i1(mESX)** and afatinib (Figure 2.12B). These results demonstrate that by targeting both EGFR/Her2 protein levels in concert with EGFR/Her2 kinase activities, that highly active therapeutic combinations can be developed against HNSCC.

*In vivo efficacy of **i1**/afatinib combination in preclinical mouse model of HNSCC*

Finally, the *in vivo* efficacy of **i1(mESX)** and afatinib as single agents and in combination were assessed in a preclinical mouse model of HNSCC. CAL27 cells (1×10^6) were implanted into the flank of 8-week-old athymic nude mice and tumors were allowed to develop without treatment. At 3 weeks after tumor cell implantation, mice with established tumors were randomly assigned to 4 treatment arms; vehicle, **i1(mESX),**

afatinib, and a combination of **i1(mESX)** and afatinib. Single agent **i1(mESX)** decreased tumor volume by 51% and single agent afatinib decreased tumor volume by 87% compared to vehicle. Importantly, the combination of **i1(mESX)** and afatinib reduced tumor volume by 94% compared to vehicle(Figure 2.13A). It should also be noted that treatment with either of the single agents or the combination treatment in mice did not produce abnormal behavior nor significant weight loss compared to the vehicle treatments.

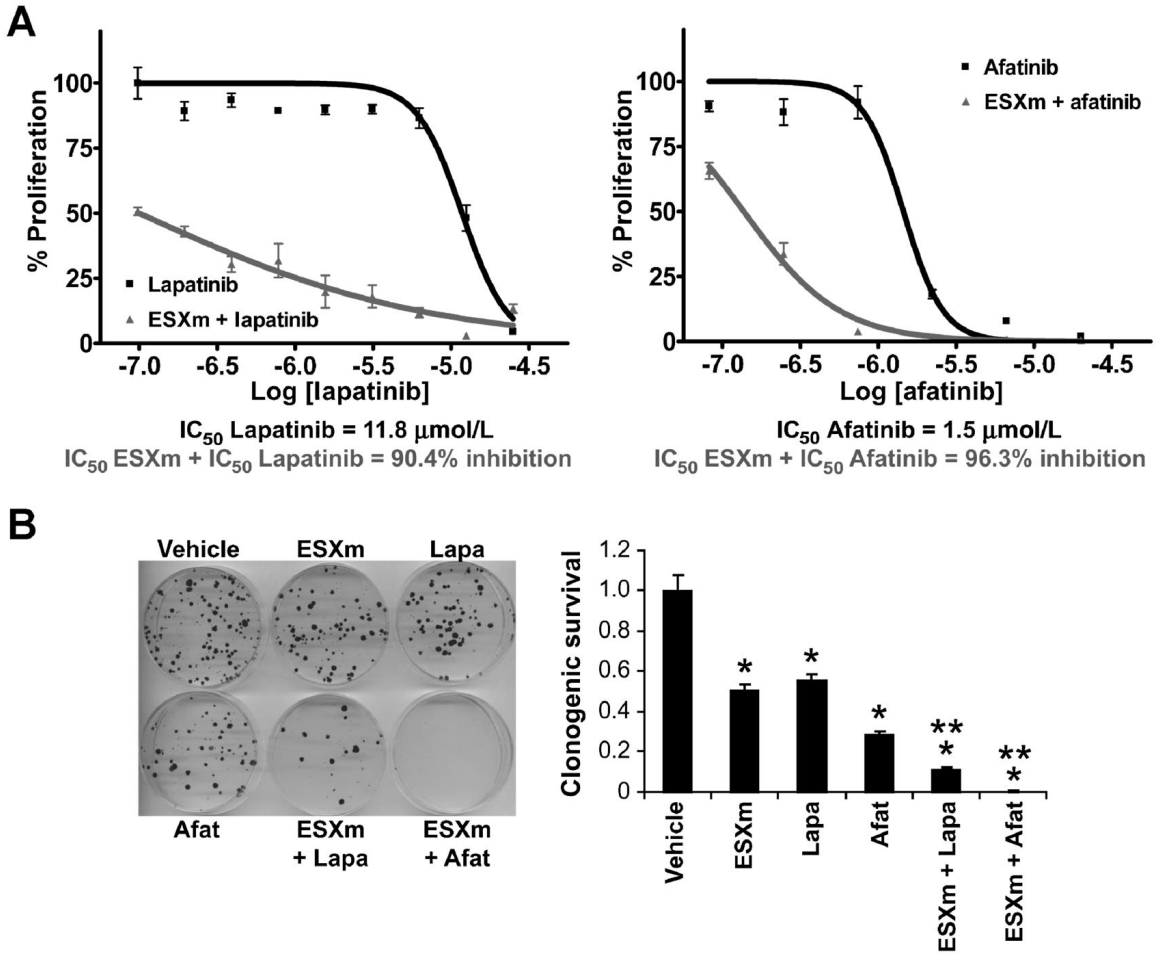

Figure 2.12 i1(mESX) potentiates the antitumor efficacy of afatinib *in vitro* Performed by Pan lab. A, cell proliferation. CAL27 cells were treated with lapatinib(Lapa) or afatinib (Afat) at various concentrations with and without an IC_{50} dose of biphenyl isoxazolidine (ESXm). Cell proliferation was assessed using the CCK-8 reagent to detect metabolically active cells. Dose–response curves and IC_{50} values were generated using GraphPad Prism 4.0. IC_{50} was 11.8 µmol/L for lapatinib and 1.5 µmol/L for afatinib in CAL27 cells. IC_{50} ESXm + IC_{50} lapatinib decreased cell proliferation by 90.4% and IC_{50} ESXm + IC_{50} afatinib decreased cell proliferation by 96.3% in CAL27 cells. B, clonogenic survival. CAL27 cells were treated with vehicle, biphenyl isoxazolidine (ESXm; IC_{50} dose), lapatinib (IC_{50} dose),

afatinib (IC_{50} dose), ESXm + lapatinib, or ESXm + afatinib. Colonies were stained with crystal violet. Data are normalized to shRNA-control/vehicle cells and presented as mean ± SEM. *, P < 0.01, vehicle versus treatment; **, P < 0.01 single-agent treatment versus combination treatment, n = 3. Reproduced from Zhang, M et al. *Mol Cancer Ther* **2013**, *12*, 1515-1525.

Immunohistochemical analysis of the tumors after treatment assessed levels of total and phosphorylated EGFR and Her2. From this analysis, it was demonstrated that both the intratumoral levels of total and phosphorylated EGFR and Her2 was decreased with treatment of single-agent **i1(mESX)** or afatinib. In contrast, the combination of **i1(mESX)** and afatinib led to further decreases in total and phosphorylated Her2 levels compared to the single-agent treatments. Interestingly, afatinib altered the cellular localization of phosphorylated EGFR from the cytosol to the nucleus; however, in the combination treatment, phosphorylated EGFR was not detected in the nucleus but in the cytosol of most of the tumor cells albeit at a lower intensity that the vehicle treatment. As noted earlier, one of the possible reasons that HNSCC patients may not respond to anti-EGFR therapies is due to the kinase independent actions of EGFR, more specifically, the translocation from the cellular membrane to the nucleus to activate target genes responsible for cell proliferation and survival. The results observed suggest that afatanib actually enhanced the nuclear-dependent actions of EGFR, whereas the **i1(mESX)**/afatinib reduced the nuclear accumulation of EGFR and reduced the levels of Her2.

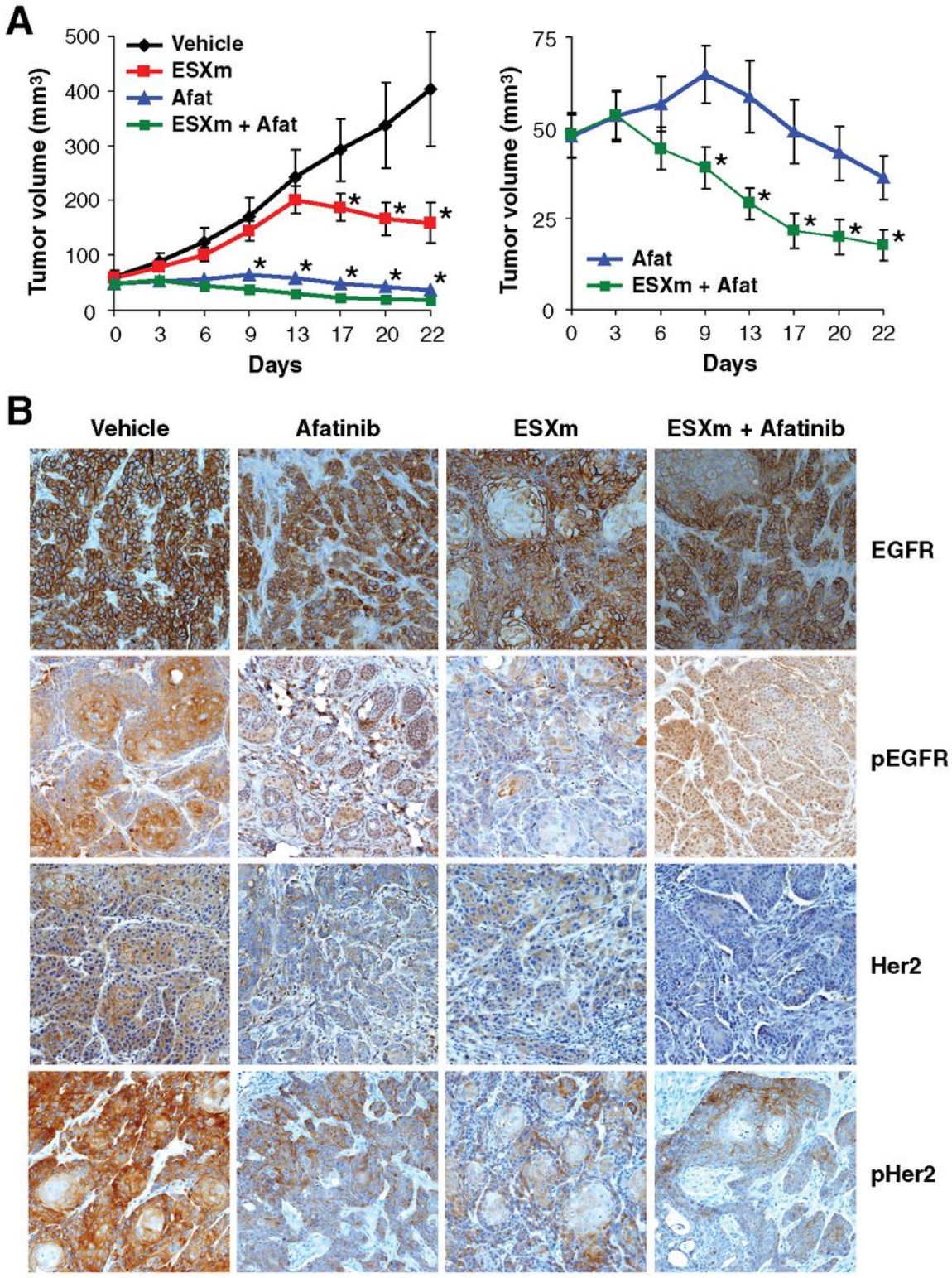

Figure 2.13 Biphenyl isoxazolidine potentiates the antitumor efficacy of afatinib (Afat) *in vivo*. Performed by Pan lab. A, tumor volume. Athymic nude mice with palpable CAL27 tumors (~50 mm^3) were randomly assigned to 4 experimental groups; vehicle,

biphenyl isoxazolidine (100 μg/mouse, 5x week), afatinib (0.4 mg/mouse, 5x week), or biphenyl isoxazolidine + afatinib. Tumors were measured using a digital caliper and tumor volumes were calculated. Data are presented as mean ± SEM. *, $P < 0.01$; n = 10. B, immunohistochemical staining. EGFR, pEGFR (Y1173), Her2, and pHer2 (Y1221/1222) staining is shown for a representative tumor from each treatment arm. Reproduced from Zhang, M et al. *Mol Cancer Ther* **2013**, *12*, 1515-1525.

IDENTIFYING OTHER SYNERGISTIC SMALL MOLECULE COMBINATIONS

There are two accepted and quantitative measures of evaluating synergistic combinations of small molecules. One is an effect based methods that was developed by Bliss and the other is an isobolographic method, which measures the dose reduction as developed by Loewe and Chou. [19,30,31] The Bliss method looks at statistically expected additive effects of two separate agents (A and B) at particular doses. When combined, these two doses of A and B are expected to have an effect equal to (eA + eB)-(eA*eB), where eA and eB are the effects of A and B. For example, if a dose of A causes a 50% viability reduction in a cell population and a dose of B also causes a 50% viability reduction of the same cell population, the calculated effect of the A and B combination would be a 75% viability reduction in cell population (Figure 2.14). For a synergistic combination, the combined effect will be greater than 75%. This method was recently demonstrated by Cokol and coworkers with a small molecule combinations against *S cerevisae.*[18]

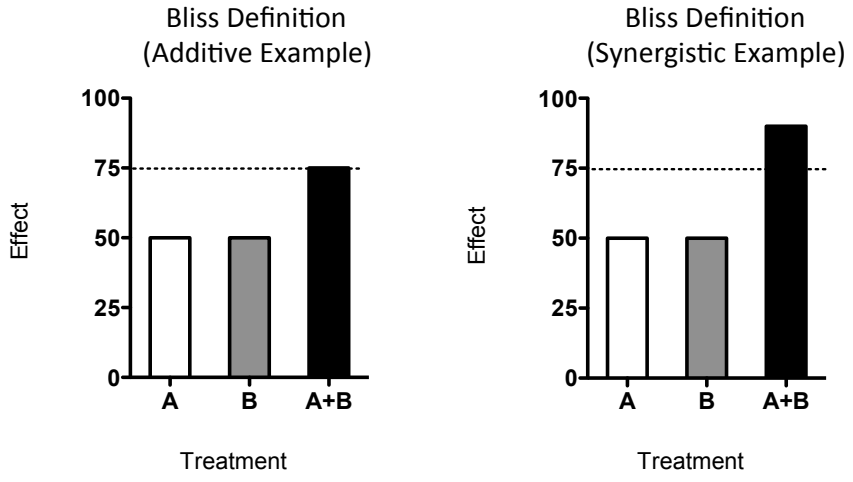

Figure 2.14 Bliss definition of synergy. A graphical representation of both an additive example and a synergistic example as defined by the Bliss method. In both examples, we demonstrate that A and B have 50% effects as single agents. In the additive example, the individual 50% effects exhibited in B would be calculated to have a 75% effect, whereas the synergistic example the effect would add up to have an effect greater than 75%.

Although this method is relatively straight forward, it does not account for effects observed at multiple dose values. The isobolographic method for evaluating synergy is based on the principle of dose equivalence and accounts for the effects demonstrated at several A+B combinations. This is accomplished through dose-effect curves evaluated for both of the individual agents and for several fixed ratio combinations. The IC_{50} for each of the single agents is determined as well as the IC_{50} for each of the agents in some combination of A+B. To calculate the dose fraction, you divide the IC_{50} of the selected agent by the IC_{50} for the single agent. For example, to determine the dose fraction of A used as a single agent, the IC_{50} of the single agent A is divided by the IC_{50} of the single agent A, providing you with a dose fraction of 1. For the fixed combination of A+B, the IC_{50} of the combination of A as a combination with B is divided by the IC_{50} of the single agent A (Figure 2.15).

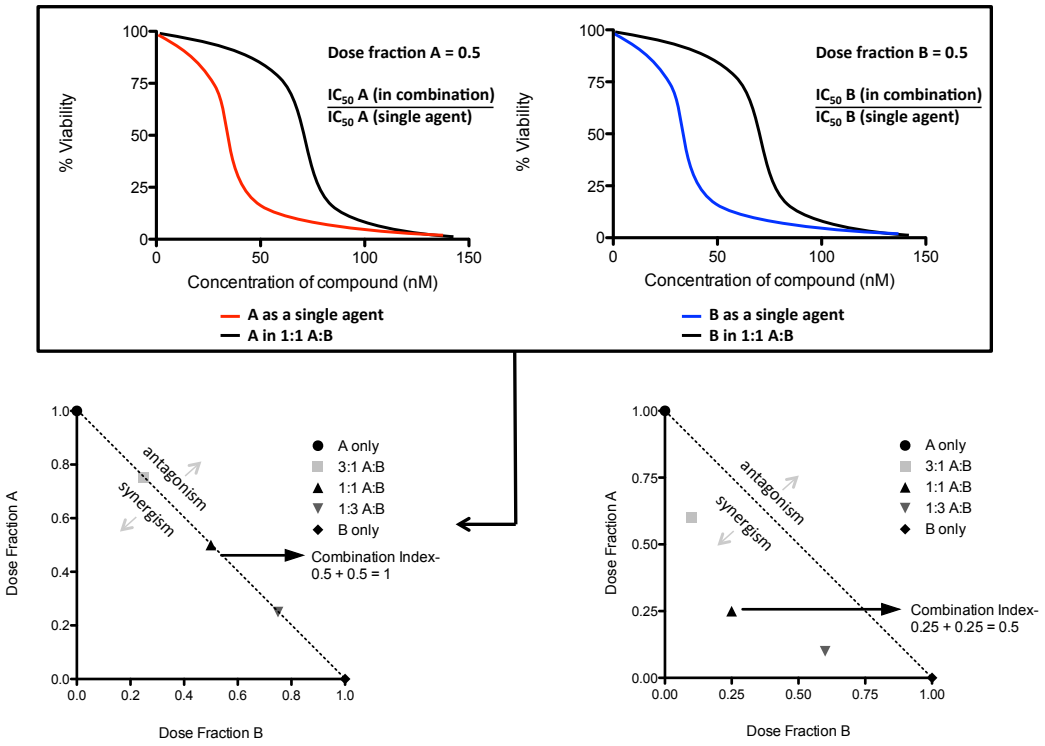

Figure 2.15 The isolobolographic definition of synergy Hypothetical combinations tested for inhibition using the Loewe (isobolographic) method. This method uses dose response curves generated for fixed dose ratios. Each combination has two IC_{50}s that are normalized to the IC_{50}s of the individual components and each combination is plotted on the x, y coordinate plot. The dotted line is the calculated effect based on the amount of compound required for 50% effect in the combination divided by the amount of the same agent in isolation for 50%. The example above is looking at an additive example. A synergistic combination would result in a dose response curve that is left-shifted, resulting in a lower dose fraction.

In figure 2.15, we demonstrate a hypothetical set of dose curves for an additive combination example. More specifically, the graph is depicting the set of curves that would result form a 1:1 combination of agent A and agent B. In the above hypothetical example, both single agent A and single agent B have an IC_{50} of 75 μM, whereas in the combination of 1:1 A:B, single agent A and single agent B have an IC_{50} of 37.5 μM. When dividing the combination IC_{50} by the single agent IC_{50}, the resulting dose fraction is equal to 0.5. These dose fractions are then plotted out on an isobologram with the additivity line indicated (dotted line). Single agents are always represented as a value of one on isobolograms, setting where the line of additivity should be indicated. Combination indexes (CIs) are the sum of the dose fraction of A and the dose fraction of B. For additive combinations, the combination index is equal to 1 (CI = 1). For combinations that are antagonistic, the combination index is > 1 (CI > 1), and for combinations that are synergistic, the combination index is < 1 (CI < 1). The above examples are for an additive combination, but in the case of a synergistic combination, the combination curves would be left-shifted, resulting in a lower IC_{50}. These lower IC_{50}s would result in lower dose fractions, which would result in synergistic combination indexes for the various ratios of combinations used (CI < 1) (Figure 2.15, lower right).

One pathway that has been of significant interest to us, is the crosstalk between Her2 and NF-κB in breast cancer. It has recently been demonstrated that overexpression of Her2 leads to constitutive activation of NF-κB activity. [32-34] Together these two pathways result in a highly aggressive breast cancer phenotype that is prone to metastasis, resulting in lower survival rates for patients.[35] It has been hypothesized that the mechanism of this dual activation of the Her2/NF-κB pathway is due to overexpression of Her2. This results in amplification of Her2 protein levels and activation through dimerization with EGFR and erbB3 to activate the canonical NF-κB, resulting in constitutive activation of the NF-κB pathway (Figure 2.16 A and B).

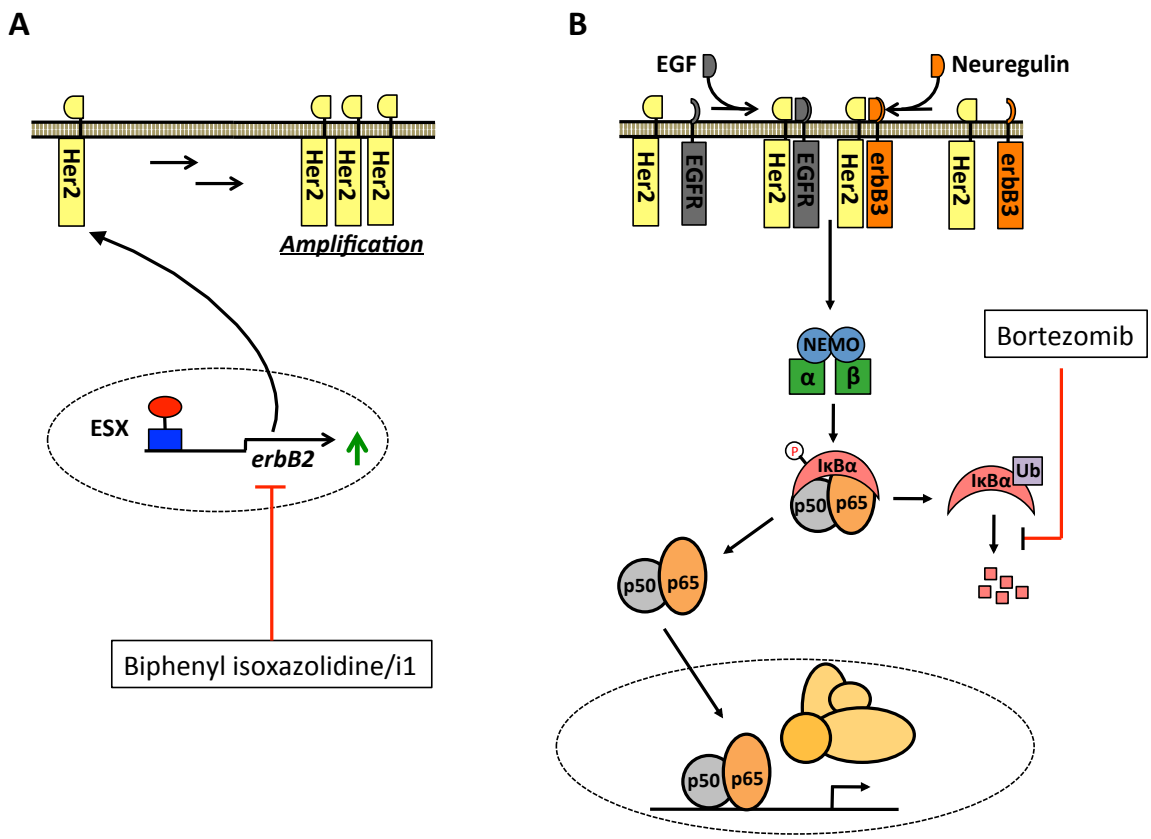

Figure 2.16 Mechanism of Her2 overexpression and resulting constitutive NF-κB activation A. Dysregulation of ESX results in overexpression and amplification of Her2 protein levels. An inhibitor of ESX transcriptional acitivity is biphenyl isoxazolidine (**i1**). B. Overactivation of the Her2 signaling pathway leads to activation of the canonical NF-κB activation pathway, resulting in constitutive activation. An inhibitor of constitutive NF-κB activity is bortezomib, a protease inhibitor.

Based on the new crosstalk observed with Her2 and NF-κB, we hypothesize that inhibitors targeting both ESX transcriptional activator activity and the NF-κB activation pathway will result in combinations of molecules that exhibit synergistic inhibition. We chose to measure these effects by using viability assays to monitor inhibitor combinations on SkBr3 (Her2+), MCF7 (Her2-), and IMR90 (Her2-) cells. SkBr3 breast cancer cells have been previously demonstrated to be Her2 overecpressing, serving as our model cell line.[22] MCF7 breast cancer cells express little to no Her2 and no constitutive NF-κB activity,[34] serving as a direct comparison for inhibitor combinations on different breast cancer models. IMR90 fibroblast cells are non-tumorigenic and serve as reference to examine selectivity of inhibitor combinations.[17] In order to test this inhibitor combination hypothesis, we used biphenyl isoxazolidine (**i1**) synthesized and characterized in chapter 2 as our ESX

transcriptional activator inhibitor. For NF-κB inhibitors, we chose to use KG-501, an inhibitor of the p65-CBPKIX interaction[36] and bortezomib, a proteasome inhibitor responsible for degradation of the inhibitor of κB (IκB). Results of these combinations are depicted in Figure 2.17.

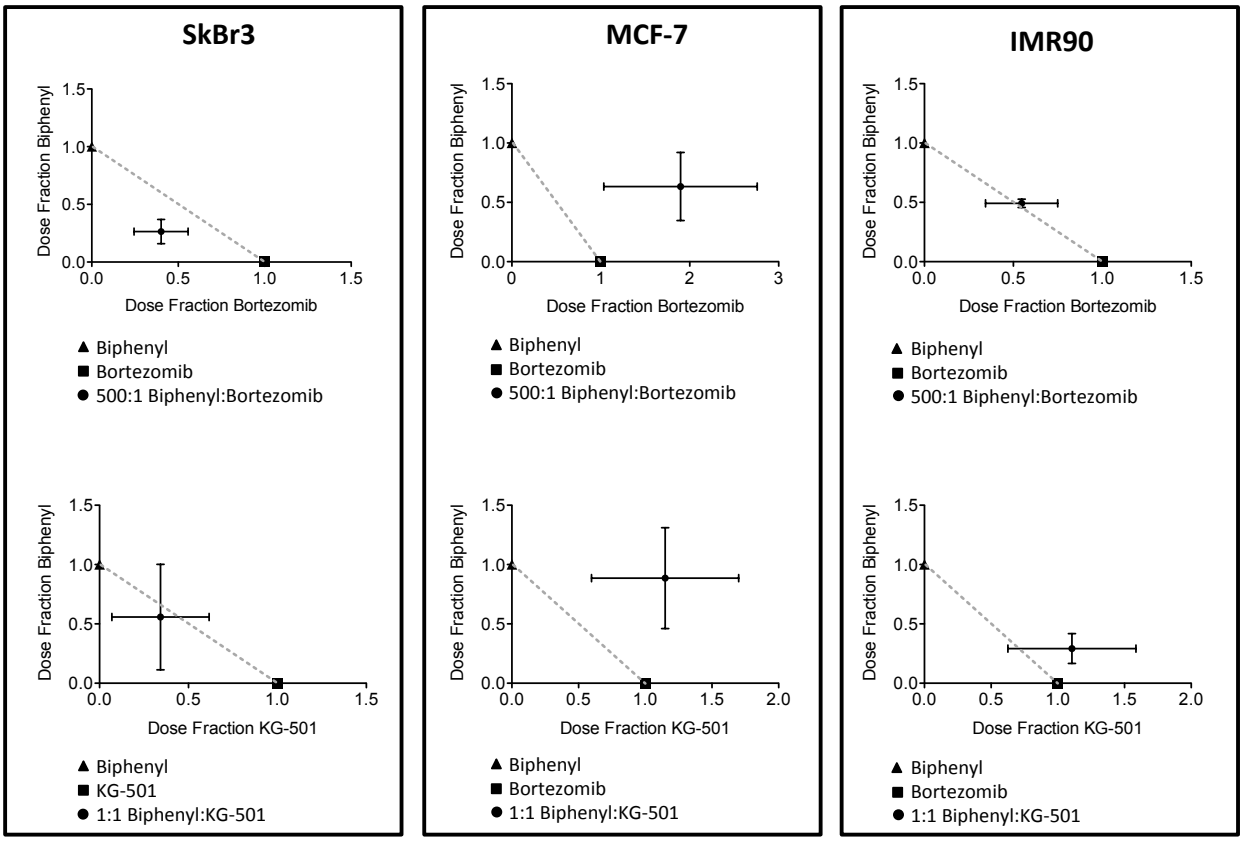

Figure 2.17 Isobolograms of biphenyl isoxazolidine (i1) and NF-κB inhibitor combinations in SkBr3, MCF-7, and IMR90 cells Performed by Paul Bruno. The two combinations that were tested were 1:1 biphenyl:KG-501 and 500:1 biphenyl:bortezomib. The ratio used for the combinations were pre-determined in a previous viability assay.

For the two combinations tested, the results are presented for SkBr3 cells (left panel), MCF-7 cells (middle panel), and IMR90 cells (right panel). The biphenyl:KG-501 combination did not exhibit synergy against any of the cell lines. Interestingly, the biphenyl:bortezomib did exhibit synergy against SkBr3 cells, whereas no synergy was demonstrated against MCF-7 cells and IMR90 cells. This result is compelling because it validates the crosstalk between the two signaling pathways. Additionally, the combination is only synergistic in SkBr3 cells, which are characterized as Her2 overexpressing with constitutive NF-κB activation, whereas MCF-7 cells are not Her2 positive and do not display constitutive NF-κB activation.

This is important because this combination validates the crosstalk between Her2 and NF-κB in Her2 overexpressing cells, whereas it had no synergistic effects against another breast cancer cell line (MCF-7) that are not characterized by Her2 overexpression. Furthermore, the effects appear additive in non-tumorigenic fibroblast IMR90 cells, suggesting that this combination would be more selective compared to the single agents. Based on these results, we plan to test other ratios with the biphenyl:bortezomib combination to validate the synergistic effects observed as well as test other NF-κB inhibitors in combination with biphenyl isoxazolidine to see if more synergistic combinations exist.

2.4 Conclusions

Herein, we described how a top-down approach could be used to develop an inhibitor of the ESX-Med23 interaction. The ESX-Med23 relies on a critical tryptophan residue (Trp 138) for interaction with Med23. Through the ESX-Med23 interaction, the transcriptional activator ESX is presumably able to recruit the rest of the transcriptional machinery, resulting in activation of target genes such as Her2. Her2 is a particularly important oncogene overexpressed in breast cancer and strategies that have the ability to reduce the cellular protein levels of Her2 would have immense benefit as a therapeutic strategy. By utilizing an isoxazolidine scaffold, a tryptophan mimetic was developed utilizing the α-helix mimetic isoxazolidine scaffold. This molecule, **i1(mESX)** was previously demonstrated to downregulate Her2 mRNA levels and protein levels in Her2+ breast cancer calls. Additionally, combination therapy utilizing **i1(mESX)** in concert with other inhibitors targeting Her2-mediated cellular events such as protein folding or kinase activity results in combinations that were 15-fold more potent and 30-fold more selective than either or the single agents.

HNSCC is the sixth most common cancer reported globally. EGFR protein levels are universally upregulated in HNSCC, yet HNSCC patients often do not responds to anti-EGFR therapies that have proven to be effective against other cancers with the EGFR-overexpression phenotype such as breast cancer. Genetic studies performed with HNSCC cells demonstrated that there is a correlation between ESX, Her2, and EGFR in HNSCC with ESX activity regulating the relative protein levels of Her2 and EGFR. Knockdown of ESX in

HNSCC cells decreased cellular proliferation, cell invasion, and cell migration, leading to an overall decrease in tumorigenicity of HNSCC. Knockdown of ESX also sensitized and increased the potency of anti-EGFR therapies against HNSCC cells. Based on these findings, we sought to determine if the same effects could be achieved through chemical targeting of ESX, resulting in inhibitor **i1(mESX)** being used to chemically target ESX. In order to complete a full study of *in vitro, in cellulo,* and *in vivo* of chemically targeting ESX gram quantities of **i1(mESX)** had to be synthesized, purified, characterized, and quality checked. In order to accomplish this feat, we optimized the 11-step synthesis of **i1(mESX)** previously reported. The major steps that were optimized included: N-alkylation at the N2 position, conversion of the C5 alcohol to a nosylate leaving group, which resulted in higher yields for the azide displacement, and a citric acid catalyzed dihydroxylation that dramatically reduced reaction times and reduced mol% of osmium tetroxide 10-fold. Using this optimized synthetic route, we produced gram quantities of **i1(mESX)** for the first time. This allowed for a full study on the effects of **i1(mESX)** and **i1(mESX)**/afatinib combinations in a preclinical mouse model of HNSCC. The combination therapy of **i1(mESX)**/afatinib in the preclinical mouse model resulted in 100% response rate and an average tumor volume reduction of 94% compared to the vehicle, demonstrating that highly active therapeutic combinations can be developed for HNSCC.

In addition to demonstrating the effectiveness of **i1(mESX)** and afatinib combinations in HNSCC cell and mouse models, we also demonstrated other potential combinations utilizing **i1(mESX)** with inhibitors of the NF-κB signaling pathway. In one particular example, combinations of **i1(mESX)** in combination with bortezomib, a protease inhibitor of the NF-κB signaling pathway, demonstrated synergistic inhibition against Her2+ breast cancer cells, suggesting that there are other potential combination approaches that can utilized using **i1(mESX)**.

2.5 Materials and methods

Chemicals and Instrumentation

Unless otherwise noted, starting materials and reagents were obtained from commercial sources and were used without additional purification. All reactions were carried out under anhydrous conditions (N_2 atmosphere) unless otherwise noted. Et_3N was distilled from CaH_2. Purification by flash chromatography was carried out with E. Merck Silica Gel 60 (230-400 mesh) according to the procedure of Still, Kahn, and Mitra. ^1H spectra were recorded in $CDCl_3$ at 400 MHz or 500 MHz. Large-scale purification of final product was carried out on a Jones Chromatography FlashMaster II using a gradient of ethyl acetate and hexanes as the mobile phase. Purification of final product was verified using analytical reverse-phase HPLC purification on a Hitachi 7000 series using a Beckman Coulter FC (Fraction Collector) Module. The HPLC was equipped using a C18 (8x100mm) Radial-Pak™ cartridge using a gradient of 0.1% TFA in H_2O and CH_3CN as the mobile phase.

Cells

SkBr3, IMR90, SCC15, SCC25, and CAL27 cells were purchased from American Type Culture Collection (ATCC). SkBr3 and IMR90 cells were grown in Dulbecco's Modified Eagle Medium (DMEM). SCC15 and SCC25 cells were grown in a 1:1 mixture of Ham's F-12 and DMEM supplemented with 10% FBS, 0.4 mg/mL hydrocortisone, 2 mmol/L L-glutamine, 100 mg/mL streptomycin, and 100 U/mL penicillin. CAL27 cells were grown in DMEM supplemen- ted with 10% FBS, 2 mmol/L L-glutamine, 100 mg/mL streptomycin, and 100 U/mL penicillin. Cell lines were authenticated using short tandem repeat profiling (ATCC).

Generation of CAL27/shRNA-ESX cells

CAL27 cells were transduced with shRNA-control or shRNA-ESX (10:1 MOI, pGIPZ Lentiviral shRNAmir; Open Biosystems) and selected in puromycin to generate polyclonal CAL27/shRNA-control and CAL27/shRNA- ESX cells.

Western blot analysis

Cells were washed in ice-cold PBS and lysed in buffer containing 1% Triton X-100, 50 mmol/L HEPES, pH 7.4, 10% glycerol, 137 mmol/L NaCl, 10 mmol/L NaF, 100 mmol/L

Na3VO4, 10 mmol/L Na4P2O7, 2 mmol/L EDTA, 10 mg/mL leupeptin, and 1 mmol/L phenylmethylsulfo- nylfluoride. Whole-cell lysates were mixed with Laemmli loading buffer, boiled, separated by SDS-PAGE, and trans- ferred to a nitrocellulose membrane. Subsequently, immu- noblot analysis was conducted using an ESX-specific anti- body (GenWay Biotech), an EGFR-specific antibody (Cell Signaling Technology), a Her2-specific antibody (Santa Cruz Biotechnology), or a glyceraldehyde-3-phosphate dehydrogenase (GAPDH)-specific antibody (Sigma).

Cell proliferation

CAL27 and SCC15 cell proliferation was assessed using the CCK-8 reagent to detect metabolically active cells (Dojindo Inc.). The absorbance at 450 nm was quantitated using a microplate reader (Molecular Devices). Dose–response curves and IC50 values were generated using GraphPad Prism 4.0 (GraphPad Software). SkBr3 and IMR90 cell proliferation was assessed using WST-1 reagent (Roche). The absorbance at 440 nm was quantified using a microplate reader (Genios Pro, TECAN). Dose response curves and IC50 values were generated using GraphPad Prism 4.0 (Graphpad Software).

Cell invasion and migration

Cell invasion was determined as described from the Cell Invasion Assay Kit (Chemicon International). Cells were harvested and resuspended in serum-free medium. An aliquot (1 105 cells) of the prepared cell suspension was added to the top chamber and 10% FBS was added to the bottom chamber. After 24 hours, noninvading cells were gently removed from the interior of the inserts with a cotton-tipped swab. Invasive cells were stained and visualized. Cell migration was determined using the wound-healing assay. Cells were seeded and allowed to grow until confluence. Confluent monolayers were scr- atched using a sterile pipette tip, washed, and incubated in complete medium.

EGFR and Her2 promoter activity

Cells were cotransfected with an EGFR or Her2 pro- moter-Renilla luciferase vector and a CMV-Firefly lucif- erase vector (SwitchGear Genomics) using FuGENE HD (Promega). After 24 hours, cells were washed with PBS, lysed in passive lysis buffer, and measured for

Renilla/ Firefly luciferase activities in a luminometer using the Dual-Light System (Applied Biosystems). EGFR and Her2 promoter Renilla luciferase activities were normalized with Firefly luciferase activities to control for transfection efficiency.

Gene expression analysis of primary HNSCC tumors

Sixteen primary tumors were collected at The Ohio State University James Cancer Hospital (Columbus, OH) from patients with HNSCC at the time of surgical resec- tion between 1997 and 2000. All tissues were diagnosed histologically as HNSCC by a board certified pathologist. Written informed consent, as required by the Institutional Review Board, was obtained from all patients. Collected samples were stored immediately in liquid nitrogen at _80_C until analysis. Total RNA was isolated from the frozen tumors with TRIzol (Invitrogen). Expression of ESX, EGFR, and Her2 was determined using the Applied Biosystems 7900HT Fast Real-Time PCR System with validated TaqMan gene expression assays (Applied Bio- systems). Gene expression was normalized to GAPDH using theDDCt method.

In vivo tumorigencity and efficacy

For the in vivo tumorigenicity study, CAL27/shRNA- control or CAL27/shRNA-ESX cells (1 106 cells) mixed with Matrigel (1:1) were implanted into the flanks of 6- to 8- week-old female athymic nude mice (National Cancer Institute, Frederick, MD). Tumors were measured and resected for analysis at 18 days postimplantation. For the in vivo efficacy study, CAL27 cells (1 106 cells) mixed with Matrigel (1:1) were implanted into the flanks of 6- to 8- week-old female athymic nude mice (National Cancer Institute). Mice with palpable tumors ($50 mm3) were randomly assigned to 4 experimental groups; vehicle (vehicle intratumoral injection and oral gavage), biphenyl isoxazolidine (100 mg/mouse intratumoral injection, 5 week), afatinib (0.4 mg/mouse oral gavage, 5 week), or biphenyl isoxazolidine þ afatinib. Tumors were measured using a digital caliper and tumor volumes were calculated using the formula: tumor volume 1/4 length width height 0.5. Any mouse with a tumor volume equal to or more than 1,000 mm3 was euthanized and removed from the study. All animal work was conducted in accordance with and approved by the Institutional Animal Care and Use Committee at the Ohio State University.

Immunohistochemical analysis

Resected tumors were fixed in 10% formalin and paraf- fin-embedded. Slides were incubated in citrate buffer (pH 6.0) for antigen retrieval and immunohistochemical staining was carried out using Peroxidase Histostain-Plus Kit (Invitrogen) according to the manufacturer's protocol. ESX antibody (LifeSpan Biosciences Inc.) was used at a 1:500 dilution, EGFR antibody (Millipore) was used at a 1:10 dilution, Her2 antibody (Santa Cruz Biotechnology) was used at a 1:100 dilution, pEGFR-Y1173 antibody (Millipore) was used at 1:100 dilution, and pHer2-Y1221/1222 anti- body (Cell Signaling Technology) was used at 1:100 dilu- tion. Slides were counterstained with hematoxylin and coverslipped using glycerin.

Statistical analysis

Data were analyzed by two-tailed Student t test. P values less than 0.05 were considered significant.

2.6 Synthesis and characterization of i1 and intermediates

3-methylbutanal oxime (i1-2)

Hydroxylamine hydrochloride (13.9 g, 200 mmol) and sodium carbonate (21.0 g, 200 mmol) were combined in 400 mL and heated to 70° C for 1 hour with continuous stirring. Reaction was cooled and isovaleraldehyde (21.7 mL, 200 mmol) was added dropwise. The reaction was stirred for additional 5 mins and was then heated to a light reflux (100° C) and stirred for an additional 4 hours until complete by TLC. The reaction mixture turned from a pale orange with white precipitate to a colorless opaque solution upon heating. After 4 hours, the reaction mixture was cooled, filtered through a scintered glass frit, and washed with toluene. The filtrate was concentrated under reduced pressure and distilled at 100° C under reduced pressure using an aspirator to yield **i1-2** as pale yellow oil (19.1 g, 93%).

(3-isobutyl-4,5-dihyrdoiisoxazol-5-yl)methanol (i1-3)

Oxime **i1-2** (9.46 g, 93 mmol) and allyl alcohol (50 mL, 700 mmol) were combined in 100 mL toluene in a foil wrapped round bottom flask with vigorous stirring, cooled to 0° C. A 6% solution of sodium hypochlorite ('Chlorox bleach', 250 mL, 200 mmol hypochlorite) was added dropwise using an addition funnel. The reaction was allowed to warm up to room termperature and stirred for an additional 12 hours upon warming to room temperature. The crude reaction was partitioned between toluene and water. Organics were dried over sodium sulfate and concentrated under reduced pressure to yield isoxazoline **i1-3** as a yellow oil (9.6 g, 62%).

3-allyl-3-isobutylisoxazolidin-5-y)methanol (i1-4)

Distilled BF_3•Et_2O over CaH under reduced pressure at 150° C using a still head distillation apparatus according to procedure outlined in *Purification of Laboratory Chemicals, 1997*. All glassware was oven dried prior to running reaction. Distilled BF_3•Et_2O (11.2 mL, 90 mmol) was added to isoxazoline **i1-3** (4.8 g, 30 mmol) in 300 mL dry tetrahydrofuran under nitrogen at -78° C. Monitored temperature of reaction using a cold temperature thermometer. Allylmagnesium chloride (2M in hexanes, 75 mL, 150 mmol) was added dropwise using a syringe pump over 45 minutes. Let reaction slowly warm up to room temperature and let stir for an additional 8 hours. Quenched reaction in 1M HCl. Added 1M NaOH until aqueous layer had pH of 10. Extracted aqueous layer with ethyl acetate. Combined organics were dried over sodium sulfate, concentrated under reduced pressure and purified by column chromatography to yield isoxazolidine **i1-4** (9.5 g, 79%).

2-([1,1'-biphenyl]-4-ylmethyl)-3-allyl-3-isobutylisoxazolidin-5-yl)methanol (i1-6)

Tert-butyldimethylsilyl trifluoromethanesulfonate (0.72 mL, 3.125 mmol) was added to a solution of isoxazolidine **i1-4** (0.5 g, 2.5 mmol) and imidazole (0.452 g, 6.25 mmol) in 25 mL dry THF under nitrogen. Reaction was stirred at room temperature and monitored by TLC. After 1 hour, 15 mL of 3M NaOH was added dropwise to reaction. The crude mixture was partitioned with water and extracted with DCM The combined organics were dried over magnesium sulfate and concentrated under reduced pressure. Crude product (**i1-5**) was dissolved with 20 mL dry THF under nitrogen. The crude mixture was cooled to 78° C

with temperature monitored with a cold temperature thermometer. After the crude mixture was sufficiently cooled, nBuLi (2.38M in hexanes, 1.15 mL, 2.75 mmol) was added to dropwise and left with continuous stirring for 15 minutes. Added a solution of bromomethyl biphenyl (0.925 g, 3.75 mmol) in 5 mL of dry THF dropwise to the crude reaction mixture. The crude reaction mixture turned from pale yellow, to orange, to blood red, and finally back to pale yellow. Allowed reaction to slowly warm to room temperature and left stirring for an additional 8 hours. Quenched reaction by adding saturated ammonium chloride until solution no longer bubbled upon addition of saturated ammonium chloride solution. Extracted reaction mixture with hexanes, dried combined organics over magnesium chloride, filtered and concentrated under reduced pressure. Dissolved crude product with 10 mL dry THF under nitrogen. Added tetra-n-butylammonium fluoride (1M in THF, 3.75 mL, 3.75 mmol) dropwise to reaction mixture. Reaction was stirred at room temperature an monitored by TLC. After 1 hour, added 10 mL of 3M NaOH dropwise to the crude reaction mixture. Crude reaction mixture turned into a cloudy white solution. Removed THF under reduced pressure. Extracted aqueous solution with ethyl acetate, dried combined organics over magnesium sulfate, filtered, and concentrated under reduced pressure and purified by column chromatography to yield **i1-6** (0.48 g, 63%).

2-([1,1'-biphenyl]-4-ylmethyl)-3-allyl-5-(azidomethyl)-3-isobutylisxazolidine (i1-7)

Dissolved isoazolidine **XX** (1.78 g, 5 mmol) in 200 mL of dry DCM and added Et_3N (1.4 mL, 10 mmol), and a catalytic amount of dimethylaminopyridine (0.122g, 1 mmol) to the reaction solution. Once all solids were dissolved, 2-nitrobenzene sulfonyl chloride (1.65 g, 7.5 mmol) was added to the crude mixture. Reaction was left at room temperature with vigorous stirring for 2 hours and monitored by TLC. After 2 hours, saturated ammonium chloride was added to the crude mixture. Extracted aqueous layer with DCM, combined organics, dried over magnesium sulfate, and concentrated under reduced pressure to a pale yellow oil. Crude product was dissolved in 25 mL dry DMF under nitrogen atmosphere. Let solution vigorously stir until all solids were dissolved and added sodium azide to the solution. All steps were carried out behind blast shield. Upon addition of sodium azide, reaction mixture changed from pale yellow to orange. Reaction mixture was stirred at room

temperature for 1 hour with vigorous stirring at which point, reaction mixture was heated to 50° C and left to stir for additional 12 hours. Added 100 mL of H_2O to reaction mixture and extracted with diethyl ether. Combined organics, dried over magnesium sulfate, concentrated under reduced pressure, and purified by column chromatography to yield **i1-7** (1.61 g, 85%).

2-([1,1'-biphenyl]-4-ylmethyl)-5-(azidomethyl)-3-isobutylisoxazolidin-3-yl)ethanol (i1)

Osmium tetroxide (as a 2.5% solution in tert butanol, 1.55 mL, 0.1235 mmol) was added to isoxazolidine **i1-7** (4.3 g, 11 mmol), N-methylmorpholine-N-oxide (2.17 g, 18.3 mmol), and citric acid monohydrate (5.19 g, 24.7 mmol) in a mixture of tBuOH/THF/H_2O (1:1:1). Reaction mixture turned from pale green to light brown after 1 hour. Reaction was quenched with sodium sulfite. The crude mixture was diluted with a saturated sodium chloride solution. Extracted aqueous layer with ethyl acetate, combined organics, dried over magnesium sulfate, filtered, concentrated under reduced pressure, and purified by column chromatography. Minor diastereomer was separated from major diastereomer using column chromatography. The isolated major diastereomer was concentrated under reduced pressure and immediately carried onto the next step of the synthesis (2.8 g, 60%). Isoxazolidine (2.8 g, 6.6 mmol) was dissolved in 50 mL of DCM. Added (diacetoxyiodo)benzene (4.0 g, 12.4 mmol) to the reaction mixture with vigorous stirring and monitored reaction progress by TLC. After 1 hour, added sodium borohydride (0.265g, 7.0 mmol) dissolved in 5 mL ethanol to the reaction mixture. Let reaction stir with vigorous stirring for 12 hours. Performed acid/base workup on crude reaction mixture. Combined organics, dried over sodium sulfate, filtered to remove solids, concentrated under reduced pressure, and purified by column chromatography to yield **i1** (1 g, 40%).

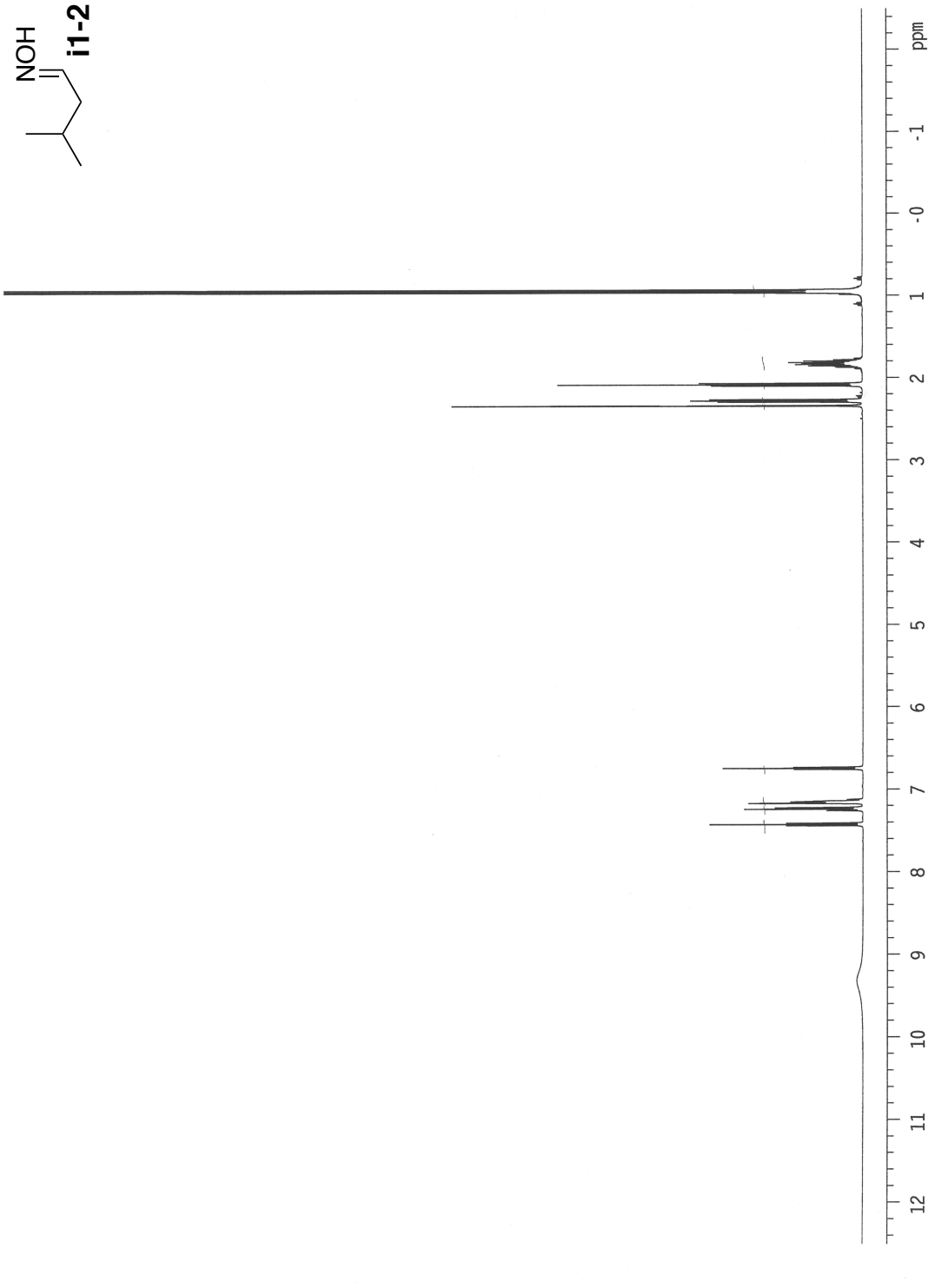
NOH
i1-2
ppm
-1
-0
1
2
3
4
5
6
7
8
9
10
11
12

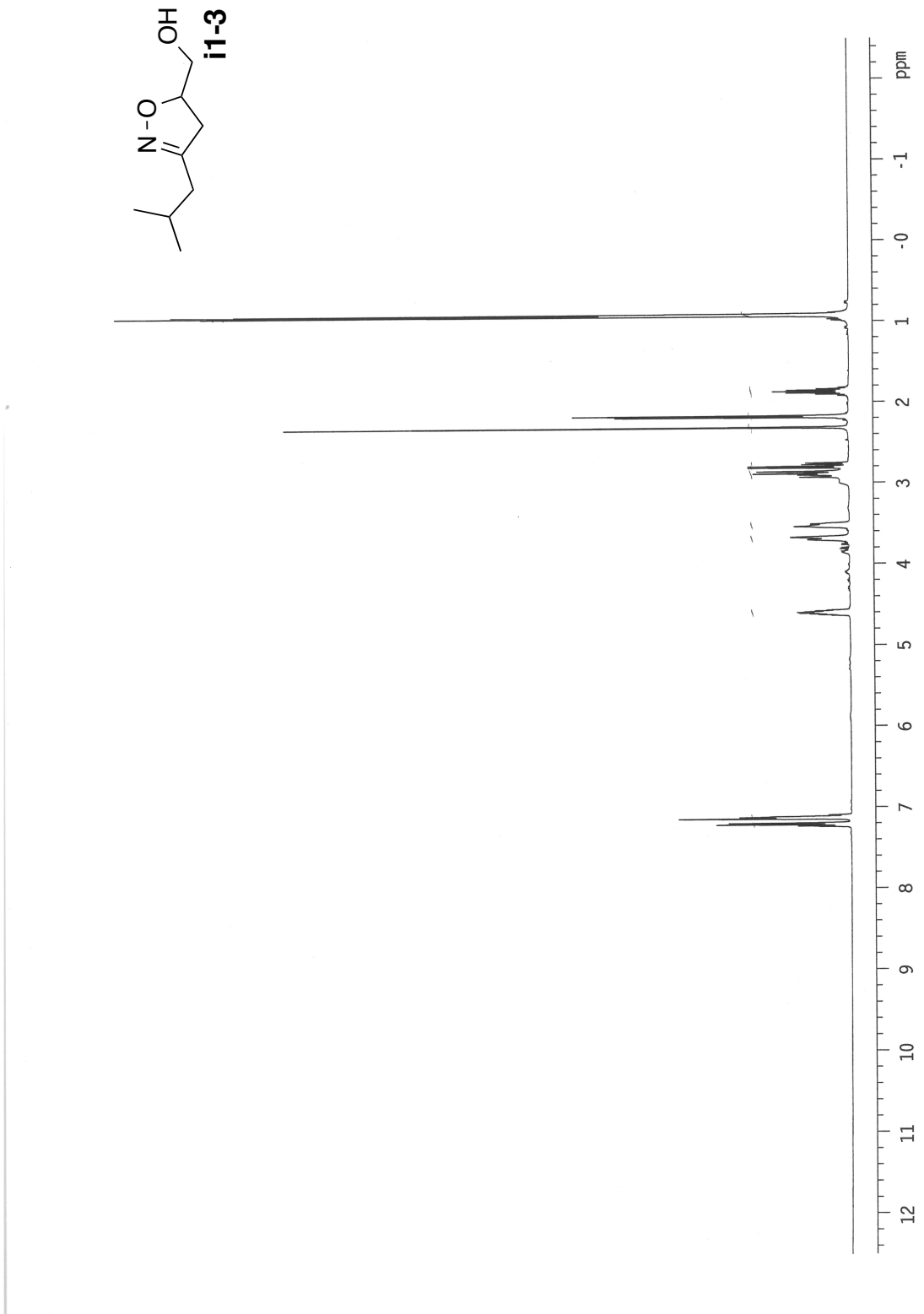
OH
N-O
i1-3
ppm
12
11
10
9
8
7
6
5
4
3
2
1
-0
-1

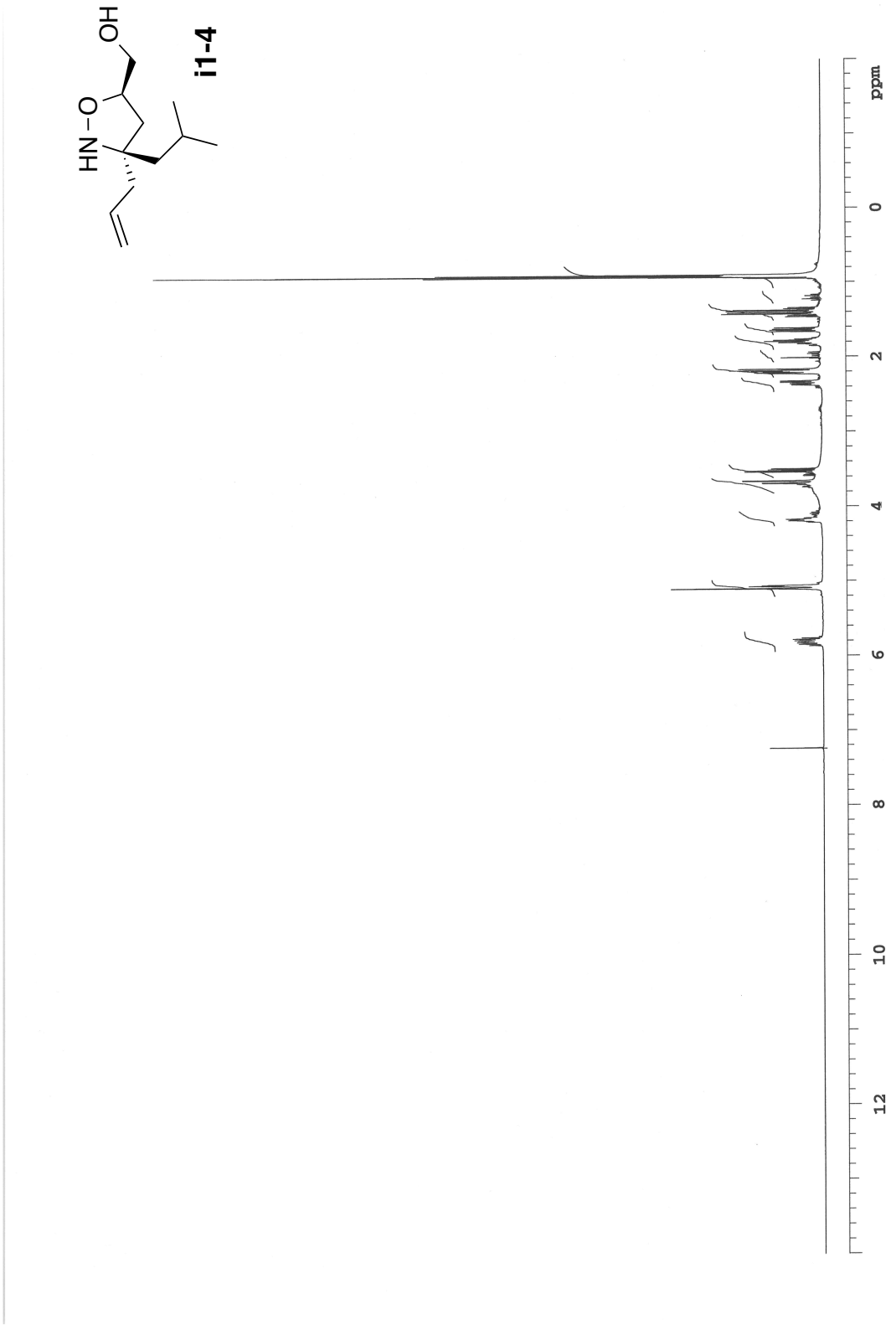
OH
HN–O
i1-4
ppm
0
2
4
6
8
10
12

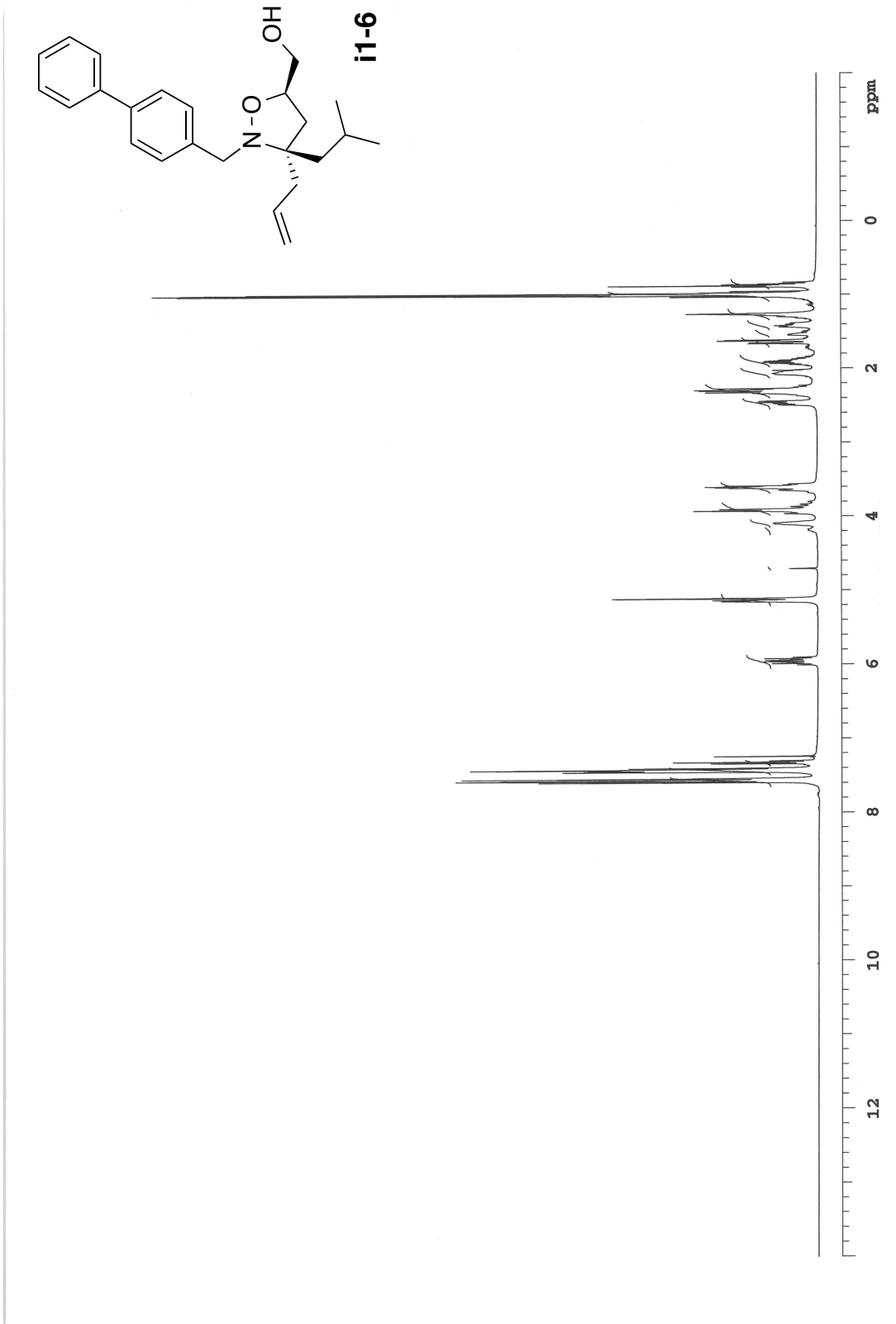
i1-6
OH
N-O
ppm
0
2
4
6
8
10
12

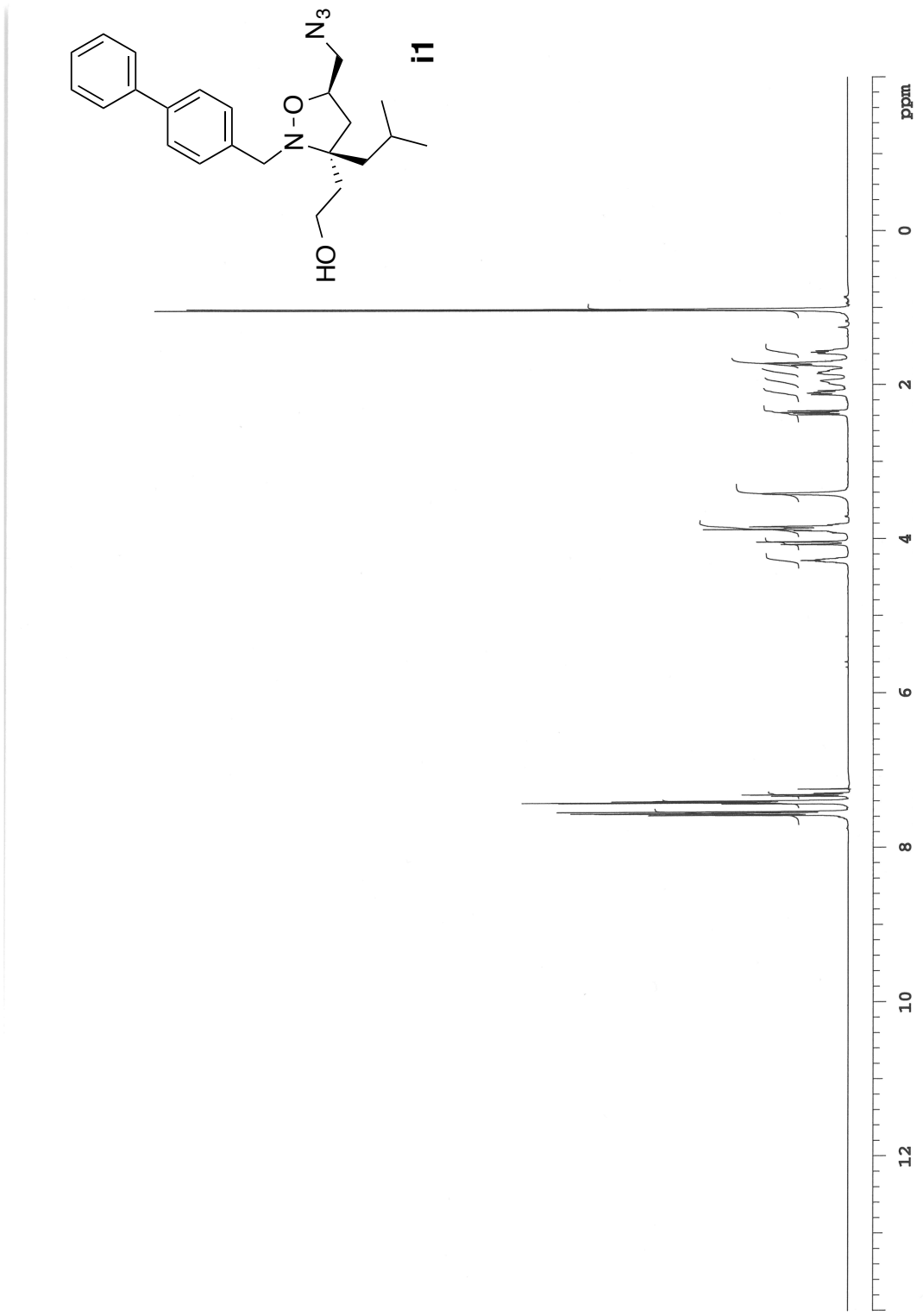
N3
N-O
HO
i1
ppm
0
2
4
6
8
10
12

Analytical HPLC trace of **i1** used for cellular and *in vivo* work

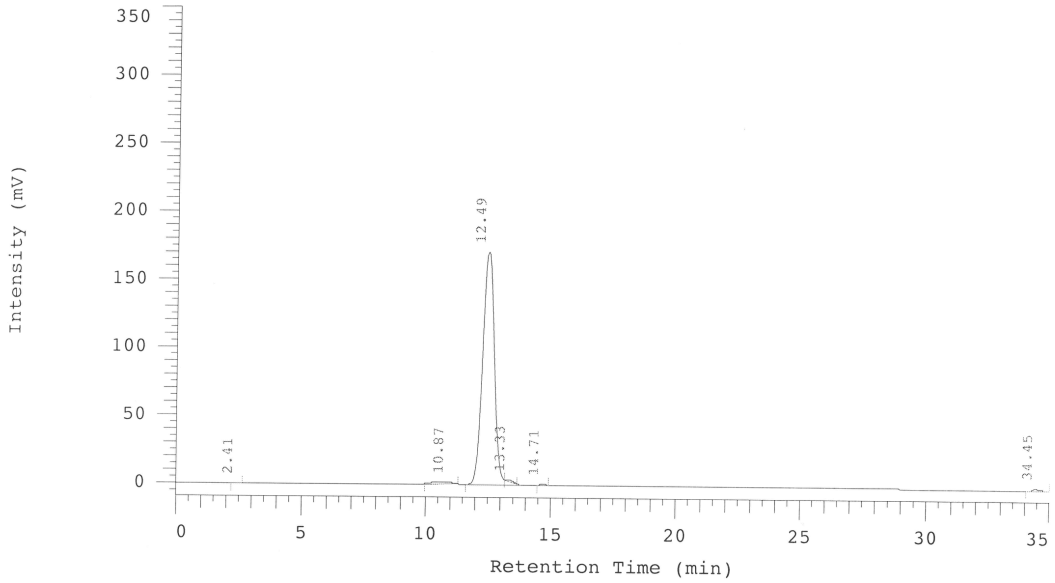

2.7 References

(1) Kamangar, F.; Dores, G. M.; Anderson, W. F. Patterns of Cancer Incidence, Mortality, and Prevalence Across Five Continents: Defining Priorities to Reduce Cancer Disparities in Different Geographic Regions of the World. *J. Clin. Oncol.* **2006**, *24*, 2137–2150.

(2) Choong, N. W.; Cohen, E. E. W. Epidermal Growth Factor Receptor Directed Therapy in Head and Neck Cancer. *Crit. Rev. Oncol. Hematol.* **2006**, *57*, 25–43.

(3) Weihua, Z.; Tsan, R.; Huang, W.-C.; Wu, Q.; Chiu, C.-H.; Fidler, I. J.; Hung, M.-C. Survival of Cancer Cells Is Maintained by EGFR Independent of Its Kinase Activity. *Cancer Cell* **2008**, *13*, 385–393.

(4) Wang, S.-C.; Hung, M.-C. Nuclear Translocation of the Epidermal Growth Factor Receptor Family Membrane Tyrosine Kinase Receptors. *Clinical Cancer Research* **2009**, *15*, 6484–6489.

(5) Erjala, K.; Sundvall, M.; Junttila, T. T.; Zhang, N.; Savisalo, M.; Mali, P.; Kulmala, J.; Pulkkinen, J.; Grenman, R.; Elenius, K. Signaling via ErbB2 and ErbB3 Associates with Resistance and Epidermal Growth Factor Receptor (EGFR) Amplification with Sensitivity to EGFR Inhibitor Gefitinib in Head and Neck Squamous Cell Carcinoma Cells. *Clinical Cancer Research* **2006**, *12*, 4103–4111.

(6) Oikawa, T.; Yamada, T. Molecular Biology of the Ets Family of Transcription Factors. *Gene* **2003**, *303*, 11–34.

(7) Cabral, A.; Fischer, D. F.; Vermeij, W. P.; Backendorf, C. Distinct Functional Interactions of Human Skn-1 Isoforms with Ese-1 During Keratinocyte Terminal Differentiation. *J Biol Chem* **2003**, *278*, 17792–17799.

(8) Schedin, P. J.; Eckel-Mahan, K. L.; McDaniel, S. M.; Prescott, J. D.; Brodsky, K. S.; Tentler, J. J.; Gutierrez-Hartmann, A. ESX Induces Transformation and Functional Epithelial to Mesenchymal Transition in MCF-12A Mammary Epithelial Cells. *Oncogene* **2004**, *23*, 1766–1779.

(9) Asada, S.; Choi, Y.; Yamada, M.; Wang, S.-C.; Hung, M.-C.; Qin, J.; Uesugi, M. External Control of Her2 Expression and Cancer Cell Growth by Targeting a Ras-Linked Coactivator. *Proc Natl Acad Sci USA* **2002**, *99*, 12747–12752.

(10) Neve, R. M.; Ylstra, B.; Chang, C.-H.; Albertson, D. G.; Benz, C. C. ErbB2 Activation of ESX Gene Expression. *Oncogene* **2002**, *21*, 3934–3938.

(11) Thompson, A. D.; Dugan, A.; Gestwicki, J. E.; Mapp, A. K. Fine-Tuning Multiprotein Complexes Using Small Molecules. *ACS Chem. Biol.* **2012**, *7*, 1311–1320.

(12) Lee, L. W.; Mapp, A. K. Transcriptional Switches: Chemical Approaches to Gene Regulation. *Journal of Biological Chemistry* **2010**, *285*, 11033–11038.

(13) J, B.; L, P.; M, E.; N, S.; C, H.; H, M.; I, K.; J, A.; D, A.; P, C. The Selectivity of Protein Kinase Inhibitors: a Further Update. *Biochem. J.* **2007**, *408*, 297.

(14) Karaman, M. W.; Herrgard, S.; Treiber, D. K.; Gallant, P.; Atteridge, C. E.; Campbell, B. T.; Chan, K. W.; Pietro Ciceri; Davis, M. I.; Edeen, P. T.; Faraoni, R.; Floyd, M.; Hunt, J. P.; Lockhart, D. J.; Milanov, Z. V.; Morrison, M. J.; Pallares, G.; Patel, H. K.; Pritchard, S.; Wodicka, L. M.; Zarrinkar, P. P. A Quantitative Analysis of Kinase Inhibitor Selectivity. *Nature Biotechnology* **2008**, *26*, 127–132.

(15) Kim, G. W.; Song, J. S.; Choi, C.-M.; Rho, J. K.; Kim, S. Y.; Jang, S. J.; Park, Y. S.; Chun, S.-M.; Kim, W. S.; Lee, J.-S.; Kim, S.-W.; Lee, D. H.; Lee, J. C. Multiple Resistant Factors in Lung Cancer with Primary Resistance to EGFR-TK Inhibitors Confer Poor Survival. *Lung Cancer* **2015**, *88*, 139–146.

(16) Heinrich, M. C.; Corless, C. L.; Demetri, G. D.; Blanke, C. D.; Mehren, von, M.; Joensuu, H.; McGreevey, L. S.; Chen, C.-J.; Van den Abbeele, A. D.; Druker, B. J.; Kiese, B.; Eisenberg, B.; Roberts, P. J.; Singer, S.; Fletcher, C. D. M.; Silberman, S.; Dimitrijevic, S.; Fletcher, J. A. Kinase Mutations and Imatinib Response in Patients with Metastatic Gastrointestinal Stromal Tumor. *JCO* **2003**, *21*, 4342–4349.

(17) Taylor, C. E.; Pan, Q.; Mapp, A. K. Synergistic Enhancement of the Potency and Selectivity of Small Molecule Transcriptional Inhibitors. *ACS Med. Chem. Lett.* **2011**, *3*, 30–34.

(18) Cokol, M.; Chua, H. N.; Tasan, M.; Mutlu, B.; Weinstein, Z. B.; Suzuki, Y.; Nergiz, M. E.; Costanzo, M.; Baryshnikova, A.; Giaever, G.; Nislow, C.; Myers, C. L.; Andrews, B. J.; Boone, C.; Roth, F. P. Systematic Exploration of Synergistic Drug Pairs. *Molecular Systems Biology* **2011**, *7*, 544–544.

(19) Lehár, J.; Krueger, A. S.; Avery, W.; Heilbut, A. M.; Johansen, L. M.; Price, E. R.; Rickles, R. J.; Short, G. F., III; Staunton, J. E.; Jin, X.; Lee, M. S.; Zimmermann, G. R.; Borisy, A. A. Synergistic Drug Combinations Tend to Improve Therapeutically Relevant Selectivity. *Nature Biotechnology* **2009**, *27*, 659–666.

(20) Perez, E. A. Carboplatin in Combination Therapy for Metastatic Breast Cancer. *Oncologist* **2004**, *9*, 518–527.

(21) Jorissen, R. Epidermal Growth Factor Receptor: Mechanisms of Activation and Signalling. *Experimental Cell Research* **2003**, *284*, 31–53.

(22) Carlsson, J.; Nordgren, H.; Sjöström, J.; Wester, K.; Villman, K.; Bengtsson, N. O.; Ostenstad, B.; Lundqvist, H.; Blomqvist, C. HER2 Expression in Breast Cancer Primary Tumours and Corresponding Metastases. Original Data and Literature Review. *British Journal of Cancer* **2004**, *90*, 2344–2348.

(23) Slamon, D. J.; Clark, G. M.; Wong, S. G.; Levin, W. J.; Ullrich, A.; McGuire, W. L. Human Breast Cancer: Correlation of Relapse and Survival with Amplification of the HER-2/Neu Oncogene. *Science* **1987**, *235*, 177–182.

(24) Trastuzumab and Breast Cancer. *N Engl J Med* **2001**, *345*, 995–998.

(25) Scott, G. K.; Daniel, J. C.; Xiong, X.; Maki, R. A.; Kabat, D.; Benz, C. C. Binding of an ETS-Related Protein Within the DNase I Hypersensitive Site of the HER2/Neu Promoter in Human Breast Cancer Cells. *J Biol Chem* **1994**, *269*, 19848–19858.

(26) Chang, C. H.; Scott, G. K.; Baldwin, M. A.; Benz, C. C. Exon 4-Encoded Acidic Domain in the Epithelium-Restricted Ets Factor, ESX, Confers Potent Transactivating Capacity and Binds to TATA-Binding Protein (TBP). *Oncogene* **1999**, *18*, 3682–3695.

(27) Lee, L. W.; Taylor, C. E. C.; Desaulniers, J.-P.; Zhang, M.; Højfeldt, J. W.; Pan, Q.; Mapp, A. K. Inhibition of ErbB2(Her2) Expression with Small Molecule Transcription Factor Mimics. *Bioorganic & Medicinal Chemistry Letters* **2009**, *19*, 6233–6236.

(28) Baselga, J.; Mendelsohn, J. The Epidermal Growth Factor Receptor as a Target for Therapy in Breast Carcinoma. *Breast Cancer Res. Treat.* **1994**, *29*, 127–138.

(29) Dupau, P.; Epple, R.; Thomas, A. A.; Fokin, V. V.; Sharpless, K. B. Osmium-Catalyzed Dihydroxylation of Olefins in Acidic Media: Old Process, New Tricks. *Advanced Synthesis & Catalysis* **2002**, *344*, 421–433.

(30) Borisy, A. A.; Elliott, P. J.; Hurst, N. W.; Lee, M. S.; Lehár, J.; Price, E. R.; Serbedzija, G.; Zimmermann, G. R.; Foley, M. A.; Stockwell, B. R.; Keith, C. T. Systematic Discovery of Multicomponent Therapeutics. *Proc Natl Acad Sci USA* **2003**, *100*, 7977–7982.

(31) Lehár, J.; Zimmermann, G. R.; Krueger, A. S.; Molnar, R. A.; Ledell, J. T.; Heilbut, A. M.; Short, G. F.; Giusti, L. C.; Nolan, G. P.; Magid, O. A.; Lee, M. S.; Borisy, A. A.; Stockwell, B. R.; Keith, C. T. Chemical Combination Effects Predict Connectivity in Biological Systems. *Molecular Systems Biology* **2007**, *3*, 659-666.

(32) Biswas, D. K.; Iglehart, J. D. Linkage Between EGFR Family Receptors and Nuclear Factor kappaB (NF-κB) Signaling in Breast Cancer. *J. Cell. Physiol.* **2006**, *209*, 645–652.

(33) Biswas, D. K.; Shi, Q.; Baily, S.; Strickland, I.; Ghosh, S.; Pardee, A. B.; Iglehart, J. D. NF-Kappa B Activation in Human Breast Cancer Specimens and Its Role in Cell Proliferation and Apoptosis. *Proc Natl Acad Sci USA* **2004**, *101*, 10137–10142.

(34) Singh, S.; Shi, Q.; Bailey, S. T.; Palczewski, M. J.; Pardee, A. B.; Iglehart, J. D.; Biswas, D. K. Nuclear Factor-kappaB Activation: a Molecular Therapeutic Target for Estrogen Receptor-Negative and Epidermal Growth Factor Receptor Family Receptor-Positive Human Breast Cancer. *Mol. Cancer Ther.* **2007**, *6*, 1973–1982.

(35) Montagut, C.; Tusquets, I.; Ferrer, B.; Corominas, J. M.; Bellosillo, B.; Campas, C.; Suarez, M.; Fabregat, X.; Campo, E.; Gascon, P.; Serrano, S.; Fernandez, P. L.; Rovira, A.; Albanell, J. Activation of Nuclear Factor-Kappa B Is Linked to Resistance to Neoadjuvant Chemotherapy in Breast Cancer Patients. *Endocr Relat Cancer* **2006**, *13*, 607–616.

(36) Best, J. L.; Amezcua, C. A.; Mayr, B.; Flechner, L.; Murawsky, C. M.; Emerson, B.; Zor, T.; Gardner, K. H.; Montminy, M. Identification of Small-Molecule Antagonists That Inhibit an Activator: Coactivator Interaction. *Proc Natl Acad Sci USA* **2004**, *101*, 17622–17627.

Chapter 3

Identifying Depside and Depsidone Inhibitors of Med25 ACID-mediated Transcription*

3.1 Abstract

Mediator subunit 25 (Med25) is a component of the megadalton Mediator complex, whose recruitment is required for the expression of most genes in eukaryotic organisms. [1,2] The **Ac**tivator **I**nteraction **D**omain (ACID) is a key component of the Med25 protein that has been recently shown to make critical contacts with several transcription factors, allowing for the recruitment of the full mediator complex to target genes (Figure 3.1). These transcription factors include VP16, a crucial component of the herpes simplex virus (HSV) responsible for the switch from latent to lytic infection[3,4]; ATF6α, an endoplasmic reticulum stress response transcription factor[5]; and ERM, a member of the Ets family of transcription factors that has been implicated in the progression of cancer. [6,7] Given the functional

* The research described in chapter 3 is a collaborative effect. P.A. Bruno and S. M. Sturlis synthesized and purified tracers, expressed and purified protein, developed high-throughput assay, performed pilot screen with high-throughput assay, performed mass spectrometry of covalent adducts, and performed screen with natural product extracts. S. M. Sturlis performed KIX counter screen, mutational analysis with ACID protein, and investigated effects of electrostatics. P. A. Bruno performed mass spectrometry analysis for other aldehyde containing molecules, cellular assays with ATF6α, ERM, and RAR, Protein NMR and performed additional counter screens. Felicia Grey (Cierpicki Lab) performed protein NMR analysis. Jessica Gagnon (Brooks Lab) performed molecular dynamics experiments. Identified compounds were obtained from Giselle Tamayo-Castillo. Screen was performed in University of Michigan Center for Chemical Genomics. Parts of this chapter are reproduced in Paul A. Bruno,+ Steve M. Sturlis,+ Felicia Grey, Jessica K Gagnon, Giselle Tamayo-Castillo, David H. Sherman, and Anna K. Mapp* Identifying Depside and Depsidone Inhibitors of Med25 ACID-mediated transcription. *Manuscript in progress*.

importance of Med25 recruitment by various transcription factors, inhibitors of these interactions would be useful mechanistic probes for interrogating Med25 dependent gene expression. Herein chapter 3, we demonstrate how a high-throughput assay can be developed based on the Med25-VP16 interaction. Using this assay that we developed, we performed high-throughput screening to yield depside and depsidone inhibitors of Med25 ACID. These inhibitors described herein are the first discovered inhibitors of ACID and demonstrate inhibition of Med25-dependent transcription is achievable with small molecules.

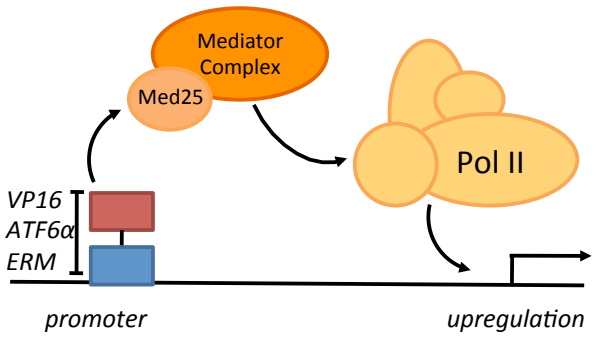

Figure 3.1 Mediator subunit (Med25) mediated gene upregulation The transcriptional activation domains of VP16, ATF6α, and ERM make specific interaction with Med25. This interaction recruits the Mediator complex, leading to assembly of the transcriptional machinery and target gene upregulation.

3.2 Introduction

Virtually all cellular processes are governed through the activity of multimeric protein complexes organized through specific protein-protein interactions (PPI). [1,2] One such process is transcriptional regulation, which allows for the selective expression of relevant genes in a context and tissue dependent manner. Specifically, the binding of transcriptional activators to conserved genomic sequences allows for the recruitment of necessary coregulatory proteins and the transcriptional machinery to gene promoters, resulting in the expression of the target gene. [8,9] The dysregulation of this process is implicated in the vast majority of human diseases as either a cause or consequence, underscoring the therapeutic potential of developing methodologies to alter this regulatory process.[10] The interactions between transcriptional activators and coregulatory machinery typically occur with moderate to weak affinity over broad surface areas with ill-defined topology, allowing for the assembly of functionally and compositionally distinct

complexes.[11] As a result, targeting these types of interfaces with small molecules is particularly challenging.

The megadalton Mediator complex is a critical component of the transcriptional machinery, whose recruitment is required for the expression of most genes in eukaryotic organisms.[1] Recently, the Activator Interaction Domain (ACID) of subunit Med25 has emerged as an important contact within this complex for several transcriptional activators, allowing for the recruitment of the full mediator complex to target genes. These transcriptional activators include VP16[3,4], a crucial component of the herpes simplex virus (HSV) responsible for the switch from latent to lytic infection; ATF6α, an endoplasmic reticulum stress response transcription factor[5,12]; and ERM, a member of the Ets family of transcription factors that has been implicated in the progression of a variety of cancers.[6] The ACID domain consists of a seven-stranded beta barrel flanked by three alpha-helices, a highly uncommon fold identified in only one other protein of unknown function.[13] Given the large interaction surface area of approximately 3700 Å^2 used to bind its transcriptional activators, identifying small molecule inhibitors capable of disrupting such broad interaction surfaces is a remarkable challenge. This multifaceted problem is underscored by a lack of critical structural information that identifies the minimal binding domain of transcriptional activators to Med25 or how specific mechanistic features, such as electrostatics, contribute to binding affinity. Despite these challenges, the role of Med25 dependent gene expression in cellular processes such as advanced viral infection, cancer metastasis, and stress response makes the AcID domain an extremely attractive target for small molecule intervention. Such molecules would be useful as mechanistic probes in the further characterization of Med25 dependent processes and could serve as potential lead molecules in the development of novel antiviral and anticancer therapeutics.

It has recently been reported that two subdomains of the VP16 transcriptional activation domain (TAD) interact with Med25 ACID. [3,4] However, given the limited structural information about Med25 and the intractable nature of the VP16 subdomains we sought to identify the minimal VP16 sequences required for binding to Med25 ACID as a means to reduce the interaction surface area to a size more amenable to small molecule intervention. Additionally, we identified additional biophysical contributions to binding, such as electrostatics, that could be exploited in the identification of inhibitors. From these

studies, we were able to develop a fluorescence polarization based assay that was well adapted for high-throughput screening against the ACID domain. A screen of known biologically active compounds revealed depsides and depsidones, natural products derived from lichens, as a compelling class of potential inhibitors.[14] Compounds containing the depside or depsidone core were then selected and utilized in a dose response assay, revealing norstictic acid as the first in vitro inhibitor of Med25.

BACKGROUND OF MEDIATOR SUBUNIT 25 (MED25)

The Mediator complex

Mediator subunit 25 (Med25) is a component of the Mediator complex, a coactivator required for nearly all RNA-polymerase II-dependent genes.[2] The Mediator complex serves as a bridge between the gene-specific regulatory proteins such as transcriptional activators and the basal RNA polymerase II transcription machinery.[9] When the mediator complex is recruited to gene promoter sites by direct interactions with regulatory proteins, it serves as a scaffold for the assembly of a function preinitiation complex with RNA polymerase II and the general transcription factors. The subunits of Mediator complex form at least three structurally distinct submodules: head, middle, tail, and CDK8 module, with the latter serving mostly a support role for the rest of the complex.[15] The head and middle modules of the Mediator complex interact directly with RNA polymerase II, whereas the tail submodules interacts with gene-specific regulatory proteins, such as transcriptional activators.[16] It was initially thought that Med23-30 were specific to higher eukaryotes[17], but recently Med24, Med27, and Med29 have been proposed to be distantly related orthologs of *S. cerevisiae* Mediator subunits Med5, Med3 and Med2, respectively.[18] The Mediator tail is perhaps the most evolutionarily divergent module of the Mediator complex, but this would not be surprising given the role of the Mediator tail to interact with DNA-binding transcriptional activators. [19,20] The Mediator tail includes conserved subunits Med15, Med16, in addition to the subunits Med23, Med24, and Med25. Med23 and Med25 make specific contact with a variety of transcriptional activators. In the case of Med23, specific contacts are made through its various subdomains with transcriptional activators Elk1[21], ESX[22], and even C/EBPβ[23]. As for Med25, specific interactions have been demonstrated with the activators VP16, ERM, ATF6α, RARα, and ERα. [3,4,24,25] Given the

importance of the tail Mediator subunits and their distinct role of interacting with transcriptional activators, targeting these activator-coactivator interactions could prove to be highly effective against these activators ability to upregulate their target genes.

Mediator subunit 25 (Med25), a subunit of the Mediator complex

One of the subunits that is of particular interest to us is the Med25 subunit introduced above. Biochemical experiments performed by Tomomori and coworkers demonstrated that Med25 is a *bona fide* subunit of the Mediator complex and is only found in mammals.[26] Med25 is ubiquitously expressed and found in several tissues including brain, heart, kidney, peripheral leukocytes, placenta, skeletal, muscle, and spleen tissue.[27] Furthermore, Med25 consists of three defined domains: the von Willibrand factor A domain (VWA), the activator interaction domain (ACID), and a nuclear receptor LXXLL box (Figure 3.2A).[28] The VWA domain is used for binding to the mediator complex, whereas the ACID domain is used to make specific interaction with the TADs of VP16, ERM, ATF6α, as well as the N-terminus of CBP. [24]There is also a nuclear receptor (NR) box containing the LXXLL sequence required for coactivator binding to nuclear receptors Retinoic Acid Receptor α (RARα)[24] and Estrogen Recepter α (ERα).[25] Given the importance of the ACID domain for interaction with transcriptional activators, inhibitors developed against this domain would presumably be an effective method of targeting these transcriptional activators.

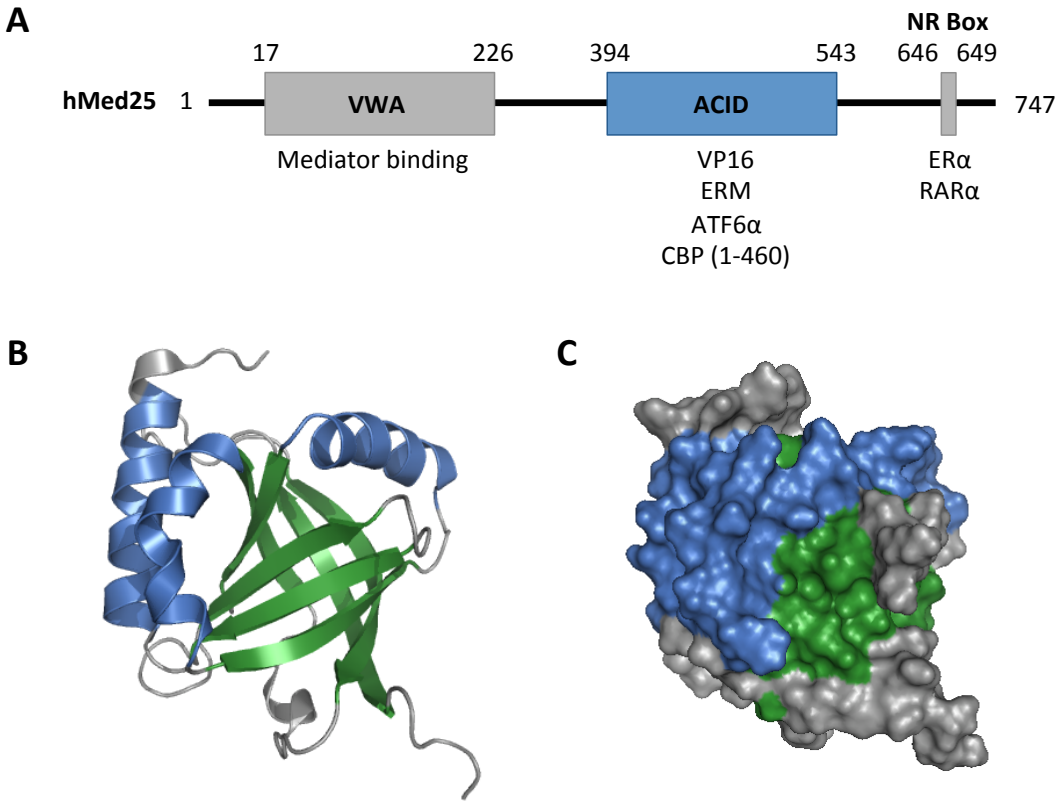

Figure 3.2 Subdomains of Med25 and unique structure of Med25 ACID A. A protein map of human Med25. The Med25 protein consists of three domains: the von Willibrand factor A domain (VWA), the activator interaction domain (ACID), and the nuclear receptor (NR) box. Known interaction partners are listed below their respective subdomains. B. NMR solution structure of Med25 ACID highlighting the 7-stranded β-barrel (green) flanked by 3 α-helices (blue). C. Surface representation of Med25 highlighting topology.

The Med25 Activator Interaction Domain (ACID)

In addition to the importance of the ACID domain for transcriptional activator binding, the unique structural features of ACID suggests that selective inhibitors can be developed against this domain due to the lack of similarities shared with other known activator interaction domains. One notable example is the KIX domain in Med15. The Med15 KIX domain is made up of purely α-helical secondary structure. This is in obvious contrast to the ACID domain, which consists of a 7-stranded β-barrel flanked by 3 α-helices(Figure 3.2B). Furthermore, the ACID domain is quite different from other activator interaction domains such as CBPKIX[29], CH1[30], BRD4[31], and NCOA3[32], which are also largely α-helical (Figure 3.3). This further highlights the unique structural characteristics of ACID domain that could possibly be exploited for development of inhibitors.

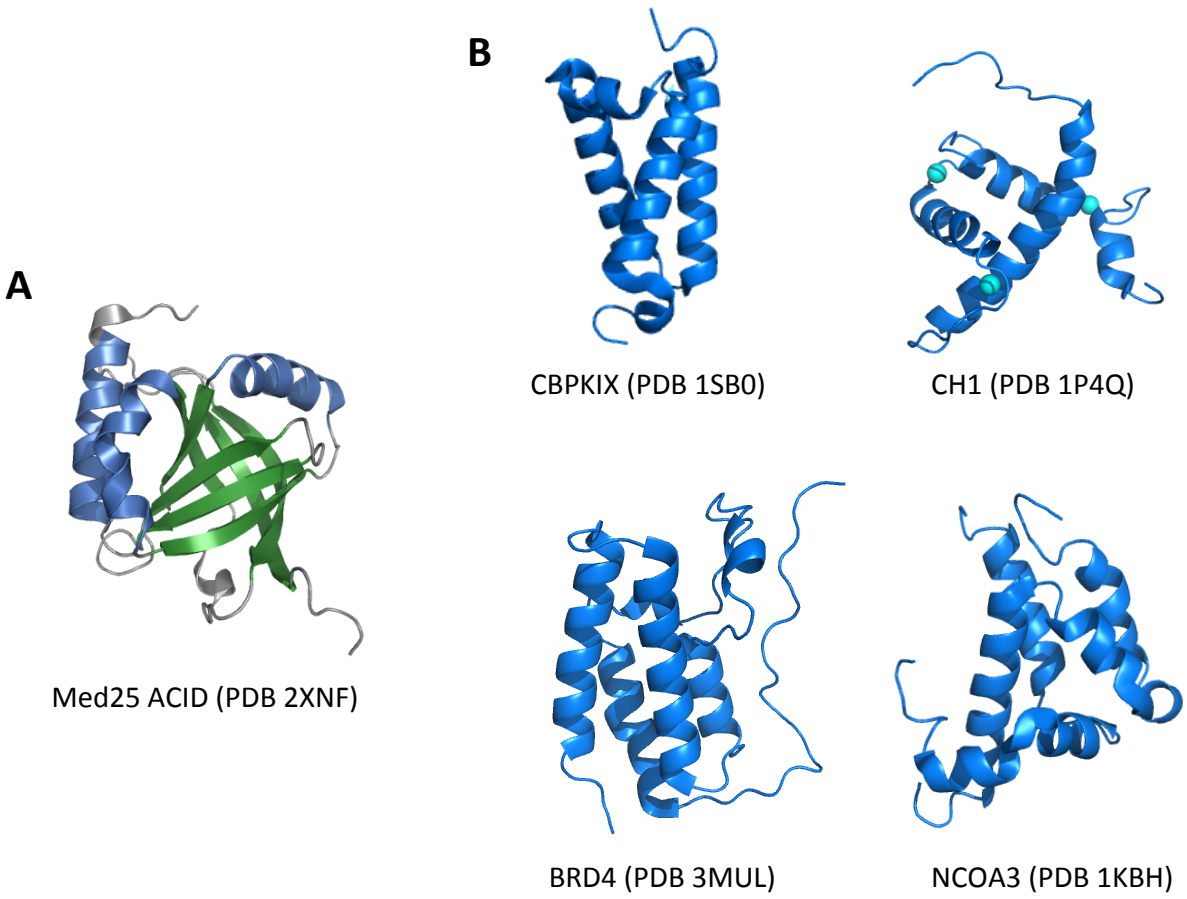

Figure 3.3 Comparing the Med25 activation interaction domain (ACID) with other activator interaction domains. A. Med25 ACID is defined by a 7-stranded β-barrel (green) flanked by 3 α-helices (blue), a unique structure for activator interaction domains. B. Structures of other activator interaction domains CBPKIX, CH1, BRD4, and NCOA3, highlighting the primarily α-helical secondary structure found in other activator interaction domains.

Recently, both Milbradt and coworkers and Vojnic and coworkers published NMR structural information of the ACID domain interaction with VP16. [3,4] Work by both of these groups identified two regions on ACID that correlate with VP16 binding, denoted as the H1 ($VP16_{413-451}$) and H2 ($VP16_{452-490}$) binding site. Milbradt and coworkers identified the VP16(413-451) domain of VP16 to be the important VP16 subdomain required for ACID binding. This is in contrast to Vojnic and coworkers who identified the VP16(452-490) domain of VP16 as the important subdomain required for ACID binding.

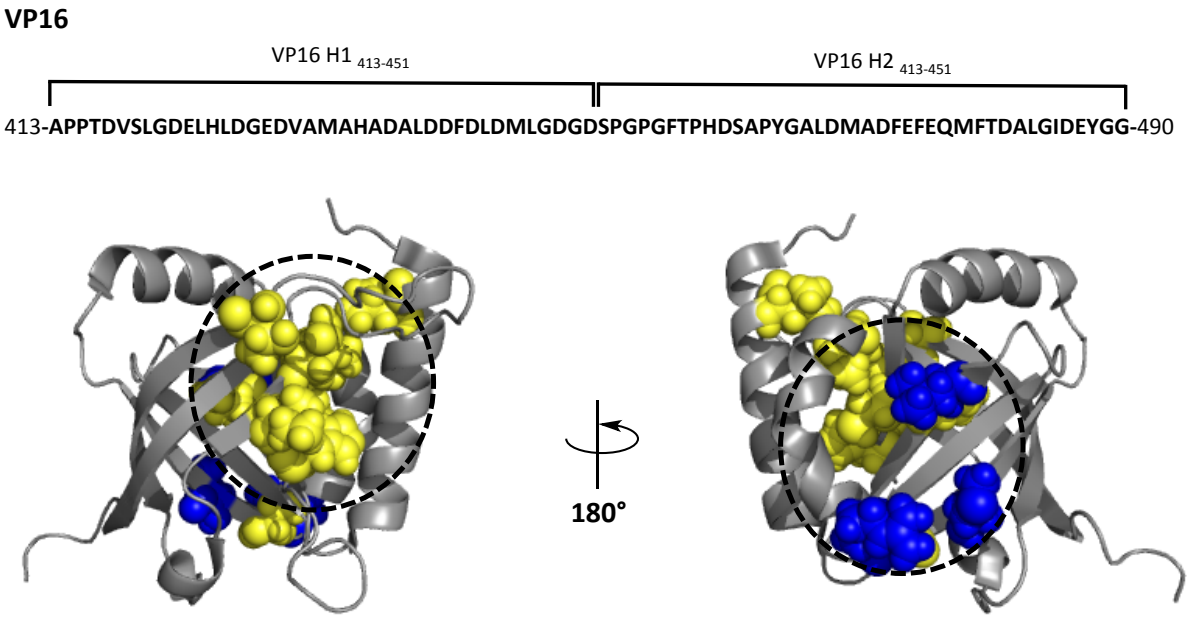

Figure 3.4 The H1 and H2 binding site on the ACID domain The VP16 transcriptional activation domain (TAD) is listed above ($VP16_{413-490}$) with the VP16 $H1_{413-451}$ and the VP16 $H2_{452-490}$ defined. On the left, the ACID H1 binding site is defined by the residues perturbed upon binding to VP16(413-451) (denoted in yellow). On the right, the ACID H2 binding site is defined by the residues perturbed upon binding to VP16(452-490) (denoted in blue). The dotted circles indicate the approximated binding sites of H1 and H2, respectively.

Experiments performed by Milbradt and coworkers identified a range of chemical shifts in the ^{1}H-^{15}N spectra of ACID with titration of VP16(413-451) peptide. From these NMR titration experiments, Milbradt identified prominent chemical shifts localized to discrete regions of ACID that included residues T424, I449, Q451, I453, S468, C497, H499, L513, and L544 (Figure 3.4, left side, yellow spheres). In contrast, experiments performed by Vojnic and coworkers identified chemical shifts in the ^{1}H-^{15}N spectra of ACID with titration of the VP16(452-490) peptide that localized to residues Leu514, Arg466, and Met470 (Figure 3.4, right side, blue spheres). These results indicate that the TAD subdomains VP16(413-451) and VP16(452-490) do not compete for the same ACID surface, but rather bind distinct surfaces within ACID.

TARGETING MED25 ACID

The utility of small molecule probes targeting Med25 ACID

The affinity of the VP16-Med25 interaction is very tight binding (50 nM), providing

rationale for how immobilized VP16 TAD can purify the Mediator complex from nuclear extracts.[33] Parallel experiments performed by Milbradt and coworkers as well as Vojnic and coworkers reached the same conclusion that Med25 ACID contains two distinct binding sites, denoted H1- and H2-binding site. However, contradicting data from both groups makes it challenging to conclude whether the H1-binding site, the H2-binding, or a combination of the two is important for the VP16-ACID interaction. With the importance of Med25 in cellular processes such as viral activation, cellular stress, and cancer, it is obvious that small molecules targeting Med25-mediated transcription would possess enormous therapeutic potential. However, given the conflicting and undetermined importance of the VP16(413-451) and VP16(452-490) subdomains to overall VP16 TAD binding, small molecule inhibitors of Med25 ACID would also prove to be highly beneficial as *in vitro* chemical probes. Developing inhibitors against ACID would allow us to determine the minimal binding interaction between VP16 and ACID as well as determine the importance of specific contributions to binding, such as electrostatics. The size of the VP16 TAD (81 amino acids) or either of the subdomains (~40 amino acids) and the large surface area used to interact with either site of ACID (1500 Å) classically defines this interaction in the large surface area regime.[11] Additionally, the affinities of both the VP16(413-451) and VP16(452-490) subdomains of VP16 have been reported to be in the high nanomolar to low micrmolar range. [3,4] Together, the large surface area and the low affinity (high nanomolar to low micromolar) classifies this protein-protein interaction as a low affinity, large surface area interaction. As noted in chapter 1, there are several challenges associated with targeting these large surface area, low affinity interactions such as the need for high effective concentrations of inhibitor needed to completely block the interaction, off-target effects, and the lack of suitable molecule libraries to target these types of interactions.

Using natural products to target the Med25-VP16 interaction

Small molecules have become powerful tools for impacting both biology and medicine. In biology, these small molecules have served as probes to aid researchers in deciphering complex biological processes.[34] In medicine, small molecules have been developed as therapeutics to combat various ailments. These characteristics have resulted

in a explosion of small molecule compound libraries to screen both phenotypic and biochemical assays. A number of these efforts have ended in disappointment, partly because we do not possess a full understanding of all the factors required to create libraries containing molecules that possess high potency, but also specific biochemical activity. It can be assumed that researchers and scientists have only sampled a small fraction of possible chemical space. This is partly due to the limits of synthetic methods as well as the inability to make an endless number of analogs. One way to tackle these challenges would be to use natural products. By testing against natural products, we are afforded the ability to encounter new chemical matter, dramatically increasing the likelihood of finding novel inhibitors. Additionally, the increased complexity of biomolecules offered by organisms provides us with the ability to test a greater range of molecules from small, hydrophobic molecules to large, polar molecules. These molecules will also have the added benefit of being amphipathic and mostly membrane permeable. This expanded range will be particularly helpful when screening against low affinity, large surface area interactions such as ACID-VP16, which are not well targeted by small molecule libraries.

3.3 Results and Discussion

ASSAY DEVELOPMENT FOR HIGH-THROUGHPUT MOLECULE SCREEN OF MED25 ACID

Protein expression

In order to carry out high-throughput screening of the VP16-ACID interaction, protein expression, purification, and characterization needed to be carried out. The Med25(392-543)-His_6 plasmid was obtained from the Cramer group.[3] The first step was to optimize the expression conditions in order to obtain enough protein for high-throughput screening. The original published procedure called for expression in LB broth and induction overnight, with average yields. In order to optimize the expression, we expressed the protein in terrific broth (TB broth). Terrific broth is useful for protein expression because it is a buffered medium, allowing for higher OD_{600} values to be obtained, resulting in a greater number of protein expression bacteria. Additionally, terrific broth also contains glycerol, as an additional carbon source for the bacterial cells to use as fuel. Using this

media in place of LB broth allowed us to obtain consistent yields of 20+ mg/L of ACID protein post purification of the protein.

Defining the minimal interaction of VP16-ACID

Next, we sought to develop tracers that we could use for our high-throughput assay. It has been previously reported that VP16 contains two regions within the TAD that can assume an α-helical structure. [35,36] These regions have been highlighted in Figure 3.6 by the underlined residues. Milbradt and coworkers performed ^{1}H-^{15}N HSQC experiments with VP16(413-451) and observed statistically significant chemical shifts upon addition of ACID for residues located between residues 435-452 of the VP16 TAD. Additionally, residues VP16(439-448) displayed chemical shifts, representing significant perturbation of these residues. Together, these results suggest that the N-terminal region does not contribute significantly to binding to ACID and that VP16(439-448) undergoes a conformational change upon binding to ACID.[4] The limited contribution of the N-terminal region of VP16(413-435) and conformational changes seen in VP16(439-448) are consistent with other studies that have investigated binding of the VP16 TAD with PC4 and TFIIB.[35] Vojnic and coworkers performed an analogous experiment where they monitored the chemical shifts of ACID in the presence of either VP16(413-490) or VP16(452-490). From these experiments, Vojnic and coworkers observed a similar subset of ACID residues were perturbed when comparing the chemical shift perturbation of ACID upon titration of VP16(413-490) or VP16(452-490), suggesting that VP16(452-490) is the major contributing subdomain for the VP16-ACID interaction. This would be consistent with other studies that have investigated the conformational dynamics associated with the VP16 TAD. Uesugi and coworkers demonstrated that the VP16 H2 (452-490) contains a stretch of amino acids from 470-484 that adopted a helical structure upon titration of hTAF.[36]

Based on the findings noted above, we sought to determine the minimal interaction surface of VP16-ACID. This was done through segmentation of the VP16(413-490) into three peptides approximately 25 amino acids in length. These fragments were synthesized to confirm that the residues located in the N-terminus of VP16(413-452) do not have affinity for ACID as observed by Milbradt and coworkers and that the fragments containing the reported α-helices demonstrate affinity to the ACID domain. Additionally, in order to

further investigate the importance of the VP16 α-helical regions for interaction with ACID, two shorter constructs were synthesized, VP16(438-454) and VP16(467-488) (Figure 3.6).

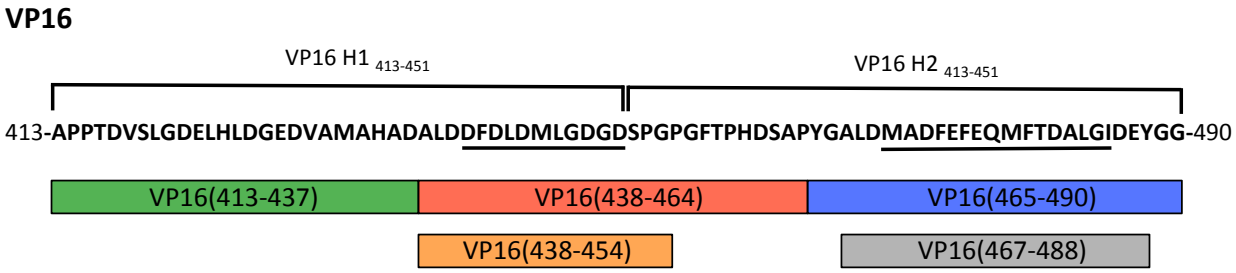

Figure 3.6 Dissecting the VP16 TAD The VP16 TAD was dissected into five separate peptides to confirm that the residues of the N-terminus of VP16 H1 do not interact with ACID as observed by Milbradt and coworkers and to investigate the importance of the reported α-helical regions for ACID binding.

We used a fluorescence polarization (FP) assay in order to develop an assay of the VP16-ACID interaction. The FP assay readout is a ratio of the emitted light measured through two perpendicular filters. The basic concept of FP is outline in Figure 3.7. A small molecule or peptide appended with a fluorescent probe (tracer) in the absence of protein will be subject to Brownian motion and tumble fast in solution, leading to low levels of polarized light. When this tracer interacts with protein, the tracer will tumble slower, resulting in an increase in polarization of emitted light. The curves produced from this change in polarized emitted light can be used to ascertain information such as the K_d of a targeted interaction.

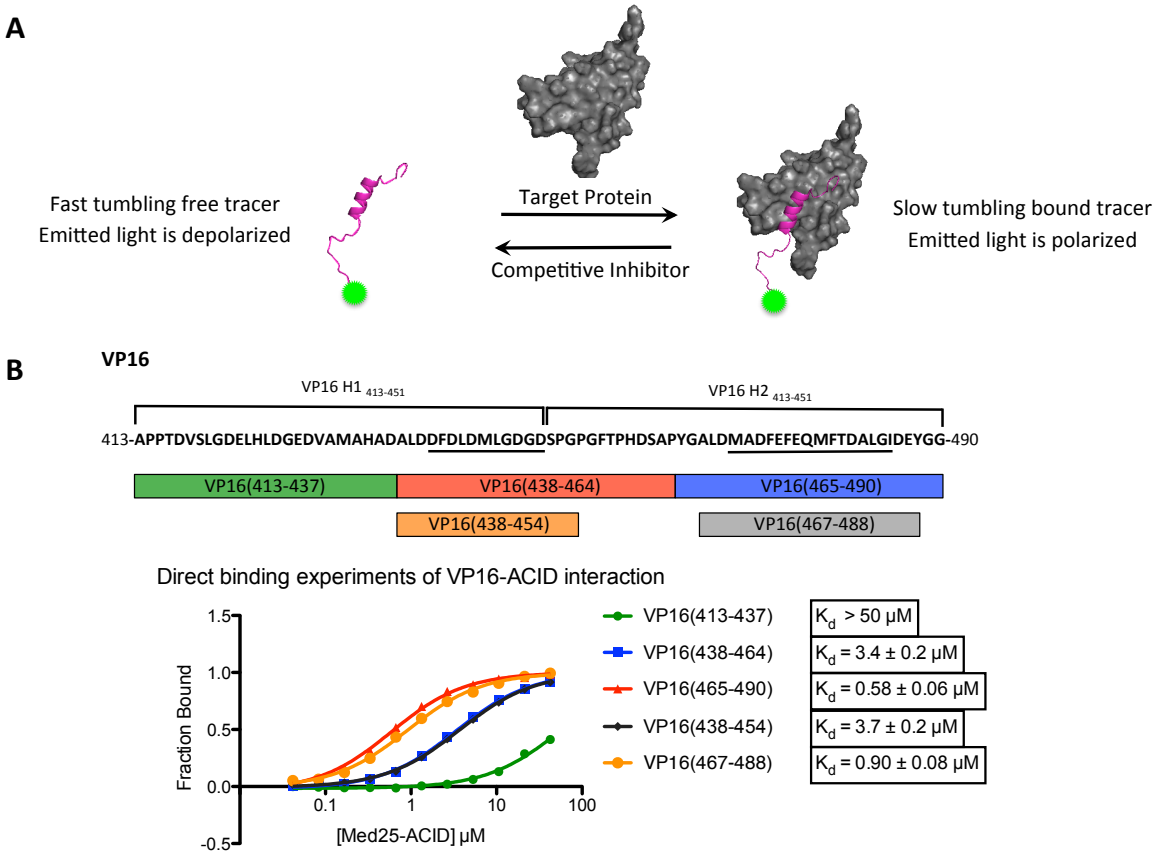

Figure 3.7 Concept of fluorescence polarization (FP) and using an FP assay to obtain K_d information about the VP16-ACID interaction Performed with Steve Sturlis A. Conceptual representation of fluorescence polarization. A free tracer is subject to Brownian motion, causing it to tumble fast and the emitted light to be depolarized, but upon binding to a protein, the tracer will tumble slower and emit polarized light. B. The binding curves obtained from VP16 peptides binding to ACID using fluorescence polarization.

The VP16 peptides described above were synthesized and conjugated with fluorescein isothiocyanate (FITC) as the fluorescent dye. An FP assay was run using these peptides and titrating in increasing concentrations of ACID ($Med25_{394-543}$). This resulted in the data points demonstrated in Figure 3.7B. Fitting these data points resulted in in the direct binding curves depicted and their respective K_ds as illustrated in Figure 3.7B. As evidenced in Figure 3.7B, the N-terminus of VP16(413-451), denoted as VP16(413-437) had a K_d of >50 µM confirming the observation by Milbradt and coworkers that N-terminus of VP16(413-451) does not interact with ACID. The VP16 tracers containing the reported α-helical domains of VP16(413-451) and VP16(452-490), VP16(438-464) and VP16(465-490), produced K_ds with high nanomolar-low micromolar affinities, consistent with the

affinities reported by Milbradt et al and Vojnic et al. Perhaps more surprising were the K_ds that were obtained by VP16(438-454) and VP16(467-488), the peptides containing the minimal α-helical domains of VP16(413-451) and VP16(452-490), respectively. The K_ds obtained with the minimal α-helical domains were within error of the larger parent peptides. This result suggests the majority of the binding affinity of the VP16-ACID interaction is provided by the interaction of ACID with the two α-helical domains of VP16, a hallmark of activator-coactivator protein-protein interactions.[37] Additionally, smaller peptides capable of recapitulating the binding affinity of the larger VP16(413-451) and VP16(452-490) subdomains validates that there are smaller, more specific interactions that can be targeted to inhibit the VP16-ACID interaction compared to the originally predicted 3000 $Å^2$ VP16-ACID interaction. Although beyond the scope of this dissertation, binding studies with various VP16 mutants to identify specific amino acids that most contribute to the binding interaction are a critical next step and are the focus of others in the research group.

Determining parameters for high-throughput screening of FP assay

Based on the excellent dynamic range observed with Flo-VP16(465-490) in the binding assays of Figure 3.6 and the affinity comparable to the longer VP16 peptides, this was chose as the tracer for the development of an assay suitable for high-throughout screening. First, we determined whether tracer concentration had a substantial effect on the dynamic range obtained from our tracer. We decided to test two different concentrations (20 nM and 50 nM) of our tracer based on previous FP assay developed in our lab.[14] Results from directing binding experiments using Flo-VP16(465-490) demonstrated that 20 nM of tracer could be used in the high-throughput assay since 50 nM did not boost the dynamic range (Figure 3.8).

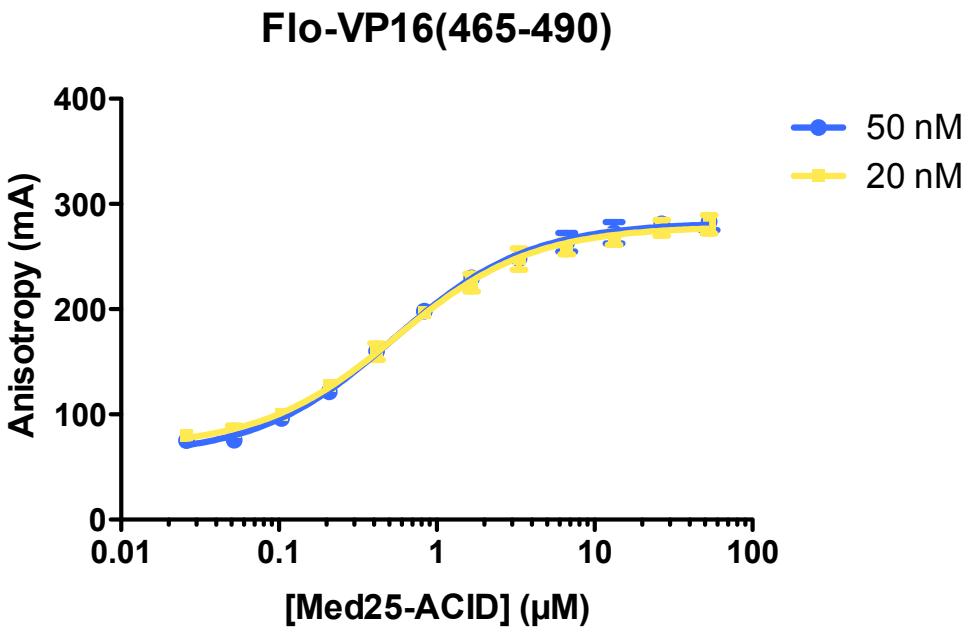

Figure 3.8 Comparison of tracer concentration Performed with Steve Sturlis. Compared the effects of either 20 nM or 50 nM of Flo-VP16(465-490) on dynamic range of FP assay. Less than 5% change in dynamic range observed with 50 nM trace compared to 20 nM tracer.

We also tested the effects of DMSO and NP-40 on our FP assay. When testing against compounds in a high-throughput screen, samples are added as a solution of DMSO and it is sometimes necessary to use high concentrations of DMSO in order to obtain the appropriate effective concentration to test compound stocks at lower starting concentrations or to obtain full dose curves when validating initial hits. Therefore, it is critical to determine the effects of DMSO on the high-throughput assay. Additionally, NP-40 is often used in high-throughput assays in order to inhibit non-specific binding and also to help solubilize less soluble compounds to prevent them from precipitating in the assay buffer. It is often sufficient to add NP-40 to a final concentration of 0.001% v/v. The results of the assay looking at the effects of DMSO and NP-40 on the Flo-VP16(465-490)-ACID interaction are depicted in Figure 3.9. Based on the results demonstrated in Figure 3.9, we conclude that NP-40 (0.001% v/v) has no effects on the high-throughput assay and DMSO up to 5% v/v is well tolerated as evidenced by the K_d being perturbed only 2-fold from the original K_d determined (Figure 3.9).

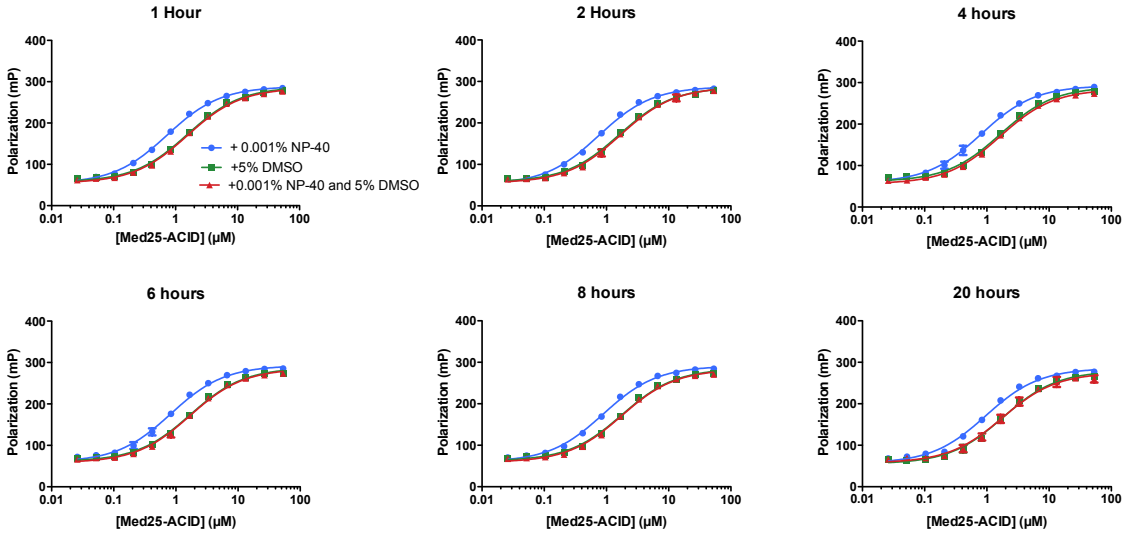

	K_d of Flo-VP16(465-490)-ACID interaction					
	1 hour	2 hour	4 hour	6 hour	8 hour	20 hour
+ NP-40	0.72 μM	0.75 μM	0.80 μM	0.81 μM	0.88 μM	0.95 μM
+DMSO	1.5 μM	1.6 μM	1.6 μM	1.7 μM	1.7 μM	1.8 μM
+ NP-40 and DMSO	1.5 μM	1.7 μM	1.6 μM	1.7 μM	1.7 μM	1.8 μM

Figure 3.9 Effect of DMSO and NP-40 on the K_d of Flo-VP16(465-490)-ACID interaction Performed with Steve Sturlis. A directing binding assay was set up using 20 nM of tracer titrated with increasing concentration of ACID protein. Effects of DMSO, NP-40, or the a combination of the two were investigated by adding DMSO (5% v/v), NP-40 (0.001% v/v), or DMSO (5% v/v) and NP-40 (0.001% v/v). These three conditions were monitored over 6 time points: 1, 2, 4, 6, 8, and 20 hours.

The last parameter that we investigate for the high-throughput screen was determining the Z' score of our assay. The Z' statistic is used to determine the quality of the assay. The Z' score was determined at three protein concentrations: 500 nM, 850 nM, and 2.5 μM using the following equation:

$$Z' = 1 - \frac{3(\sigma_p + \sigma_n)}{|\mu_p - \mu_n|}$$

(Equation 3.1)

σ = standard deviation of positive/negative population

μ = mean value of positive and negative population

All three protein concentrations, produced Z' scores >0.75, substantially higher than the 0.6 Z' score used to define a good high-throughput assay.[38] Therefore, we chose to use the 850 nM concentration point for the high-throughput screen. Utilizing this concentration point for ACID allows us to obtain Z' scores >0.8 and allows us to use 3-fold less protein than afforded by the 2.5 μM concentration of ACID point, all whiling obtaining a suitable dynamic range for the assay.

Together all of these results demonstrate that we can develop a very robust high-throughput assay against the VP16-ACID interaction. We demonstrated that we can express and purify ACID protein in high yield (> 20 mg/L) and that we can develop effective tracers that define the minimal binding interaction of VP16-ACID. Through development of these tracers, we obtained data that suggests that the majority of the VP16-ACID binding affinity is derived from the reported α-helical domains of VP16. The effects of DMSO and NP-40 had minimal effects on the binding affinity of the tracer and the assay was incredibly stable over long periods of time as evidenced by the minimal drift in K_d seen during the time course as illustrated in Figure 3.9. Lastly, using the parameters noted above, we were able to consistently obtain Z' scores > 0.8, resulting in a robust assay with a suitable dynamic range required for high-throughput screening. Taken together, these results demonstrate that this is a robust assay suitable for an HTS campaign against the VP16-ACID interaction.

PILOT SCREEN OF VP16-ACID INTERACTION

Pilot screen of the VP16-ACID interaction

Using the screen developed above, a total of 4,046 compounds were screened at the University of Michigan Center for Chemical Genomics (CCG), which included compounds from the MS Spectrum 2000, Focused Collections, BioFocus NCC compound libraries. The pilot screen had a Z' score of 0.84 and had a hit rate of 1.6%. The threshold for hits was set at 3 standard deviations from the mean. Compounds were removed if they had been flagged as reactive from previous screens or displayed significant fluorescence (>10% of the fluorescence of tracer). All the hits were tested in triplicate to confirm their activity. This filtering resulted in the identification of CCG-38381, CCG-38361, CCG-40171, and CCG-40095 as confirmed hits (Figure 3.10).

A

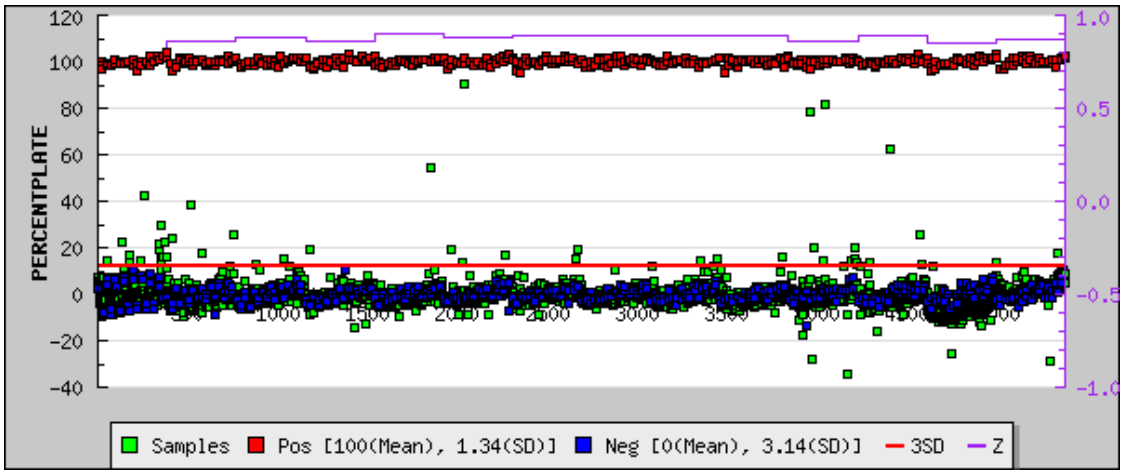

B

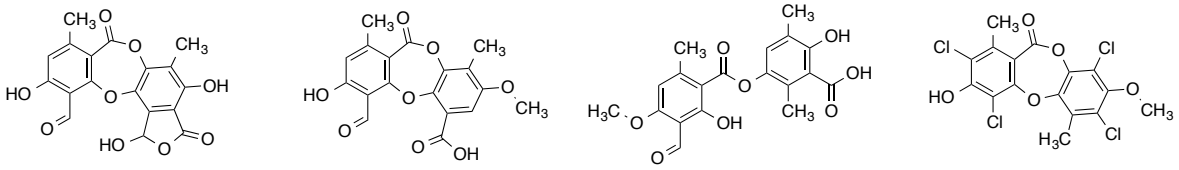

CCG-38381
VP16: 17.6%

CCG-38361
VP16: 23.6%

CCG-40171
VP16: 19.3%

CCG-40095
VP16: 15.3%

Figure 3.10 Pilot screen against the Flo-VP16-ACID interaction Performed with Steve Sturlis. A. Campaign view of the pilot screen run against 4,046 compounds. The red and blue dots represent the negative and positive controls, respectively. Green dots represent the tested compounds with all compounds above the red line (>3SD) representing hits. B. The identified hits from the pilot screen with the initial inhibitions noted as a %.

Substructure search of compounds containing the depside or depsidone scaffold

These results were exciting based on the fact that we saw a reoccurrence of the privileged scaffold that was first identified in a natural product extract screen of the MLL-KIX interaction. Based on the observation that our confirmed hits shared a common scaffold previously identified against another activator-coactivator PPI, we performed a substructure search of the CCG database for other compounds that contained the depside and depsidone core, yielding 15 additional molecules to be tested against the Flo-VP16-ACID interaction (Figure 3.11).

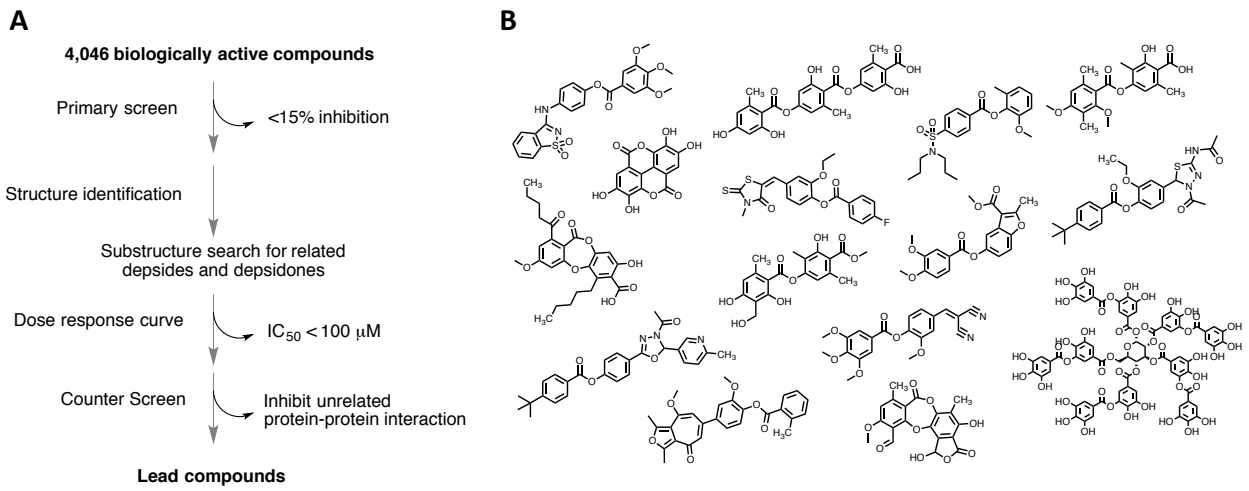

Figure 3.11 Flowchart of VP16-ACID pilot screen and results of substructure search Performed with Steve Sturlis. A. Flowchart used to identify lead compound inhibitors of the VP16-ACID interaction. B. Results of the substructure search of the CCG molecule database.

By performing a substructure screen, we can test the inhibitory properties of other compounds containing the depside and depsidone core. In order to assess their inhibition, we performed dose response curves with the compounds identified as hits from the pilot screen (Figure 3.11B) and the 15 additional molecules from the CCG molecule database containing the depside and depsidone core, these molecules are depicted in Figure 3.11B. From these dose response curves produced with these compounds, we observed several interesting feature of the identified compounds. First, the compounds identified from the pilot screen produced micromolar IC_{50}s against the VP16-ACID interaction, confirming their inhibitory properties in a dose-dependent manner. Second, compounds previously identified in a high-throughput screen of the MLL-KIX protein-protein interaction did not inhibit the VP16-ACID interaction. This is a noteworthy finding because it demonstrates that molecules possessing the depside and depsidone scaffold is not the only compound criterion necessary to inhibit the VP16-ACID interaction (Figure 3.12). This demonstrates that the substituents attached to the depside and depsidone core are important for the selectivity and that substituting these substituents could possibly be a strategy for developing other PPI inhibitors in the future.

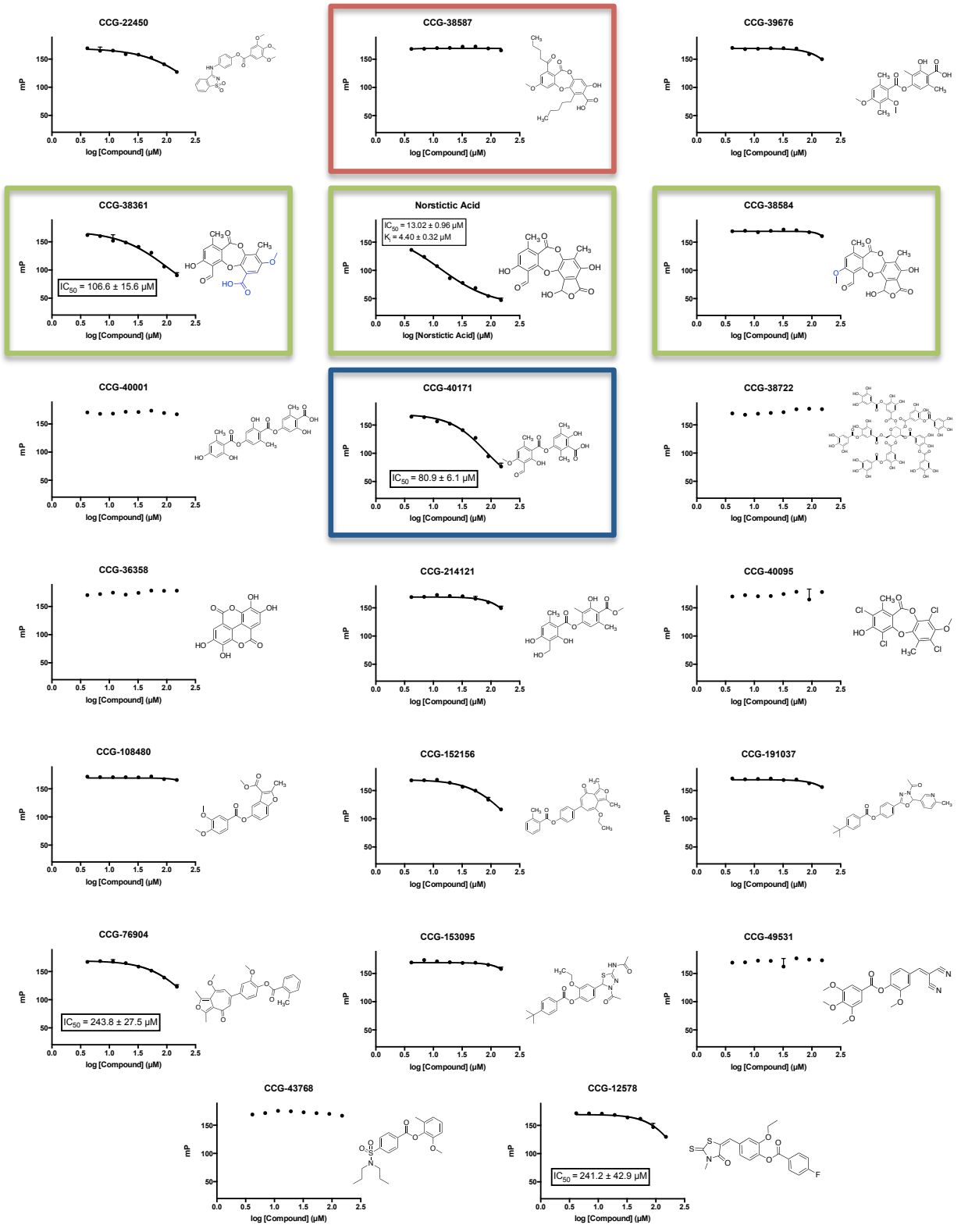

Figure 3.12 Dose response curves generated with initial hits and compounds identified in the CCG database with the depside and depsidone core Performed with

Steve Sturlis. All DRCs were produced with 8 dose points run in triplicate and fitted using graphpad 4.0

In the first row of Figure 3.12, lobaric acid (CCG-38587) is highlighted with a red box to demonstrate the lack of inhibition observed with this compound (IC_{50} >> 250 μM). This is a significant finding because lobaric acid was identified as an inhibitor of the MLL-KIX protein-protein interaction, but exhibits no inhibition against the VP16-ACID protein-protein interaction, suggesting that the substituents on the depside/depsidone core affect selectivity of the protein-protein interaction that these molecules inhibit. In the second row, are three compounds outlined in green boxes. In the middle is compound CCG-38381 (norstictic acid) and directly adjacent to norstictic acid are two closely related analogs, CCG-38361 (psoromic acid) and CCG-38584 (stictic acid). Psoromic acid exhibited modest inhibition (IC_{50} = 106 μM) against the VP16-ACID interaction, whereas stictic acid displayed no inhibition (IC50 >250 μM). Norstictic acid contains a lactone ring that can tautomerize between the open and closed ring. In the open form, norstictic acid contains a carboxylic acid and an aldehyde substituent, but in the closed form, it contains a lactone ring, suggesting that the presence of a carboxylic acid is required for binding to ACID. Conversely, the presence of carboxylic acid functionality does not seem to be sufficient for binding to ACID. In the case of stictic acid, methylation of the ortho phenol to aldehyde on the A ring abolished the inhibitory activity observed with norstictic acid, suggesting the presence of an ortho phenol to the aldehyde on the A ring is required for inhibition of ACID (Figure 3.13).

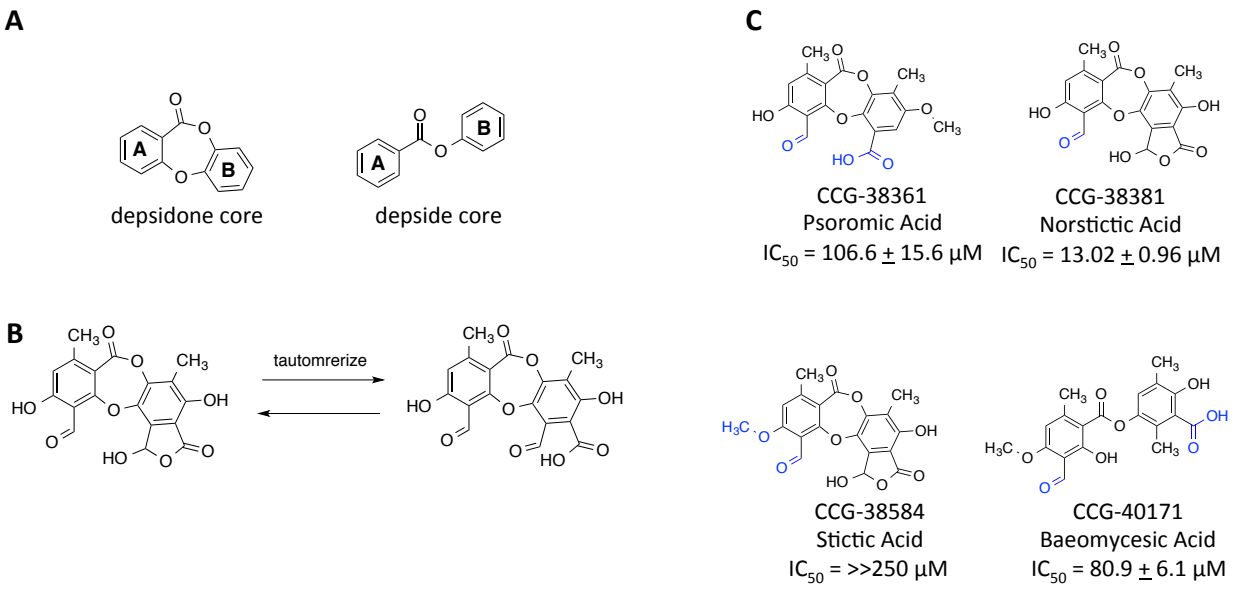

Figure 3.13 Inhibition of depsidone derivatives on the VP16-ACID interaction A. The depsidone and depside core with the A and B rings highlighted. B. Tautomerization of the lactone ring in norstictic acid. C. IC_{50}s of depsidones and depsides against the VP16-ACID interaction.

Confirmation of inhibition with obtained compounds

Fresh compound was obtained from vendors as outlined in the materials and methods section in the chapter. This was done in order to confirm that the observed inhibition was due to the compound that was identified in the database, not due to some oxidized fragment of the parent compound or byproduct. Based on availability, we could not obtain CCG-40171, limiting our studies to the depsidones identified in the screen. Using newly obtained compounds, we obtained IC_{50}s in the single digit micromolar range, much tighter than the IC_{50}s obtained from the dose response curves generated with the molecule stocks used in pilot screen (Figure 3.14).

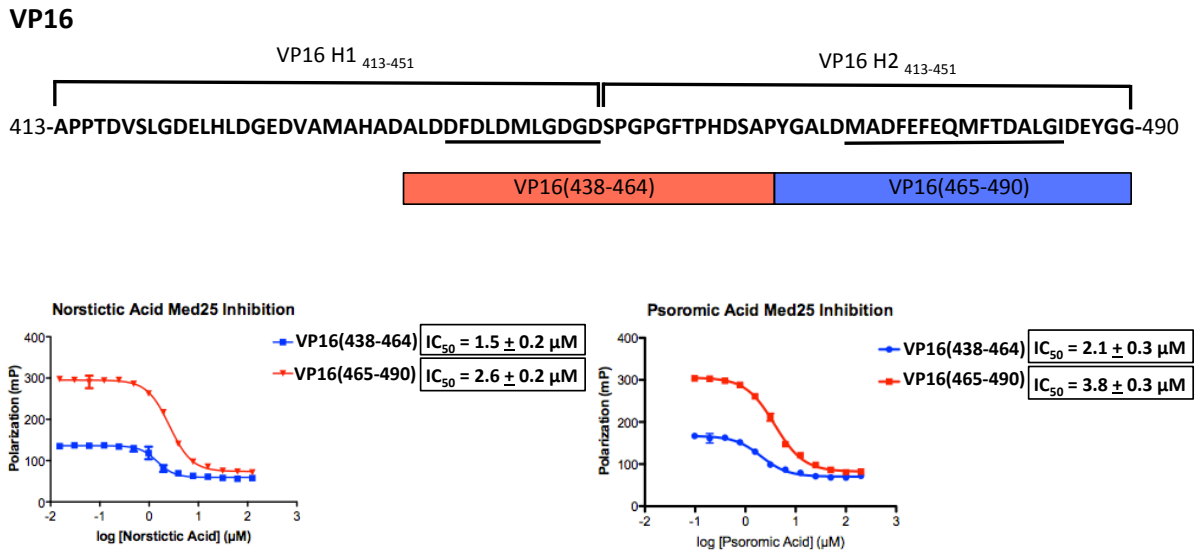

Figure 3.14 Inhibition IC_{50} curves generation with new stocks of compounds Performed with Steve Sturlis. Tested the inhibition potential of the compounds against both the VP16(438-464)-ACID interaction and the VP16(465-490)-ACID interaction. Data points were fit with dose response curves using Graphpad software 4.0.

We chose to test the compounds against both the VP16(438-464) and VP16(465-490) tracers to assess whether the compounds identified were site-specific inhibitors. As noted earlier, protein NMR studies investigating the VP16(413-451)-ACID interaction and the VP16(452-490)-ACID interaction suggest that there are two binding sites on ACID, denoted the H1 and H2 binding site. From the dose response data generated above, it can be concluded that the molecules identified in the screen are acting as either dual orthosteric inhibitors or combination orthosteric/allosteric inhibitors. Combination orthosteric/allosteric inhibitors have been developed for other proteins such as GPCRs[39,40], but dual orthosteric inhibitors are a relatively rare mode of action, especially for targeting PPIs. We traditionally think about PPIs as modular interactions between protein A and protein B, but in the case of VP16, we have two subdomains that cooperatively bind to ACID as demonstrated by Vojnic and coworkers.[3] In the VP16-ACID example, we have protein A (ACID) that interacts with VP16 subdomain A ($VP16_{413-451}$ or $VP16_{452-490}$) and then cooperatively with VP16 subdomain B ($VP16_{413-451}$ or $VP16_{452-490}$). This cooperative binding demonstrated by VP16 is in part, why there is such high affinity between the VP16 TAD and ACID (50 nM). Furthermore, there exists an entire regime of PPIs that rely on interactions in the high-nanomolar to low-micromolar affinity range. In the case of VP16,

which has two subdomains that possess high-nanomolar to low-micromolar affinities for ACID, it may be absolutely crucial to inhibit both interactions in order to obtain the desired inhibition. This sets up a scenario where a dual orthosteric or dual orthosteric/allosteric inhibitor of the interaction between the two VP16 subdomains and ACID would be highly desirable.

Assessing selectivity with counter screens

Based on the inhibition that we observed with the compounds identified from the pilot screen, we tested their inhibitory properties on an assay developed for another protein-protein interaction. We chose to investigate the inhibitory properties of the identified compounds against the MLL-KIX interaction and the CREB-KIX interaction. We choose to use this counter screen for several reasons. First, the KIX protein is a domain of the central hub coactivator CBP/p300 and is utilized by several different transcriptional activators to upregulate transcription of target genes including: NF-κB[41], p53[42], MLL[43], c-Myb[44], and CREB[45]. We reasoned that inhibition of this domain with the identified inhibitors would likely translate to off-target effects since there are structurally similar KIX domains in several proteins such as CBP, p300, and Med15. Second, KIX has two binding sites similar to ACID, which have been identified as the "MLL site" and the "CREB site". If our inhibitors were general amphipathic helix mimics, we should see inhibition of both MLL-KIX and CREB-KIX. Third, using MLL-KIX and CREB-KIX would allow us to determine if the identified molecules demonstrate inhibition consistent with a general dual orthosteric or dual orthosteric/allosteric mechanism as observed with ACID. The KIX domain serves as a good surrogate to test this possibility due to the presence of two binding sites and the well-defined allosteric communication between the two binding sites.[46-48]

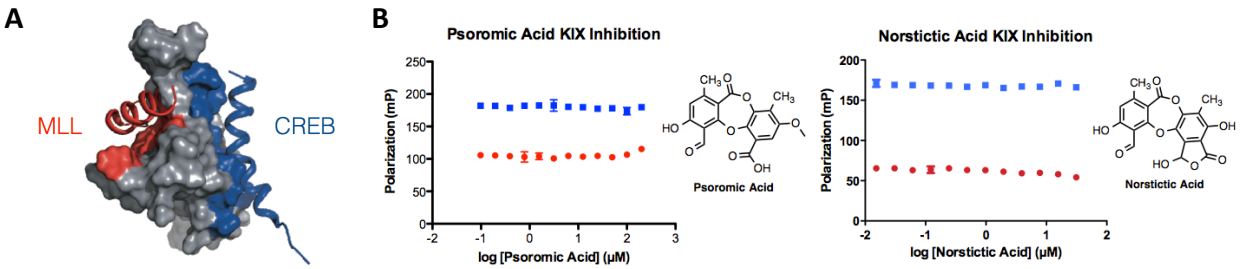

Figure 3.15 Inhibitory effects of depsidones against MLL-KIX and CREB-KIX interaction Performed by Steve Sturlis. A. The KIX protein with the identified "MLL site" and "CREB site" denoted in red and blue, respectively. B. Dose response curves generated with the depsidones against the MLL-KIX and CREB-KIX interaction. On the left graph, the dose response curve for psoromic acid against the MLL-KIX and CREB-KIX interaction is depicted. On the right graph, the dose response curve for norstictic acid against the CREB-KIX interaction is depicted.

Interestingly, the depsidone inhibitors identified in the pilot screen did not inhibit the MLL-KIX or the CREB-KIX interaction (Figure 3.15). This result suggests that the inhibition of ACID is selective over other coactivator domains such as KIX. Furthermore, the results demonstrate that the dual orthosteric or dual orthosteric/allosteric inhibition observed with VP16-ACID is unique to ACID and is not a general phenomenon observed with other proteins such as KIX, a coactivator with two binding sites and well defined allostery.

It has previously been demonstrated that depsides and depsidones, sekikaic acid and lobaric acid, can inhibit the KIX domain. The results above demonstrate that the depside and depsidone core may be a 'privileged scaffold' based on the observation that these types of molecules have demonstrated low micromolar IC_{50}s against two unique coactivator domains, ACID and KIX. Furthermore, the selective inhibition observed with different depsides and depsidones, suggests that the substituents on these scaffolds can greatly affect the inhibitor's selectivity for the target domain. Based on the observation that these depsidones exhibit selectivity for the target activator-coactivator PPI (VP16-ACID) over unrelated activator-coactivator PPIs (MLL-KIX, CREB-KIX) is a promising result, validating future utility of these molecules. One possible explanation for the observed inhibition seen with these depsidones, is that they are general VP16 helix mimetics. In order to determine if the molecules are general VP16 helix mimetics, we tested the ability of these compounds to inhibit the VP16(438-454), VP16(467-488), and VP16-derived VP2 interaction with $Med15_{1-345}$. The VP16 TAD has been demonstrated to interact with four

distinct domains with Med15. [49-51] This implication of this promiscuous binding profile is that a helix mimetic of the VP16 TAD would exhibit significant off-target effects due to inhibition of multiple activator-coactivator domains simultaneously. In order to test this, we looked at the ability of norstictic acid and psoromic acid to inhibit the Med15 A+B box ($Med15_{1-345}$) interaction with VP16(438-454), VP16(467-488), and VP2 (Figure 3.16).

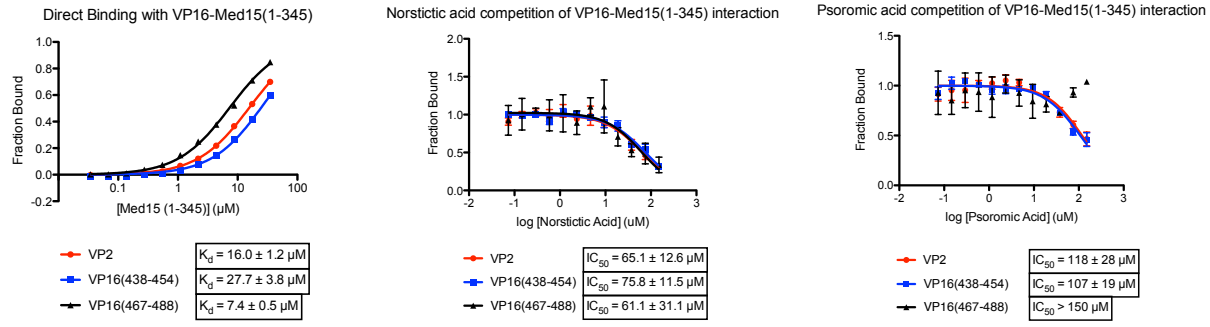

Figure 3.16 Investigating inhibition of the Med15 interaction with VP16 using norstictic acid and psoromic acid Performed with Steve Sturlis. In the left panel, we present direct binding data with $Med15_{1-345}$ with the three VP16 derived tracers. In the middle panel, we present assay data of norstictic acid competition with VP16(438-454), VP16(467-488), and VP2 binding to $Med15_{1-345}$. In the right panel, we present present assay data of psoromic acid to compete with VP16(438-454), VP16(467-488), and VP2 binding to $Med15_{1-345}$.

The results of these competition assays demonstrated that norstictic acid and psoromic acid are not potent inhibitors of the VP16-Med15 interaction (Figure 3.16). All the IC_{50}s generated with norstictic acid and psoromic acid against the VP16-Med15 interaction were greater than 30-fold higher than the IC_{50} values obtained against the VP16-Med25 interaction (Figure 3.14). This observed results suggests that the identified depsidones from the pilot screen are selective for the ACID domain and do not generally act as VP16 helix mimetics.

DETERMINING ELECTROSTATIC CONTRIBUTIONS TO MED25 ACID BINDING

Molecular dynamics experiment with small molecule and Med25 ACID

A molecular dynamics (MD) simulation was performed with Med25 ACID and norstictic acid in order to investigate potential sites the molecule could interact with the protein. The added benefit of an MD simulation performed with ACID and norstictic acid is that information about lowest energy binding state of the molecule on the protein can be

determined. Additionally, areas on the protein that binds the highest density of ligand can be highlighted, providing additional information about the inhibitors possible mechanism of action. An MD simulation performed with ACID and norstictic acid revealed that norstictic acid clustered at the lysines on ACID. This is somewhat unsurprising considering that there are several lysines on the ACID protein and norstictic acid contains a carboxylic acid that is part of the lactone on ring B, suggesting that electrostatics likely plays an important role in the interaction between the depsidones and ACID. The highest density of norstictic acid on ACID and the lowest energy members of norstictic acid on ACID can be seen in Figure 3.17 A and B.

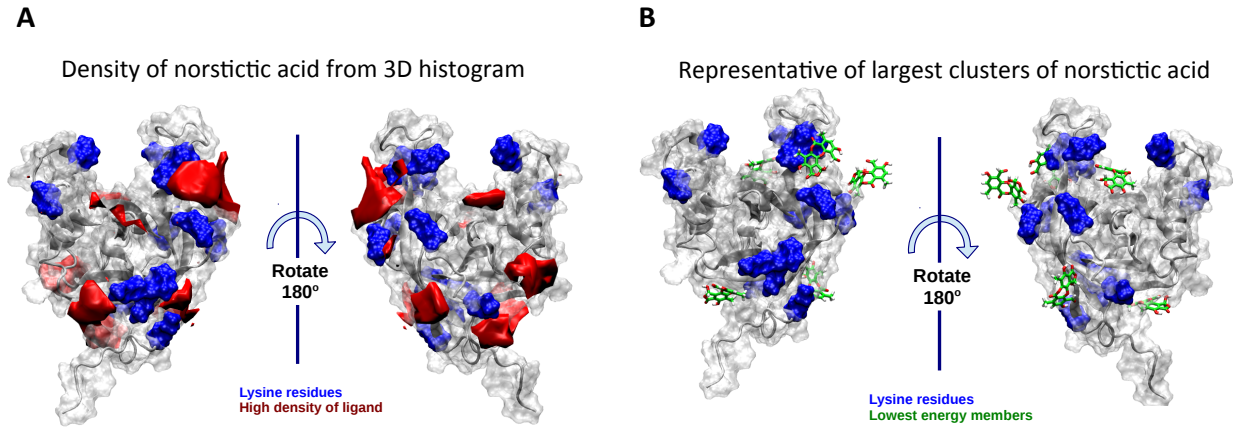

Figure 3.17 Molecular dynamics (MD) simulation with norstictic acid and ACID Performed by Jessica Gagnon. A. MD simulation identifying where the highest density of norstictic acid is found on ACID. B. MD simulation demonstrating what the lowest energy members of norstictic acid and ACID are based on where the highest density of norstictic acid is found.

The effects of salt on ACID binding to VP16 and inhibition with norstictic acid

There have been separate studies that have identified the importance of electrostatics for both ACID and the VP16 TAD. In the case of ACID, it was recently reported that the arabadopsis Med25-ACID and human Med25-ACID relied on electrostatics for binding to dehydration responsive element binding protein 2A (Dreb2A). This was determined by looking at the ΔH and TΔS values using isothermal titration calorimetry (ITC), which identified large contributions from enthalphy compared to entropic contributions of the interaction.[52] Based on the observation that ACID relies on electrostatics for interaction with other activators, it is likely that electrostatics contribute to binding with other

activators and possibly with inhibitors of the domain. The importance of electrostatics on VP16 has also been investigated. Experiments performed by Jonker and coworkers using HADDOCK docking and protein NMR to look at the VP16-PC4 interaction demonstrated that several of the negatively charged residues in the α-helical region of VP16 made electrostatic contacts with positively charged lysines and arginines on PC4. This observation suggests that both hydrophobic and electrostatic interactions are important for VP16.[35] Based on the importance of electrostatics in these previous studies, we sought to determine the importance of electrostatics in the VP16-ACID interaction. One way to assess the importance of electrostatics on the VP16-ACID interaction is to perform direct binding assays in the presence of increasing concentrations of sodium chloride (NaCl). We demonstrated that the K_d of the VP16(465-490)-ACID interaction steadily increases in the presence of increasing salt (Figure 3.18).

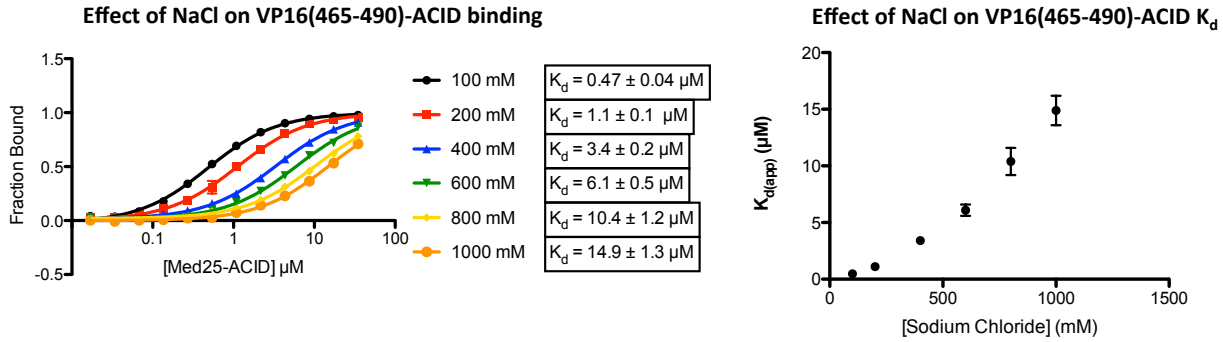

Figure 3.18 Effects of NaCl on the VP16(465-490)-ACID interaction Performed by Steve Sturlis. Direct binding experiments between VP16(465-490) and ACID were carried out in the presence of 100, 200, 400, 600, 800, and 1000 mM sodium chloride as previously described. A plot of sodium chloride vs K_d was plotted to illustrate the steady increase in K_d values.

We observed higher K_d values with steadily increasing sodium chloride salt concentrations. Overall, we observed a greater that 30x increase in K_d between the 100 mM and 1000 mM NaCl concentrations, demonstrating that the VP16-ACID interaction is partially dependent on electrostatics for interaction with VP16. Based on the observation that the VP16-ACID interaction is electrostatically driven, we sought to determine if inhibition with the depsidone inhibitors was also an electrostatically driven interaction. In order to determine if the inhibition observed with the identified depsidones is an electrostatically driven interaction, we performed competition assays with the depsidones in the presence of

increasing salt concentrations to investigate the effect salt would have on the inhibition. Similar to the effects seen in the direct binding experiments, we saw the IC_{50} of the compounds steadily increase in the presence of increasing salt concentration, suggesting that the interaction between the inhibitor and ACID is also at least partially dependent on electrostatics for inhibition (Figure 3.19).

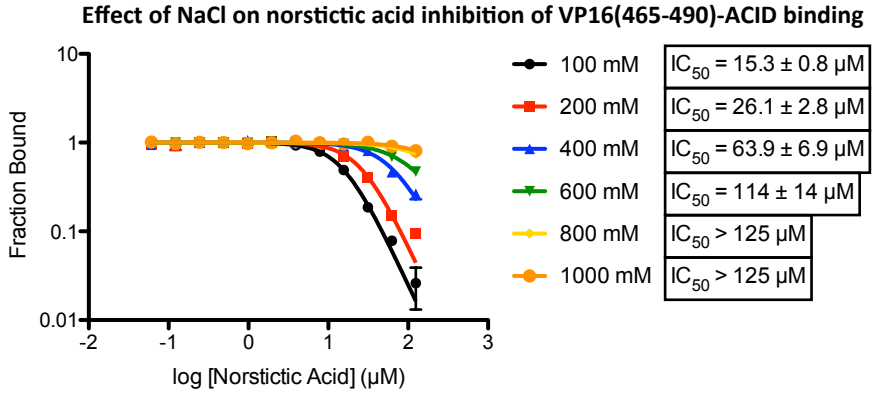

Figure 3.19 Effect of sodium chloride on norstictic acid inhibition of VP16(465-490)-ACID binding Performed by Steve Sturlis. Carried out competition assays with norstictic acid against the VP16(465-490)-ACID interaction in the presence of increasing concentrations of sodium chloride (NaCl).

COVALENT MODIFICATION OF MED25 ACID WITH DEPSIDONES

Q-TOF mass spectrometry data demonstrating covalent binding to Med25 ACID

Next, we sought to determine if the depsidones and depsides that we identified could be covalently modifying the protein. During the substructure search, we noticed that the molecules that we identified in the screen contained aldehydes on the A ring of the depsidones or depsides. Others have identified aldehyde-containing molecules that label target proteins through a Schiff-base (imine) [53,54] and therefore, we wanted to determine if our aldehyde containing inhibitors covalently modify ACID through formation of an imine (Figure 3.20).

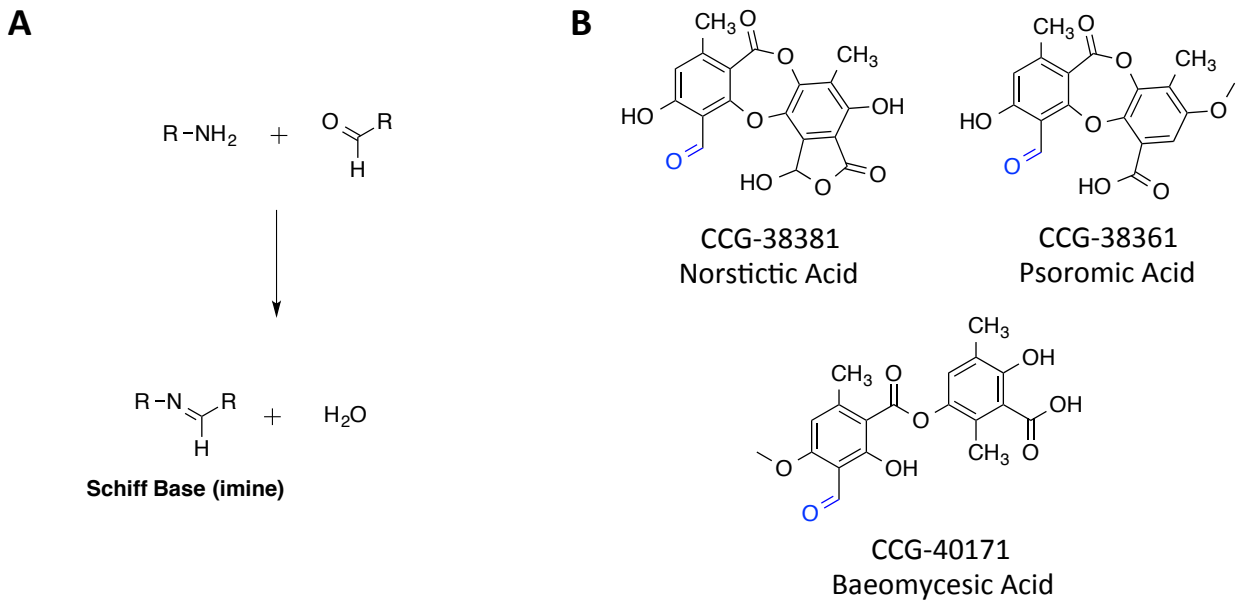

Figure 3.20 Formation of Schiff bases and identifying aldehydes in inhibitors A. Scheme illustrating how Schiff bases (imine) are formed. Formation of an imine results in the loss of water. B. Highlighting the presence of aldehydes (blue) in depsidone and depside inhibitors identified from the pilot screen.

In order to determine if the depsidones are covalent inhibitors, we incubated ACID protein with 4 equivalents of norstictic acid or psoromic acid. We chose to look at the percentage of labeling with 4 equivalents of psoromic or norsticitic acid in relation to the concentration of ACID because the IC_{50}s for both the molecules are about four times the concentration of the protein concentration used in the assay (Figure 3.21).

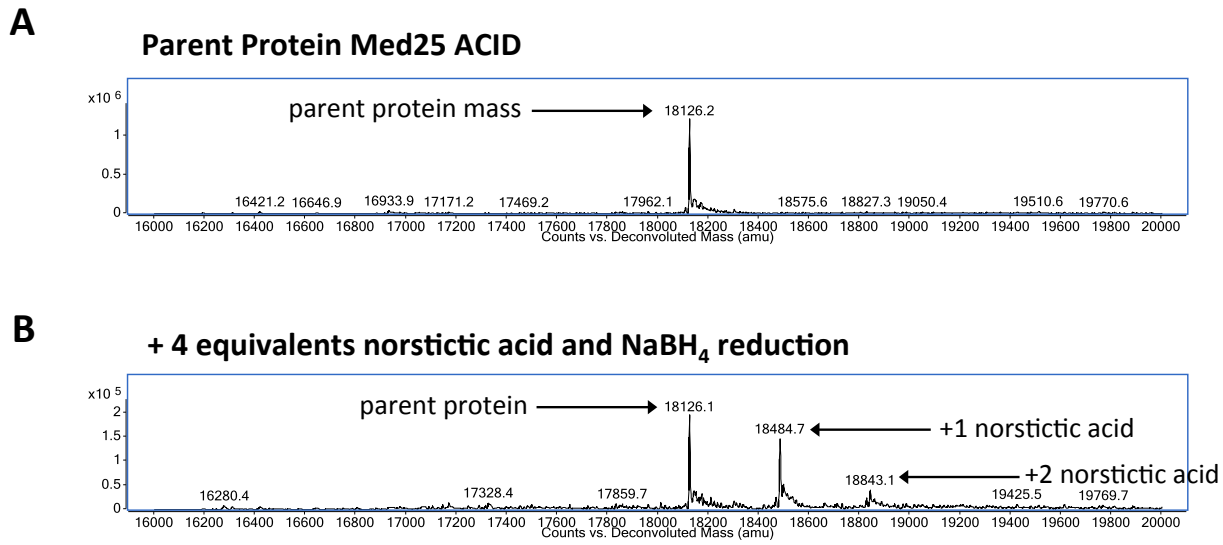

Figure 3.21 Mass spectrometry analysis of ACID in the presence of norstictic acid Performed with Steve Sturlis. A. Spectra of ACID protein to provide a reference mass. B. Spectra of ACID in the presence of 4 equivalents of norstictic acid post reduction with sodium borohydride ($NaBH_4$). To obtain spectra, 10 μM ACID was incubated with 4 equivalents of norstictic acid and left incubating for 2h at room temperature. Then, complex mixture was reduced with $NaBH_4$ at a final concentration of 1 mM and dialyzed overnight to get rid of excess molecule and salt. The sample was analyzed using mass spectrometry to obtain spectra.

From the mass spectrometry analysis, it is demonstrate that norstictic acid can covalently label ACID. We observed similar results with psoromic acid. Although it may be possible to get higher labeling species upon addition of more molecule, these species are likely irrelevant to inhibiting the VP16-ACID interaction since the IC_{50}s of the molecules are obtained at a 4:1 ratio of inhibitor to protein as demonstrated by the dose response curves. Based on the masses observed, the labeling event is consistent with imine formation. In the case of norstictic acid (372 Da), formation of the imine would result in the loss of water (-18 Da), resulting in a mass addition of 354 Da. As an example, the addition of one norstictic acid to ACID (18126 Da) would result in a mass of 18480 Da. Additionally, reduction with sodium borohydride ($NaBH_4$) would produce a mass increase in 4 Da due to the reduction of the imine formed on ring A as well as reduction of the aldehyde that is tied up in the lactone on ring B (Figure 3.21B and Figure 3.22).

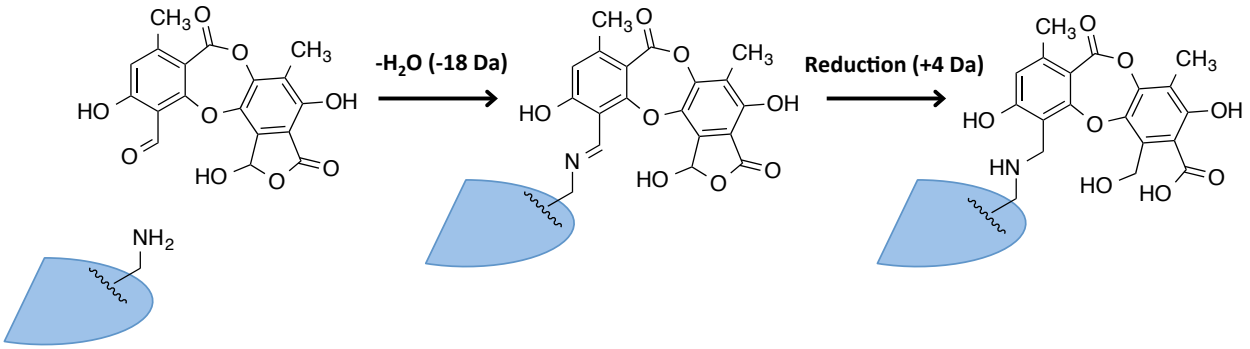

Figure 3.22 Schematic of inhibitor imine formation and reduction with sodium borohydride In the first step, the depsidone inhibitor forms the imine with an amine on the protein, resulting in the loss of water (-18 Da). Next, the addition of sodium borohydride ($NaBH_4$) causes reduction of the imine on ring A and reduction of the aldehyde that is a part of the lactone on ring B, resulting in an increase of 4 Da.

Investigating the ability to label Med25 ACID with other aldehyde containing molecules

Based on the observation that these depsidone inhibitors are capable of forming covalent adducts with ACID lysine side chains to form an imine, we sought to determine if ACID is sensitive to other aldehyde containing molecules. We observed during the substructure search that the presence of an ortho phenol to the aldehyde on ring A was important for activity. Therefore, we sought to determine if the lysines on ACID were generally sensitive to other aldehyde containing molecules. It has previously been demonstrated that benzaldehyde can label protein lysines through formation of an imine[54] and more generally, aldehydes can be used as a general lysine modification process. [55,56] In order to determine if ACID is sensitive to modification with other aldehyde containing molecules, ACID was incubated with 4 equivalents of benzaldehyde using the same procedure as outlined for norstictic acid and psoromic acid. The complex mixture was analyzed by mass spectrometry to determine the degree of labeling by benzaldehyde (Figure 3.23).

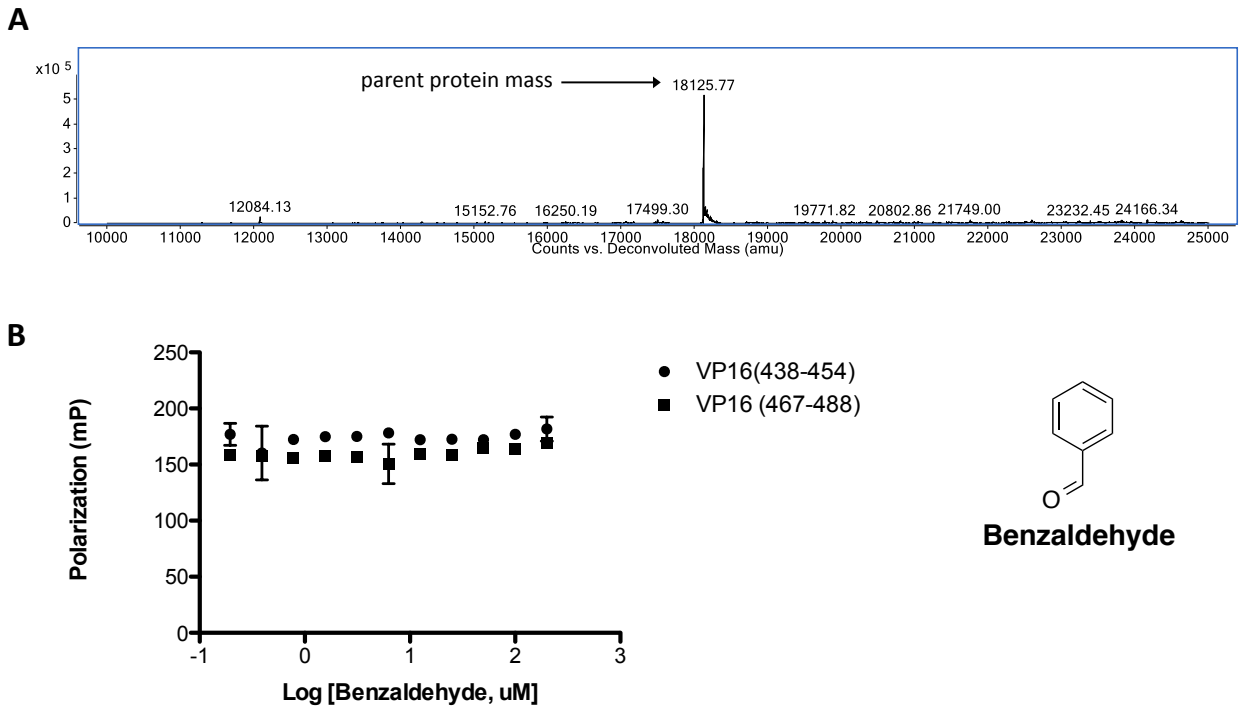

Figure 3.23 Mass spectrometry analysis of Med25 ACID in the presence of benzaldehyde Performed by Paul Bruno. A. Spectra of ACID protein in the presence of 4 equivalents of benzaldehyde. To obtain mass spectra, 10 μM ACID was incubated with 4 equivalents of benzaldehyde (40 μM) and complex was left to incubate for 2 hours. Sample of mixture was analyzed using mass spectrometry to obtain spectra. B. Competition assay with benzaldehyde against the VP16(438-454)-ACID and VP16(467-488)-ACID interaction.

As demonstrated in Figure 3.23, benzaldehyde was unable to covalently label ACID. This result demonstrates that the reactivity of the aldehyde is not sufficient for covalent labeling of ACID (Figure 3.23A), further validating the importance of the ortho phenol to the aldehyde on the A ring. Additionally, benzaldehyde is also incapable of inhibiting either the VP16(438-454)-ACID and VP16(467-488)-ACID interaction in a competition assay (Figure 3.23B). This result is important because it suggests that norstictic acid and psoromic acid need to first interact with ACID, which will place the molecule in proximity to a lysine to form an imine, highlighting the importance of norstictic acid and psoromic acid interacting with ACID. One possible explanation for benzaldehyde not being able to label ACID could be that the phenyl group does not have affinity for ACID, causing the molecule to never be in proximity to a lysine for imine formation.

Performing ^{1}H-^{15}N heteronuclear single quantum coherence (HSQC) protein NMR with Med25 ACID and norstictic acid

Based on the results from the MD simulation with depsidones and ACID, we observed the greatest density of the inhibitor localized around the lysines, presumably driven by an electrostatic interaction. Mass spectrometry analysis of complex mixtures of depsidones and ACID confirmed imine formation between the depsidone aldehydes and lysine residues on ACID. Based on IC_{50} data generated with the depsidones and the observation that covalent adducts are formed between the depsidones and ACID, we sought to determine if these depsidones induced chemical shift perturbations on ACID that are consistent with the above observations. In order to perform the ^{1}H-^{15}N HSQC protein NMR experiment with ACID and the depsidones, we first expressed and purified ^{15}N-ACID protein. The protein was expressed and purified as described in the materials and methods section. The expression, purification, and identification of the protein was confirmed by mass spectrometry (Figure 3.24)

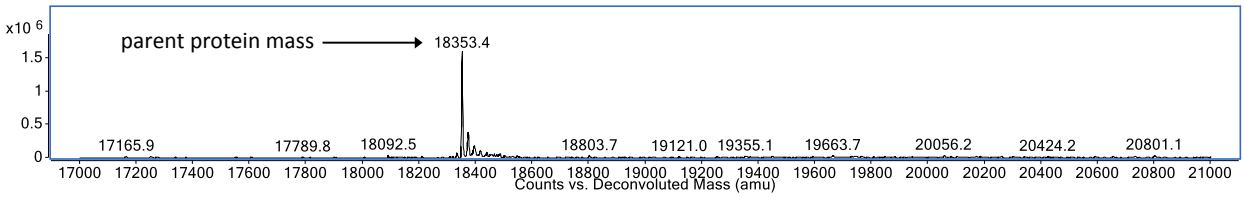

Figure 3.24 Confirmation of expression and purification of ^{15}N-labeld ACID Performed with Steve Sturlis. The ^{15}N-labeled ACID was expressed and purified as outlined in the materials and methods section. Confirmation of protein identity was accomplished using mass spectrometry.

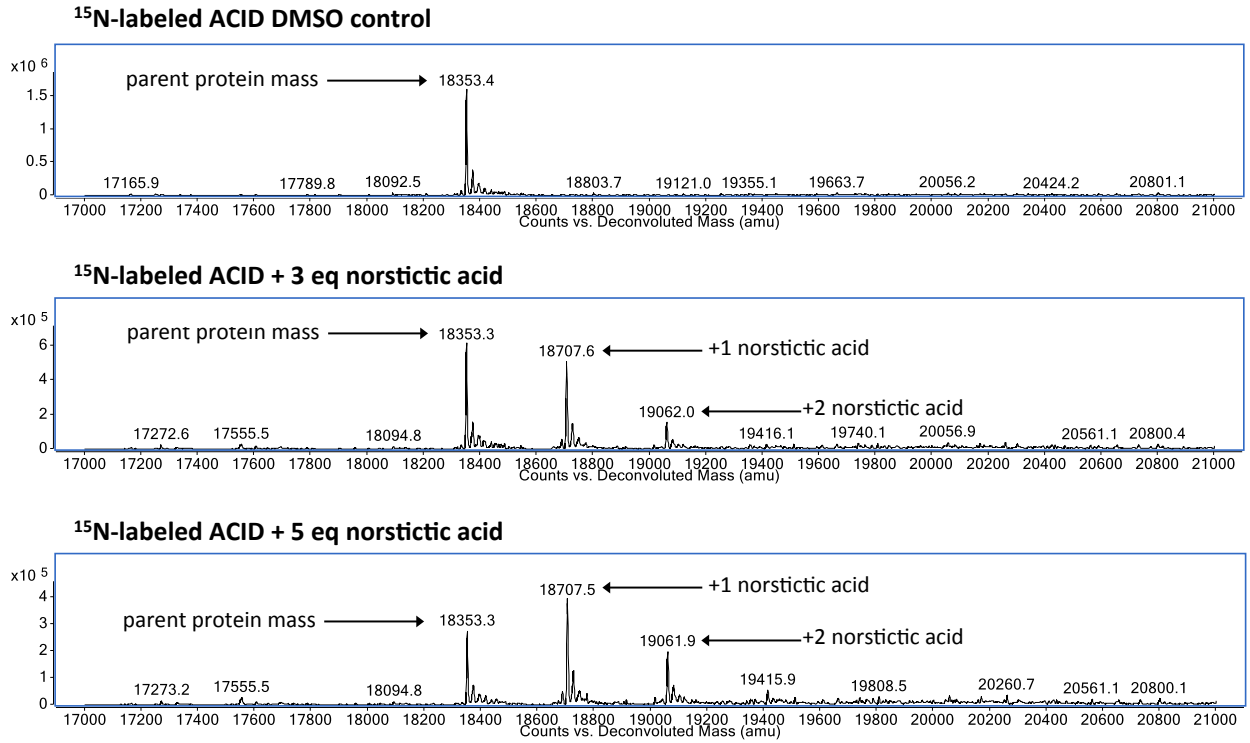

Figure 3.25 Mass spectrometry analysis of ^{15}N-labeled ACID in the presence of DMSO and norstictic acid Performed by Paul Bruno. The ACID protein (30 μM) was incubated with DMSO, 3 equivalents norstictic acid, and 5 equivalents norstictic acid. Complex mixtures were incubated for 2 hours at room temperature. Samples of the complex mixtures were analyzed using mass spectrometry to confirm covalent adduct formation.

In order to investigate ACID chemical shift perturbations in the presence of norstictic acid, samples of ^{15}N-labeled ACID were incubated with DMSO (negative control), 3 equivalents norstictic acid, or 5 equivalents norstictic acid. These samples were left to incubate for 2 hours at room temperature. After the 2 hour incubation, samples of the complex mixtures were analyzed using mass spectrometry to confirm covalent adduct formation (Figure 3.25). Once the covalent adduct formation was confirmed, the sample was submitted for ^{1}H-^{15}N HSQC protein NMR. This was done to minimize precipitation of the protein during the experiment. The NMR buffer and ^{15}N-labeled protein stocks do not contain glycerol or NP-40, which significantly help solubilize the protein therefore, all samples were prepared and analyzed immediately before submission for ^{1}H-^{15}N HSQC protein NMR. The protein was assigned using the assignments previously described for Med25 ACID.[4] Initial observations of the protein NMR experiment confirmed that norstictic acid does not destabilize the protein as indicated by the resolved amide backbone signals maintained

throughout the experiment. If the molecule had destabilized the protein, we would have observed a time-dependent clustering of residues in the ^{1}H-^{15}N spectra, which we did not observe in our experiment. Additionally, there were no far-shifted signals in the ^{1}H-^{15}N spectra to indicate that there was major global restructuring occurring upon ACID binding to norstictic acid, suggesting that any restructuring of ACID upon binding to norstictic acid is subtle. The amide backbone shifts that were observed were mostly peak broadening and small shifts in amide backbone signals. A large number of the peaks can be assigned using the assignment previously described, but not all the residues could accurately be assigned using this method. Interestingly, the chemical shift perturbations that were observed were mostly clustered at two major areas on the protein. In particular, chemical shift perturbations were observed for ACID residues W408, Q409, G462, L483, G485, L486, G491, G493, G496, C497, V498, L513, S516, L525, and N535. In Figure 3.25, we illustrate the chemical shifts observed for ACID in the presence of DMSO (red signals), 3 equivalents of norstictic acid (purple signals), and 5 equivalents of norstictic acid (blue signals). In order to demonstrate the chemical shift perturbations that were observed, snapshots were taken of G462, L464/K520/N535, and C497 (Figure 3.26).

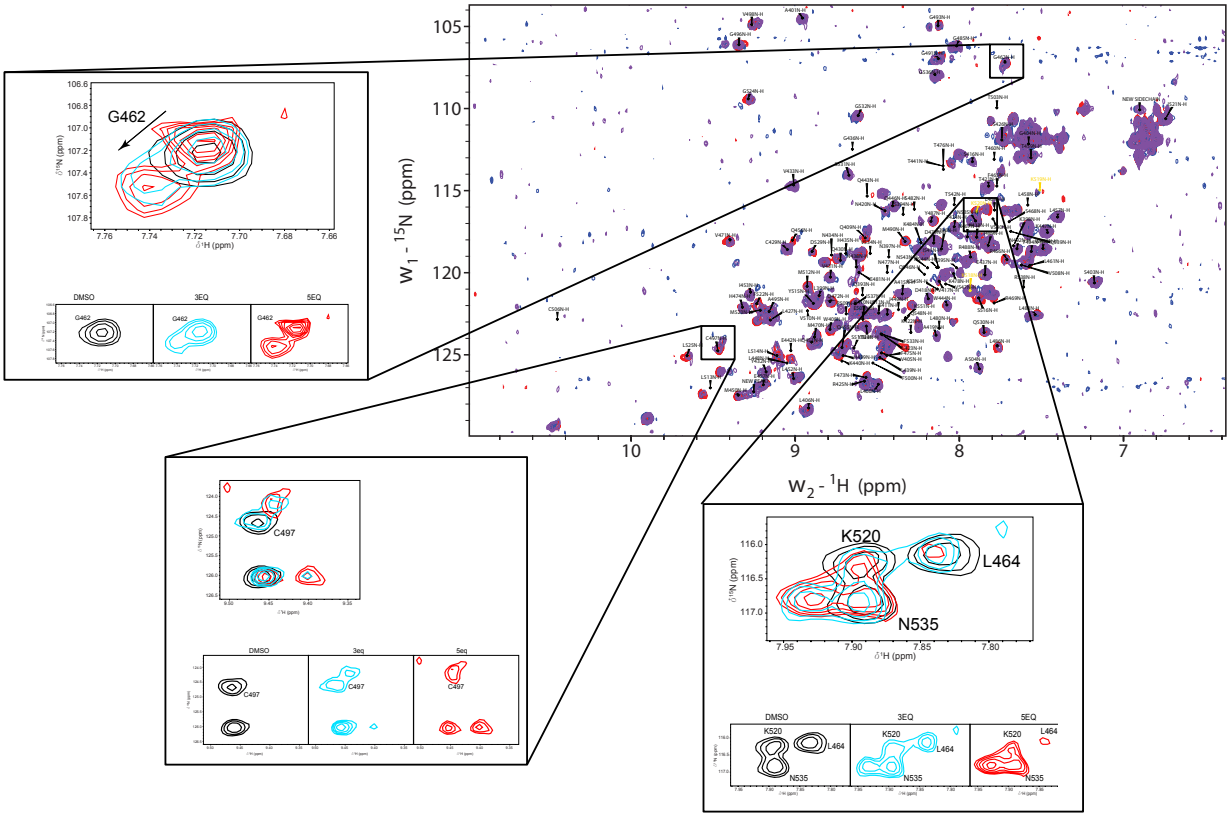

Figure 3.26 ^{1}H-^{15}N HSQC experiment performed with Med25 ACID and norstictic acid
Performed with Felicia Grey. ^{15}N-labeled ACID protein (30 μM) was incubated with DMSO (negative control), 3 equivalents norstictic acid, or 5 equivalents of norstictic acid. The spectra from the experiment are overlaid: DMSO (red signals), 3 equivalents (purple signals), and 5 equivalents norstictic acid (blue signals). Snapshots of 3 different regions of the overlaid experiment are presented.

From the results of this experiment, it is apparent that norstictic acid induces chemical shift perturbations on ^{15}N-labeled ACID. As illustrated in Figure 3.26, we observed both peak broadening and small chemical shifts upon labeling ACID with norstictic acid. These observed chemical shift perturbations further support the notion that norstictic acid can interact with ACID. Interestingly, the observed chemical shifts are localized to two specific regions on the protein, specifically the H1 and H2 binding sites. Overlaying the observed chemical shifts with norstictic acid and the previously reported chemical shifts from VP16 H1 and VP16 H2 binding to ACID, we see that there is considerable overlap between the sets of shifts (Figure 3.27B). This result suggests that norstictic acid binds to sites on ACID similar to the native ligands VP16 H1 and VP16 H2.

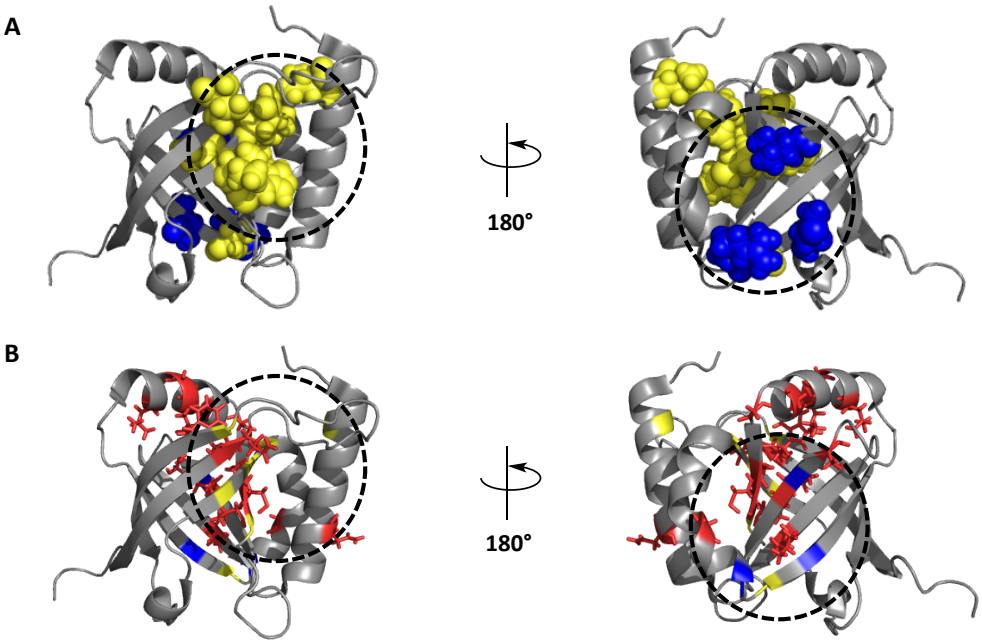

Figure 3.27 Comparing ^{1}H-^{15}N HSQC chemical shifts from VP16 H1 and VP16 H2 with the ^{1}H-^{15}N HSQC chemical shifts from norstictic acid A. The observed chemical shifts with VP16 H1 (yellow) and VP16 H2 (blue). B. Chemical shifts observed with norstictic acid (red) overlaid with VP16 H1 and VP16 H2 chemical shifts. The dashed circles are indicating where the proposed H1 and H2 binding sites are located.

Additionally, the observed chemical shifts were encouraging since there were no chemical shifts observed at more distal regions of the protein, similar to the effects seen with the natural ligands. Based on the observed chemical shifts with norstictic acid, we sought to identify potential lysines that norstictic acid can form imines with that would be consistent with the observed chemical shifts. In Figure 3.28A, we have highlighted all the lysines in ACID (green residues). Additionally, we have identified lysines that are directly adjacent to the H1 binding site and H2 binding site on ACID (Figure 3.28B). We hypothesize that these lysines are the likely sites of imine formation based on the their proximity to the observed chemical shifts with norstictic acid. Additionally, the other lysines that are not in immediate proximity to the H1 and H2 binding sites face away from the binding sites, suggesting they are not involved in the inhibition mode of action of norstictic acid. Therefore, we investigated the importance of the lysines in close proximity to the binding sites through conservative point mutants (K(Lys) → R(Arg)) that will be discussed in greater detail below.

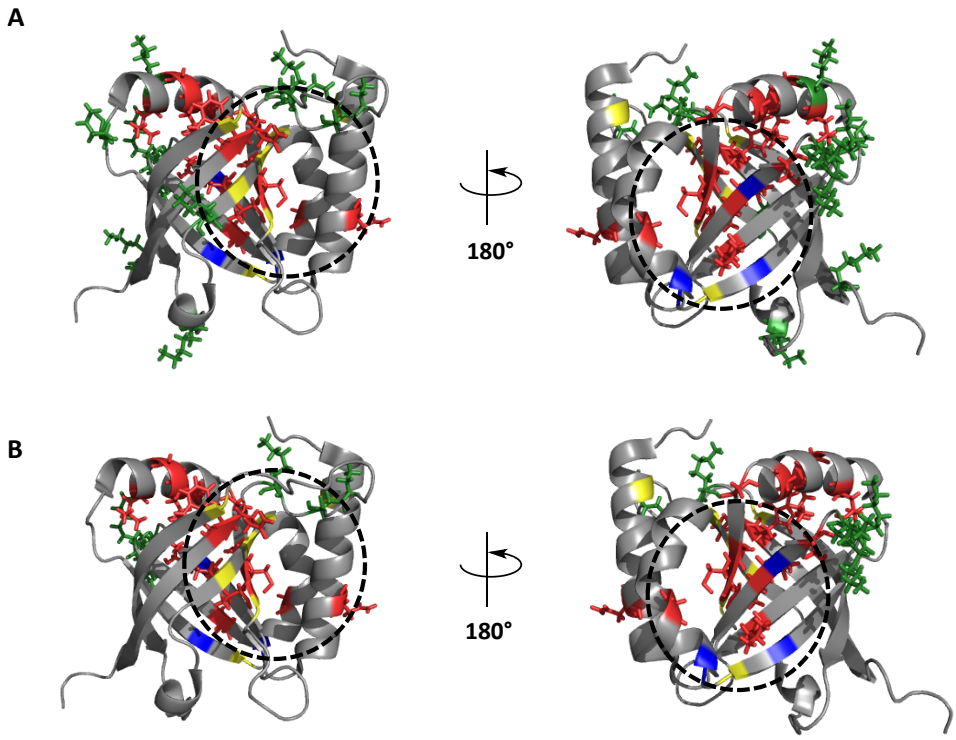

Figure 3.28 Demonstrating lysine proximity to the observed chemical shifts with norstictic acid A. Med25 ACID is depicted with the H1 (yellow) and H2 (blue) site highlighted. The chemical shifts observed with norstictic acid are highlighted in red. The lysines on ACID are highlighted in green. B. Identifying the lysines in closest proximity to the observed chemical shifts with norstictic acid. The highlighted regions are the same as noted in A, but only the lysines (green) in closest proximity to the observed chemical shifts with norstictic acid are highlighted. The dashed circles highlight the general H1 and H2 binding sites on ACID.

Investigating the effects of conservative point mutations on VP16-ACID direct binding and norstictic acid inhibition

The lysines that were identified in immediate proximity to the observed chemical shifts observed with norstictic acid included K411, K413, K518, K519, and K520. In order to test whether the compounds were targeting the hypothesized lysines mentioned above, we decided to make point mutations of these identified lysines. There are a number of different point mutations that could be made to assess the importance of these lysines. We can make K→E/D mutations, also known as charge inversion. Alternatively, we could also make alanine mutation K→A, these have been good for making mutation that need to maintain α-helical secondary structure.[57] Lastly, we could make conserved mutations consisting of K→R mutations in order to maintain the positive charge. We decided to

investigate effects of K→R point mutations on VP16-ACID direct binding and norstictic acid inhibition. First, the conservative mutations of K→R will maintain the positive charge as noted above. These conserved mutations are important because we demonstrated earlier that the VP16-ACID interaction and norstictic acid inhibition are both heavily dependent on electrostatics for interaction. If we used charge inversion (K→E/D) point mutations, we would potentially affect the electrostatics of the interactions in addition to affecting potential sites of imine formation with norstictic acid, making it difficult to deconvolute any observed effects. Alanine mutations (K→A) would present similar problems since we would lose the positive charge attributed to a lysine that could be important for electrostatic interaction as well as a potential amine that could be used for imine formation. Therefore, conserved point mutations were used to look at the important lysine residues for inhibition with norstictic acid. By using conserved K→R mutations we maintain the electrostatic interactions required for both VP16-ACID interaction and inhibition with norstictic acid. Additionally, by using conserved K→R mutations, we remove residues capable of forming imines, allowing us to investigate the inhibition of norstictic acid without the covalent contribution. These mutations will also allow us to determine if the previously highlighted lysines in close proximity to the observed chemical shift perturbations are the likely sites of imine formation with norstictic acid. There was one site on ACID that was of particular interest to us, a triple lysine loop (K518-K520) that is directly adjacent to the VP16 H2 binding site on ACID. We decided to focus our efforts on this loop first. We made five mutations of this loop, K518R, K519R, K520R, KK518RR, and KKK518RRR in order to investigate the effects of these mutations on VP16-ACID direct binding and the effects on norstictic acid inhibition.

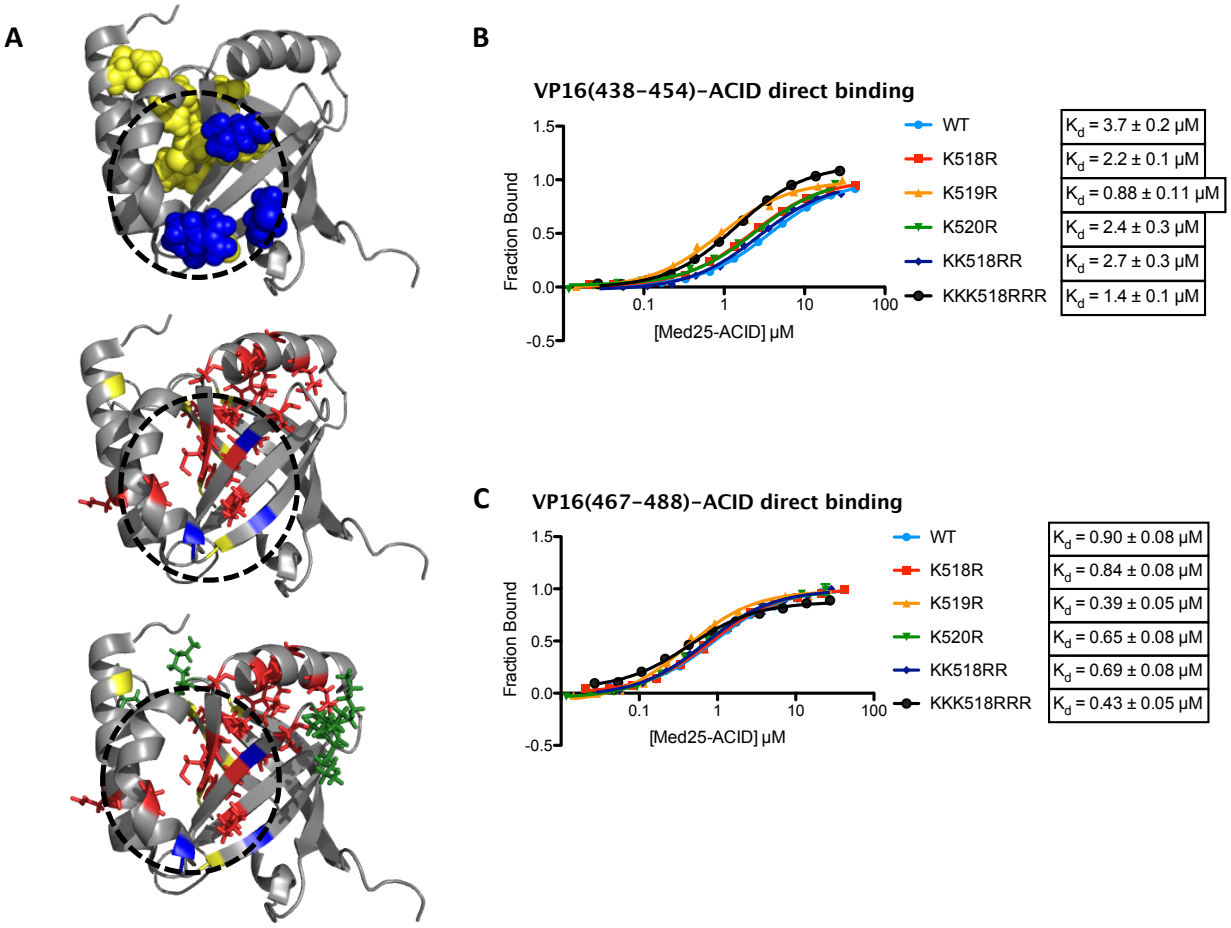

Figure 3.29 Effects of H2 lysine mutations on VP16(438-454)-ACID and VP16(467-488)-ACID direct binding Performed with Steve Sturlis. A. In the top panel, ACID is highlighted with the perturbed residues in the H2 binding pocket of ACID (blue). In the middle panel, the chemical shifts perturbations observed with norstictic acid binding (red) are overlaid with the H2 binding site perturbations. In the bottom panel, the triple lysine stretch directly adjacent to the H2 binding site is highlighted (green). B. Direct binding experiments of the VP16(438-454)-ACID interaction and the VP16(467-488)-ACID interaction performed with each of the mutants. K_ds from the resulting direct binding experiments are as indicated. Each point is representative of the mean and standard deviation of conditions run in triplicate. The data was fitted using graphpad prism 4.0.

From the direct binding experiments that were performed with each of the ACID H2 site mutants (K518R, K519R, K520R, KK518RR, and KKK518RRR) we see that these mutants had little effect on the K_d of the VP16(438-454)-ACID or VP16(467-488)-ACID interaction. As evidenced in Figure 3.29, we see that the K_d was not affected by the mutants more than 2-fold from the K_d observed with the wild type protein. These results are encouraging because it suggests that the conservative K→R mutations are capable of recapitulating the

electrostatic interactions made by the native lysines with the VP16 TAD without affecting binding. Next, we sought to determine if these K→R mutations affect the inhibition of norstictic acid. We hypothesize that the mutation of lysines in close proximity to the chemical shift peturbations observed with norstictic acid inhibition would lead to increased IC_{50} values. The K→R mutations would retain the electrostatic interactions, but would prevent norstictic acid from forming the imine, leading to an increase in IC_{50} due to the loss of covalent binding with the molecule.

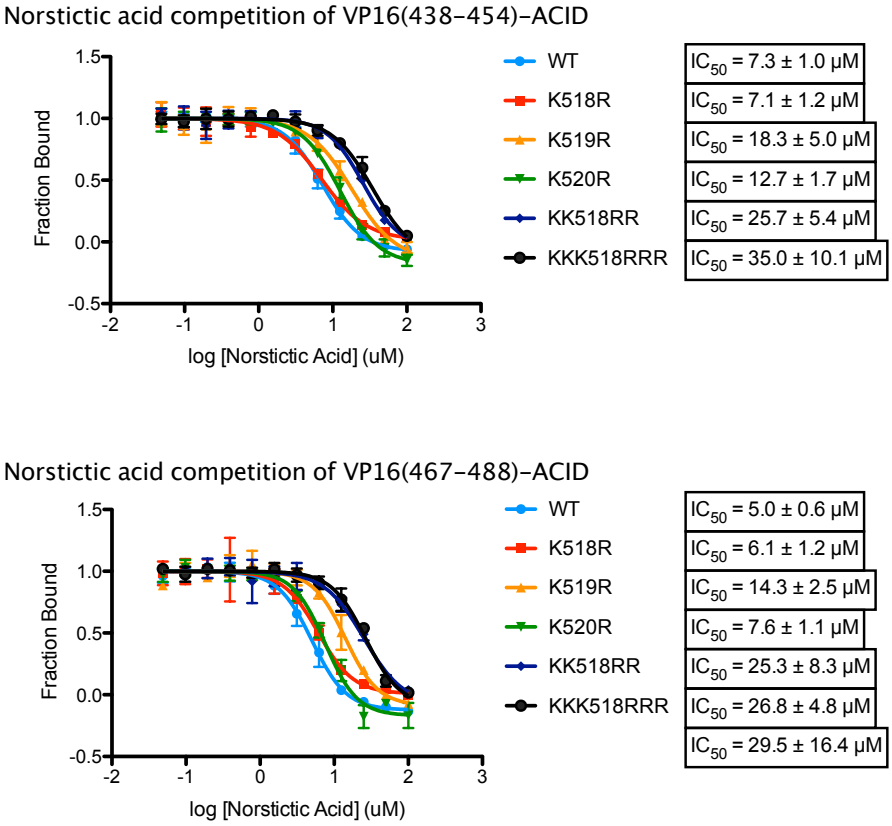

Figure 3.30 Effects of H2 site lysine mutations in competition assays performed with norstictic acid on the VP16(438-454)-ACID and VP16(467-488)-ACID interaction Performed by Steve Sturlis.

As demonstrated in Figure 3.30, we observed steadily increased IC_{50}s as the number of lysines mutated to arginines increased. As depicted in Figure 3.29, no single lysine mutation to arginine was capable of recapitulating the effect observed with the triple lysine mutant. This result suggests that there is not a specific lysine responsible for imine formation with norstictic and that imine formation is likely possible with any of the lysines

in the triple lysine loop. Next, we sought to determine if we could observe similar nostictic acid IC_{50} shifts with lysine mutations in the H1 site of ACID.

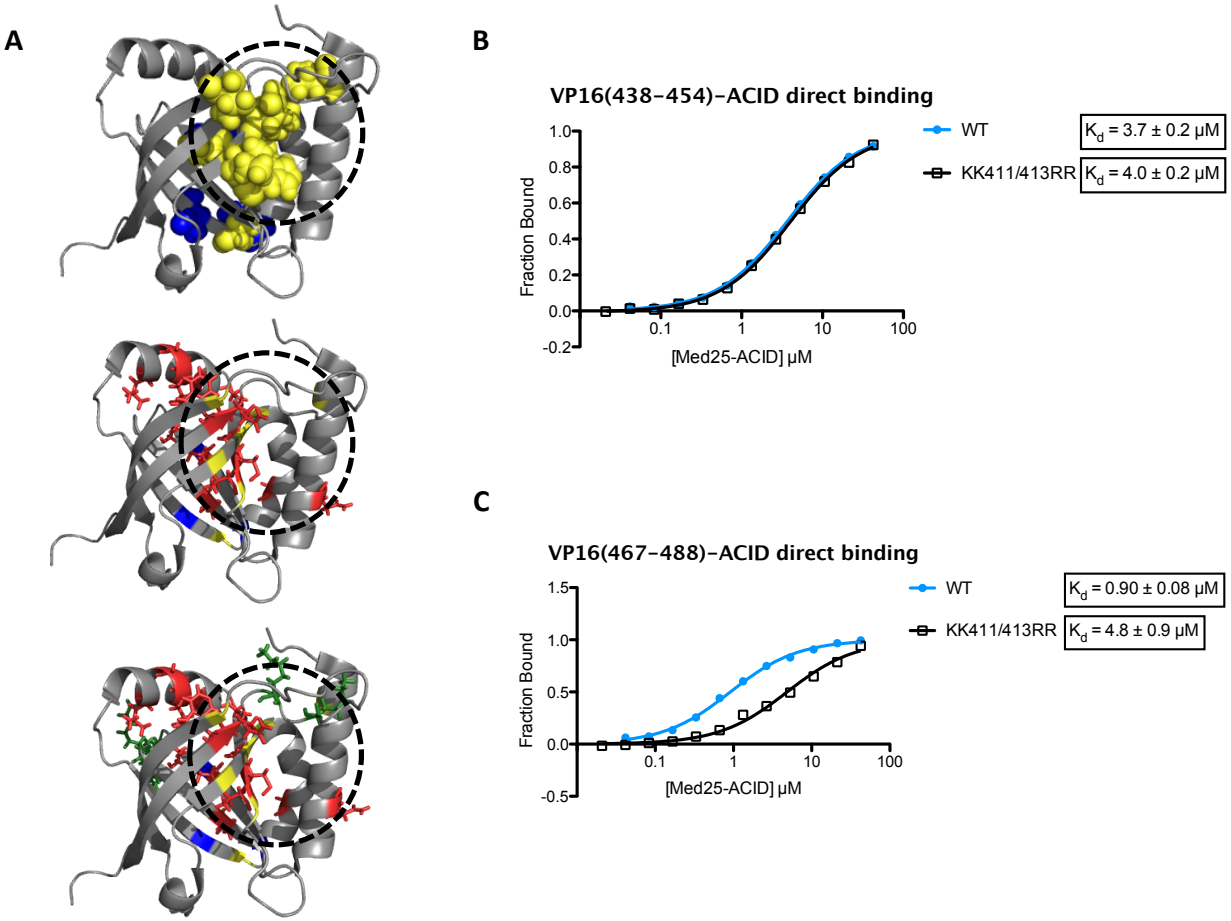

Figure 3.31 Effects of H1 lysine mutations on VP16(438-454)-ACID and VP16(467-488)-ACID direct binding Performed with Steve Sturlis. A. In the top panel, ACID is highlighted with the perturbed residues in the H1 binding pocket of ACID (yellow). In the middle panel, the chemical shifts perturbations observed with norstictic acid binding (red) are overlaid with the H1 binding site perturbations. In the bottom panel, the two lysines directly adjacent to the H1 binding site is highlighted (green). B. Direct binding experiments of the VP16(438-454)-ACID interaction and the VP16(467-488)-ACID interaction performed with the H1 mutant. K_ds from the resulting direct binding experiments are as indicated. Each point is representative of the mean and standard deviation of conditions run in triplicate. The data was fitted using graphpad prism 4.0.

Similar to the effects observed in direct binding experiments preformed with the H2 lysines mutations, we saw minimal effects on direct binding with the H1 lysine mutations. Interestingly, the H1 lysine mutations did have a slight effect on direct binding with the α-helical region of the VP16 H2 interaction with ACID (VP16(467-488)-ACID), contrary to the

results that would be expected. Investigations of this observed result will be tested more thoroughly in future experiments (Figure 3.31).

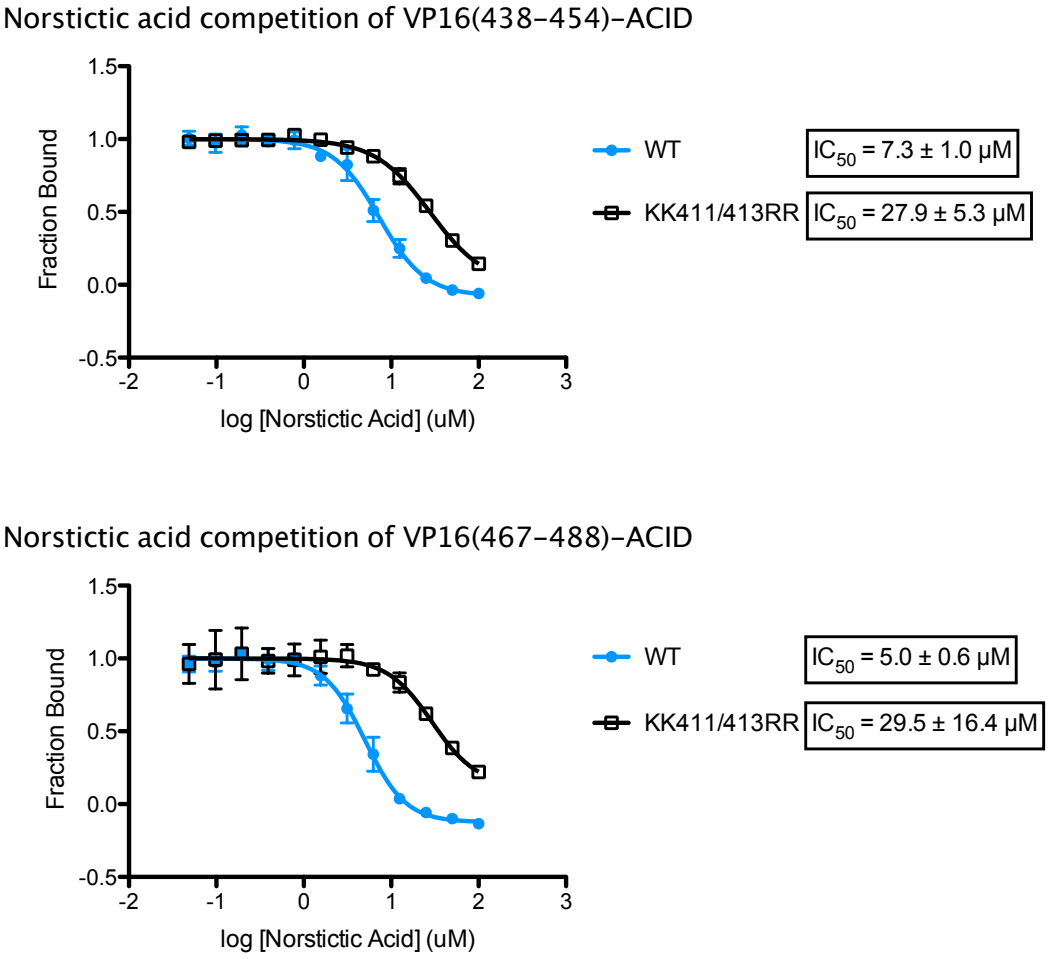

Figure 3.32 Effects of H1 site lysine mutations in competition assays performed with norstictic acid on the VP16(438-454)-ACID and VP16(467-488)-ACID interaction Performed by Steve Sturlis.

As demonstrated in Figure 3.32, lysine mutations in the H1 site of ACID lead to a nearly identical increase in IC_{50} as was observed with the triple lysine mutation in the H2 site of ACID. The increase in IC_{50} values with H1 site lysine mutations suggests that these lysines are also targets of imine formation, consistent with their close proximity to the observed chemical shifts perturbations observed with norstictic acid.

Overall, mutation of lysines in the H1 or H2 site had minimal effects on direct binding of the α-helical H1 peptide and the α-helical H2 peptide. Surprisingly, lysines mutated in the H1 or H2 site did not solely affect the IC_{50} values associated with the H1 or

H2 interaction. For example, the KK411/413RR mutation in the H1 binding site would be expected to only cause the norstictic acid IC_{50} to increase for the VP16(438-454)-ACID interaction, but we also observe the norstictic acid IC_{50} increase for the VP16(467-488)-ACID interaction. This result is contrary to the expected results from mutating lysines to arginines in either the H1 or H2 site. One possibility that could explain this observation could be due to allosteric effects from the molecule. In figure 3.26, we demonstrated that there was significant overlap of the ^{1}H-^{15}N HSCQ chemical shift perturbations with norstictic acid and the previously observed chemical shifts reported for ACID interaction with VP16 H1 and VP16 H2. However, we identified a region of chemical shift perturbations with norstictic acid on helix 2 of Med25 ACID that were unique to the molecule (Figure 3.33).

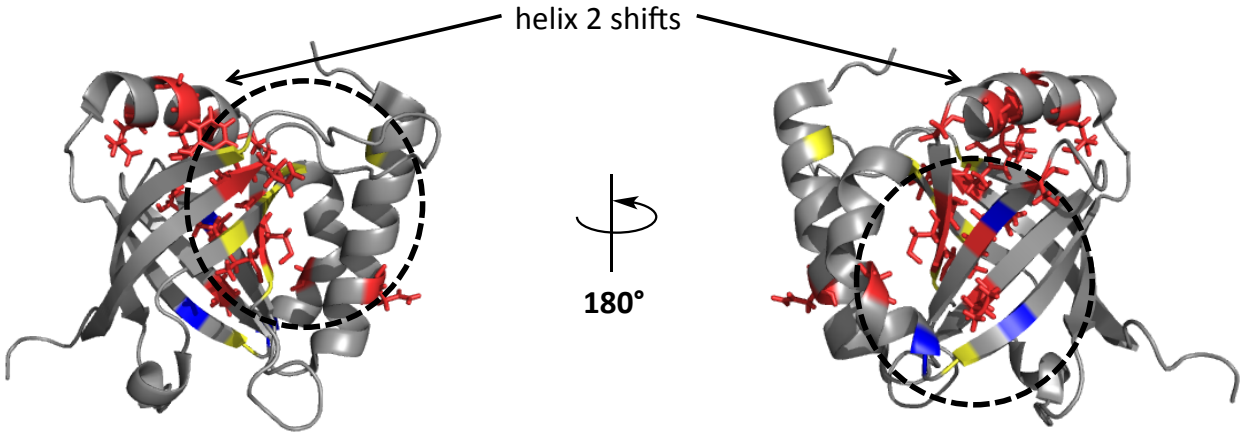

Figure 3.33 Chemical shift perturbations with norstictic acid identified on helix 3 of Med25 ACID On the left, chemical shift perturbations for VP16 H1 binding are labeled in yellow with the dashed circle identifying the H1 binding site on ACID. On the right, chemical shift perturbations for VP16 H2 binding are labeled in blue with the dashed circle identifying the H2 binding site on ACID. Chemical shift perturbations observed with norstictic acid are identified in red. A number of the chemical shift perturbations observed with norstictic acid overlap with the chemical shift perturbations for VP16 H1 and VP16 H2. Chemical shift perturbations unique to norstictic acid are highlighted on helix 2 of ACID.

These unique chemical shifts observed with norstictic acid are localized to helix 2 on ACID. Helix 2 spans a region that connects with both the H1 and H2 binding site. Based on the unique chemical shifts identified with norstictic acid, one possibility to explain the observations above is that norstictic acid binding in either the H1 or H2 binding site could induce an allosteric conformational change that affects inhibition in the other site. Further

expanding on the possible allosteric mechanisms of norstictic acid, we also need to consider the role of cooperative binding. Others have previously identified cooperativity with the VP16 TAD[58-60], suggesting that binding of one subdomain of the VP16 TAD ($VP16_{413-451}$ or $VP16_{452-490}$) causes increased binding of the other VP16 subdomain. If inhibitors such as norstictic acid can bind in the same sites as the native ligands VP16(413-451) and VP16(452-490), it is possible that inhibition could also be acting cooperatively. In a cooperative model of inhibition, mutations that decreased affinity of the inhibitor and decreased binding on one site would cause decreased binding on the other site since cooperative inhibition would be inhibited, providing a possible explanation the observed effects with norstictic acid inhibition and H1/H2 arginine mutants.

CELLULAR EXPERIMENTS TESTING THE EFFECTS OF NORSTICTIC AND PSOROMIC ACID

Inhibition of Med25 ACID-mediated transcriptional activity of ATF6α

Next, we sought to determine if the inhibition that we observed *in vitro* could be observed in cellular assays. We first attempted to develop an assay to investigate the ability of these compounds to inhibit a Gal4-VP16TAD chimera from activating a Gal4-driven luciferase reporter. We normalized the luciferase output of this assay with a constitutively expressed β-Gal reporter. Unfortunately, in our hands the Gal4-VP16TAD construct was very toxic to the cells and made assaying compounds with this method difficult. We are currently pursuing additional studies to look at Gal4 fusions based on just the VP16 H1 or H2 domain to minimize toxicity. Due to the toxicity observed with the Gal4-VP16 chimera, we looked at other analogous cellular assays to assay the inhibitory effects of our compounds. Experiments performed by Sela and coworkers looked at the ER stress transcription factor activating transcription factor 6 (ATF6α) and its interaction with the Mediator complex.[12] More specifically, their studies found that ATF6α TAD is responsible for recruiting the Mediator complex. Within the ATF6α TAD is an 8 amino acid sequence, DFDLDLMP that closely resembles the VP16 TAD sequence, DFDLDMLG, referred to as VN8.[61] Competition using the VN8 sequence against ATF6α demonstrated that VN8 can compete with ATF6α for binding to the Mediator complex, suggesting that ATF6α and VP16 have the same or overlapping interaction surfaces on Mediator complex. Given the recent

studies demonstrating VP16 binds to the Mediator complex through Med25[27] and more specifically, the ACID domain of Med25, [3,4] suggests that ATF6α could also interact with the Med25, and possibly through interaction with the ACID domain. Follow-up studies by Sela and coworkers demonstrated that the ATF6α TAD did in fact, interact with the Med25 ACID domain and that the VN8 peptide was able to compete with the ATF6α TAD-ACID interaction, suggesting that the ATF6α TAD and VP16 TAD use overlapping interaction surfaces on ACID. Given the ability of our depsidones to inhibit the VP16-ACID interaction, we reasoned that our depsidones should also be able to inhibit the ATF6α Med25-mediated transcriptional processes through inhibition of the ACID domain. One such ATF6α-mediated transcriptional process that that was demonstrated to be dependent on Med25 interaction is the ER stress-induced HSPA5 gene.[5] We hypothesized that pre-treating cells with norstictic acid or psoromic acid before inducing HSPA5 expression would result in inhibition of HSPA5 expression compared to untreated cells (Figure 3.34).

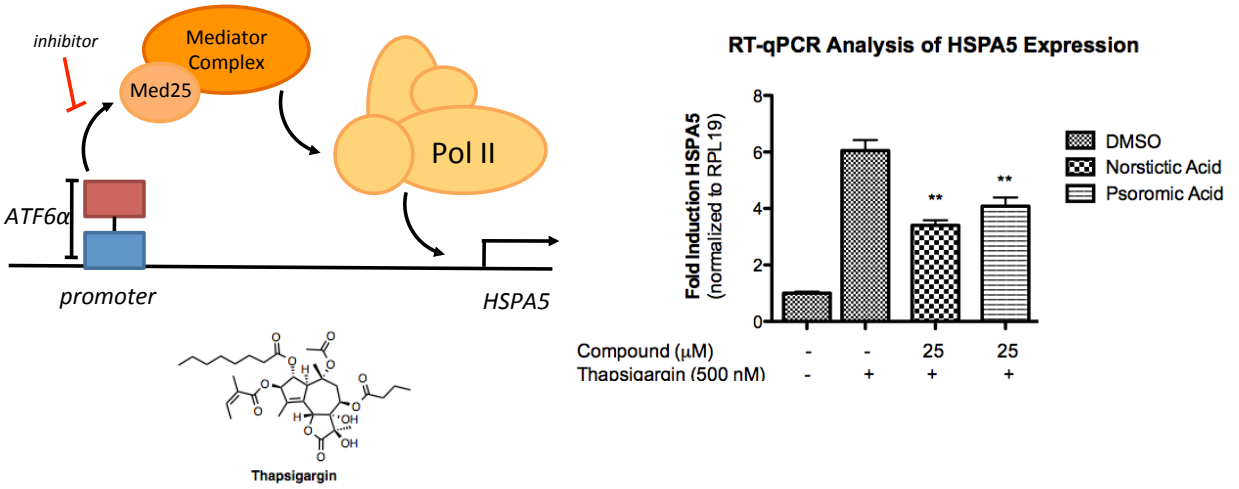

Figure 3.34 Inhibition of ATF6α Med25-mediated HSPA5 expression Performed by Paul Bruno. Diagram illustrating the ATF6α Med25-mediated transcriptional activation of the HSPA5 gene. On the right, is a graph demonstrating inhibition of HSPA5 activation using norstictic acid and psoromic acid. Cells were incubated with DMSO (negative control) or 25 μM of norstictic acid or psoromic acid for 12 hours at which point, thapsigargin was added to cells at a final concentration of 500 nM and left to incubated with treated cells for 3 hours to stimulate HSPA5 expression. After the 3 hour incubation with thapsigargin, cells lysed and isolated mRNA was quantified for HSPA5 activation. All cells treated with control (DMSO) or compounds contained 0.5% v/v DMSO. All signals are the mean and standard deviation of 3 technical replicates. **, $P < 0.01$, $n = 3$.

The observed inhibition with norstictic acid and psoromic acid on HSPA5 expression demonstrates that the identified depsidones are capable of inhibiting Med25-mediated transcriptional processes that rely on interaction with the Med25 ACID domain. Based on this observation we sought to determine if inhibition could be observed with other Med25-mediated transcriptional processes dependent on interaction with the ACID domain.

Inhibition of Med25 ACID-mediated transcriptional processes of ERM

Recently, ERM, one of the transcriptional activators in the PEA3 subfamily of Ets proteins, has been reported to make direct interaction with the Med25 ACID domain. A combination of luciferase assays, pull-downs, and squelching experiments identified a 34 amino acid region in the ERM TAD that is responsible for interaction with Med25 ACID. Furthermore, isothermal titration calorimetry (ITC) performed with this 34 amino acid sequence of the ERM TAD (ERM_{38-72}) was demonstrated to have a K_d of 543 $\pm$ 40 nM with Med25 ACID,[6] similar to the affinities observed with the VP16 H1 and H2 subdomains. A sequence comparison comparing the VP16 TAD and the ERM TAD demonstrates the ERM(38-72) subdomain share high sequence similarity with VP16 H1 (Figure 3.35A). We adapted the ERM(38-72) peptide for an FP assay by conjugating the peptide to fluorescein isothiocyanate. Direct binding experiments performed with this peptide and purified ACID confirmed the reported K_d for ERM(38-72) (Figure 3.35B). Furthermore, we see that the ACID H1 and H2 lysine to arginine mutations do not affect direct binding between ERM(38-72) and ACID, similar to the effects observed with VP16(438-454) and VP16(467-488). We also observed similar inhibition potency with norstictic acid against the ERM(38-72)-ACID interaction. This results is consistent with what would be expected given the sequence similarity between ERM and VP16 H1 and the observed effects of norstictic acid inhibition against the VP16(438-454)-ACID interaction.

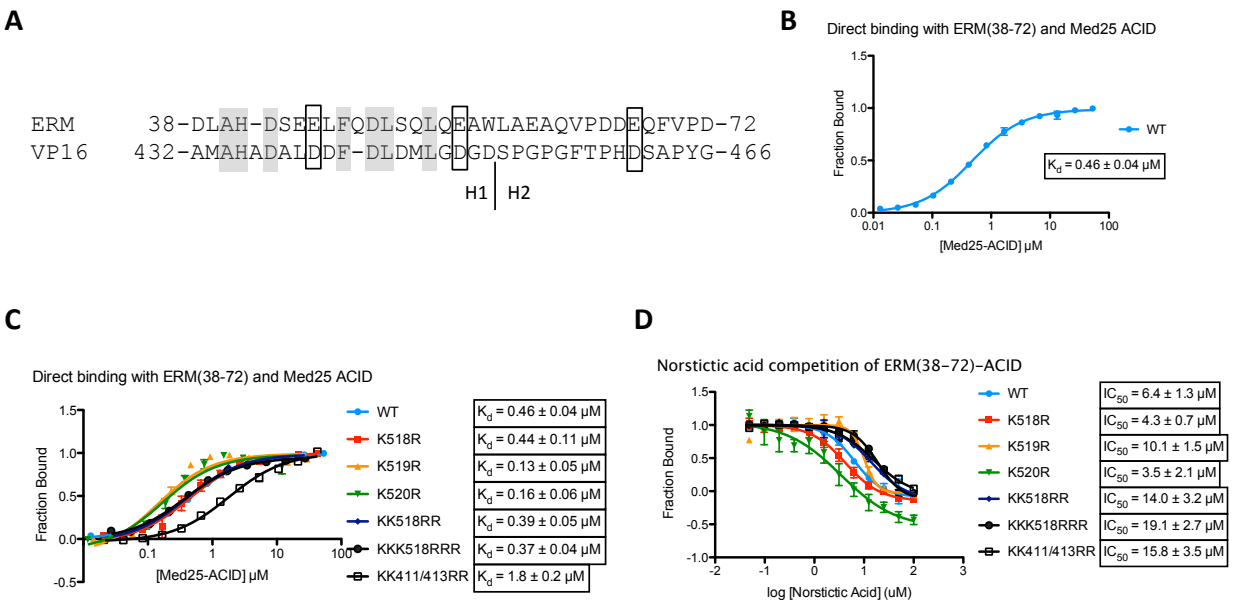

Figure 3.35 The ERM-ACID interaction and inhibition of interaction with norstictic acid Performed with Steve Sturlis. A. A sequence alignment of the ERM TAD and the VP16 TAD, residues with the same identity are highlight in grey and conserved residues are outlined in a black box. B. Evaluating the K_d of the ERM(38-72)-ACID interaction using a direct binding FP assay using a fluorescein-tagged ERM(38-72) peptide and purified ACID protein ($Med25_{394-543}$). C. The effects of lysine to arginine mutations in the ACID H1 and H2 site on ERM direct binding. D. The effects of lysine to arginine mutations in the ACID H1 and H2 site on norstictic acid competition of the ERM(38-72)-ACID interaction. All data points are represented as the mean and standard deviation of conditions performed in triplicate. Curves were fitted using non linear regression fit in graphpad prism software 4.0.

Based on the observation that norstictic acid has a low micromolar IC_{50} against the ERM(38-72)-ACID interaction, we sought to determine if these results could be recapitulated against a cellular process. One such process that is regulated by the ERM transcriptional activator and its interaction with the ACID domain to recruit the transcriptional machinery is MMP-1.[6] MMP-1 has previously been demonstrated to be very important for migration in breast cancer and inhibition of MMP-1 has been demonstrated to inhibit the migration of MDA-MB-231 breast cancer cells.[62] Therefore, we sought to determine if norstictic acid and psoromic acid could inhibit migration of MDA-MB-231 cells. In order to assess the ability of norstictic acid and psoromic acid to inhibit migration of MDA-MB-231 cells, we performed wound healing assays with MDA-MB-231 cells in the presence of DMSO or compound. In general, these wound healing assays are performed by

scratching a cell monolayer with a pipette tip to form a wound, compounds are added and closure of the wound (migration) is monitored. In wound healing assays performed with MDA-MB-231 cells, we demonstrated greater migration (wound closure) for DMSO controls compared to cells in the presence of either norstictic acid or psoromic acid, suggesting that these compounds are capable of reducing migration of MDA-MB-231 (Figure 3.36).

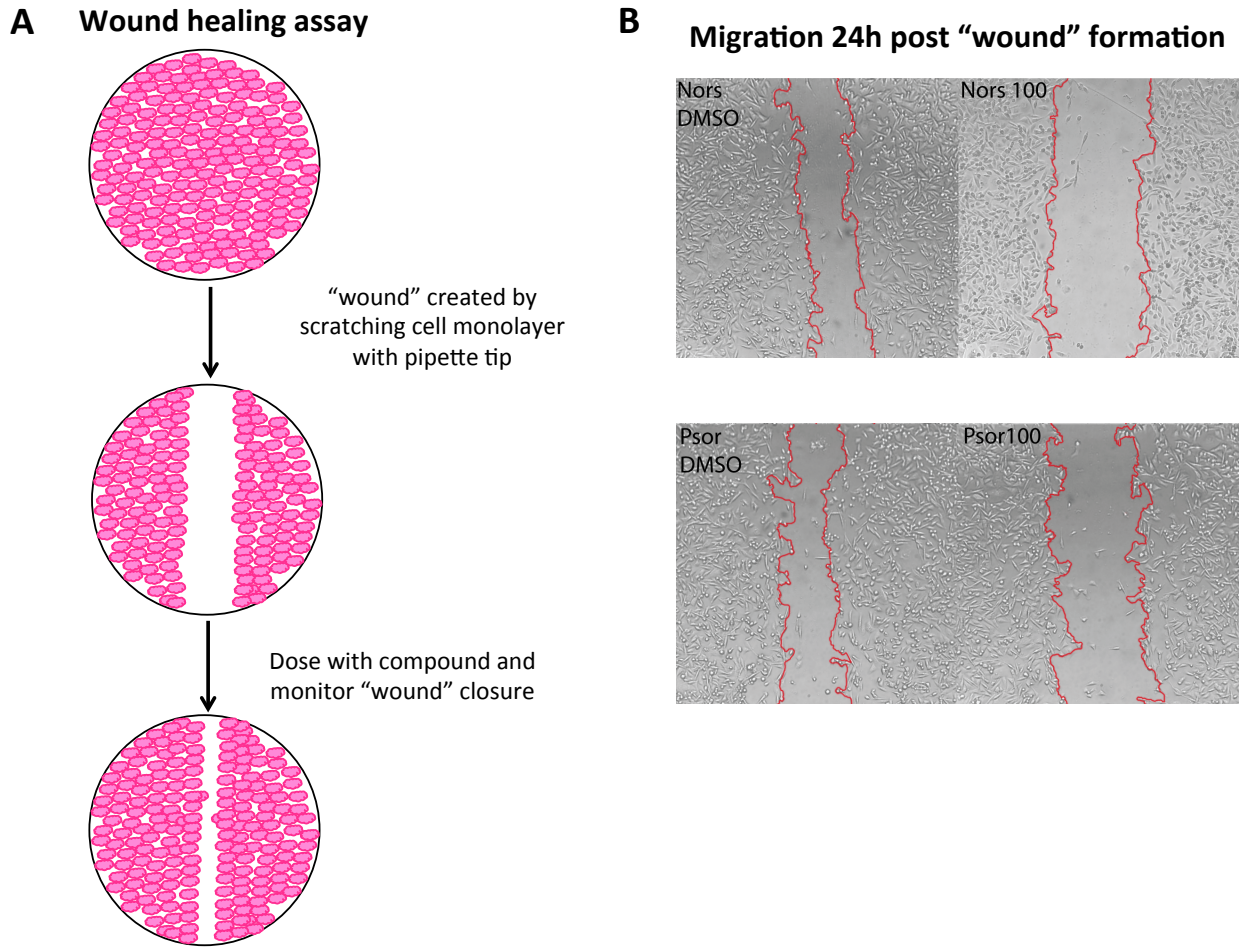

Figure 3.36 Monitoring migration of MDA-MB-231 cells dosed with norstictic acid and psoromic acid Performed by Paul Bruno. A. General procedure for monitoring cell migration using wound healing assay. B. Migration of MDA-MB-231 cells in the presence of DMSO, 100 μM norstictic acid, and 100 μM psoromic acid. Images are of cell "wounds" 24 hours post "wound" formation.

Inhibition of Med25 ACID-mediated transcriptional processes of RAR

Another transcriptional process that has been demonstrated to be Med25-dependent and reliant on interaction with the ACID domain is the retinoic acid receptor (RAR). Lee and

coworkers performed two-hybrid assays with the RAR ligand-binding domain, identifying the Med25 as an interaction partner.[24] The interaction was localized to the NR box of Med25 and the RAR ligand-binding domain; however, assays that overexpressed Med25 did not result in greatly enhanced activity of RAR, suggesting that recruitment of Med25 is not solely sufficient for transcriptional upregulation. It has been previously demonstrated that CBP, [63-65] a histone acetyl transferase (HAT), is recruited to induce RAR target gene upregulation, resulting in a hypothesis that both CBP and Med25 need to both be recruited to induce RAR transcriptional activity. Pull-downs with the Med25 domains VWR, ACID, and NR box demonstrated that the ACID domain interacts with CBP, specifically to the N-terminus of CBP. This result provides a possible mechanism for how RAR can recruit both Med25 and CBP to its promoter. More specifically, an interaction between RAR and the NR box of Med25 recruits Med25 to the RAR promoter then, Med25 can recruit CBP through the Med25 ACID domain and the N-terminus of CBP, resulting in CBP recruitment to the RAR promoter[24] (Figure 3.34). Overexpression of both Med25 and CBP resulted in substantial increases in transcriptional activity at the RAR promoter, when compared to overexpression of Med25 or CBP individually. This result suggests that interruption of Med25 ACID and CBP N-terminus interaction would result in reduced recruitment of CBP to the RAR promoter and reduced transcriptional activity at the RAR promoter. We hypothesize that using psoromic acid and norstictic acid to inhibit the Med25 ACID interaction with the CBP N-terminus will result in reduced activity at the RAR promoter. In order to test this hypothesis, we co-dosed cells transfected with a luciferase reported containing a retinoic acid receptor promoter (pRARE-luc) along with a constitutively expressed β-Gal reporter (pCMV-β-Gal) to monitor off-target effects. All luciferase signals were normalized to β-Gal signal. The results of the assay are as illustrated in Figure 3.37.

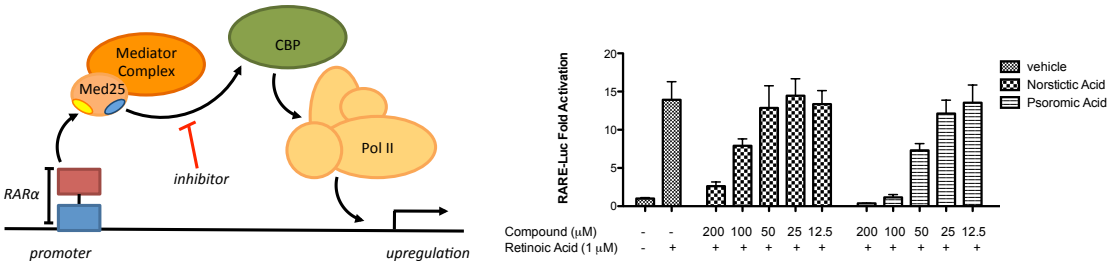

Figure 3.37 Inhibiting RARα transcriptional activity with psoromic acid and norstictic acid Performed by Paul Bruno. On the left, is a diagram of RARα coactivator

recruitment as described by Lee and coworkers. RARα makes specific contacts with the Med25 NR box (yellow) and the ACID domain (blue) recruits CBP through interaction with CBP N-terminus. On the right, we demonstrate decreased RARα transcriptional activity in the presence of ACID inhibitors norstictic acid and psoromic acid. Cells transfected with pRARE-luciferase reporter and pCMV-β-Gal were co-dosed with retinoic acid and either DMSO or compound as noted above. All DMSO levels were kept below 1% v/v for cellular dosings. All signals were normalized to β-Gal activity and represent the mean and standard deviation of 4 replicates.

Given the observed inhibition using norstictic acid and psoromic acid against three different Med25 ACID-mediated transcriptional processes, we are confident that these depsidone inhibitors can effectively inhibit the Med25 ACID domain. The success that we had identifying inhibitors of the VP16-ACID interaction using a pilot screen against our high-throughput assay suggests to us that a larger screen could yield other interesting and more potent inhibitors of ACID.

FULL NATURAL PRODUCT EXTRACT SCREEN AGAINST THE ERM(38-72)-ACID INTERACTION

When we initially had started this project to find inhibitors of the Med25 ACID domain, there was limited structural information of the ACID domain and even less literature identifying potential interaction partners. This lead us to develop the assay and perform the screen based on the information known about the VP16-ACID interaction. During the course of our screen and validation of the hits, additional papers were published identifying new transcriptional activators that interact with ACID such as ERM and ATF6α. The activity of these transcriptional activators was also demonstrated to be at least partially dependent on the interaction with ACID to upregulate target genes, suggesting that identification of an inhibitor would be highly valuable as a mechanistic tool for these newly identified interactions and for identifying new therapeutic strategies against these transcriptional activators. One such transcriptional activator that is of particular interest to us is ERM, a transcriptional activator of the PEA3 subfamily of Ets transcription factors. The ERM transcriptional activator has been implicated in several diseases such as breast cancer[66,67] and prostate cancer.[7] More specifically, ERM dysregulation has been associated with tumors with greater metastatic potential, which correlates with poorer clinical outcome. Additionally, the TAD of ERM has only been demonstrated to contain one

subdomain capable of interaction with ACID, whereas VP16 contains two subdomains capable of interacting with ACID. This observation suggests that ERM may prove to be easier to target by inhibiting ACID compared to VP16. Given the role of ERM in human disease and the fact that only one subdomain needs to be inhibited to block the ERM-ACID interaction, we performed a high-throughput screen using the natural product extract library in the CCG. We chose to use the natural product extract library due to the identification of natural products from the pilot screen of the VP16-ACID interaction. Additionally, identification of two structurally related depsidone inhibitors of Med25 ACID suggests that there are privileged scaffolds that may be well suited to inhibit Med25 ACID. This was further supported by an additional assay looking to see if other depsidone and depsides exist that could possibly target the ACID domain. It has been well documented that lichen organisms are rich in depsides and depsidones, with some organisms containing as much as 5-10% of their dry weight in depsides and depsidones.[68] Using our VP16-ACID high-throughput assay, we looked a plate containing different lichen extracts from various lichen organism to assess whether additional depside and depsidone inhibitors may exist that can inhibit this interaction (Figure 3.38).

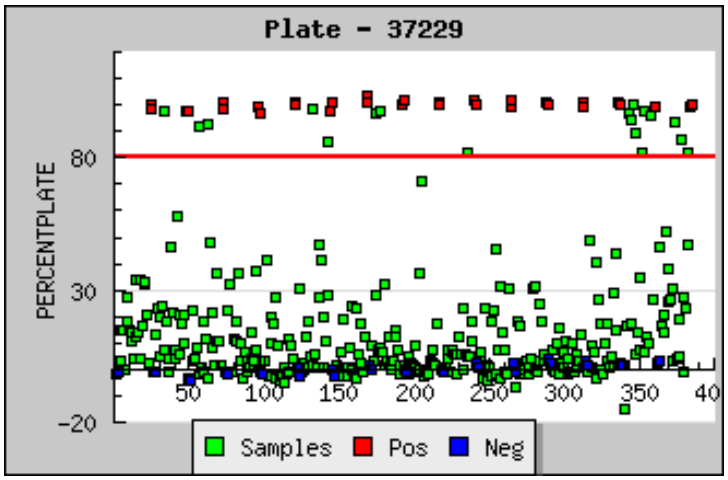

Figure 3.38 Investigating inhibition with lichen extracts against the VP16(467-488)-ACID interaction Performed with Steve Sturlis. We identified the plate by searching for plates that were rich in lichen organism extracts. The inhibition assay was performed the same way as the pilot screen. Z' score was 0.89 and 18 hits exhibited >80% inhibition.

We observed a significantly higher amount of inhibition when testing the lichen extracts against the VP16(467-488)-ACID interaction. In the original pilot screen, we had a 1.6% hit rate as compared to the lichen extracts, which had a 53% hit rate. This observation is not

entirely surprising since we identified two depsidones and one depside inhibitor of Med25 ACID from the pilot screen, suggesting that this core may serve as a 'privileged scaffold' for ACID inhibition. This is further supported by the high hit rate of this lichen extract plate, which contains extracts that are rich in depsides and depsidones and validates our previous hypothesis. Based on this observation, we reasoned that screening the natural product extracts would provide molecules with greater potency as well as access to other possible 'privileged scaffolds' afforded by the unique chemical matter contained in this library. Using the same assay conditions developed for the VP16(467-488)-ACID high-throughput pilot screen with the ERM(38-72)-ACID interaction, we tested the complete set of ~36,000 natural product extracts (NPEs) (Figure 3.39).

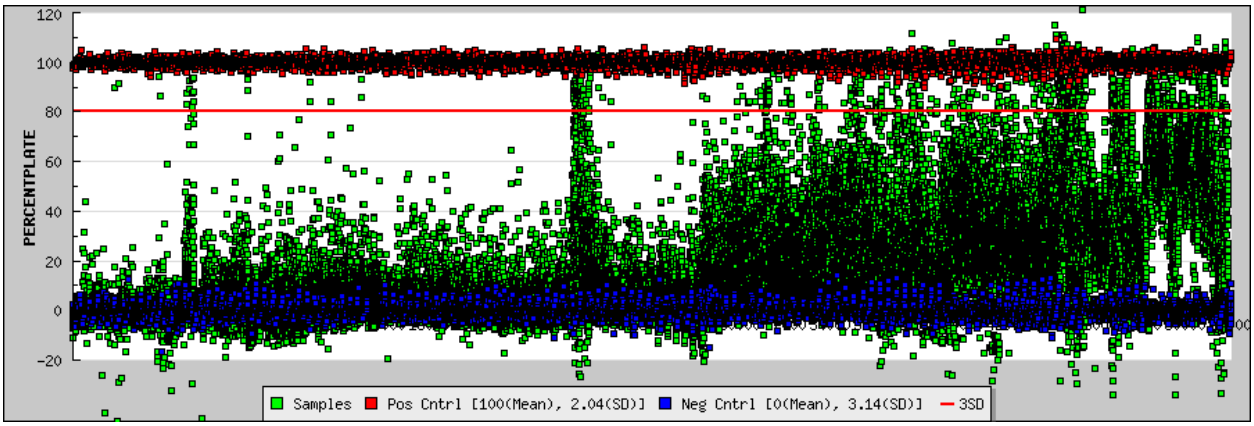

Figure 3.39 Full natural product extract screen against ERM(38-72)-ACID interaction Performed with Steve Sturlis. High-throughout assay was performed with ~36,000 natural product extracts, producing the data above.

As evidenced in Figure 3.39, we observed several extracts that demonstrated potency against the ERM(38-72)-ACID interaction. We are currently in the process of deconvoluting these extracts to determine the identity of the active compounds in the extracts with greatest potency. Future studies will be completed to determine the identity and effects of these compounds on Med25-mediated ERM transcriptional activity.

3.4 Conclusions

Herein in chapter 3, we described a high-throughput assay could be developed to screen against the Med25 ACID-VP16 interaction. Through an iterative process used to truncate the VP16 TAD, we were able to identify the minimal interaction domains required

for ACID binding. From these experiments, we were able to determine that the affinity afforded by the two subdomains of VP16 ($VP16_{413-451}$ and $VP16_{452-490}$) could be recapitulated with the minimal α-helical regions of the two subdomains, suggesting that these regions are the major contributing regions for binding to the ACID domain. By identifying the minimal interaction regions of VP16 binding to ACID, we were able to adapt a high-throughput assay based on the minimal interaction interface, a feat that would not have been possible with full-length VP16 due to its limited solubility. Further validation was completed with our high-throughput assay demonstrating its stability to DMSO (up to 5% v/v), detergents (NP-40) and the large dynamic range that allowed for consistent Z' scores >0.8.

Using this assay, we performed a pilot screen of 4,046 compounds in the known bioactive molecules set at the CCG. The initial hits from the pilot screen were validated, resulting in identification of depside (baeomycesic acid) and depsidone (norstictic acid and psoromic acid) inhibitors of the ACID domain. We demonstrated good selectivity against another activator-coactivator PPI (MLL-KIX and CREB-KIX) and demonstrated that these inhibitors were not general helix mimetics of the VP16 TAD as evidenced by the high IC_{50} values obtained against another reported VP16 interaction. Additional studies including molecular dynamics and salt titrations in direct binding assays, demonstrated that both the VP16-ACID interaction and inhibition of ACID with depsidones are at least partially drive by electrostatics. Mass spectrometry demonstrated that these depsidone inhibitors were capable of covalently modifying ACID through imine formation on lysine side chains. Protein NMR experiments with ACID and norstictic acid demonstrated that the chemical shift perturbations closely overlapped with the shifts observed with the natural ligands ($VP16_{413-451}$ and $VP16_{452-490}$), suggesting that norstictic acid and the natural ligands utilize similar binding sites on ACID. Based on the observed imine formation with the depsidones and the overlapping binding sites between the molecules and the natural ligands as evidenced by protein NMR and MD simulations, we were able to identify a select set of lysines hypothesized to be the site of imine formation. This set of lysines include K518, K519, and K520 in the ACID H2 site and K411 and K413 in the ACID H1 site. Mutation of these lysines to arginines allowed us to observe the inhibition effects of norstictic acid without the imine formation. These experiments resulted in higher IC_{50}s for

the inhibitor, which suggests identification of key residues necessary for imine formation. Surprisingly, these mutations resulted in decreased binding of ligands that bound in the opposite face. This result suggests that in addition to the orthosteric inhibition demonstrated by the molecule, there might also be an allosteric contribution from the inhibitor. Protein NMR data with norstictic acid identified shifts in helix 2 of ACID, a helix that connects the H1 and H2 face of the protein, providing a possible explanation for how norstictic acid could allosterically regulate ACID binding.

The inhibitory effects of these depsidones were also evident in several cellular assays dependent on Med25 ACID-mediated transcriptional events. We demonstrated that the depsidones were capable of inhibiting ATF6α driven HSPA5 expression, decreased migration of MDA-MB-231 cells through presumed MMP-1 inhibition, and inhibition of a RARE-luciferase reported through presumed inhibition of the Med25-CBP interaction. Together, these results identification of the first reported inhibitors of Med25 ACID and inhibition of Med25 ACID-mediated transcription.

3.5 Materials and methods

Plasmids

The plasmid encoding the His_6-tagged KIX from mouse CBP (residues 586-672) has been previously described ($pHis_6$-PL-KIX). [69]. Plasmid pET-21b-Med25(394-543)-His_6 was a kind gift from Patrick Cramer (pACID-His_6). Protein expression plasmids pACID(K518R)-His_6, pACID(K519R)-His_6, pACID(K520R)-His_6, pACID(KK518RR)-His_6, pACID(KKK518RRR)-His_6 were generated by Steven M. Sturlis, and pACID(KK413RR)-His_6 was generated by Paul A. Bruno using site-directed mutagenesis (SDM) as previously described.[70] pGL3-RARE-luciferase was purchased from Addgene and previously described.[71] pCMV-β-Gal and pBSSK (non-coding plasmid) were kind gifts from Jorge Iñiguez-Lluhí.

Protein expression

Non-labeled Med25 ACID ($Med25_{394-543}$) protein was expressed and purified together with Steven M. Sturlis. Plasmid pET-21b-Med25(394-543)-His_6 (pACID-His_6) was a kind gift from Patrick Cramer. This plasmid was transformed into Rosetta pLysS cells (Novagen). Rosetta pLysS cells transformed with pACID-His_6 were used to inoculate a 25 mL TB starter culture with 0.1 mg/mL ampicillin and 0.034 mg/mL chloramphenicol. The next morning, 5 mL from the starter culture was added to 1L TB with ampicillin and bacteria were grown at 37 °C until an OD_{600} of 0.8 is reached. Temperature was reduced to 18 °C and IPTG was added to a final concentration of 0.5 mM to induce expression. Cells were left overnight at 18 °C. Cell suspensions were collected and centrifuged at 5000xg for 20 mins at 4 °C. Cell pellets were frozen at -80 °C until ready to use. Cell pellet from expression was thawed on ice and resuspended in 20 mL 50 mM phosphate buffer (pH 6.8, 300 mM sodium chloride, 10 mM imidazole). Cells are lysed by sonication on ice. Cellular lysates were cleared by centrifugation at 9500 rpm, 20 min at 4 °C and added to Ni-NTA beads (Qiagen). After 1 hour incubation at 4 °C, resin is pelleted with centrifugation at 2500 rpm, 2 min, 4 °C and washed with phosphate buffer above containing 30 mM imidazole. This washing step is repeated an additional 4 times. Protein is eluted with 2 mL of phosphate buffer containing 400 mM imidazole three times. The combined eluates are purified by cation exchange FPLC (Source 15S, GE Healthcare; 0-1M NaCl in 50 mM PBS containing 1 mM DTT). The FPLC purified protein is dialyzed overnight into 10 mM phosphate buffer, pH 6.8 containing 50

mM sodium chloride, 10% glycerol, and 0.01% NP-40 as noted. After dialysis, protein is concentrated using Millipore 3000 kDa cut-off centrifuge concentrators. The protein is >90% pure as determine by coomassie stained polyacrylamide gel. Protein concentration is determined by UV-Vis (ε = 22460 M^{-1} cm^{-1}).

^{15}N-labeled Med25 ACID ($Med25_{394-543}$) was expressed together with Steven M. Sturlis. Rosetta pLys transformed with pACID-His_6 were used to inoculate 25 mL of LB broth starter cultures with 0.1 mg/mL ampicillin and 0.034 mg/mL chloramphenicol. The next morning, 5 mL of the starter culture was added to 1 L LB broth with ampicillin, and bacteria were grown at 37 °C until an OD_{600} of 0.8 is reached. Cells were pelleted and washed with M9 minimal media. Cells from 1 L culture are resuspended in 1 L M9 minimal media with ampicillin and BioXpress (Cambridge Isotope Laboratories) added. Cells grown in shaker at 37 °C for 1 hr before temperature is reduced to 18 °C and IPTG is added at a final concentration of 0.5 mM. Cells were left at 18 °C overnight. Cell suspensions were collected and centrifuged at 5000xg for 20 mins at 4 °C. Cell pellets were frozen at -80 °C until ready to use. Cell pellet from expression was thawed on ice and resuspended in 20 mL 50 mM phosphate buffer (pH 6.8, 300 mM sodium chloride, 10 mM imidazole). Cells are lysed by sonication on ice. Cellular lysates were cleared by centrifugation at 9500 rpm, 20 min at 4 °C and added to Ni-NTA beads (Qiagen). After 1 hour incubation at 4 °C, resin is pelleted with centrifugation at 2500 rpm, 2 min, 4 °C and washed with phosphate buffer above containing 30 mM imidazole. This washing step is repeated an additional 4 times. Protein is eluted with 2 mL of phosphate buffer containing 400 mM imidazole three times. The combined eluates are purified by cation exchange FPLC (Source 15S, GE Healthcare; 0-1M NaCl in 50 mM PBS containing 1 mM DTT). The FPLC purified protein is dialyzed overnight into 10 mM phosphate buffer, pH 6.8 containing 50 mM sodium chloride. After dialysis, protein is concentrated using Millipore 3000 kDa cut-off centrifuge concentrators. The protein is >90% pure as determine by coomassie stained polyacrylamide gel. Protein concentration is determined by UV-Vis (ε = 22460 M^{-1} cm^{-1}).

Med25 ACID K518R was expressed and purified by Steven M. Sturlis. Protein was expressed and purified as reported above for Med25 ACID ($Med25_{394-543}$).

Med25 ACID K519R was expressed and purified by Steven M. Sturlis. Protein was expressed and purified as reported above for Med25 ACID ($Med25_{394-543}$).

Med25 ACID K520R was expressed and purified by Steven M. Sturlis. Protein was expressed and purified as reported above for Med25 ACID ($Med25_{394-543}$).

Med25 KK518RR was expressed and purified by Steven M. Sturlis. Protein was expressed and purified as reported above for Med25 ACID ($Med25_{394-543}$).

Med25 KKK518RRR was expressed and purified by Steven M. Sturlis. Protein was expressed and purified as reported above for Med25 ACID ($Med25_{394-543}$).

Med25 KK411/413RR was expressed and purified together with Steven M. Sturlis. Protein was expressed and purified as reported above for Med25 ACID ($Med25_{394-543}$).

Non-labeled Med15(1-345) was expressed and purified as previously reported by Paul A. Bruno.[14] Non-labeled KIX protein was expressed and purified with Steven M. Sturlis as previouisly reported.[69] Lab stocks of Gal(1-100) was used for counter screen. This protein has been previously reported.[72]

Peptide synthesis

Peptides are synthesized on CLEAR amide resin (Peptides International) using standard HBTU/HOBT/DIEA coupling conditions.

Flo-VP16(413-437) was synthesized and purified. Fluorescein isothiocyanate and beta-alanine was coupled to a sequence containing VP16 residues 413-437 to make FITC-βA-APPTDVSLGDELHLDGEDVAMAHAD. It was purified by reverse phase HPLC (Agilent 1260) on a C18 poroshell column (Agilent) with 20 mM ammonium acetate in water and acetonitrile as eluents. A gradient of 10-40% acetonitrile over 30 min was used. Analytical HPLC trace is included in section 3.6. Peptide was lyophilized to a fine powder and

reconstituted as a DMSO stock and diluted in PBS buffer to an appropriate working concentration. The concentration of Flo-VP16(413-437) was determined by UV-Vis in 10 mM PBS pH 7.4, using ε = 72,000 M^{-1} cm^{-1} according to manufacturer (Pierce).

Flo-VP16(438-464) was synthesized and purified. Fluorescein isothiocyanate and beta-alanine was coupled to a sequence containing VP16 residues 438-464 to make FITC-βA-ALDDFDLDMLGDGDSPGPGFTPHDSAP. It was purified by reverse phase HPLC (Agilent 1260) on a C18 poroshell column (Agilent) with 20 mM ammonium acetate in water and acetonitrile as eluents. A gradient of 10-40% acetonitrile over 30 min was used. Analytical HPLC trace is included in section 3.6. Peptide was lyophilized to a fine powder and reconstituted as a DMSO stock and diluted in PBS buffer to an appropriate working concentration. The concentration of Flo-VP16(438-464) was determined by UV-Vis in 10 mM PBS pH 7.4, using ε = 72,000 M^{-1} cm^{-1} according to manufacturer (Pierce).

Flo-VP16(465-490) was synthesized and purified. Fluorescein isothiocyanate and beta-alanine was coupled to a sequence containing VP16 residues 465-490 to make FITC-βA-YGALDMADFEFEQMFTDALGIDEYGG. It was purified by reverse phase HPLC (Agilent 1260) on a C18 poroshell column (Agilent) with 20 mM ammonium acetate in water and acetonitrile as eluents. A gradient of 10-40% acetonitrile over 30 min was used. Analytical HPLC trace is included in section 3.6. Peptide was lyophilized to a fine powder and reconstituted as a DMSO stock and diluted in PBS buffer to an appropriate working concentration. The concentration of Flo-VP16(465-490) was determined by UV-Vis in 10 mM PBS pH 7.4, using ε = 72,000 M^{-1} cm^{-1} according to manufacturer (Pierce).

Flo-VP16(438-454) was synthesized by Steve M. Sturlis and purified by Paul A. Bruno. Fluorescein isothiocyanate and beta-alanine was coupled to a sequence containing VP16 residues 438-454 to make FITC-βA-ALDDFDLDMLGDGDSPG. It was purified by reverse phase HPLC (Agilent 1260) on a C18 poroshell column (Agilent) with 20 mM ammonium acetate in water and acetonitrile as eluents. A gradient of 10-40% acetonitrile over 30 min was used. Analytical HPLC trace is included in section 3.6. Peptide was lyophilized to a fine powder and reconstituted as a DMSO stock and diluted in PBS buffer to an appropriate

working concentration. The concentration of Flo-VP16(438-454) was determined by UV-Vis in 10 mM PBS pH 7.4, using ε = 72,000 M^{-1} cm^{-1} according to manufacturer (Pierce).

Flo-VP16(467-488) was synthesized and purified by Steven M. Sturlis. Fluorescein isothiocyanate and beta-alanine was coupled to a sequence containing VP16 residues 467-488 to make FITC-βA- ALDMADFEFEQMFTDALGIDEY. The concentration of Flo-VP16(467-488) was determined by UV-Vis in 10 mM PBS pH 7.4, using ε = 72,000 M^{-1} cm^{-1} according to manufacturer (Pierce). Analytical HPLC trace is included in section 3.6.

Flo-ERM(38-72) was synthesized and purified by Steven M. Sturlis. Fluorescein isothiocyanate and beta-alanine was coupled to a sequence containing ERM residues 38-72 to make FITC-βA-DLAHDSEELFQDLSQLQEAWLAEAQVPDDEQFVPD. The concentration of Flo-ERM(38-72) was determined by UV-Vis in 10 mM PBS pH 7.4, using ε = 72,000 M^{-1} cm^{-1} according to manufacturer (Pierce). Analytical HPLC trace is included in section 3.6.

Flo-MLL, Flo-pKID(CREB), Flo-VP2 and Fl-DNA are as previously reported. [72,73]

Direct binding experiments

Direct binding assays were performed in triplicate with a final sample volume of 20 μL in a low volume, non-binding, black, 384-well plate (Corning), and read on a Pherastar plate reader with polarized excitation at 485 nm and emission intensity measured through a parallel and perpendicularly polarized 535 nm filter. FITC (fluorescein isothiocyanate) labeled peptides were diluted in storage buffer (10 mM PBS, 100 mM NaCl, 0.001% NP-40, 10 % glycerol, pH 6.8) to a centration of 40 nM. Then, 10 μL of the peptide solution was added to a 10 uL solution of ACID protein that had been previously serially diluted 2-fold using the storage buffer noted above for the number of desired dose points. This resulted in a final concentration of 20 nM for the FITC peptides. The samples were incubated for 30 minutes at room temperature before the fluorescence anisotropy was measured (Pherastar microplate reader). A binding isotherm that accounts for ligand depletion (assuming a 1:1 binding model of peptide to ACID) was fit to the observed anisotropy values as a function of ACID to obtain the apparent equilibrium dissociation, K_d:

$$y = c + (b - c) \times \frac{[(K_d + a + x) - \sqrt{(K_d + a + x)^2 - 4ax}]}{2a}$$

Equation 3.2

Where "a" and "x" are the total concentrations of fluorescent peptide and ACID, respectively, "y" is the observed anisotropy at a given ACID concentration, "b" is the maximum observed anisotropy value, and "c" is the maximum observed anisotropy value. Each data point is an average of three independent experiments with the indicated error representing the standard deviation of the three replicated. Data analysis was performed using GraphPad Prism 4.0.

Direct binding assays testing the effect of tracer concentration, DMSO, and NP-40 effects on direct binding were performed using the procedure above including either a higher concentration of tracer, including DMSO (5% v/v), or NP-40 (0.001% v/v).

Pilot screen of VP16-ACID interaction

Pilot screen was performed with Steven M. Sturlis. The concentration of ACID protein (850 nM), tracer used (Flo-VP16(465-490)), tracer concentration (20 nM), and inclusion of NP-40 (0.001% v/v) are based on optimization experiments performed in chapter 3. For pilot screen of VP16-ACID interaction, used a final sample volume of 20 µL in a low volume, non-binding, black, 384-well plate (Corning), and read on a Pherastar plate reader with polarized excitation at 485 nm and emission intensity measured through a parallel and perpendicularly polarized 535 nm filter. First, 5 µL of storage buffer was added to each well of the 384-well plates using a Multidrop dispenser (Thermo Fisher Scientific). Next, compounds were added to each well using a pin tool. For wells that were used as negative and positive controls, DMSO was added to the wells in place of compound. Next, 5 µL of ACID at a concentration of 3.4 µM was added to each well using a Multidrop dispenser (Thermo Fisher Scientific). For positive control wells, 5 µL of storage buffer was added. Once protein was added to the wells containing compound, added 10 µL Flo-VP16(465-490) at a concentration of 40 nM, bringing the final volume to 20 µL in each well. Let plates incubate for 30 minutes before reading fluorescence polarization values using Pherastar

microplate reader. The parameters used for reading fluorescence polarization are outlined above. Data was analyzed using MScreen database software.

Substructure search of CCG database and testing of the molecules

Substructure search was performed together with Steven M. Sturlis. In order to identify other molecules that contained the depside or desidone core, structures of either the depside or depsidone core was used as a scaffold to cross-reference in the database. The structures that were used to cross-reference are as noted in Figure 3.13A. This substructure identified an additional 15 molecules that were not tested in the original pilot screen. The 15 molecules that were identified in the substructure search were tested with the 5 molecules containing the depside and depsidone core from the pilot screen. These 20 molecules were tested in a dose dependent fashion using 8 dose points that were prepared by the CCG with the highest final concentration tested at 125 μM. Data was exported to graphpad prism 4.0. Curves and IC_{50}s were generated using the non-linear regression fit for log(inhibitor) vs response. All data points were represented as the mean and standard deviation of conditions run in triplicate.

Competition assay dose response curve with norstictic and psoromic acid

Competition assay was performed by Steven M. Sturlis. All samples were performed in triplicate and assay was read as in direct binding experiments. All assays were incubated for 30 minutes at room temperature before the fluorescence emission was read in a Pherastar microplate reader. All tracer-protein complexes were set at 50% bound and normalized to fraction bound of 1. Tracer-protein complexes tested are as noted in the graph. All tracer-protein complexes were incubated for 30 minuntes at room temperature to reach equilibrium before being added to inhibitor solution. Compounds was serially diluted in storage buffer and subsequent two-fold dilutions were made for the data points that were tested in a volume of 10 μL. After the dose points were plated, 10 μL of the tracer-protein complex was added to each well. Then, incubated plate for 30 minutes at room temperature before reading fluorescence emission on Pherastar microplate reader. The anisotropy data was plotted in graphpad prism software 4.0 and fitted with the

nonlinear regression equation "log(inhibitor) vs. response - variable slope" in order to determine the IC_{50} of the compounds tested.

Direct binding experiments with salt titration

The direct binding experiments were performed as noted above. Assay was performed by Steven M. Sturlis. Storage buffer (dilution buffer) had salt added to the appropriate concentration prior to adding components to 384-well plate. All data points, fitted curves, and resulting K_ds were generated using Graphpad Prism 4.0 software.

Competition assay with norstictic acid and salt titration

Competition assay was performed by Steven M. Sturlis. All samples were performed in triplicate and assay was read as in direct binding experiments. All competition assays were performed as reported above. In order to test for effects of salt titration on inhibition, salt at the indicated concentration was pre-dissolved in storage buffer prior to running the assay.

Mass spectrometry analysis of depsidone covalent adducts

ACID protein was diluted appropriately in storage buffer to a concentration of 10 μM protein. Compound was added to the diluted protein to a concentration equal to 4 equivalents of compound to protein (40 μM). The protein-small molecules complex mixture was incubated for 2 hours at room temperature with gentle shaking using an orbital shaker. After the two hour incubation, performed mass spectroscopy using an Agilent Q-TOF HPLC-MS. The complex mixture was run on a Poroshell 300SB-C8 reverse phase column. A gradient of 5-100% acetonitrile with 0.1% formic acid in water with 0.1% formic was used to purify and analyze the complex mixture. Analysis was performed using Agilent Qualitative Analysis Program. Workflow was configured for "Bioconfirm" and extraction data format was set to use Centroid for chromatogram data and Profile for mass spectral data. Extracted mass spectrometry spectrum had the background subtracted, before deconvoluting spectra using maximum entropy deconvolution using the mass range provided.

Mass spectrometry of depsidone reduced imine covalent adducts

Sample set-up was performed the same way as noted above for mass spectrometry analysis of depsidone covalent adducts. After 2 hour incubation time, 100 mM solution of freshly prepared sodium borohydride was added to the protein-small molecule mixture to a final concentration of 1 mM sodium borohydride. A hole was made in the top of the tube containing protein, molecule, and sodium borohydride to prevent pressure from building. Let sodium borohydride incubate with protein and small molecule for 1 hour before diluting 5-fold and dialyzing overnight to remove excess salt and molecule from the sample. Mass spectrometry was performed as noted above to determine the presence of the reduced imine and the overall degree of labeling of protein with small molecule.

Mass spectrometry analysis of benzaldehyde covalent adducts

Procedure was repeated as outlined in the procedure for mass spectrometry analysis of depsidone covalent adducts. Instead of depsidones, 4 equivalents of benzaldehyde was added to the protein and left to incubate for 2 hours before performing mass spectrometry analysis.

^{1}H-^{15}N HSQC protein NMR with ACID and norstictic acid

^{15}N-labeled ACID protein was expressed, purified, and concentrated as outlined above. Frozen aliquot of protein was thawed and diluted to the appropriate concentration for the desired signal strength in the ^{1}H-^{15}N HSQC spectra. This concentration was determined in a control experiment with protein (data not shown) at an earlier date. ^{15}N-labeled protein was diluted to a concentration of 30 μM. Then, DMSO (negative control), 3 equivalents of norstictic acid, or 5 equivalents of norstictic acid was added to the ^{15}N-labeled protein. The protein-molecule mixture was incubated for 2 hours at room temperature. At the end of the incubation period, a sample of the complex mixture was submitted for mass spectrometry analysis to confirm covalent adduct formation between the molecule and protein. Sample was immediately submitted for ^{1}H-^{15}N HSQC analysis perform by Felicia Gray (Cierpicki Lab). All protein-molecule samples were prepared so that they could be immediately submitted for ^{1}H-^{15}N HSQC analysis after mass spectrometry confirmation of covalent adduct formation.

Assaying inhibitory effects of norstictic acid and psoromic acid against ATF6α endogenous HSPA5 gene expression

For endogenous gene expression analysis, $1x10^5$ HeLa cells were seeded into a 24-well plate and allowed to adhere overnight. Media was removed and replaced with Opti-Mem media containing vehicle or compound delivered in DMSO (0.5% v/v) at the indicated concentrations. After incubating for 12 h, cells were treated with thapsigargin at a final concentration of 500 nM. After 3 h, the media was removed and total RNA was isolated using RNeasy Plus RNA isolation kits (Qiagen) according to manufacturer's instructions. Each RNA sample was used to synthesize cDNA using iScript cDNA synthesis kits (Bio-Rad). Quantitative real-time PCR (qRT-PCR) reactions were carried out in triplicate in an Applied Biosystems StepPlusOne using SYBR green master mix and primers for human RPL19 (Forward, 5'-ATGTATCACAGCCTGTACCTG-3'; Reverse, 5'-TTCTTGGTCTCTCTTCCTCCTTG-3'), HSPA5 (Forward, 5'- CTGGGTACATTTGATCTGACTGG-3'; Reverse, 5'-CTTACCGACCTTTCGGTGGTCCTACG-3'). RT-qPCR analysis was carried out using the comparative C_T Method ($\Delta\Delta C_T$ Method) as described in chapter 4 to estimate HSPA5 mRNA levels and IL-8 mRNA levels relative to the reference RPL19 mRNA levels.

Wound healing assays performed with norstictic acid and psoromic acid

Wound healing assays were performed as outlined in chapter 2.

RARα luciferase reporter assay

The RARα luciferase reporter containing 3 tandem RARα sites (RARα-luc) was obtained from Addgene. CMV-β-Gal, and pBSSK were generously provided by Dr. Jorge Iñigues-Lluhí (The University of Michigan Pharmacology Department). All cells were maintained in 5% CO_2 at 37°C. HeLa cells were grown in Dulbecco's modified Eagle's medium (DMEM, Invitrogen) supplemented with 10% FBS. For luciferase assays, $4x10^5$ cells were seeded in a 6-well dish and allowed to adhere overnight. The media was removed and cells were transfected in Opti-Mem (Invitrogen) with 1 μg RARα-luc, 200 ng CMV-β-Gal, and 800 ng pBSSK using Lipofectamine 2000 (Life Technologies) according to manufacturer's instructions. After 4.5 h, transfection solution was removed and replaced with DMEM containing 10% FBS. At 24 h after transfection, cells were trypsinized and resuspended in

DMEM supplemented with 10% FBS and seeded into a 96-well plate at a density of $8x10^3$ cells per well. After an additional 16 h, media was removed and replaced with Opti-Mem containing vehicle or NPE (0.1% v/v) as a solution in DMSO co-dosed with retinoic acid (1 μM). After cells incubated with either vehicle or compound and retinoic acid for 16 h, media was removed and cells were lysed with 60 μL of passive lysis buffer. Luciferase and β-Galactosidase activities were determined as previously described. RARα luciferase activity and response curve analysis was performed using GraphPad software.

3.6 Characterization of synthesized compounds

Analytical HPLC chromatogram of purified of Flo-VP16(413-437)

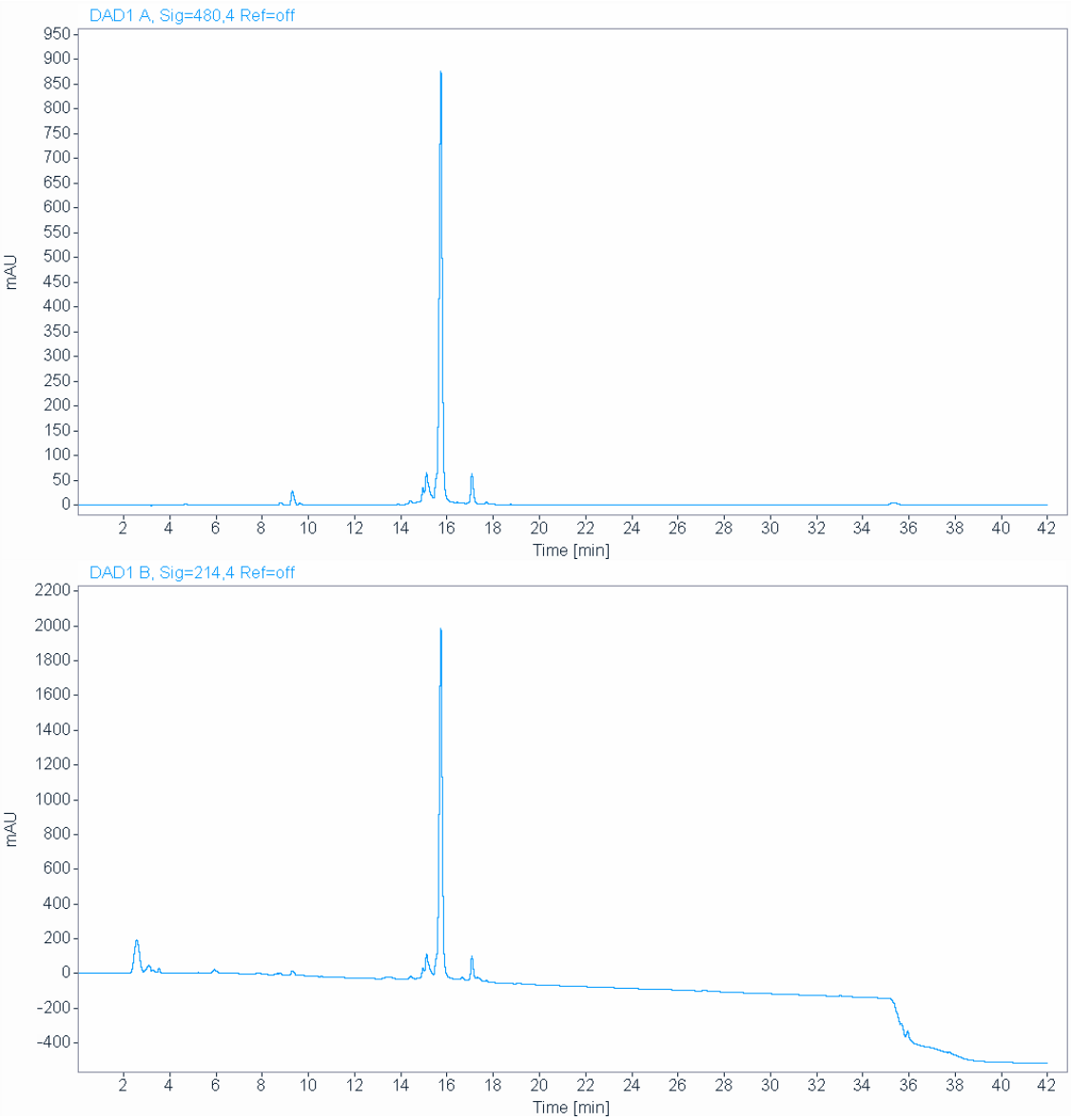

Analytical HPLC chromatogram of purified Flo-VP16(438-464)

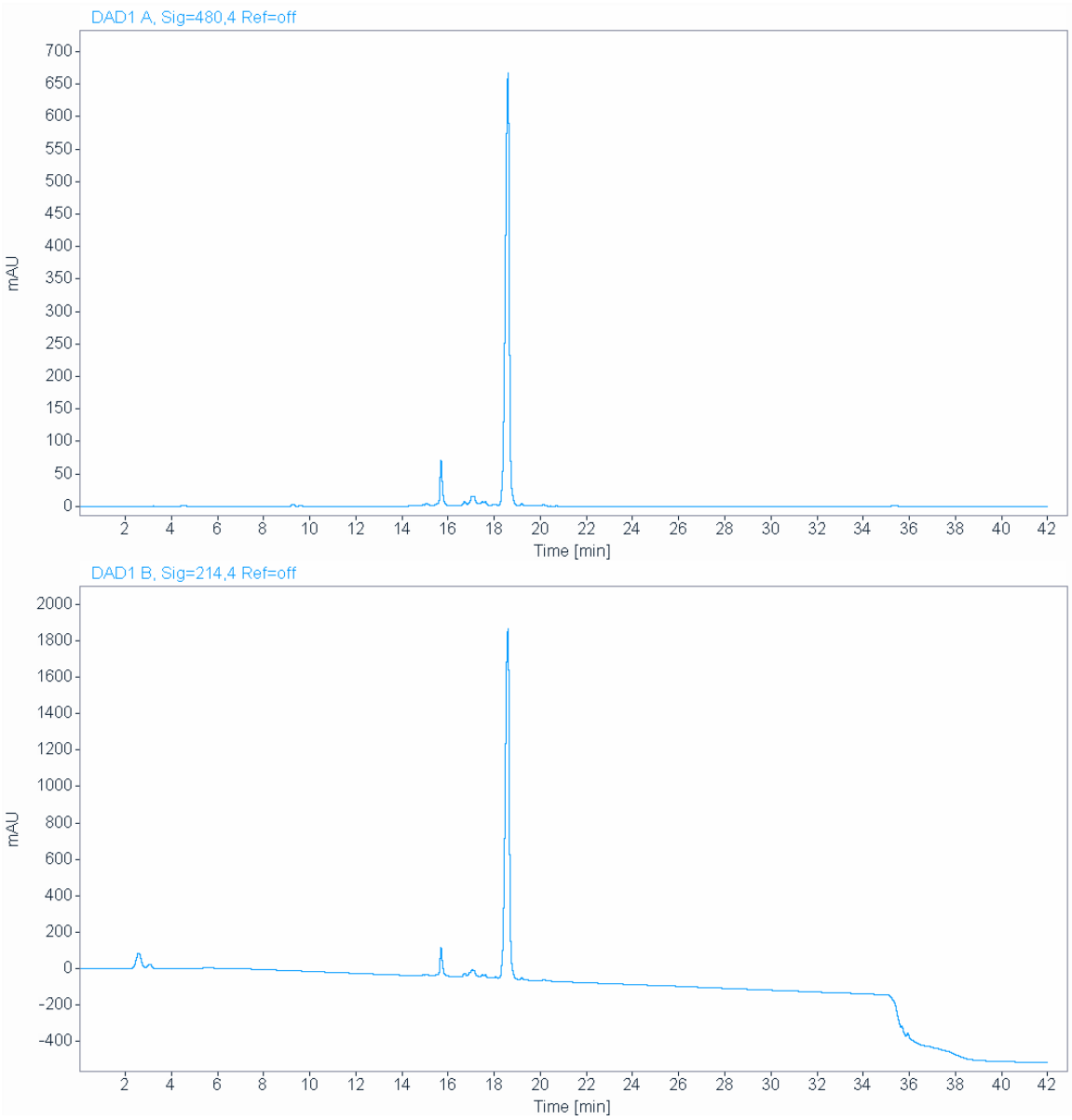

Analytical HPLC chromatogram of purified Flo-VP16(465-490)

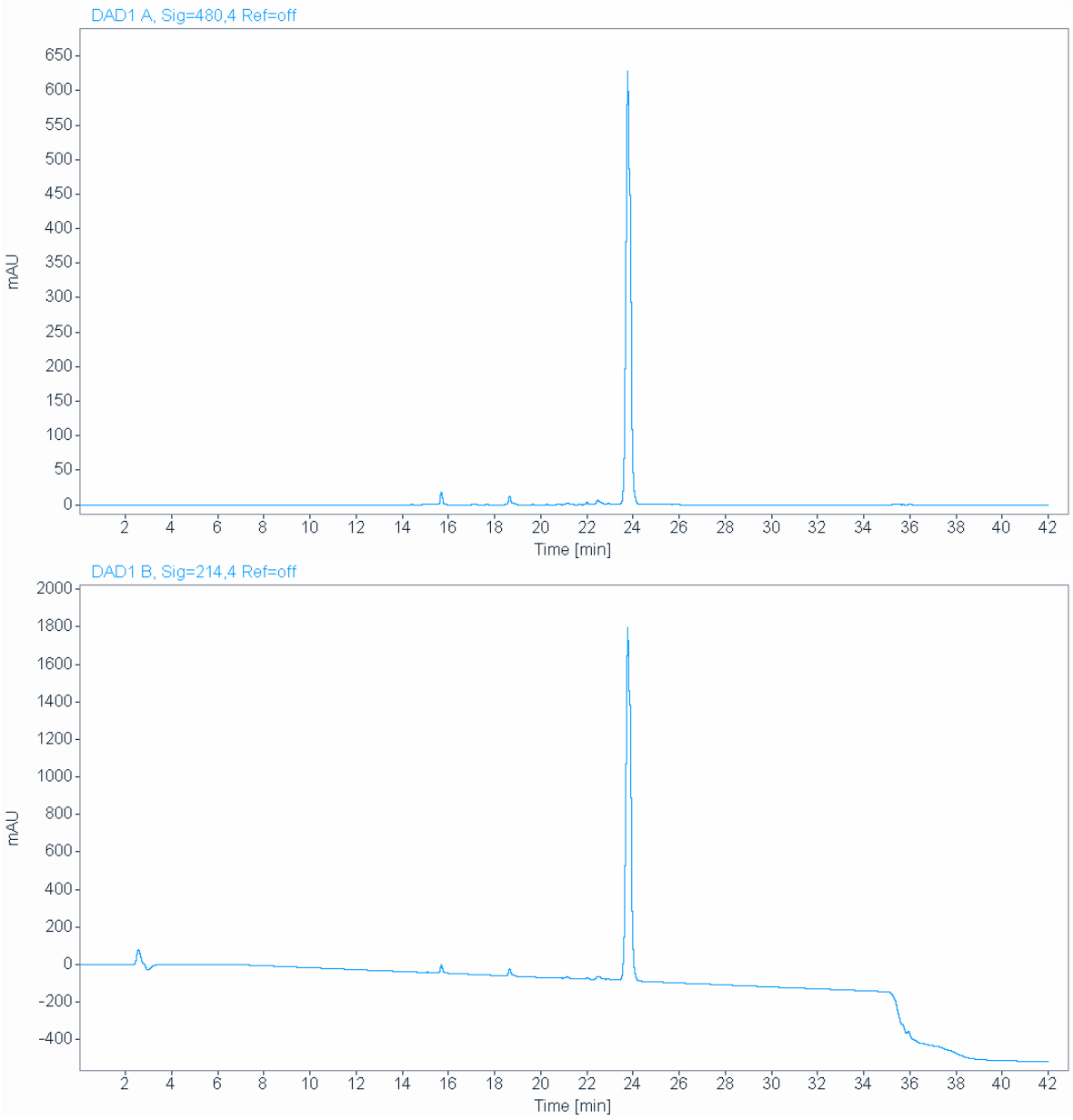

Analytical chromatogram of purified Flo-VP16(438-454)

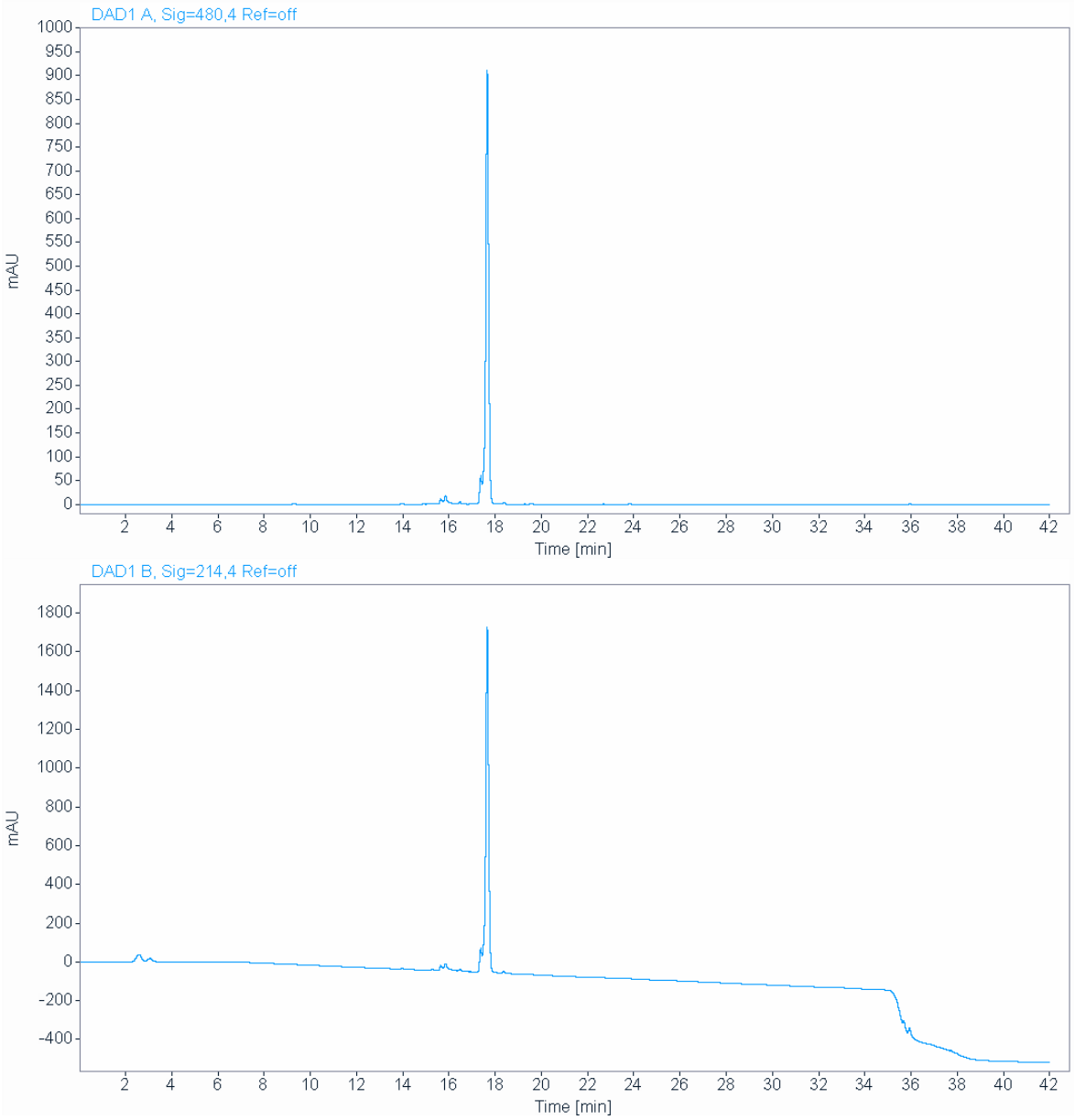

Analytical HPLC chromatogram of purified Flo-VP16(467-488)

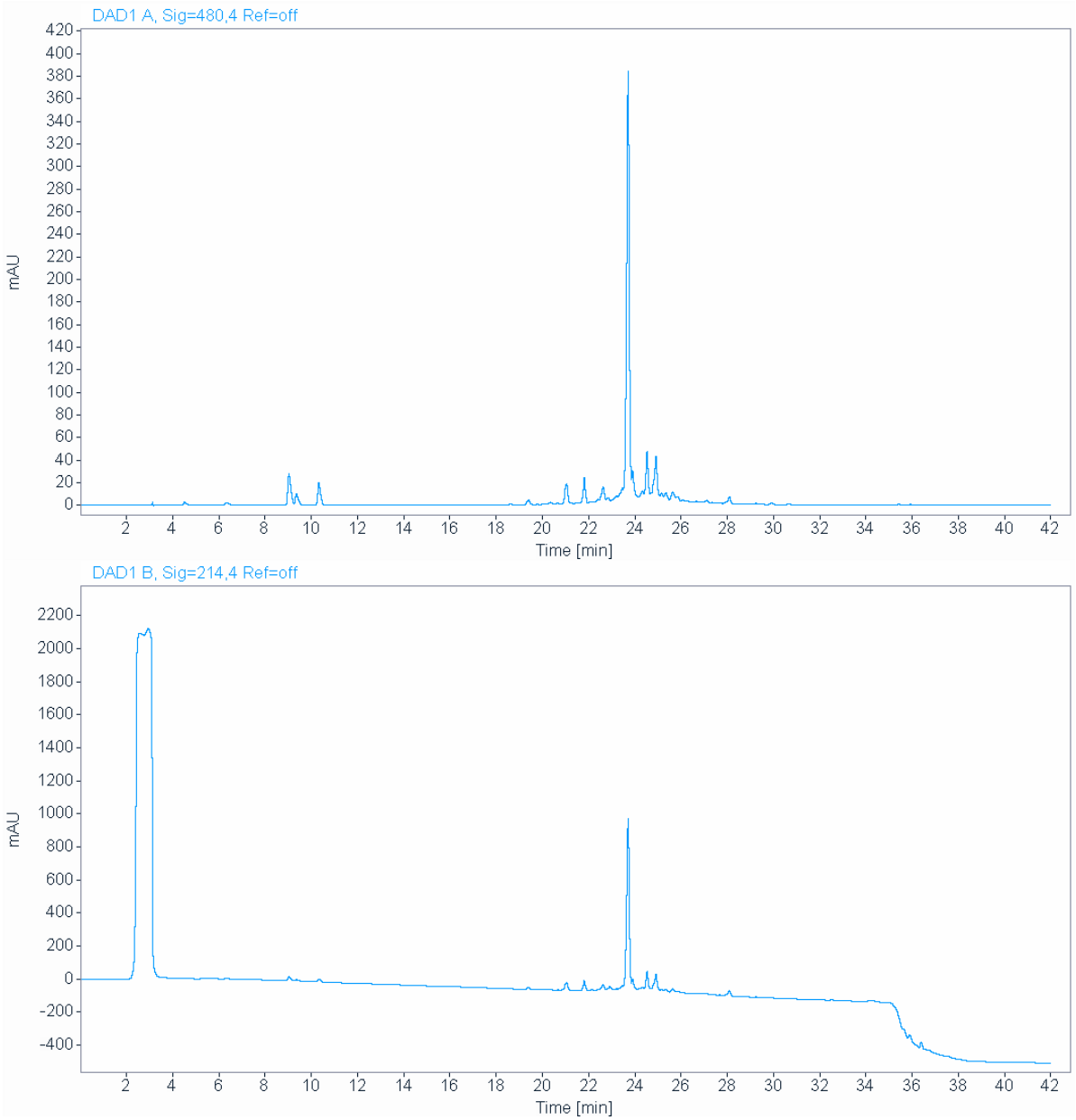

Analytical HPLC chromatogram of purified Flo-ERM(38-72)

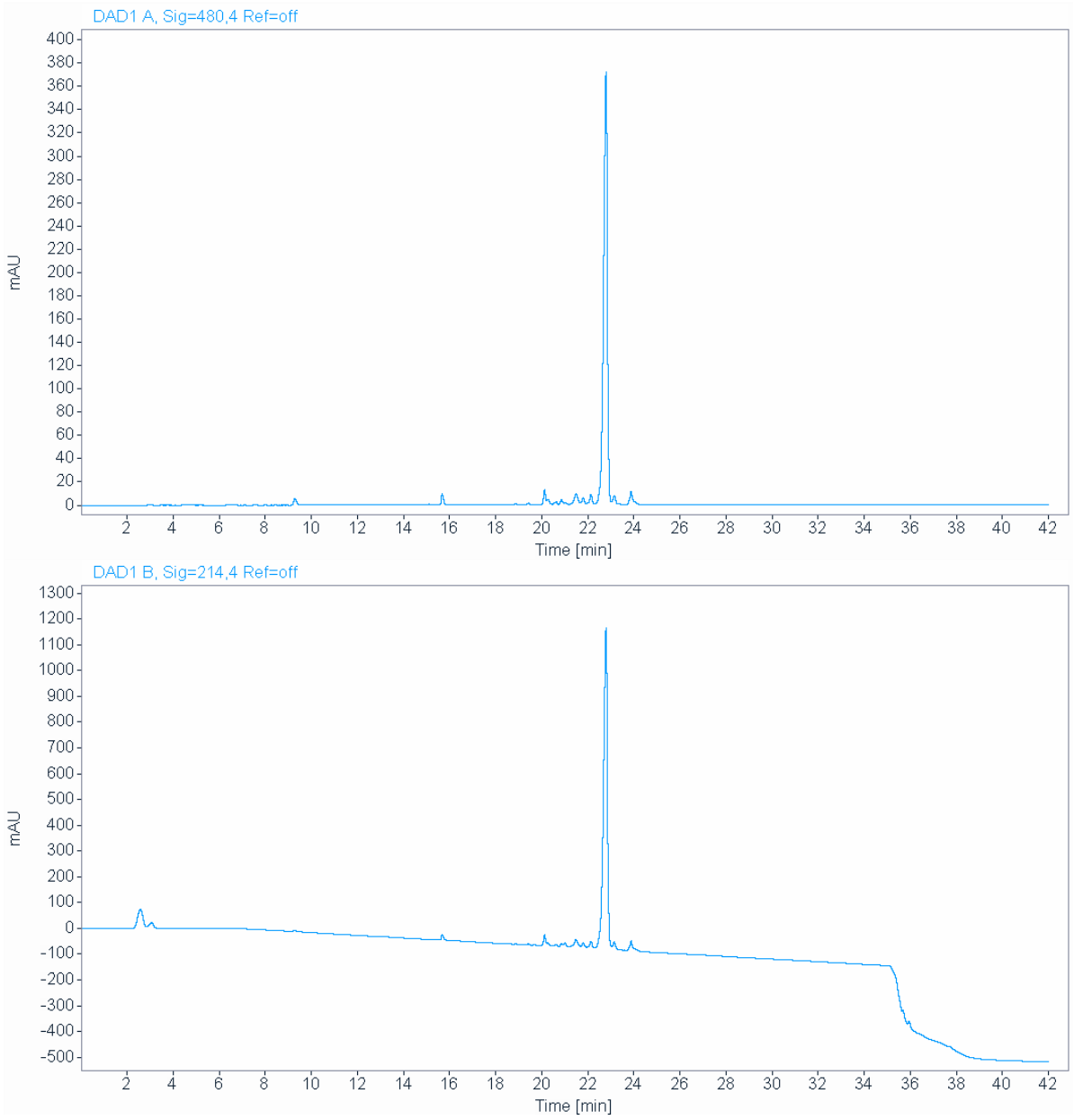

3.7 References

(1) Ptashne, M.; Gann, A. *Genes and Signals*; CSHL Press, 2002.

(2) Conaway, R. C.; Conaway, J. W. Origins and Activity of the Mediator Complex. *Seminars in Cell & Developmental Biology* **2011**, *22*, 729–734.

(3) Vojnic, E.; Mourão, A.; Seizl, M.; Simon, B.; Wenzeck, L.; Larivière, L.; Baumli, S.; Baumgart, K.; Meisterernst, M.; Cramer, P. Structure and VP16 Binding of the Mediator Med25 Activator Interaction Domain. *Nat Struct Mol Biol* **2011**, *18*, 7.

(4) Milbradt, A. G.; Kulkarni, M.; Yi, T.; Takeuchi, K.; Sun, Z. J.; Luna, R. E.; Selenko, P.; Näär, A.; Wagner, G. Structure of the VP16 Transactivator Target in the Mediator. *Nat Struct Mol Biol* **2011**, *18*, 7.

(5) Sela, D.; Conkright, J. J.; Chen, L.; Gilmore, J.; Washburn, M. P.; Florens, L.; Conaway, R. C.; Conaway, J. W. Role for Human Mediator Subunit MED25 in Recruitment of Mediator to Promoters by Endoplasmic Reticulum Stress-Responsive Transcription Factor ATF6α. *Journal of Biological Chemistry* **2013**, *288*, 26179–26187.

(6) Verger, A.; Baert, J.-L.; Verreman, K.; Dewitte, F.; Ferreira, E.; Lens, Z.; de Launoit, Y.; Villeret, V.; Monté, D. The Mediator Complex Subunit MED25 Is Targeted by the N-Terminal Transactivation Domain of the PEA3 Group Members. *Nucleic Acids Research* **2013**, *41*, 4847–4859.

(7) Clucas, J.; Valderrama, F. ERM Proteins in Cancer Progression. *Journal of Cell Science* **2014**, *127*, 267–275.

(8) Ptashne, M. Gene Regulation by Proteins Acting Nearby and at a Distance. *Nature* **1985**, *322*, 697-701

(9) Maniatis, T.; Goodbourn, S.; Fischer, J. A. Regulation of Inducible and Tissue-Specific Gene Expression. *Science* **1987**, *236*, 1237–1245.

(10) Lee, L. W.; Mapp, A. K. Transcriptional Switches: Chemical Approaches to Gene Regulation. *Journal of Biological Chemistry* **2010**, *285*, 11033–11038.

(11) Thompson, A. D.; Dugan, A.; Gestwicki, J. E.; Mapp, A. K. Fine-Tuning Multiprotein Complexes Using Small Molecules. *ACS Chem. Biol.* **2012**, *7*, 1311–1320.

(12) Sela, D.; Chen, L.; Martin-Brown, S.; Washburn, M. P.; Florens, L.; Conaway, J. W.; Conaway, R. C. Endoplasmic Reticulum Stress-Responsive Transcription Factor ATF6α Directs Recruitment of the Mediator of RNA Polymerase II Transcription and Multiple Histone Acetyltransferase Complexes. *Journal of Biological Chemistry* **2012**, *287*, 23035–23045.

(13) Benedit, P.; Paciucci, R.; Thomson, T. M.; Valeri, M.; Nadal, M.; Càceres, C.; de Torres, I.; Estivill, X.; Lozano, J. J.; Morote, J.; Reventós, J. PTOV1, a Novel Protein Overexpressed in Prostate Cancer Containing a New Class of Protein Homology Blocks. *Oncogene* **2001**, *20*, 1455–1464.

(14) Majmudar, C. Y. Sekikaic Acid and Lobaric Acid Target a Dynamic Interface of the Coactivator CBP/P300. *Angewandte Chemie International Edition* **2012**, *51*, 11258–11262.

(15) Conaway, R. C.; Conaway, J. W. Function and Regulation of the Mediator Complex. *Current Opinion in Genetics & Development* **2011**, *21*, 225–230.

(16) Malik, S.; Roeder, R. G. Dynamic Regulation of Pol II Transcription by the Mammalian Mediator Complex. *Trends in Biochemical Sciences* **2005**, *30*, 256–263.

(17) Boube, M.; Joulia, L.; Cribbs, D. L.; Bourbon, H.-M. Evidence for a Mediator of RNA Polymerase II Transcriptional Regulation Conserved From Yeast to Man. *Cell* **2002**, *110*, 143–151.

(18) Bourbon, H.-M. Comparative Genomics Supports a Deep Evolutionary Origin for the Large, Four-Module Transcriptional Mediator Complex. *Nucleic Acids Research* **2008**, *36*, 3993–4008.

(19) Lewis, B. A.; Reinberg, D. The Mediator Coactivator Complex: Functional and Physical Roles in Transcriptional Regulation. *Journal of Cell Science* **2003**, *116*, 3667–3675.

(20) Yudkovsky, N.; Ranish, J. A.; Hahn, S. A Transcription Reinitiation Intermediate That Is Stabilized by Activator. *Nature* **2000**, *408*, 225–229.

(21) Wang, W.; Huang, L.; Huang, Y.; Yin, J.-W.; Berk, A. J.; Friedman, J. M.; Wang, G. Mediator MED23 Links Insulin Signaling to the Adipogenesis Transcription Cascade. *Dev. Cell* **2009**, *16*, 764–771.

(22) Asada, S.; Choi, Y.; Yamada, M.; Wang, S.-C.; Hung, M.-C.; Qin, J.; Uesugi, M. External Control of Her2 Expression and Cancer Cell Growth by Targeting a Ras-Linked Coactivator. *Proc Natl Acad Sci USA* **2002**, *99*, 12747–12752.

(23) Mo, X.; Kowenz-Leutz, E.; Xu, H.; Leutz, A. Ras Induces Mediator Complex Exchange on C/EBPβ. *Mol Cell* **2004**, *13*, 241–250.

(24) Lee, H.-K.; Park, U.-H.; Kim, E.-J.; Um, S.-J. MED25 Is Distinct From TRAP220/MED1 in Cooperating with CBP for Retinoid Receptor Activation. *EMBO J* **2007**, *26*, 3545–3557.

(25) Shi, Z.; Yang, W.; Goldstein, J. A.; Zhang, S.-Y. Med25 Is Required for Estrogen Receptor Alpha (ERα)-Mediated Regulation of Human CYP2C9 Expression. *Biochem. Pharmacol.* **2014**, *90*, 425–431.

(26) Tomomori-Sato, C.; Sato, S.; Parmely, T. J.; Banks, C. A. S.; Sorokina, I.; Florens, L.; Zybailov, B.; Washburn, M. P.; Brower, C. S.; Conaway, R. C.; Conaway, J. W. A Mammalian Mediator Subunit That Shares Properties with Saccharomyces Cerevisiae Mediator Subunit Cse2. *J Biol Chem* **2004**, *279*, 5846–5851.

(27) Yang, F.; DeBeaumont, R.; Zhou, S.; Näär, A. M. The Activator-Recruited Cofactor/Mediator Coactivator Subunit ARC92 Is a Functionally Important Target of the VP16 Transcriptional Activator. *Proc Natl Acad Sci USA* **2004**, *101*, 2339–2344.

(28) Youn, H.-S.; Park, U.-H.; Kim, E.-J.; Um, S.-J. PTOV1 Antagonizes MED25 in RAR Transcriptional Activation. *Biochem. Biophys. Res. Commun.* **2011**, *404*, 239–244.

(29) Zor, T.; De Guzman, R. N.; Dyson, H. J.; Wright, P. E. Solution Structure of the KIX Domain of CBP Bound to the Transactivation Domain of C-Myb. *J. Mol. Biol.* **2004**, *337*, 521–534.

(30) Freedman, S. J.; Sun, Z.-Y. J.; Kung, A. L.; France, D. S.; Wagner, G.; Eck, M. J. Structural Basis for Negative Regulation of Hypoxia-Inducible Factor-1alpha by CITED2. *Nat. Struct. Biol.* **2003**, *10*, 504–512.

(31) Vollmuth, F.; Geyer, M. Interaction of Propionylated and Butyrylated Histone H3 Lysine Marks with Brd4 Bromodomains. *Angew. Chem. Int. Ed. Engl.* **2010**, *49*, 6768–6772.

(32) Demarest, S. J.; Martinez-Yamout, M.; Chung, J.; Chen, H. Mutual Synergistic Folding in Recruitment of CBP/P300 by P160 Nuclear Receptor Coactivators. *Nature* **2002**, *415*, 449-453.

(33) Näär, A. M.; Beaurang, P. A.; Zhou, S.; Abraham, S.; Solomon, W.; Tjian, R. Composite Co-Activator ARC Mediates Chromatin-Directed Transcriptional Activation. *Nature* **1999**, *398*, 828–832.

(34) Welsch, M. E.; Snyder, S. A.; Stockwell, B. R. Privileged Scaffolds for Library Design and Drug Discovery. *Curr Opin Chem Biol* **2010**, *14*, 347–361.

(35) Hendrik R A Jonker; Rainer W Wechselberger; Rolf Boelens; Gert E Folkers, A.; Kaptein, R. Structural Properties of the Promiscuous VP16 Activation Domain†. *Biochemistry* **2004**, *44*, 827-839

(36) Uesugi, M.; Nyanguile, O.; Lu, H.; Levine, A. J.; Verdine, G. L. Induced Alpha Helix in the VP16 Activation Domain Upon Binding to a Human TAF. *Science* **1997**, *277*, 1310–1313.

(37) Jochim, A. L.; Arora, P. S. Assessment of Helical Interfaces in Protein-Protein Interactions. *Mol Biosyst* **2009**, *5*, 924–926.

(38) Chung, T.; Oldenburg, K. R. A Simple Statistical Parameter for Use in Evaluation and Validation of High Throughput Screening Assays. *J Biomol Screen* **1999**, *4*, 67-73.

(39) Valant, C.; Sexton, P. M. Orthosteric/Allosteric Bitopic Ligands. *Molecular Interventions* **2009**, *9*, 125-135.

(40) Valant, C.; Gregory, K. J.; Hall, N. E.; Scammells, P. J.; Lew, M. J.; Sexton, P. M.; Christopoulos, A. A Novel Mechanism of G Protein-Coupled Receptor Functional Selectivity. Muscarinic Partial Agonist McN-a-343 as a Bitopic Orthosteric/Allosteric Ligand. *J Biol Chem* **2008**, *283*, 29312–29321.

(41) Zhong, H.; Voll, R. E.; Ghosh, S. Phosphorylation of NF-Kappa B P65 by PKA Stimulates Transcriptional Activity by Promoting a Novel Bivalent Interaction with the Coactivator CBP/P300. *Mol Cell* **1998**, *1*, 661–671.

(42) Lee, C. W.; Ferreon, J. C.; Ferreon, A. C. M.; Arai, M.; Wright, P. E. Graded Enhancement of P53 Binding to CREB-Binding Protein (CBP) by Multisite Phosphorylation. *Proc Natl Acad Sci USA* **2010**, *107*, 19290–19295.

(43) Ernst, P.; Wang, J.; Huang, M.; Goodman, R. H.; Korsmeyer, S. J. MLL and CREB Bind Cooperatively to the Nuclear Coactivator CREB-Binding Protein. *Molecular and Cellular Biology* **2001**, *21*, 2249–2258.

(44) Shammas, S. L.; Travis, A. J.; Clarke, J. Remarkably Fast Coupled Folding and Binding of the Intrinsically Disordered Transactivation Domain of cMyb to CBP KIX. *J Phys Chem B* **2013**, *117*, 13346–13356.

(45) Radhakrishnan, I.; Pérez-Alvarado, G. C.; Parker, D.; Dyson, H. J.; Montminy, M. R.; Wright, P. E. Solution Structure of the KIX Domain of CBP Bound to the Transactivation Domain of CREB: a Model for Activator:Coactivator Interactions. *Cell* **1997**, *91*, 741–752.

(46) Brüschweiler, S.; Konrat, R.; Tollinger, M. Allosteric Communication in the KIX Domain Proceeds Through Dynamic Repacking of the Hydrophobic Core. *ACS Chem. Biol.* **2013**, *8*, 1600–1610.

(47) Brüschweiler, S.; Schanda, P.; Kloiber, K.; Brutscher, B.; Kontaxis, G.; Konrat, R.; Tollinger, M. Direct Observation of the Dynamic Process Underlying Allosteric Signal Transmission. *J. Am. Chem. Soc.* **2009**, *131*, 3063–3068.

(48) Wang, N.; Lodge, J. M.; Fierke, C. A.; Mapp, A. K. Dissecting Allosteric Effects of Activator-Coactivator Complexes Using a Covalent Small Molecule Ligand. *Proc Natl Acad Sci USA* **2014**, *111*, 12061–12066.

(49) Majmudar, C. Y.; Wang, B.; Lum, J. K.; Håkansson, K.; Mapp, A. K. A High-Resolution Interaction Map of Three Transcriptional Activation Domains with a Key Coactivator From Photo-Cross-Linking and Multiplexed Mass Spectrometry. *Angew. Chem. Int. Ed. Engl.* **2009**, *48*, 7021–7024.

(50) Lum, J. K.; Majmudar, C. Y.; Ansari, A. Z.; Mapp, A. K. Converting Inactive Peptides Into Potent Transcriptional Activators. *ACS Chem. Biol.* **2006**, *1*, 639–643.

(51) Majmudar, C. Y.; Lee, L. W.; Lancia, J. K.; Nwokoye, A.; Wang, Q.; Wands, A. M.; Wang, L.; Mapp, A. K. Impact of Nonnatural Amino Acid Mutagenesis on the in Vivo Function and Binding Modes of a Transcriptional Activator. *J. Am. Chem. Soc.* **2009**, *131*, 14240–14242.

(52) Aguilar, X.; Blomberg, J.; Brännström, K.; Olofsson, A.; Schleucher, J.; Björklund, S. Interaction Studies of the Human and Arabidopsis Thaliana Med25-ACID Proteins with the Herpes Simplex Virus VP16- and Plant-Specific Dreb2a Transcription Factors. *PLoS ONE* **2014**, *9*, 1-8.

(53) McMillen, D. A.; Volwerk, J. J.; Ohishi, J.; Erion, M.; Keana, J. F.; Jost, P. C.; Griffith, O. H. Identifying Regions of Membrane Proteins in Contact with Phospholipid Head Groups: Covalent Attachment of a New Class of Aldehyde Lipid Labels to Cytochrome C Oxidase. *Biochemistry* **1986**, *25*, 182–193.

(54) Takeuchi, S.; Nakagawa, K.; Hayase, E. Interaction of Benzaldehyde to the Membrane Protein of Escherichia Coli. *Agricultural and Biological Chemistry* **1979**, *4*, 1775-1777.

(55) Jentoft, J. E.; Dearborn, D. G.; Gerken, T. A.; Jentoft, N. Detection of Intramolecular Interactions of Lysyl and N-Terminal Amino Groups of Reductively Methylated Proteins by C Nuclear Magnetic Resonance. *Biophys. J.* **1980**, *32*, 97–99.

(56) Jentoft, N.; Dearborn, D. G. Labeling of Proteins by Reductive Methylation Using Sodium Cyanoborohydride. *J Biol Chem* **1979**, *254*, 4359–4365.

(57) Lin, J. C.; Barua, B.; Andersen, N. H. The Helical Alanine Controversy: an (Ala)6 Insertion Dramatically Increases Helicity. *J. Am. Chem. Soc.* **2004**, *126*, 13679–13684.

(58) Triezenberg, S. J.; Kingsbury, R. C.; McKnight, S. L. Functional Dissection of VP16, the Trans-Activator of Herpes Simplex Virus Immediate Early Gene Expression. *Genes & Development* **1988**, *2*, 718–729.

(59) Greaves, R.; Goding, C. R.; O'Hare, P. The C-Terminal 79 Amino Acids of the Herpes Simplex Virus Regulatory Protein, Vmw65, Efficiently Activate Transcription in Yeast and Mammalian Cells in Chimeric DNA-binding protein. *EMBO J* **1989**, *8*, 2337-2342.

(60) Sadowski, I.; Ma, J.; Triezenberg, S.; Ptashne, M. GAL4-VP16 Is an Unusually Potent Transcriptional Activator. *Nature* **1988**, *335*, 563-564.

(61) Thuerauf, D. J.; Morrison, L. E.; Hoover, H.; Glembotski, C. C. Coordination of ATF6-Mediated Transcription and ATF6 Degradation by a Domain That Is Shared with the Viral Transcription Factor, VP16. *J Biol Chem* **2002**, *277*, 20734–20739.

(62) Boire, A.; Covic, L.; Agarwal, A.; Jacques, S.; Sherifi, S.; Kuliopulos, A. PAR1 Is a Matrix Metalloprotease-1 Receptor That Promotes Invasion and Tumorigenesis of Breast Cancer Cells. *Cell* **2005**, *120*, 303–313.

(63) Torchia, J.; Rose, D. W.; Inostroza, J.; Kamei, Y.; Westin, S.; Glass, C. K.; Rosenfeld, M. G. The Transcriptional Co-Activator P/CIP Binds CBP and Mediates Nuclear-Receptor Function. *Nature* **1997**, *387*, 677–684.

(64) Kamei, Y.; Xu, L.; Heinzel, T.; Torchia, J.; Kurokawa, R.; Gloss, B.; Lin, S.-C.; Heyman, R. A.; Rose, D. W.; Glass, C. K.; Rosenfeld, M. G. A CBP Integrator Complex Mediates Transcriptional Activation and AP-1 Inhibition by Nuclear Receptors. *Cell* **1996**, *85*, 403–414.

(65) Kawasaki, H.; Eckner, R.; Yao, T.-P.; Taira, K.; Chiu, R.; Livingston, D. M.; Yokoyama, K. K. Distinct Roles of the Co-Activators P300 and CBP in Retinoic-Acid-Induced F9-Cell Differentiation. *Nature* **1998**, *393*, 284–289.

(66) Firlej, V.; Ladam, F.; Brysbaert, G.; Dumont, P.; Fuks, F.; de Launoit, Y.; Benecke, A.; Chotteau-Lelievre, A. Reduced Tumorigenesis in Mouse Mammary Cancer Cells Following Inhibition of Pea3- or Erm-Dependent Transcription. *Journal of Cell Science* **2008**, *121*, 3393–3402.

(67) Ding, L.; Ellis, M. J.; Li, S.; Larson, D. E.; Chen, K.; Wallis, J. W. Genome Remodelling in a Basal-Like Breast Cancer Metastasis and Xenograft. *Nature* **2010**, *464*, 995-1005.

(68) Thadhani, V. M.; Choudhary, M. I.; Khan, S.; Karunaratne, V. Antimicrobial and Toxicological Activities of Some Depsides and Depsidones. *Nat Prod Res* **2012**, *25*, 1827-1837.

(69) Wang, N.; Majmudar, C. Y.; Pomerantz, W. C. Ordering a Dynamic Protein via a Small-Molecule Stabilizer. *J Am Chem Soc* **2013**, *135*, 3363-3366.

(70) Pomerantz, W. C.; Wang, N.; Lipinski, A. K.; Wang, R.; Cierpicki, T.; Mapp, A. K. Profiling the Dynamic Interfaces of Fluorinated Transcription Complexes for Ligand Discovery and Characterization. *ACS Chem. Biol.* **2012**, *7*, 1345–1350.

(71) Hoffman, L. M.; Garcha, K.; Karamboulas, K.; Cowan, M. F.; Drysdale, L. M.; Horton, W. A.; Underhill, T. M. BMP Action in Skeletogenesis Involves Attenuation of Retinoid Signaling. *J. Cell Biol.* **2006**, *174*, 101–113.

(72) Wands, A. M.; Wang, N.; Lum, J. K.; Hsieh, J.; Fierke, C. A.; Mapp, A. K. Transient-State Kinetic Analysis of Transcriptional Activator·DNA Complexes Interacting with a Key Coactivator. *Journal of Biological Chemistry* **2011**, *286*, 16238–16245.

(73) Majmudar, C. Y.; Labut, A. E.; Mapp, A. K. Tra1 as a Screening Target for Transcriptional Activation Domain Discovery. *Bioorganic & Medicinal Chemistry Letters* **2009**, *19*, 3733–3735.

Chapter 4

Inhibiting the NF-κB IKK Complex Using a Stabilized Peptide

4.1 Abstract

NF-κB is a ubiquitous transcription factor responsible for the expression of genes that regulate numerous processes including inflammation, cell proliferation, and cell differentiation. Additionally, the mis-regulation of NF-κB signaling is often the result of constitutive activation of the NF-κB pathway thus, highlighting the need for inhibitors of NF-κB signaling. A pre-requisite for NF-κB activation requires assembly of the tetrameric complex between the dimer of the NF-κB essential modifier (NEMO, IKKγ) and the c-terminal tails of IKKα/β. The C-termini of IKK α/β are highly conserved and it has been previously demonstrated that a six-amino acid sequence (^{737}LDWSWL^{742}) within IKK α/β is crucial for IKK complex formation. Furthermore, when a cell-permeable peptide is appended to this NEMO binding domain (NBD), only modest inhibition can be achieved (IC_{50} >100 μM), likely due to proteolytic instability. Herein, we describe a peptidomimetic strategy using olefin metathesis on peptides to inhibit NF-κB activity. Through incorporation of two olefins into the NBD sequence, we performed ring-closing metathesis to generate a constrained peptide. This constrained peptide demonstrates greater potency (8-10-fold) and efficacy compared to the unmodified NBD, representing a new strategy for inhibiting the assembly of the IKK complex that has not previously been explored.

4.2 Introduction

Nuclear factor kappa-light-chain-enhancer of activated B cells (NF-κB) is a transcriptional activator that was discovered in the lab of David Baltimore at promoter of the immunoglobulin light-chain enhancer in B cells.[1] NF-κB consists of five family members: RelA(p65), RelB, c-Rel, p50, and p52 (Figure 4.1). All of these family members

contain a Rel homology domain (RHD) that consists of the DNA-binding portion of the protein, the dimerization domain/IκB binding region, and the nuclear localization sequence (NLS). The family members RelA(p65), RelB, and c-Rel contain c-terminal transcriptional activation domains, whereas p50 and p52 do not have c-terminal transcriptional activation domains. This observation suggests that RelA(p65), RelB, and c-Rel effect gene regulation largely through activation while p50 and p52 most likely serve as repression proteins.[2]

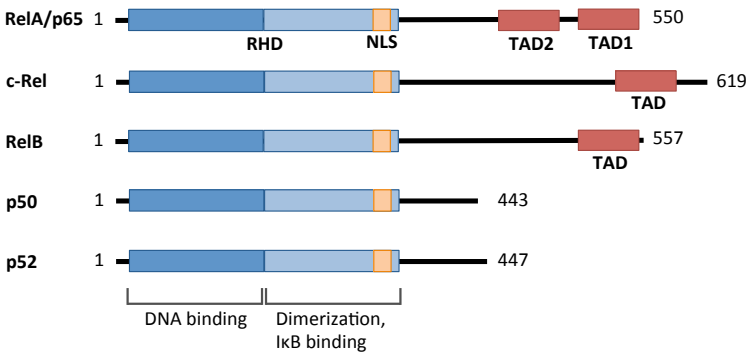

Figure 4.1 NF-κB family members Protein map representation of the individual NF-κB family members. All of the family members contain a Rel homology domain (RHD) that is capable of DNA binding, dimerization with other family members, IκB binding, and an nuclear localization sequence. The RelA, c-Rel, and RelB family members also contain c-terminal transcriptional activation domains.

These family members are capable of both homo- and hetero-dimerization, allowing for gene expression that is dependent on the availability of the individual family member to homo- or hetero-dimerize at the target promoter. This homo- and hetero-dimerization control of gene expression is illustrated in Table 1.1 of Chapter 1. A prerequisite to the homo- and hetero-dimerization of these family members to regulate target genes is activation of the NF-κB pathway, promoting the localization of these family members to the nucleus to effect gene expression. Within the NF-κB activation pathway, there are two major pathways generally known as the canonical activation pathway and the non-canonical activation pathway. In the canonical pathway activation from chemokines, cytokines, or genotoxic stress lead to activation of the inhibitor of κB kinase (IKK) complex. The IKK complex is responsible for phosphorylation of the inhibitor of κB (IκB) which leads to ubiquination and proteosomal degradation, releasing NF-κB homo- and heterodimers to activate target gene expression. In the non-canonical pathway, activation of B-cell activation factor (BAFFR), CD40, or lymphotoxin β-receptor (LTβR) leads to activation of

IKKα by the NF-κB-inducing kinase (NIK). This activation of IKKα leads to phosphorylation of p100 leads to polyubiquination and its subsequent proteosomal processing to p52. The p52-RelB heterodimer can then activate their respective target genes.[3]

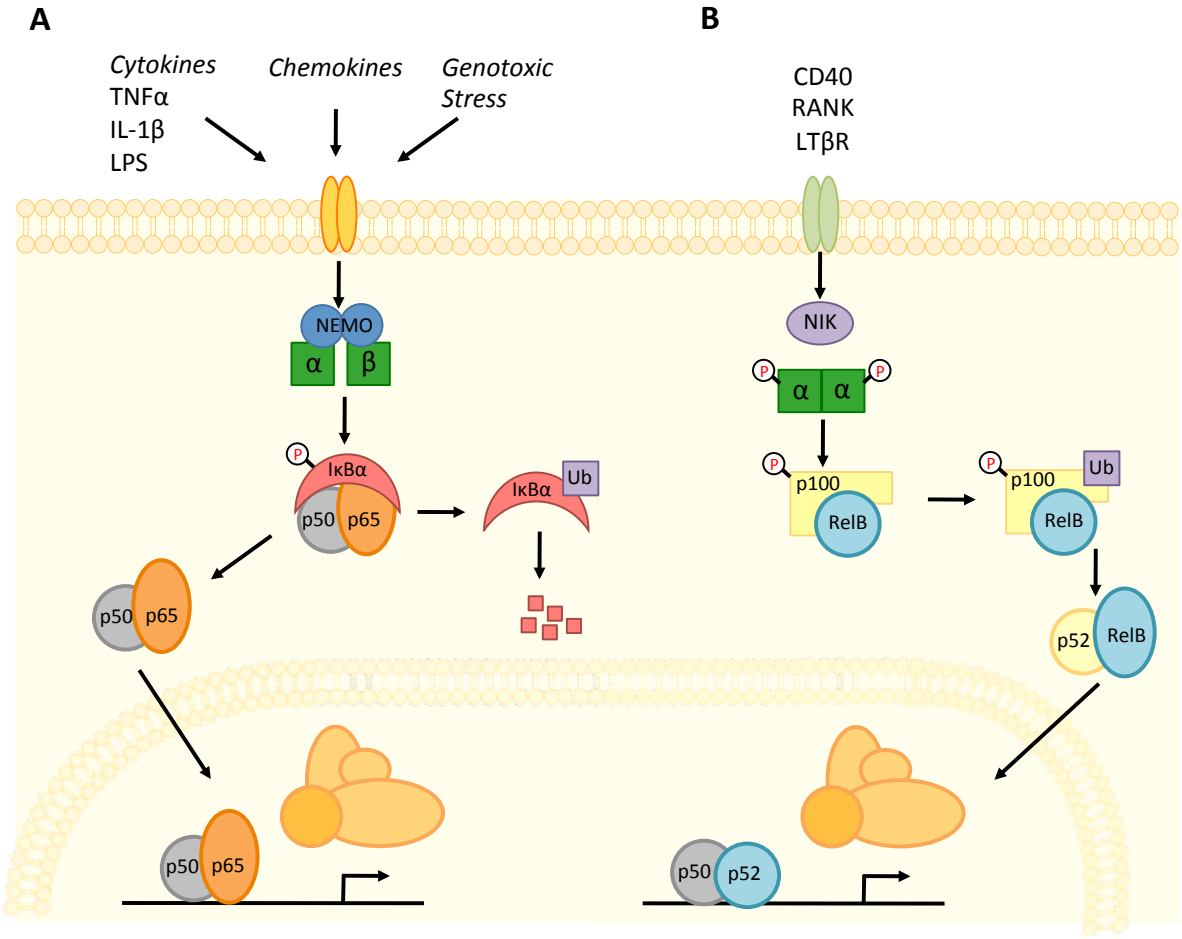

Figure 4.2 The canonical and non-canonical NF-κB activation pathways A) The canonical NF-κB signaling pathway is activated by cytokines, chemokines, and genotoxic stress leading to activation of the IKK complex. This IKK complex phosphorylates IκB, causing the resulting polyubiquination, prompting proteosomal degradation and release of NF-κB homo- and heterodimers to activate their target genes. B) The non-canonical pathway is activated through CD40, receptor activator for nuclear factor kappa B (RANK) and lymphotoxin β-receptor (LTβR) resulting in IKKα activation by NF-κB-inducing kinase (NIK). IKKα goes on to phosphorylate p100, leading to polyubiquination and proteosomal processing to p52. The p52-RelB heterodimers localize to the nucleus and activate their target genes.

There are several types of cancer in which constitutive NF-κB activity is the key driver for both tumor cell survival and growth including breast cancer, colon cancer, prostate cancer, lymphoid cancer. [4-6] For many types of cancers, this constitutive activation is due to the

chronic stimulation of the IKK complex within the canonical pathway, [7-9] highlighting the potential therapeutic potential of targeting parts of the canonical pathway to inhibit IKK acitivity and subsequent NF-κB activation.

The identity of NF-κB has been known for over 25 years and knowledge of the canonical pathway has been documented for well over a decade. In that time, several successful strategies have been employed to target the canonical pathway of NF-κB activation with the most successful endeavors involving development of monoclonal antibodies,[10] kinase inhibitors, [11,12] protease inhibitors,[13] and glucocorticoids.[14] (Figure 4.3).

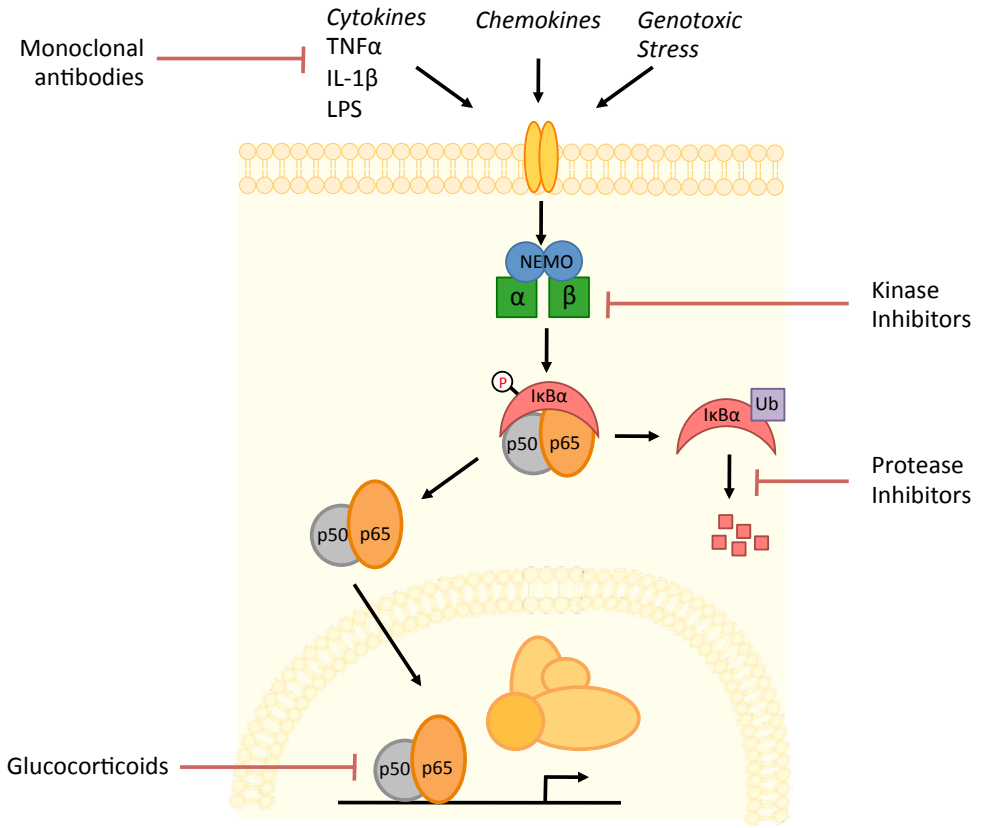

Figure 4.3 Major strategies used to target the canonical activation pathway of NF-κB
The figure above demonstrates the major successful strategies used to target the NF-κB canonical pathway. These strategies have lead to the development of monoclonal antibodies, kinase inhibitors, protease inhibitors, and glucocorticoids.

However, these strategies all have their challenges that limit their utility both as mechanistic tools and as clinical treatment options. As a central regulator, NF-κB has been demonstrated to have significant crosstalk with other pathways.[15] This attribute is

beneficial for fine-tuning the NF-κB activation response through activation of other pathways for the desired response. Because of this crosstalk, NF-κB can exert a great variety of responses compared to more linear signaling pathways. However, the crosstalk with NF-κB and other activation pathways makes it extremely difficult to target the NF-κB activation specifically. For example, several kinase inhibitors have been developed for both IKKα and IKKβ, but their long-term utility has been limited due to their off-target effects against other signaling pathways reliant on the kinase independent activity of IKKα and IKKβ. In the case of IKKα, there are several independent functions of IKKα that are involved in crosstalk with other pathways. IKKα has been demonstrated to regulate cyclin D1 levels,[16] inhibit interferon production through phosphorylation of IRF5/IRF7,[17] as well as upregulate activity of both ERα[18] and β-catenin,[19] all through the independent phosphorylation activity of IKKα. The independent function of IKKβ has been demonstrated to result in cell cycle arrest through phosphorylation of Foxo3a,[20] insulin resistance through IRS-1 phosphorylation,[21] and mast cell degranulation through SNAP23 phosphorylation.[22] Similar independent effects of proteasomes in the NF-κB activation signaling pathway have been reported. The 26S proteasome is very important in the NF-κB signaling pathway including both the proteasomal processing of p102 to p50[23] as well as degradation of IκB,[24] resulting in release of the activated p50-p65 transcriptional heterodimer. The importance of the 26S proteasome pathway for activation of NF-κB would suggest that this pathway is an important possible therapeutic target to inhibit NF-κB activation; however, the 26S proteasome pathway has been implicated in several other pathways such as endoplasmic reticulum (ER) stress, the androgen receptor (AR), and activator protein-1 (AP-1).[25] Therefore, it would seem unlikely that inhibitors of the 26S proteasome would yield NF-κB-specific inhibitors. Monoclonal antibodies also have limited utility in the case of resistance conferred through mutations in the target receptor. [26,27] Furthermore, glucocorticoids have been demonstrated to bind directly to the NF-κB transcriptional activator, inhibiting NF-κB from being able to activate its respective target genes.[28] However, glucocorticoids have obvious off-target effects from their activation of the glucocorticoid receptor (GR) pathway, ultimately limiting their use for any long-term treatment.[29] Based on these observations, it is absolutely critical to identify processes that are specific to the NF-κB pathway when thinking about how to develop new inhibitors of

NF-κB. Given the importance of several of the processes noted above for activation of both the canonical and non-canonical NF-κB pathway as well as the activation of other signaling pathways, identification of signaling events specific to the canonical signaling pathway will be crucial. One possible target that fits the criteria laid out above is the IKK complex of the NF-κB canonical activation pathway.

THE NF-κB IKK COMPLEX

Background

The NF-κB IκB kinase (IKK) complex is a tetramer protein complex specific to the canonical activation pathway of NF-κB. This tetramer is made up of two subunits of the NF-κB Essential Modifer (NEMO/IKKγ), IKKα, and IKKβ. Furthermore, knockdown of NEMO inhibited the activation of the NF-κB activation pathway.[30] Additionally, it was demonstrated with NEMO knockdowns that the NEMO is not required for activation of the non-canonical activation pathway, exhibiting no effects on the independent activity of IKKα. Together, these results demonstrate that NEMO is essential for assembly of the IKK complex required for activation of the canonical NF-κB signaling pathway. Furthermore, these results demonstrate that NEMO is not required for activation of the non-canonical NF-κB signaling pathway and inhibition of NEMO does not affect the independent functions of the IKKα/IKKβ proteins, which are required for several other cellular pathways as highlighted in Section 4.2. These findings suggest that targeting NEMO by either inhibiting NEMO dimerization or inhibiting binding of IKKα and IKKβ to the NEMO dimer, could provide selective inhibitors of canonical NF-κB activation.

Studies to define the structural requirements of the IKK complex were performed by May and coworkers. Using pull-downs with truncated versions of NEMO used as bait along with full length IKKα and IKKβ and conversely, pull-downs with IKKα and IKKβ truncations as bait with full length NEMO, May and coworkers were able to localize the interaction to the N-terminus of NEMO ($NEMO_{44-86}$). Interestingly, May and coworkers found that the IKKα and IKKβ interaction with NEMO could be localized to the same 10 residues ($IKK\alpha/\beta_{735-745}$). Upon further investigation, May and coworkers found that the IKKα/β interaction with NEMO required the same 6-amino acid sequence to interact with NEMO, demonstrating that IKKα and IKKβ share a highly conserved interaction region with NEMO

(Figure 4.4A). This highly conserved sequence was also dependent on the presence of residues D738, W739, and W741 as evidenced by co-IPs with NEMO mutants. Furthermore, when a cell penetrating peptide was appended to this conserved sequence, May and coworkers observed inhibition of HeLa cells transfected with a NF-κB luciferase reporter, suggesting that this sequence was capable of inhibiting the formation of the IKK complex (Figure 4.4B). This peptide loss the ability to inhibit NF-κB luciferase reporter when the critical tryptophans were mutated to alanines, suggesting the importance of the hydrophobic interactions made with these tryptophans and NEMO. [31]

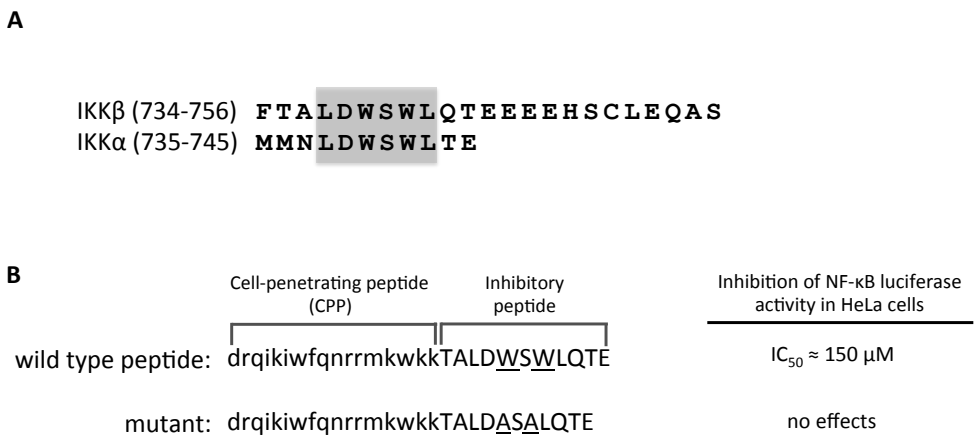

Figure 4.4 Identification of a conserved NEMO interaction domain in IKKα/β and resulting inhibition of this sequence against NF-κB luciferase activity A) The C-terminal sequence of IKKα and IKKβ demonstrated to interact with the N-terminus of NEMO. Gray box identified that conserved residues necessary for IKKα and IKKβ interaction with NEMO. B) A cell penetrating peptide appended to this conserved sequence was able to inhibit NF-κB luciferase activity in HeLa cells. Mutation of the tryptophans to alanines in this conserved sequences resulted in the loss of inhibition.

Perhaps the most exciting result from this initial study of the IKKα/β interaction with NEMO is that IKKα and IKKβ use a conserved 6-amino acid sequence to interact with NEMO. This result suggests that an inhibitor developed against the NEMO-IKK interaction domain would presumably inhibit the formation of the IKK complex with NEMO and both IKKα and IKKβ. Surprisingly, no small molecules have been developed against the NEMO-IKKα/β interaction. Over 50 publications have been published using this peptide inhibitor and more recently, a phase I clinical trial was completed using this peptide[32] against Activated B-Cell (ABC) Diffuse Large B-Cell Lymphoma (DLBCL) in spite of the poor proteolytic stability of peptide inhibitors. This suggests that the utility of an inhibitor

against the NEMO-IKK would be useful both as a mechanistic probe, but also as possible therapeutic agent. We hypothesize that a major contributing factor to the absence of inhibitors against the NEMO-IKK complex is: 1) The general challenges associated with targeting PPIs and 2) the amphipathic characteristics of the IKKα/β interaction sequence ^{737}LDWSWL^{742} may have been hypothesized to be an amphipathic α-helix, which may have derailed previous attempts to find inhibitors such as utilizing small molecule libraries designed for α-helices.

Structural information of the NEMO$_2$-IKKα-IKKβ heterotetramer

More recently, a crystal structure of the minimal NEMO-IKK interaction was reported which illuminated the molecular details of the complex with 2.2 Å resolution. This crystal structure revealed a heterotetramer consisting of a NEMO dimer and two IKK peptides.[33] The heterodimeric complex consists of an elongated and atypical parallel four-helix bundle (Figure 4.5A). The dimer of N-terminal NEMO aligns head-to-head to form a dimerization interface for the IKK peptide. The IKK peptides run along the interface formed by the NEMO dimer. The IKK peptides are also mainly helical, except for the unwound region located between residues 732 and 742 as indicated by the black box in Figure 4.5A. Interestingly, in the unwound region between residues 732 and 742, the backbone is constrained by interactions between side chain tryptophans and the main chain amides. This structural feature is unique to IKK and differentiates the NEMO-IKK 4-helix bundle from other characterized 4-helix bundles such as the SNARE complex, which remain helical throughout the complex.[34] The C-terminus of the IKK peptide is tightly wedged between the two NEMO dimers, forming few hydrogen bonds and interaction mostly through hydrophobic side chains. Interestingly, the three major hydrophobic residues (F or M734, W739, W741) of NEMO interact with the NEMO dimer (Figure 4.5B), causing the IKK backbone to form a unique kinked structure in the IKK peptide stabilized by intramolecular hydrogen bonds between the amide backbone and the conserved tryptophans as well as a hydrogen bond between the D738 and S740, stabilizing this kinked conformation (Figure 4.5C). From these results, it would appear that a region determined critically important for the NEMO-IKK interaction would be unstructured; however, mutation of the two critical

tryptophan to alanine reduced affinity of the IKK peptide by 100-fold, suggesting that this unstructured region serves as a sort of "molecular anchor" for the NEMO-IKK interaction.

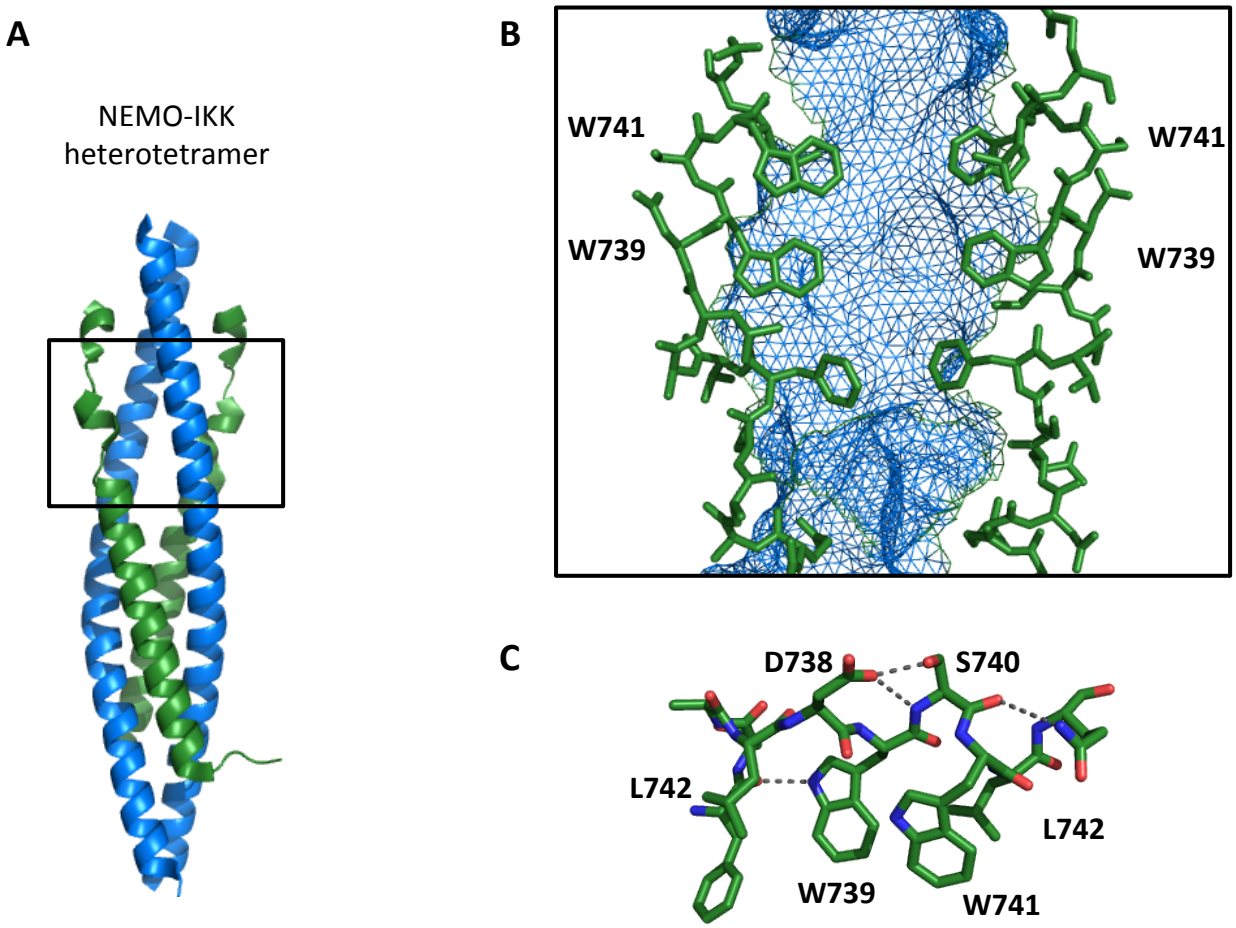

Figure 4.5 The minimal NEMO-IKK heterotetramer A. The crystal structure of the minimal NEMO-IKK interaction, 3BRV. Non-helical structure identified by black box. B. A snapshot of the unstructured region of the NEMO-IKK interaction demonstrating the interaction of the major IKK hydrophobic residues (green) in contact with the NEMO protein surface (blue). These residues are all facing towards the NEMO dimer, creating a kinked formation. C. Demonstrating the key hydrogen bonds stabilizing the kinked formation of IKK with the hydrogen bonding between D738 and S740 playing a major role.

Identifying hot spots in the NEMO-IKK interaction

Based on the data presented thus far, it seems somewhat serendipitous that developing a peptide inhibitor against the NEMO-IKK interaction is possible. The NEMO-binding domain (NBD) peptide lacks overall structure and makes up only a fraction of the residues that interact in the extended 4-helix bundle that makes up the NEMO-IKK interaction. Traditionally, it is thought that extended α-helices often use 3 or more hot spot

residues to bind to their target.[35] These hot spot residues are based on the change in free energy ($\Delta\Delta G_{avg}$) when a residue in a helix is mutated to an alanine, with a cutoff of 2 kcal/mol. A well-known example of an extended helix containing multiple hot spots is p53. It was demonstrated that the p53 interaction with mdm2 is reliant on hot spot residues F19, W23, and L26 making up residues i, i+4, and i+7 of the extended α-helix. This observation would suggest that the IKK extended helix contains multiple hot spot residues. However, Golden and coworkers challenged this notion with an experimental analysis investigating the location of hot spots at the NEMO-IKK interface through a systematic alanine scan of the IKKβ peptide used in the crystal structure noted above.[36] From this data, they were able to determine the specific binding energy of each residue at the NEMO-IKK interface. The results of their study are presented in Figure 4.6.

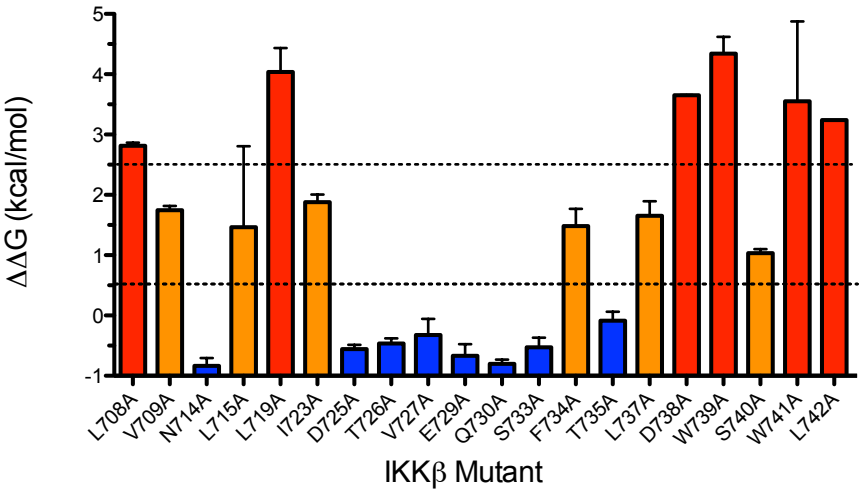

Figure 4.6 Hot spots determined by alanine scanning mutagenesis The histogram above shows the calculated contribution to the NEMO-IKK binding energy for each amino acid. $\Delta\Delta G = -RT\ln(K_{D2(mutant)}/K_{D2(WT)})$ using the K_{D2} values obtained from Golden et al. *J. Am. Chem. Soc* **2013**, *135*, 6242-6256. The horizontal dashed lines represent cutoff thresholds indicating which ΔΔG values are considered to represent strong (red, ΔΔG > 2.5 kcal/mol), moderate (orange, ΔΔG = 0.5-2.5 kcal/mol), and weak (blue, ΔΔG < 0.5 kcal/mol) effects on NEMO binding.

From the studies that Golden and coworkers performed, they found that there were relatively few residues with the extended α-helix that contributed to the overall binding energy of the IKK interaction with NEMO. This is not to say that there were no residues that contributed to the binding energy of the IKK interaction with NEMO. Residue L708 and L719 both crossed the ΔΔG threshold of > 2 kcal/mol to be considered hot spots. [37,38] There

are some additional residues that do contribute > 1 kcal/mol to the over binding energy of the NEMO-IKK interaction, but these values are lower than what is traditionally seen with extended helices such as p53. Interestingly, the IKK residues 737-742 that possess the highly conserved 6-amino acid sequence required for IKKα/β binding to NEMO, contained four residues (D738, W739, W741, and L742) that would be defined as hot spots with the other two residues (L737 and S740) having moderate effects on binding. Together, these results suggest that IKK(737-742) truly serves as a "molecular anchor" for the IKK interaction with NEMO. Additionally, this data provides a rationale for how the NEMO binding domain (NBD) peptide can inhibit the predominantly α-helical NEMO-IKK interaction. Therefore, we hypothesize that developing a stabilized peptidomimetic of the NBD peptide will result in a more potent inhibitor of NF-κB activation.

PEPTIDE STABILIZATION STRATEGY USING OLEFIN METATHESIS

Traditional peptide stabilization strategies using olefin metathesis

Olefin metathesis has gained considerable popularity over the past two decades and more recently, it has been adapted for several biological applications. Some of these other applications that olefin metathesis has been adapted for include: sugars,[39] proteins,[40] antibodies,[41] and peptides.[42] The Grubbs group first demonstrated the utilization of olefin metathesis on a heptapeptide studied by Karle and coworkers that consisted of two repeats of valine-alanine-leucine separated by α-aminoisobutyric acid.[43] Blackwell and coworkers demonstrated that substitution of the i and i+4 residue with an allyl serine derivative could be cyclized using ring closing metathesis facilitated by grubbs catalyst.[44] Additionally, Blackwell and coworkers were able to demonstrate that ring closing metathesis can be utilized to pre-organize α-helices as well as maintain α-helicity better than the unconstrained parent peptide. Traditionally, the olefin metathesis stabilization strategy has been applied to peptides that have intrinsic helicity and adopt greater α-helicity upon binding to the target protein. Over the years, other groups have championed the utility of olefin metathesis to stabilize peptides for use as chemical probes. The Verdine and Walensky groups demonstrated the use of side chain-to-side chain olefin metathesis of L-peptides to synthesize constrained α-helix peptides of p53 and BCL-2. [45,46] From these studies, Verdine and Walensky were able to demonstrate that these constrained,

metathesized α-helices were stable to denaturants and proteases. This increased stability is hypothesized to result from "locking" the peptide in an α-helix, which does not allow these peptides to adopt the extended chain structure favored by proteases. Furthermore, the presence of the hydrocarbon bridge is hypothesized to interfere with the protease from binding to the peptide backbone. The Schepartz group demonstrated that the use of side-to-side chain olefin metathesis of β-peptides could be used to synthesize constrained 14-helices, the helical structure adopted by β-peptides.[47] The Schepartz demonstrated that this strategy could be utilized to reactivate p53. The Arora group demonstrated that the use of side chain-to-backbone olefin metathesis as a hydrogen bond surrogate (HBS) could be used to synthesize constrained α-helix peptides of HIF-1α.[48] In studies with denaturants, they observed similar stabilization of α-helical structure with the metathesized construct compared to the unmodified sequence, further suggesting that olefin metathesis of peptides provides enhanced stability compared to the unmodified sequence.

Applying olefin metathesis to the NEMO-binding domain peptide

The main takeaway point from olefin metathesis with peptides is that olefin metathesis can be utilized to constrain peptides in structurally useful ways and that olefin metathesis can be used as a hydrogen bond surrogate. The highly conserved 6-amino acid sequence in IKKα and IKKβ used to interact with NEMO, also known as the NEMO-binding domain (NBD), utilizes a unique kinked structure in order to interact with NEMO. Furthermore, this NBD is associated with the highest binding energy of the NEMO-IKK interaction, suggesting that targeting this hot spot should inhibit NEMO-IKK complex formation and subsequently, inhibit NF-κB activation. May and coworkers demonstrated that a cell-penetrating peptide appended to the NBD (NBD peptide) was capable of inhibiting NF-κB, suggesting that targeting this hot spot was possible with a peptide. One of the drawbacks of the NBD peptide is that it requires high concentrations for the desired effects (IC_{50} >150 μM), presumably due to proteolytic degradation. Yet, this inhibitor is continually used in new studies and recently in a clinical phase I trial, highlighting the important utility of the NBD peptide both as a mechanistic probe and possible therapeutic agent. Therefore, we sought to determine if an olefin metathesis strategy could be applied to the NBD peptide to synthesize a more potent NF-κB inhibitor. Based on the observation

that D738 and S740 form a critical hydrogen bond that helps organize the NBD in this unique kinked structure, we focused on utilizing olefin metathesis as a hydrogen bond surrogate for this critical hydrogen bond. There have been several olefin amino acid derivatives developed over the years for olefin metathesis of peptide (Figure 4.7).

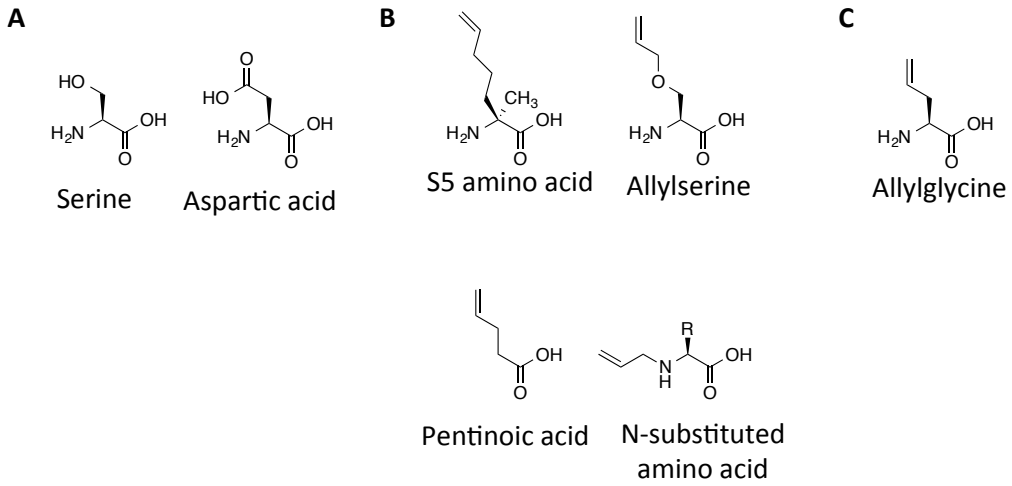

Figure 4.7 Amino acids to facilitate olefin metathesis on peptides A) Serine and aspartic acid amino acid used to make critical H-bond in NBD. B) Amino acid derivatives used to make helical peptide mimics. The S5 amino acid is used by Verdine and Walensky to constrained α-helices, allyserine has been used by Schepartz to make 14-helices with β-peptides, and Arora has made used of pentinoic acid and N-substituted amino acids to make HBS α-helices. C) Allylglycine, the amino acid used to substitute D438 and S740 in the NBD.

Although several amino acid derivatives have been synthesized to facilitate olefin metathesis on peptides, we chose not to use these derivatives to substitute the critical hydrogen bond between D738 and S740. The hydrogen bond between D738 and S740 creates a 13-membered macrocycle and to a lesser degree, D738 can also stabilize the kinked formation of the NBD through a hydrogen bond with the S740 amide nitrogen, forming a 10-membered macrocycle (Figure 4.5C).[36] Utilizing amino acid derivatives that have been previously synthesized (S5 amino acid and allylserine) for carrying out olefin metathesis on the NBD peptide would result in a 15-membered macrocycle due to the longer side chain of the S5 amino acid and allyserine derivative compare to aspartic acid and serine. If pentinoic acid and an N-substituted amino acid were used, similar to the HBS strategy utilized by the Arora group, a 10-membered macrocycle would result and would terminate. For the 15-membered macrocycles, it is possible that this macrocycle would be

too large and would not be able to maintain the kinked NBD structure as well as a smaller macrocycle. In the case of the pentinoic acid and the N-substituted amino acid, the macrocycle would only be the 10-membered macrocycle, meaning that this derivative would only be able to recapitulate one of the possible hydrogen bond stabilized kinked NBD macrocycles. In order to synthesize a constrained NBD peptide that would closely mimic the naturally occurring hydrogen bonded macrocycle, we incorporated an allylglycine residue at the D738 and S740 sites. Olefin metathesis of this construct would result in an 11-membered macrocycle, resulting in a constrained construct that is more similar to native structure (13-membered and 10-membered macrocycle) (Figure 4.8).

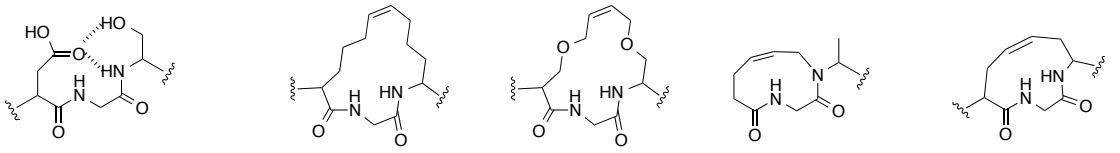

Hydrogen bond between D738 and S740
13-membered macrocycle

Hydrogen bond between D738 and S740 amide
10-membered macrocycle

S5 metathesis
15-membered macrocycle

Allylserine metathesis
15-membered macrocycle

Pentinoic acid and N-subst amino acid
10-membered macrocycle

Allylglycine
12-membered macrocycle

Figure 4.8 Comparing NBD peptide hydrogen bond macrocycles with different olefin metathesis amino acids On the left is the NBD peptide with the resulting macrocycles from the intramolecular hydrogen bonds. Additionally, the other macrocycles that would result from using different olefin metathesis amino acids are presented.

4.3 Results and Discussion

SYNTHESIZING NEMO-BINDING DOMAIN MIMICS

Incorporation of allyglycine into the NEMO-binding domain mimics was accomplished using solid phase peptide synthesis with incorporation of FMOC-allyglycine residue at the D738 and S740 positions. Once incorporation of allyglycine and synthesis of the rest of NEMO-binding domain peptide was completed, olefin metathesis was carried out on resin before continuing synthesis of the peptide to include a cell-penetrating peptide (CPP) (Figure 4.9). There are several CPPs that can be used to get cargo into cells. Some of the most commonly used CPPs include Antennapedia peptide (Antp), the Transactivator of Transcription (TAT) peptide, octaarginine (R_8), and hexaarginine (R_6), and octalysine (K_8) to name a few. Some of these CPPs have been demonstrated to be toxic, which can make

determining inhibitory potential difficult. This is particularly true for the Antp CPP.[49] We chose to use the octalysine (K_8) CPP to be used with our NEMO-binding domain mimics due to its effective transduction effects in fibroblasts and 293T cells.[50] Additionally, the octalysine CPP has also been previously demonstrated to have no toxic effects in cells and is well tolerated in animal models.[49] In order to minimize any effects that the CPP might have on NBD interaction with NEMO, a diglycine spacer was used, a common spacer used for other peptide inhibitors appended with a CPP. [51,52] In order to carryout the olefin metathesis on the NBD mimic, olefin metathesis conditions were developed to facilitate the synthesis of these macrocycles. The 11-membered macrocycle that we need to synthesize is relatively uncommon in terms of olefin macrocycles typically synthesized, and medium macrocycles (8 to 12-membered) can be difficult to cyclize using ring closing metathesis.[53]

A

Constructing the Mimics

#1 KKKKKKKKGGTALDWSWLQTE
#2 YKKKKKKKKGGTALDASALQTE

#3 met KKKKKKKKGGTALGWGWLQTE

#3 no met KKKKKKKKGGTALGWGWLQTE

#4 YKKKKKKKKGGTALGAGALQTE

B

Conditions

Peptide	Catalyst	Solvent	Time (h)	Temperature (°C)	Yield
3	HGII	DCM	12	25	0
4	HGII	DCM	12	25	0
3	HGII	DCM	12	50	0
4	HGII	DCM	12	50	0
3	GII	DCM-DMF-LiCl	65	60	trace
4	GII	DCM-DMF-LiCl	65	60	trace
3	HGII	DCM-DMF-LiCl	µwave, 0.5	100	50
4	HGII	DCM-DMF-LiCl	µwave, 0.5	100	<20

C

#3 met

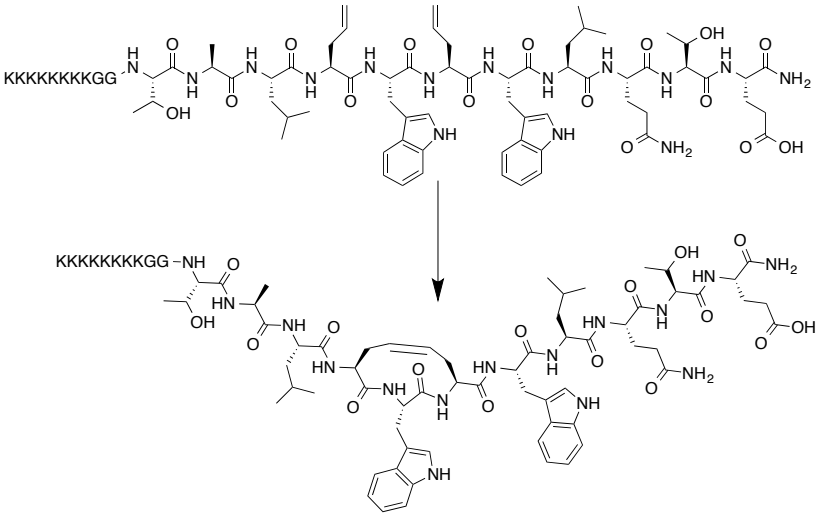

#4 met

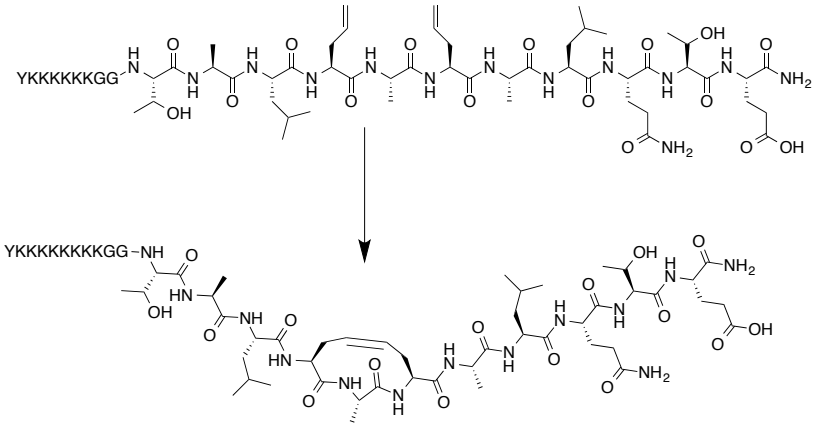

Figure 4.9 Constructing the NBD mimics and optimizing reaction conditions A. Outlining the general model used to make NBD mimics with five different NBD mimics

synthesized to test the effects of olefin metathesis stabilization. B. Initial reaction conditions tested to facilitate ring closing metathesis. C. NBD mimics #3 met and #4 both need to undergo olefin metathesis. Here we demonstrate the #3 met and #4 sequences that need to be metathesized.

In order to work out the reaction conditions needed to facilitate olefin metathesis of NBD mimics, we looked at the effects of catalyst, time, solvent, and temperature on the reaction. Initially, we sought to use conditions optimized by Bird and coworkers for olefin metathesized α-helices that utilized dichloromethane (DCM) and Grubb's 1st generation catalyst carried out at room temperature for 4h.[54] We modified this protocol by utilizing Hoyveda-Grubbs 2nd generation (HGII) catalyst, which has higher turnover cycles than Grubbs 2nd generation (GII) catalyst.[55] Additionally, we also extended the reaction time to 12 hours compared to the reported 4 hours. Unfortunately, we saw no products resulting from metathesis utilizing this protocol. We hypothesize that no reaction occurred due to the greater ring strain associated with our 11-membered macrocycle compared to the olefin metathesized α-helices reported by Bird and coworkers, which result in much larger macrocycles.[54] Next, we sought to determine if increasing the temperature would help facilitate the ring closing metathesis reaction and overcome the transition state required to facilitate the 11-membered macrocycle. We also hypothesized the higher temperature would increase the activity of the HGII catalyst since it requires higher temperatures for initiation.[56] These modifications to the reaction conditions also did not yield any of the desired products. Next, we sought to determine if aggregation was playing a role for the lack of product conversion. In order to investigate the role of aggregation, we performed the metathesis reactions in a 1:1 mixture of DCM and 10% LiCl-DMF, a solution that has been demonstrated to aid with olefin metathesis in aggregation prone reactions.[57] Additionally, we also used GII catalyst with continuous heating since it has been demonstrated that GII has a lower initiation temperature the HGII. We also let the reaction run for extended period time (65h), based on observation of other groups that some bis olefin containing peptide can take as long as 72h for complete conversion.[58] These conditions did produce trace amounts of the desired products, suggesting that we were minimizing aggregation and reaching temperatures necessary to facilitate metathesis. Based on this observation, we chose to try the same reaction conditions, but in a

microwave reactor. By performing the reaction in a microwave reactor, we can benefit from higher temperatures while minimize the safety risk associated with the high pressures generated at high temperatures. We also chose to swap the GII catalyst with HGII catalyst since the high temperatures will be enough to overcome the initiation temperature required by HGII, allowing us to benefit from the higher turnover numbers offered by HGII. With these conditions we were able to achieve 50% conversion of #3 met and a little under 20% conversion for #4. These results demonstrate that we were able to work out reaction conditions for olefin metathesis of the 11-membered NBD mimic peptide. Now, we are able to attain >90% conversion of both #3 met and #4 by performing the ring closing metathesis before adding the CPP using solid phase peptide synthesis. We hypothesize that the dramatically increased yields is due to minimization of aggregation. By performing the ring closing metathesis before adding the CPP, we provide the catalyst greater access to the olefins needed to facilitate the reaction.

STRUCTURAL CHARACTERIZATION OF NEMO-BINDING DOMAIN MIMICS

As noted earlier, all previous examples of utilizing olefin metathesis to synthesize constrained peptides have focused on constraining α-helices. Furthermore, utilizing olefin metathesis to constrain α-helices has been demonstrated to increase helicity compared to the unmodified parent construct. However, we are utilizing olefin metathesis in order to stabilize the kinked NBD peptide. The stabilization of the NBD peptide using olefin metathesis should not adopt α-helical structure and should adopt a kinked, unstructured conformation. For the purpose of circular dichroism, we hypothesize that this kinked, unstructured conformation will produce spectra consistent with random coil structure. We used circular dichroism in order to demonstrate that utilizing olefin metathesis to synthesize our NEMO-binding domain mimics adopts a structure that is not α-helical and is consistent with random coil structure (Figure 4.10).

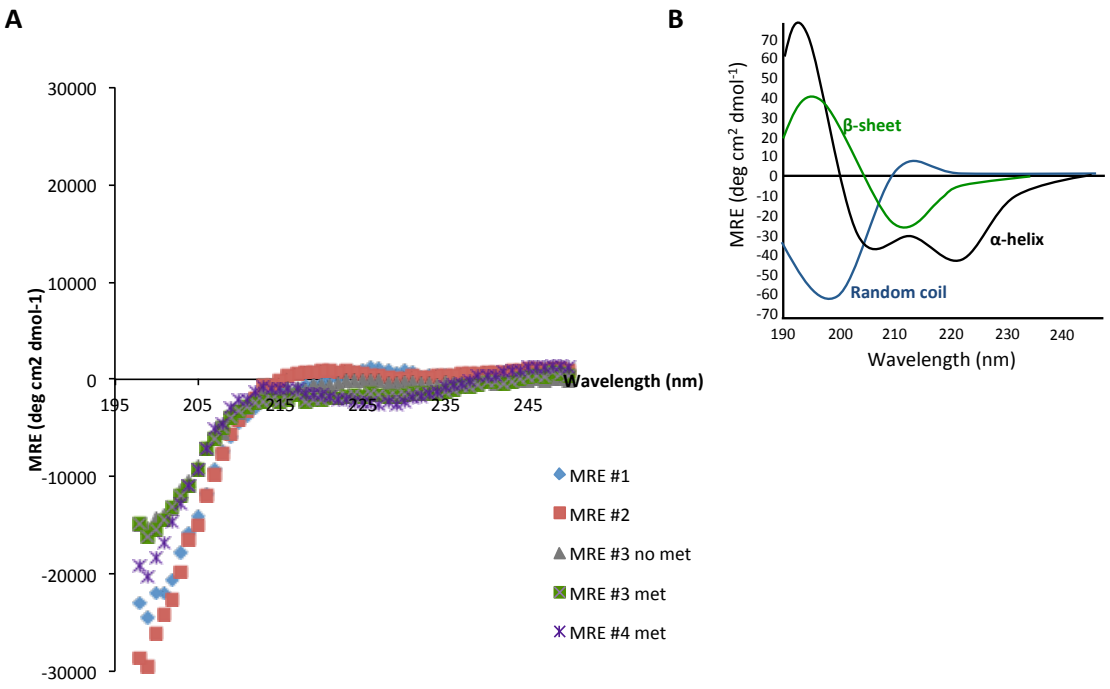

Figure 4.10 Using circular dichroism (CD) to analyze the secondary structure of NEMO-binding domain mimics A. CD spectra of NEMO-binding domain mimics, exhibiting random coil structure, consistent with published crystal structure of the NEMO-IKK interaction. B. Example curves of CD spectra for α-helix, β-sheet, and random coil.

As evidenced in Figure 4.10, we see that the NBD mimics do not exhibit secondary structure consistent with α-helical structure. Furthermore, the NBD mimics exhibit random coil structure as evidenced by the signal minima in between 195-200 nm (Figure 4.10A), consistent with the representative CD spectra of random coil structure depicted in Figure 4.10B. The random coil structure observed with the NBD mimics using circular dichroism is also consistent with the crystal structure of the NEMO-IKK interaction where it was observed that the NBD peptide was bound in a kinked, unstructured conformation.

INVESTIGATING THE PROTEOLYTIC STABILITY OF NEMO-BINDING DOMAIN MIMICS

One of the major challenges to using peptide inhibitors is the susceptibility of peptides to proteolysis.[59] Protein degradation is a natural metabolic process that exists *in vivo*, but also on a cellular level.[60] Proteolysis of peptide inhibitors results in much higher concentrations of peptide inhibitors being required to elicit their effect. This result further translates into more frequent dosing being required for peptide inhibitors. Generally,

proteases recognize peptides that adopt an extended confirmation. Therefore, introducing olefin constraints into peptides that cause them to adopt structures other than the extended structure should confer protection to the peptide against proteolysis. Additionally, the presence of a hydrocarbon bridge will also restrict protease access to some of the peptide bonds. In the case of α-helical constrained peptides synthesized using olefin metathesis, the increased helicity afforded by the introduction of a hydrocarbon bridge inhibits proteolytic degradation by proteases. [54,61] There are several proteases commercially available to assess proteolytic stability, with the selection of the protease based on the composition of the peptide inhibitor. Two common proteases used to assess proteolytic stability of peptides are trypsin, which cleaves after Arg and Lys, and chymotrypsin, which cleaves after Phe, Tyr, Trp, Leu, and Met. In the case of the NBD mimics, chymotrypsin is the best choice for us to determine if using olefin metathesis to constrain the kinked formation of IKK offers any additional proteolytic stability compared to the unmodified peptide. The information that would be obtained from a proteolytic degradation assay using trypsin with the NBD mimics would be limited since the octalysine CPP is appended to the NBD mimic. The constraint introduced into the NBD mimic is not predicted to cause the octalysine CPP to adopt any unique structure and therefore, it should exist in the fully extended state, rendering it susceptible to proteolytic degradation. Alternatively, chymotrypsin would allow us to determine if the olefin constraint introduced using metathesis offers any additional proteolytic stability. It would be predicted that the unmodified NBD would be susceptible to proteolytic degradation since the sequence is naturally unstructured; however, introduction of the olefin constraint in the NBD mimic should pre-organize the NBD in a kinked structure, causing this peptide to be in a conformation other than the extended conformation preferred by proteases. Together, this would suggest that the metathesized NBD-mimic should be more proteolytically stable to chymotrypsin than the unmetathesized version of the unmodified parent compound (Figure 4.11).

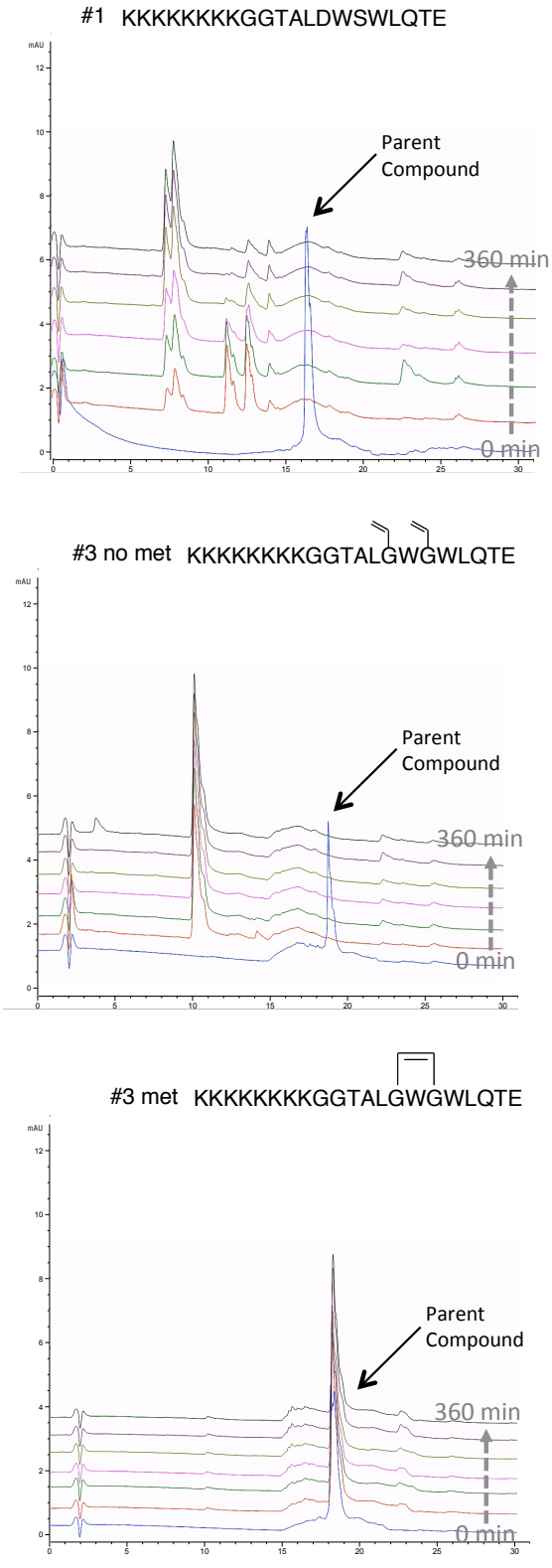

Figure 4.11 Proteolytic stability assay investigating the effects of an olefin constraint on peptide stability All peptide proteasomal stability assays were performed with

chymotrypsin. Time points tested during proteolytic stability assay: 0, 15, 30, 60, 120, 180, and 360 minutes. In the left panel, is the unmodified parent peptide inhibitor time course with chymotrypsin. In the middle pane, is the NBD mimic with the allylglycines incorporated, but no metathesis in time course with chymotrypsin. In the right panel, is the NBD mimic with metathesis in a time course with chymostrypsin

As demonstrated in Figure 4.11 (top panel), we observe immediate degradation of the parent peptide inhibitor with no modification, suggesting that the high IC_{50} observed with the inhibitor is likely due to proteolytic degradation. The unmetathesized NBD mimic with allyglycine incorporated also underwent immediate proteolytic degradation. Interestingly, the immediately degraded parent compound forms some sort of stabilized intermediate as evidenced by the peak at 10 min, with additional degradation products appearing at the later time points (180 and 360 minutes) (Figure 4.11, middle panel). As predicted, the NBD mimic containing the metathesized constraint did not appear to undergo any proteolytic degradation in the presence of chymotrypsin, demonstrating that introducing a metathesized constraint into the NBD does increase the proteolytic stability (Figure 4.11, bottom panel).

INTERACTION OF NEMO-BINDING DOMAIN MIMICS WITH NATIVE NEMO

In order to develop these NEMO-binding domain mimics, we needed to make modifications to the 6-amino acid sequence demonstrated to interact with NEMO, including substitution of D738 and S740. These two residues together accounted for over 4 kcal/mol of the binding energy of the NEMO-IKK interaction, highlighting the importance of these residues in the interaction. It is possible that through substitution of these residues to allyglycine, that we may have lost the ability to interact with native NEMO. In order to test this hypothesis, we created biotin-labeled "bait" peptides containing p-benzoyl phenylalanine (pBpa). This strategy has been used previously to demonstrate interaction of the bait peptide with the target protein. [62,63] We sought to utilize this Bpa containing peptide strategy to demonstrate interaction with native NEMO in cellular lysates. Given the importance of the 6-amino acid NBD, the residue chosen to substitute with pBpa needed to be carefully chosen so as not to inhibit the interaction with NEMO. It was demonstrated by May and coworkers that there were specific tolerances of the W739 and W741 residues to accommodate mutations in the NBD.[64] The W741 could only be mutated to a Phe and still

maintain interaction with NEMO, but mutation to Tyr or Leu abolished the interaction, suggesting that this residue is highly sensitive to mutation. Residue W739 could be mutated to Phe, Tyr, and Leu while still maintaining the interaction with NEMO, suggesting that the W739 residue is more tolerable to mutations than W741. Therefore, we incorporated Bpa at residue W739 to investigate the interaction of these "bait" peptides with NEMO. By utilizing Bpa-containing "bait" peptides, we can covalently capture protein interaction partners by irradiating the "bait" peptide with UV light, inducing radical formation and covalent bond formation with the interaction partner (Figure 4.12B). These complexes can then be pulled down using the biotin tag and probed for the target protein to demonstrate engagement of the "bait" with the target protein. The two "bait" peptides made to demonstrate interaction with NEMO in cellular lysates were construct #1 and #2 (Figure 4.12A).

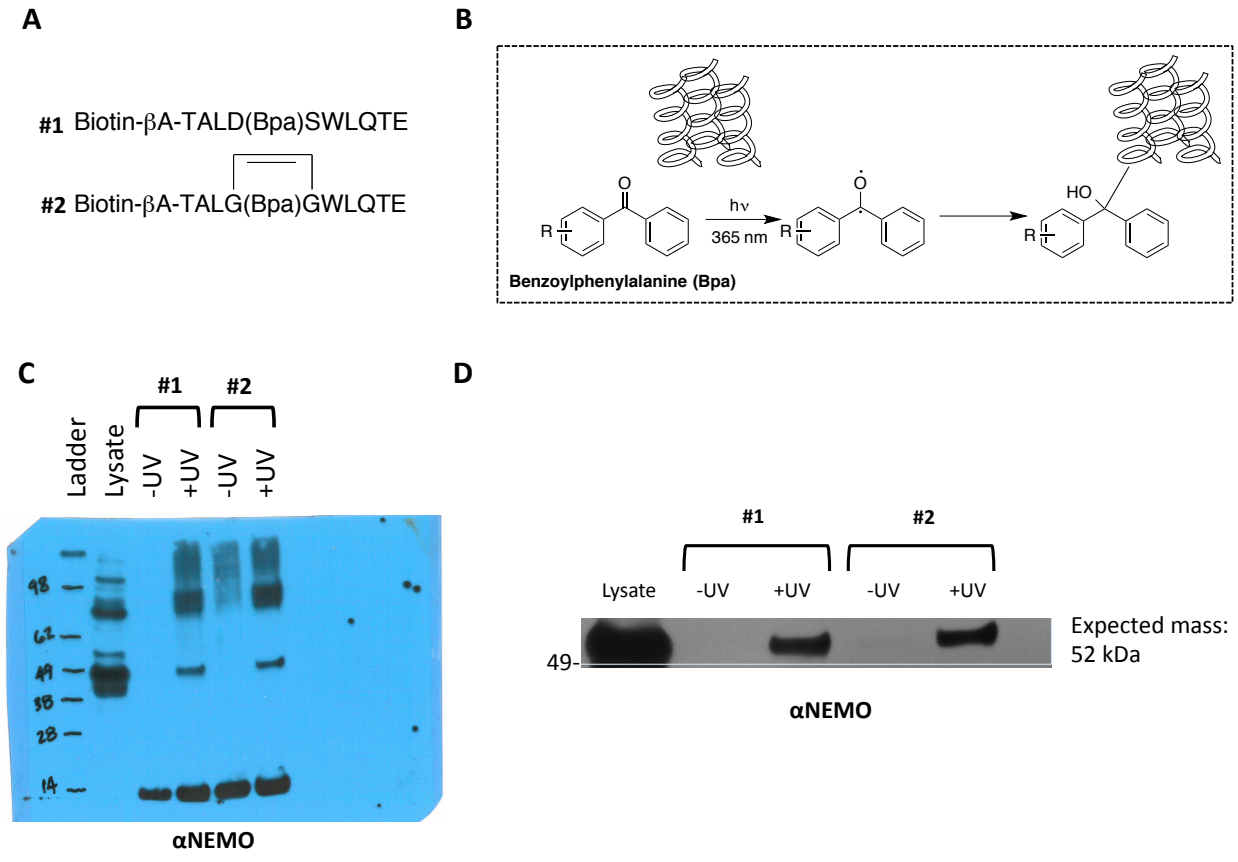

Figure 4.12 Using covalent cross-linking to demonstrate NBD mimic target engagement A. The two constructs used to demonstrate NEMO target engagement. The #1 construct will serve as the positive control. This sequence is the NBD interaction sequence with W739 replaced with pBpa. The #2 sequence is the olefin metathesis NBD mimic with

W739 substituted with pBpa. B. Inducing covalent capture of interaction partners using pBpa. Upon exposure of pBpa with UV light (365 nm), a radical is formed that can cause covalent bond formation with the interacting protein. C. The resulting western blot looking at the ability of construct #1 and #2 in part A to covalently capture NEMO from HeLa cellular lysates. D. Selected view of relevant bands from western blot in C.

Construct #1 was made as a positive control. This peptide is based on the NBD interaction sequence with W739 substituted with pBpa. We hypothesize that this peptide should be able to covalently capture NEMO in cellular lysates. Construct #2 was made to determine if the metathesis constraints introduced into the NBD sequence affect the ability of this sequence to covalently capture NEMO in cellular lysates. The results of covalent capture experiments demonstrated that both constructs are capable of interacting with NEMO in cellular lysates (Figure 4.12C). Without irradiation with UV light, these "bait" peptides are unable to pull-down NEMO, but in the presence of UV light, a covalent cross-link is formed, allowing for the protein to be pulled-down with the "bait" peptides as evidenced by the bands in the "+UV" column for both the #1 and #2 construct (Figure 4.12C). Together these results demonstrate that the NBD mimic makes a bona fide interaction with NEMO in a complex cellular environment as evidenced by the ability of construct #2 to covalently capture NEMO from cellular lysates.

NEMO-BINDING DOMAIN MIMICS INHIBIT AN NF-κB LUCIFERASE REPORTER IN HELA CELLS

Based on the above data demonstrating that we could synthesize a proteolytically stable NBD mimic that can bind to NEMO, we hypothesized that the NBD mimic would be a better inhibitor of NF-κB than the unmodified NBD peptide. In order to test this hypothesis, we investigated the ability of the NBD mimic to inhibit an NF-κB driven luciferase reporter. HeLa cells were transiently transfected with an NF-κB luciferase reporter and a constitutively expressed β-Gal reporter to monitor for off-target effects. These transfected cells were then dosed with the synthesized peptides and left to incubate for 1 hour before stimulating NF-κB activity using IL-1β. The cells, peptides, and IL-1β were left to incubate for an additional 3 hours at which point, the media was removed and cells were lysed and assayed for NF-κB activity (Figure 4.13).

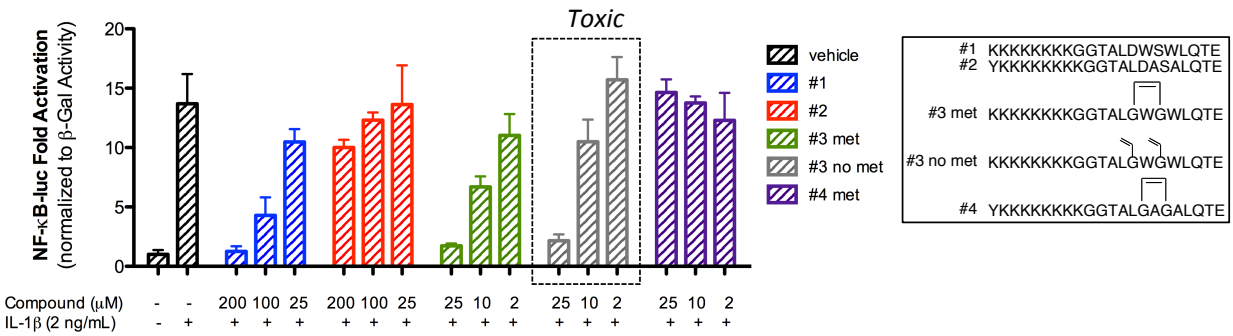

Figure 4.13 Activity of NBD peptides against an NF-κB driven luciferase reporter in HeLa cells The NBD peptides tested are listed to the right. Each of the constructs were tested in a 3-point dose response. Unmodified NBD peptides (#1 and #2) were tested at 200, 100, and 25 μM, whereas modified NBD peptides (#3 met, #3 no met, and #4) were tested at 25, 10, and 2 μM. All luciferase signals were normalized to their respective β-gal signal. All dose points represent the mean and standard deviation of 3 replicates.

From these NF-κB luciferase reporter assays, we learned several things. First, we were able to produce IC_{50}s (IC_{50} ~ 100 μM) very similar to other data obtained with NF-κB luciferase reporters and the NBD peptides (construct **#1**). We were also able to demonstrate that the NBD peptide with the two critical tryptophans mutated to alanines (construct **#2**) exhibited minimal inhibition of NF-κB luciferase activity, as expected. Interestingly, both **#3 met** and **#3 no met** exhibited potent inhibition of NF-κB luciferase activity; however, both the 25 and 10 μM dose points for **#3 no met** exhibited decreased β-Gal activity compared to the other NBD constructs, suggesting that this peptide has off-target effects. These off-target effects could be the caused by several things such as promiscuous binding to other targets or degradation into a toxic byproduct. Based on the limited proteolytic stability of the **#3 no met** construct, the inhibition demonstrated against the NF-κB luciferase reporter is not consistent. Interestingly, the **#3 no met** construct rapidly degraded within 15 minutes of trypsin addition in the proteolytic stability assay, yielding a more polar intermediate that resisted further degradation until extended time points (360 min+). Based on this observation, it is possible that this longer-lived intermediate produced upon proteolytic degradation of **#3 no met** causes off-target effects in cells. In contrast, **#3 met** displayed potent inhibition that was 8 to 10-fold better than the unmodified NBD peptide (**#1**) and did not result in inhibition of β-Gal activity. Additionally, when the **#3 met** construct had the critical tryptophan residues mutated to alanines (**#4**),

this construct was unable to inhibit an NF-κB driven luciferase reported. This result suggests that the NBD mimic (**#3 met**) relies on these critical tryptophans for inhibition of NF-κB driven luciferase activity, similar to the unmodified NBD peptide (**#1**). Together these results suggest that the NBD mimic (**#3 met**) has utility as an inhibitor in NF-κB reporter systems. Next, we sought to determine if the same inhibitory effects could be observed against native NF-κB target gene expression.

NEMO-BINDING DOMAIN MIMICS INHIBIT NF-κB TARGET GENES IN HELA CELLS

Based on the potent inhibition observed with the NBD mimics against an NF-κB luciferase reporter, we sought to determine if these results could be recapitulated for inhibition of native NF-κB target genes in HeLa cells. In order to investigate the ability of the NBD mimics to inhibit NF-κB target genes, we looked at two different NF-κB target genes, MIP3α and IL-8. The MIP3α gene is primarily regulated by p50-p65 NF-κB heterodimers,[65] whereas IL-8 is primarily regulated p65-p65 NF-κB homodimers.[66] Although different NF-κB promoter complexes regulate the MIP3α and IL-8 genes, the NF-κB canonical activation pathway mediates activation of both of these genes. Therefore, if we inhibit assembly of the IKK complex, which is critical for canonical NF-κB activation, we should not see promoter specific inhibition of MIP3α and IL-8, we should inhibition of both target genes. In order to assess the effects of the NBD peptides on MIP3α and IL-8 gene expression, we dosed cells with 100 μM of unmodified NBD peptides (**#1** and **#2**) and 10 μM of NBD mimics (**#3 met** and **#4**). Cells were left to incubate with peptides for 1 hour before stimulation of NF-κB activity using IL-1β. Cells were incubated with peptides and IL-1β for an additional 2 hours at which point the media was removed, the cells were lysed, and mRNA was isolated. Both MIP3α and IL-8 mRNA levels were assessed using RPL19 mRNA levels to normalize against (Figure 4.14).

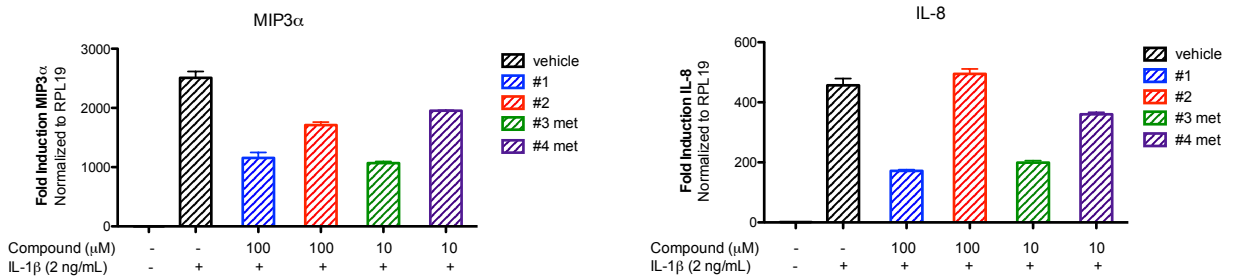

Figure 4.14 Inhibition of NF-κB target genes MIP3α and IL-8 using NBD peptides The charts above are representative of target mRNA fold induction of MIP3α and IL-8 normalized to RPL19 mRNA levels. Samples treated with NBD peptides (#1 and #2) received 100 μM doses, whereas samples treated with NBD mimics (#3 met and #4) received 10 μM doses. All data points represent the mean and standard deviation of 3 replicates.

As demonstrated in Figure 4.14, similar inhibition and potency against two different NF-κB target genes was observed, similar to the effects observed in the NF-κB driven luciferase reporter assay. The same increase in potency of NBD mimic **(#3 met**) compared to NBD peptide (**#1**) was observed with about a 10-fold increase in potency. Similarly, both the alanine mutant NBD peptide (**#2**) and alanine mutant NBD mimic (**#4**) exhibited little to no inhibition in comparison with their tryptophan containing counterparts. This result is encouraging because it suggests the NBD mimic (**#3 met**) is not only useful as an inhibitor for NF-κB reporter assays, but also as an inhibitor to investigate that effects on NF-κB target genes. The utility of the NBD mimic for inhibition of NF-κB target genes is particularly encouraging because this looks at the native NF-κB signaling pathway in cells, as opposed to NF-κB reporter systems, which are often highly artificial. The ability to use NBD mimics as an inhibitor of native NF-κB target genes also greatly expands its utility in other cellular systems such as other cell lines or even tumor primary cells from patients, whereas NF-κB reporter systems are often optimized for specific cell lines, limiting their utility.

4.4 Conclusions

Here we described how an inhibitory peptide (NBD peptide) against the NF-κB-essential modifier (NEMO) was discovered through truncation studies with NEMO and IKKα/β. Previous studies that looked at NEMO knockouts demonstrated that the IKK

complex was absolutely critical for activation of the canonical NF-κB activation pathway, highlighting the potential therapeutic applications of an inhibitor that blocked the association of the IKKα/β with NEMO. One of the primary reasons that the NBD peptide was able to successfully inhibit the IKK complex formation between NEMO and IKKα/β was through exploitation of a conserved 6-amino acid sequence shared in the C-terminus of IKKα and IKKβ and was found to be indispensible for the interaction with NEMO. This result suggests that an inhibitor developed based on that conserved sequence would be able to inhibit both IKKα and IKKβ assembly with NEMO.

Despite the successful targeting of the IKK complex with the NBD peptide, and localization of the NEMO-IKK interaction to a defined 6-amino acid sequence, no small molecules have been developed against this interaction. We hypothesize that part of the reason that no small molecules have been developed against the NEMO-IKK interaction is due to the ambiguous structure of the NBD. It was originally noted as being amphipathic, which always requires consideration of the sequence having α-helical structure. It is possible that with the assumption that the domain is helical, this interaction may have been targeted for with the wrong types of small molecule libraries or even the wrong type of peptidomimetic strategies. Given new structural data, the key 6-amino acid interaction domain is actually confirmed to be unstructured. Furthermore, studies by Golden and coworkers found that a large number of the residues that contribute to the overall binding energy of the NEMO-IKK interaction reside in this unstructured region serving as a "molecular anchor" for the NEMO-IKK interaction. This is contrary to what is traditionally observed with 4-helix bundles and with extended α-helical interactions, such as p53. Together these results suggest that targeting the highly conserved ^{737}LDWSWL^{742} in the IKKα and IKKβ C-terminus is the verified hot spot of the NEMO-IKK interaction that should be targeted for development of inhibitors of the NEMO-IKK interaction.

Our initial efforts focused on developing a peptidomimetic inhibitor of the NEMO-IKK interaction through constraining the conserved ^{737}LDWSWL^{742} sequence using olefin metathesis. Traditionally, olefin metathesis has been used to constrain alpha helices through side chain-to-side chain ring closing metathesis reactions or through backbone-to-side chain ring closing metathesis reactions as a HBS (also known as hydrogen bond surrogates). We demonstrated how ring closing metathesis reactions could be used to

uniquely target an unstructured region, adapting the idea of a hydrogen bond surrogate as a replacement and permanent kink for the conserved ^{737}LDWSWL^{742} sequence that traditionally utilizes a hydrogen bond between D738 and S740 to constrain the sequence. Using this strategy, we were able to synthesize an NBD peptide mimic that was proteolytically stable to degradation by chymotrypsin, able to interact with NEMO in cellular lysates using covalent capture, 8 to 10-fold more potent at inhibiting an NF-κB luciferase reporter in HeLa cells, and was 10-fold more potent at inhibiting endogenous NF-κB endogenous genes MIP3α and IL-8 than the unmodified NBD peptide originally developed in 2000. Together, these results suggest that our unique employment of ring closing metathesis on unstructured hot spot regions, is a strategy that can be employed to develop better peptidomimetic inhibitors.

4.5 Materials and Methods

Peptide synthesis

Peptides used in this chapter were synthesized on CLEAR amide resin (Peptides International) using FMOC protected amino acids (Peptides International), and using standard HBTU/HOBT/ DIEA coupling conditions. Anhydrous DMF and DCM used for metathesis reactions were purchased from Sigma Aldrich.

NBD peptide #1 was synthesized and purified. At the final step, the peptide was deprotected with 20% piperidine/DMF for 20 minutes, washed 3x with DMF, 3x with DCM, and 3x MeOH. A global deprotection/cleavage solution consisting of 95%/2.5%/2.5% TFA/EDT/H_2O was added to resin. The resin was agitated for 4 hours with continuous shaking. After 4 hours, the eluent was collect and TFA was removed by evaporation with N_2. The crude peptide was precipitated overnight with cold diethyl ether. Diethyl ether was decanted off and precipitate was washed 3x with cold diethyl ether. This yielded the free amine of the crude peptide:

#1 KKKKKKKKGGTALDWSWLQTE

The crude peptide was purified by reverse phase HPLC (Agilent 1260) on a C18 poroshell column (Agilent) with 0.1% TFA in water and acetonitrile as eluents. A gradient of 10-40% acetonitrile over 30 minutes was used. Analytical HPLC traces of the peptide are placed in section 4.6. HPLC fractions were combined and lyophilized to a fine powder and reconstituted as a DMSO stock. The concentration of the stock was determined by UV-Vis spectroscopy in a solution of 6M guanidium hydrochloride, 20 mM PBS, pH 6.5 using ε = 11,380 M^{-1} cm^{-1} as outlined by Gill and von Hipple.[67]

NBD peptide #2 was synthesized and purified. At the final step, the peptide was deprotected with 20% piperidine/DMF for 20 minutes, washed 3x with DMF, 3x with DCM, and 3x MeOH. A global deprotection/cleavage solution consisting of 95%/2.5%/2.5% TFA/EDT/H_2O was added to resin. The resin was agitated for 4 hours with continuous shaking. After 4 hours, the eluent was collect and TFA was removed by evaporation with N_2. The crude peptide was precipitated overnight with cold diethyl ether. Diethyl ether was

decanted off and precipitate was washed 3x with cold diethyl ether. This yielded the free amine of the crude peptide:

#2 YKKKKKKKKGGTALDASALQTE

The crude peptide was purified by reverse phase HPLC (Agilent 1260) on a C18 poroshell column (Agilent) with 0.1% TFA in water and acetonitrile as eluents. A gradient of 10-40% acetonitrile over 30 minutes was used. Analytical HPLC traces of the peptide are placed in section 4.6. HPLC fractions were combined and lyophilized to a fine powder and reconstituted as a DMSO stock. The concentration of the stock was determined by UV-Vis spectroscopy in a solution of 6M guanidium hydrochloride, 20 mM PBS, pH 6.5 using ε = 1,280 M^{-1} cm^{-1} as outlined by Gill and von Hipple.[67]

NBD peptide #3 met was synthesized up to the first diglycine linker residue. Resin was washed 3x with DMF, 3x with DCM, and 3x MeOH and dried overnight under reduced pressure. Resin was transferred to a 10 mL microwave reaction vial and dissolved in a 1:1 solution of anhydrous DMF containing 400 mM LiCl and anhydrous DCM for a total volume of 3 mL. Solution was degassed for 30 minutes by bubbling N_2 through the solution. HGII (10 mol%) was immediately dissolved in minimal anhydrous, degassed DCM before adding to resin solution. Microwave reaction vial was purged with N_2 before sealing with crimper tool. Reaction vial was transferred to a microwave reactor (Biotage) and heated for 10-15 minutes at 100 °C with continuous stirring to facilitate metathesis reaction. The reaction mixture was transferred to a peptide synthesizer vial and washed 3x with DCM and 3x with DMF in order to wash away any catalyst. Peptide synthesis was continued to add the octalysine CPP (K_8) and diglycine linker. At the final step, the peptide was deprotected with 20% piperidine/DMF for 20 minutes, washed 3x with DMF, 3x with DCM, and 3x MeOH. A global deprotection/cleavage solution consisting of 95%/2.5%/2.5% TFA/EDT/H_2O was added to resin. The resin was agitated for 4 hours with continuous shaking. After 4 hours, the eluent was collect and TFA was removed by evaporation with N_2. The crude peptide was precipitated overnight with cold diethyl ether. Diethyl ether was decanted off and precipitate was washed 3x with cold diethyl ether. This yielded the free amine of the crude peptide:

The crude peptide was purified by reverse phase HPLC (Agilent 1260) on a C18 poroshell column (Agilent) with 0.1% TFA in water and acetonitrile as eluents. A gradient of 10-40% acetonitrile over 30 minutes was used. Analytical HPLC traces of the peptide are placed in section 4.6. HPLC fractions were combined and lyophilized to a fine powder and reconstituted as a DMSO stock. The concentration of the stock was determined by UV-Vis spectroscopy in a solution of 6M guanidium hydrochloride, 20 mM PBS, pH 6.5 using ε = 11,380 M^{-1} cm^{-1} as outlined by Gill and von Hipple.[67]

NBD peptide #3 no met was synthesized and purified. At the final step, the peptide was deprotected with 20% piperidine/DMF for 20 minutes, washed 3x with DMF, 3x with DCM, and 3x MeOH. A global deprotection/cleavage solution consisting of 95%/2.5%/2.5% TFA/EDT/H_2O was added to resin. The resin was agitated for 4 hours with continuous shaking. After 4 hours, the eluent was collect and TFA was removed by evaporation with N_2. The crude peptide was precipitated overnight with cold diethyl ether. Diethyl ether was decanted off and precipitate was washed 3x with cold diethyl ether. This yielded the free amine of the crude peptide:

The crude peptide was purified by reverse phase HPLC (Agilent 1260) on a C18 poroshell column (Agilent) with 0.1% TFA in water and acetonitrile as eluents. A gradient of 10-40% acetonitrile over 30 minutes was used. Analytical HPLC traces of the peptide are placed in section 4.6. HPLC fractions were combined and lyophilized to a fine powder and reconstituted as a DMSO stock. The concentration of the stock was determined by UV-Vis spectroscopy in a solution of 6M guanidium hydrochloride, 20 mM PBS, pH 6.5 using ε = 11,380 M^{-1} cm^{-1} as outlined by Gill and von Hipple.[67]

NBD peptide #4 met was synthesized up to the first diglycine linker residue. Resin was washed 3x with DMF, 3x with DCM, and 3x MeOH and dried overnight under reduced pressure. Resin was transferred to a 10 mL microwave reaction vial and dissolved in a 1:1

solution of anhydrous DMF containing 400 mM LiCl and anhydrous DCM for a total volume of 3 mL. Solution was degassed for 30 minutes by bubbling N_2 through the solution. HGII (10 mol%) was immediately dissolved in minimal anhydrous, degassed DCM before adding to resin solution. Microwave reaction vial was purged with N_2 before sealing with crimper tool. Reaction vial was transferred to a microwave reactor (Biotage) and heated for 10-15 minutes at 100 °C with continuous stirring to facilitate metathesis reaction. The reaction mixture was transferred to a peptide synthesizer vial and washed 3x with DCM and 3x with DMF in order to wash away any catalyst. Peptide synthesis was continued to add the tyrosine chromophore, octalysine CPP (K_8) and diglycine linker. At the final step, the peptide was deprotected with 20% piperidine/DMF for 20 minutes, washed 3x with DMF, 3x with DCM, and 3x MeOH. A global deprotection/cleavage solution consisting of 95%/2.5%/2.5% TFA/EDT/H_2O was added to resin. The resin was agitated for 4 hours with continuous shaking. After 4 hours, the eluent was collect and TFA was removed by evaporation with N_2. The crude peptide was precipitated overnight with cold diethyl ether. Diethyl ether was decanted off and precipitate was washed 3x with cold diethyl ether. This yielded the free amine of the crude peptide:

The crude peptide was purified by reverse phase HPLC (Agilent 1260) on a C18 poroshell column (Agilent) with 0.1% TFA in water and acetonitrile as eluents. A gradient of 10-40% acetonitrile over 30 minutes was used. Analytical HPLC traces of the peptide are placed in section 4.6. HPLC fractions were combined and lyophilized to a fine powder and reconstituted as a DMSO stock. The concentration of the stock was determined by UV-Vis spectroscopy in a solution of 6M guanidium hydrochloride, 20 mM PBS, pH 6.5 using ε = 1,280 M^{-1} cm^{-1} as outlined by Gill and von Hipple.[67]

Biotin NEMO peptide #1 was synthesized and purified. At the final step, the peptide was washed 3x with DMF, 3x with DCM, and 3x MeOH. A global deprotection/cleavage solution consisting of 95%/2.5%/2.5% TFA/TIPS/H_2O was added to resin. The resin was agitated for 2 hours with continuous shaking. After 2 hours, the eluent was collected and TFA was

removed by evaporation with N_2. The crude peptide was precipitated overnight with cold diethyl ether. Diethyl ether was decanted off to yield the crude peptide:

#1 Biotin-βA-TALD(Bpa)SWLQTE

The crude peptide was purified by reverse phase HPLC (Agilent 1260) on a C18 poroshell column (Agilent) with 20 mM ammonium acetate in water and acetonitrile as eluents. A gradient of 20-50% acetonitrile over 30 minutes was used. Analytical HPLC traces of the peptide are placed in section 4.6. HPLC fractions were combined and lyophilized to a fine powder and reconstituted as a DMSO stock. The concentration of the stock was determined by UV-Vis spectroscopy in a solution of 10 mM PBS using $\varepsilon = 21{,}500\ M^{-1}\ cm^{-1}$.

Biotin NEMO peptide #2 was synthesized and purified. At the final step, the peptide was washed 3x with DMF, 3x with DCM, and 3x MeOH. A global deprotection/cleavage solution consisting of 95%/2.5%/2.5% TFA/TIPS/H_2O was added to resin. The resin was agitated for 2 hours with continuous shaking. After 2 hours, the eluent was collected and TFA was removed by evaporation with N_2. The crude peptide was precipitated overnight with cold diethyl ether. Diethyl ether was decanted off to yield the crude peptide:

#2 Biotin-βA-TALG(Bpa)GWLQTE

The crude peptide was purified by reverse phase HPLC (Agilent 1260) on a C18 poroshell column (Agilent) with 20 mM ammonium acetate in water and acetonitrile as eluents. A gradient of 20-50% acetonitrile over 30 minutes was used. Analytical HPLC traces of the peptide are placed in section 4.6. HPLC fractions were combined and lyophilized to a fine powder and reconstituted as a DMSO stock. The concentration of the stock was determined by UV-Vis spectroscopy in a solution of 10 mM PBS using $\varepsilon = 21{,}500\ M^{-1}\ cm^{-1}$.

Circular dichroism performed with NBD peptides

Circular dichroism with the NBD peptides were performed using an Aviv model 202 Circular Dichroism Spectrometer equipped with a 450 watt Xenon arc lamp. Data was collected using wavelength scans with a wavelength range of 190-250 nm and wavelength step of 1.00 nm. All samples are represented as an average of 3 scans. The time constant

used for the experiment if 100 ms with a monochromator/slit bandwidth of 1.00 nm. Any wavelength readings that resulted in a dynode voltage reading >600 V was omitted from the data set. All NBD peptides were dissolved in 10 mM PBS, pH 6.8 (no salt) at a final concentration of 50 μM. Calculated the mean residue molar ellipticity (MRE) using the following equation:

$$\theta(deg \cdot cm^2 \cdot dmol^{-1}) = \frac{ellipticity(mdeg) \cdot 10^6}{pathlength(mm) \cdot [protein](\mu M) \cdot n}$$

(Equation 4.1)

Where n = # of peptide bonds in protein and ellipticity is the raw data from the instrument. The resulting data was plotted as wavelength (nm) vs. MRE [θ] (deg cm^2 $dmol^{-1}$).

Proteolytic stability assays with NBD peptides

Peptides tested in the proteolytic stability assay with NBD peptides:

#1 KKKKKKKKGGTALDWSWLQTE

#3 no met KKKKKKKKGGTALGWGWLQTE

#3 met KKKKKKKKGGTALGWGWLQTE

Chymotrypisin type VII (TLCK treated to inactivate residual trypsin activity), salt free, lyophilized powder, ≥ 40 units/mg protein was dissolved in 1 mM HCl containing 2 mM $CaCl_2$ at a final concentration of 10 μg/uL. For proteolysis experiment, dissolved each construct above in proteolysis buffer (100 mM Tris, 10 mM $CaCl_2$, pH 7.8) to a final concentration of 20 μM. Added 10 μg of protease to each construct and let incubate at room temperature in a total reaction volume of 200 μL. Removed 25 μL samples at the indicated time points. Samples were dissolved in 200 μL of 1% TFA in H_2O to stop the reaction. Each time point was analyzed on HPLC to monitor degradation products. HPLC traces of the individual time point samples were organized as a 3D overlay to demonstrate shifts in the parent peak.

Pull-down of NEMO with biotin-labeled NBD peptide constructs

#1 Biotin-βA-TALD(Bpa)SWLQTE

#2 Biotin-βA-TALG(Bpa)GWLQTE

A full 10 cm^2 petri dish of HEK293T cells were trypsinized from plate and washed 3x with cold PBS. Cells were pelleted and PBS was aspirated off of cell pellet. Cell pellet was resuspended in NP-40 lysis buffer (150 mM NaCl, 1% NP-40, 50 mM Tris, pH 8.0) with HALT (1x) and transferred to an eppendorf tube. Eppendorf tube was placed on rotating carousel at 4 °C for 15 minutes. Lysate was centrifuged at 14,000 rom for 15 minutes at 4 °C. Lysate was transferred to a new tube and protein concentration was determined using Bradford assay. Lysate was adjusted to a concentration of 3.5 mg/mL. Biotin constructs #1 and #2 were added to 400 µL of cell lysate (3.5 mg/mL) to a final concentration of 10 µM. Each sample was split in a 200 µL solution and added to 1" petri dishes. Each sample was either irradiated with UV light (+UV) or shielded from light (-UV) for 1.5 hours. NeutrAvidin beads were equilibrated 3x in 200 µL binding buffer (10 mM PBS, 100 mM NaCl, 10% glycerol, 0.1% NP-40, pH 7.2). After 1.5 hour incubation for +UV and –UV solutions, the samples were added to equilibrated NeutrAvidin beads and placed on rotating carousel at 4 °C for 1 hour. NeatrAvidin beads were washed 3x with binding buffer and centrifuged at 14000 rpm for 1 minute. On last wash, supernatant was removed. To each sample of NeutrAvidin beads: 13 µL H_2O, 5 µL loading buffer, 2 µL DTT was added. For lysate input well: 11 µL H_2O, 5 µL loading buffer, 2 µL DTT, and 2 µL of total cell lysate was added. These samples were heated to 95 °C for 10 minutes with occasional mixing. Samples were centrifuged at 14000 rpm for 2 minutes. Loaded 20 µL of each sample onto a 6% stacking/8% Bis-Tris MES resolving gel and run for 1 hour at 150V. Transferred gel to PVDF membrane using wet transfer box according to manufacturer's protocol. Ran transfer at 100V, 400 mA for 1 hour at 4 °C. Blocked membrane 5% w/v in western wash buffer (PBS, 0.2% Tween-20). Washed membrane 5x with western wash buffer for 5 minutes per wash. Incubated membrane with anti-NEMO/IKKγ rabbit antibody diluted 1:1000 in 5% w/v milk in western wash buffer for 1 hour at room temperature. Washed membrane 5x with western wash buffer for 5 minutes per wash. Incubate membrane with

anti-rabbit goat-HRP antibody diluted 1:10000 in 5% w/v milk in western wash buffer for 1 hour at room temperature. Washed membrane 5x with western wash buffer for 5 minutes per wash. Developed membrane with west fempto ECL reagnets.

NF-κB luciferase reporter assay for assessing inhibition of NBD peptides

The NF-κB luciferase reporter plasmid carrying 6 tandem κB-sites, NF-κB-luc, CMV-β-Gal, and pBSSK were generously provided by Dr. Jorge Iñigues-Lluhí (The University of Michigan Pharmacology Department).[68] All cells were maintained in 5% CO_2 at 37°C. HeLa cells were grown in Dulbecco's modified Eagle's medium (DMEM, Invitrogen) supplemented with 10% FBS. For luciferase assays, $4x10^5$ cells were seeded in a 6-well dish and allowed to adhere overnight. The media was removed and cells were transfected in Opti-Mem (Invitrogen) with 400 ng NF-κB-luc, 200 ng CMV-β-Gal, and 1,400 ng pBSSK using Lipofectamine 2000 (Life Technologies) according to manufacturer's instructions. After 4.5 h, transfection solution was removed and replaced with DMEM containing 10% FBS. At 24 h after transfection, cells were trypsinized and resuspended in DMEM supplemented with 10% FBS and seeded into a 96-well plate at a density of $8x10^3$ cells per well. After an additional 16 h, media was removed and replaced with Opti-Mem containing vehicle or NBD peptides delivered in DMSO (1% v/v) at the indicated concentrations. After cells incubated with either vehicle or compound for 1 h, cells were treated with either PBS or IL-1β at a final concentration of 2 ng/mL. After an additional 3 h, media was removed and cells were lysed with 60 μL of passive lysis buffer. Luciferase and β-Galactosidase activities were determined as previously described.[69] NF-κB luciferase activity and response curve analysis was performed using GraphPad software.

Assaying inhibitory effects of NBD peptides against NF-κB endogenous gene expression

For endogenous gene expression analysis, $1x10^5$ cells were seeded into a 24-well plate and allowed to adhere overnight. Media was removed and replaced with Opti-Mem media containing vehicle or NBD peptide delivered in DMSO (1% v/v) at the indicated concentrations. After incubating for 1 h, cells were treated with either PBS or IL-1β at a final concentration of 2 ng/mL. After 2 h, the media was removed and total RNA was isolated using RNeasy Plus RNA isolation kits (Qiagen) according to manufacturer's

instructions. Each RNA sample was used to synthesize cDNA using iScript cDNA synthesis kits (Bio-Rad). Quantitative real-time PCR (qRT-PCR) reactions were carried out in triplicate in an Applied Biosystems StepPlusOne using SYBR green master mix and primers for human RPL19 (Forward, 5'-ATGTATCACAGCCTGTACCTG-3'; Reverse, 5'-TTCTTGGTCTCTCTTCCTCCTTG-3'), MIP3α[70] (Forward, 5'-CCTGGGGGAATATTCTGGTGGTGA-3'; Reverse, 5'-CATCGCTGCCTTGGGTGTTGTAT-3'), and IL-8[71] (Forward, 5'-ATGACTTCCAAGCTGGCCGTGGCT-3'; Reverse, 5'-TCTCAGCCCTCTTCAAAAACTTCT-3'). RT-qPCR analysis was carried out using the comparative C_T Method ($\Delta\Delta C_T$ Method) as previously described[72,73] to estimate MIP3α mRNA levels and IL-8 mRNA levels relative to the reference RPL19 mRNA levels.

4.6 Characterization of synthesized compounds

Analytical HPLC chromatogram of purified NBD peptide #1

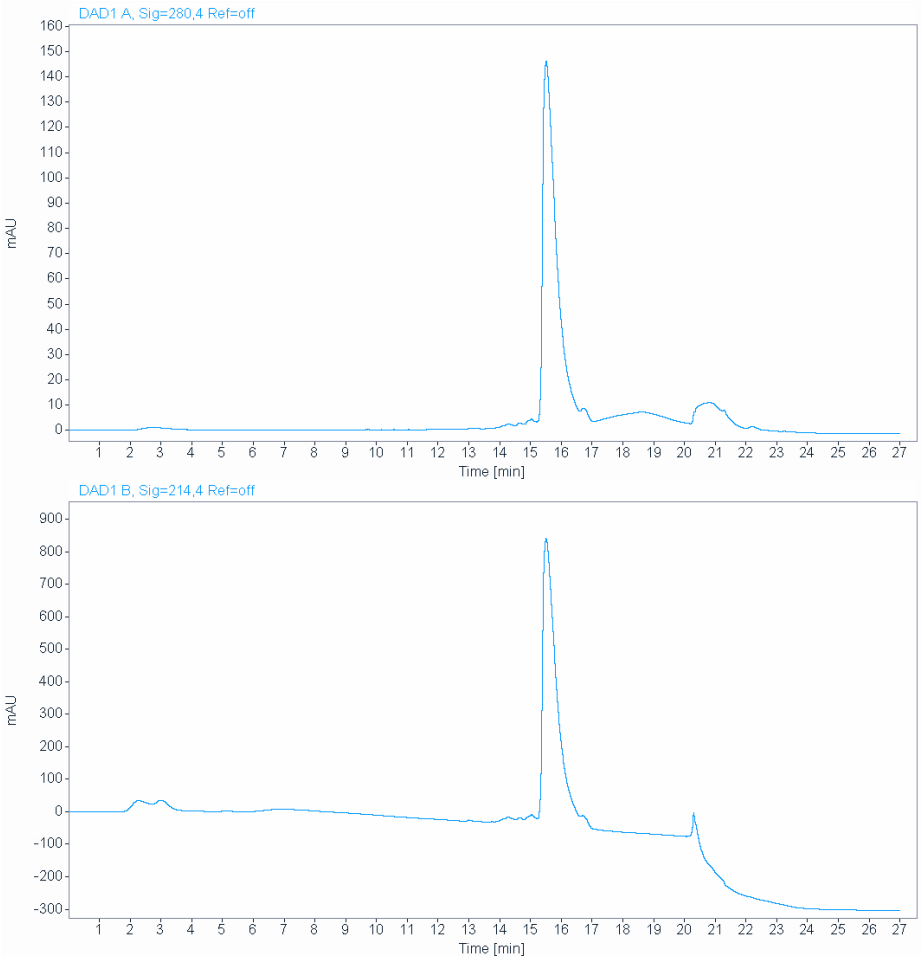

Analytical HPLC chromatogram of purified NBD peptide #2

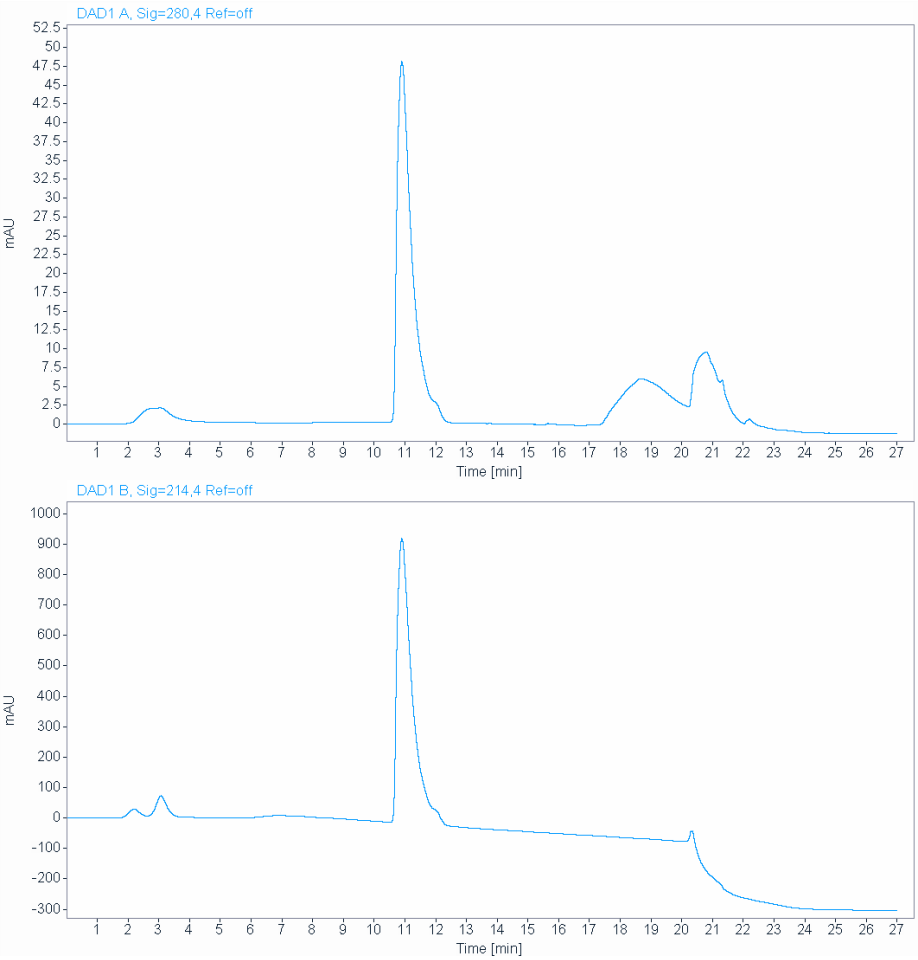

Analytical HPLC chromatogram of NBD peptide #3 no met

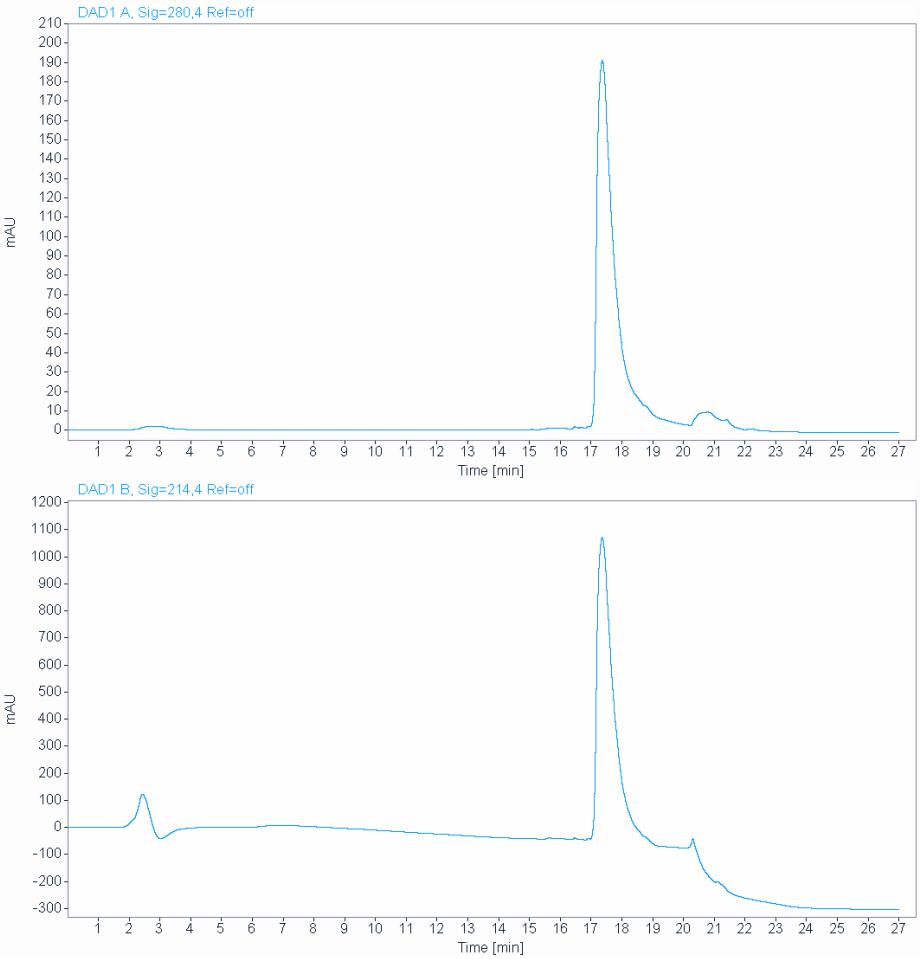

Analytical HPLC chromatogram of purified NBD peptide #3 met

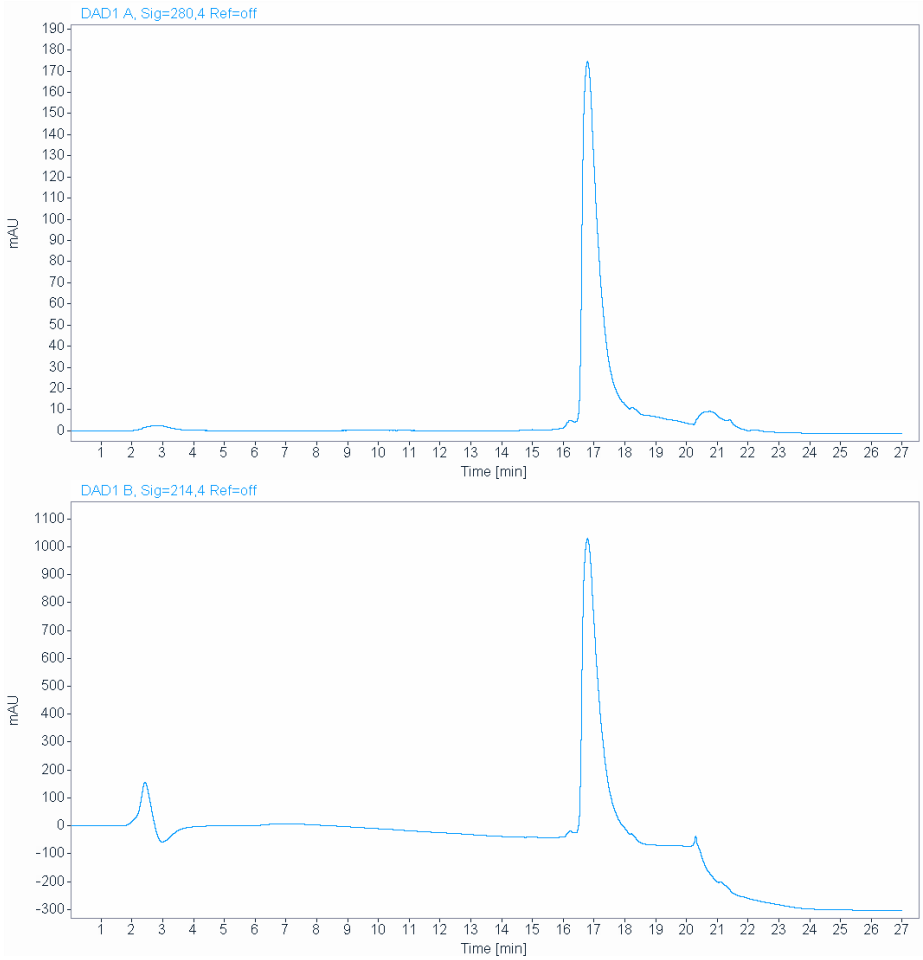

Analytical HPLC chromatogram of purified NBD peptide #4 met

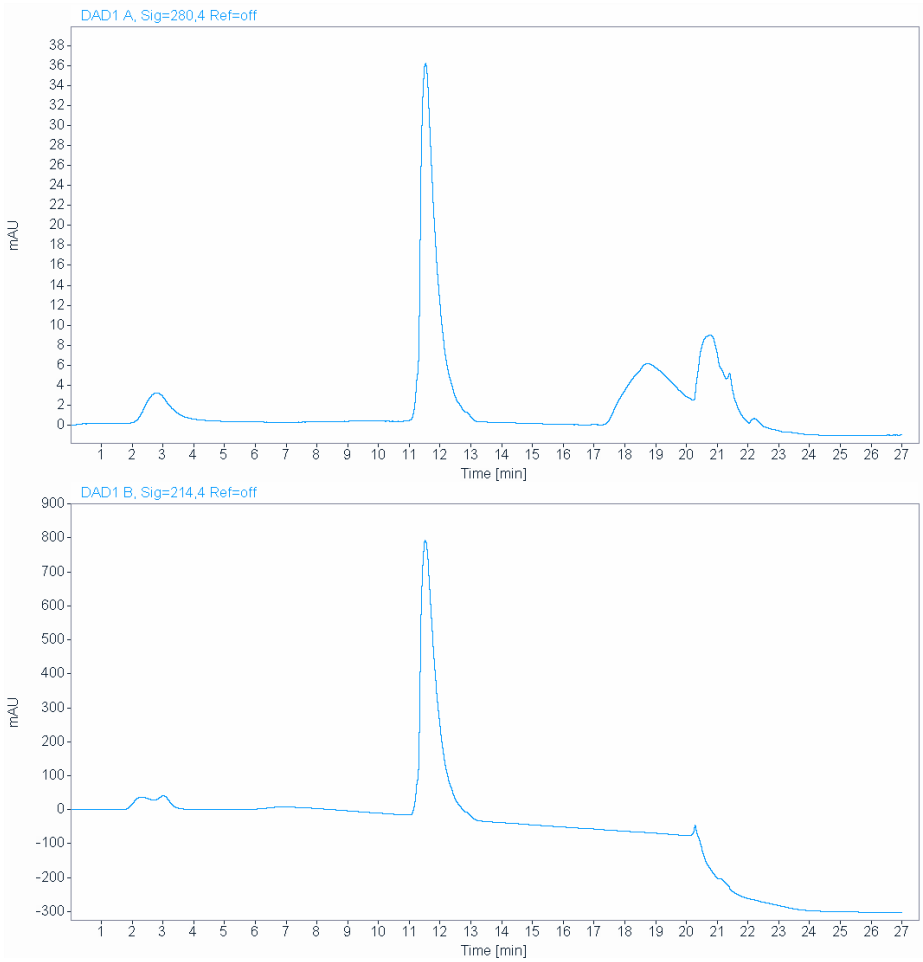

Analytical HPLC chromatogram of purified biotin NEMO peptide #1

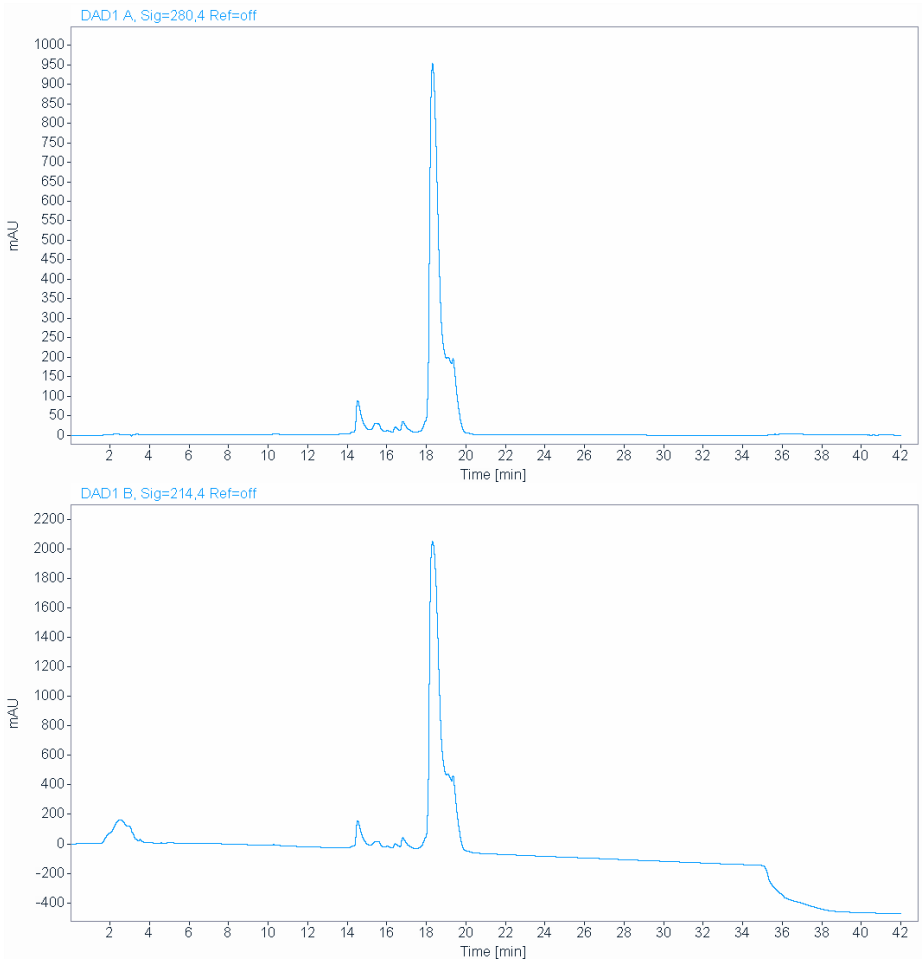

Analytical HPLC chromatogram of purified biotin NEMO peptide #2

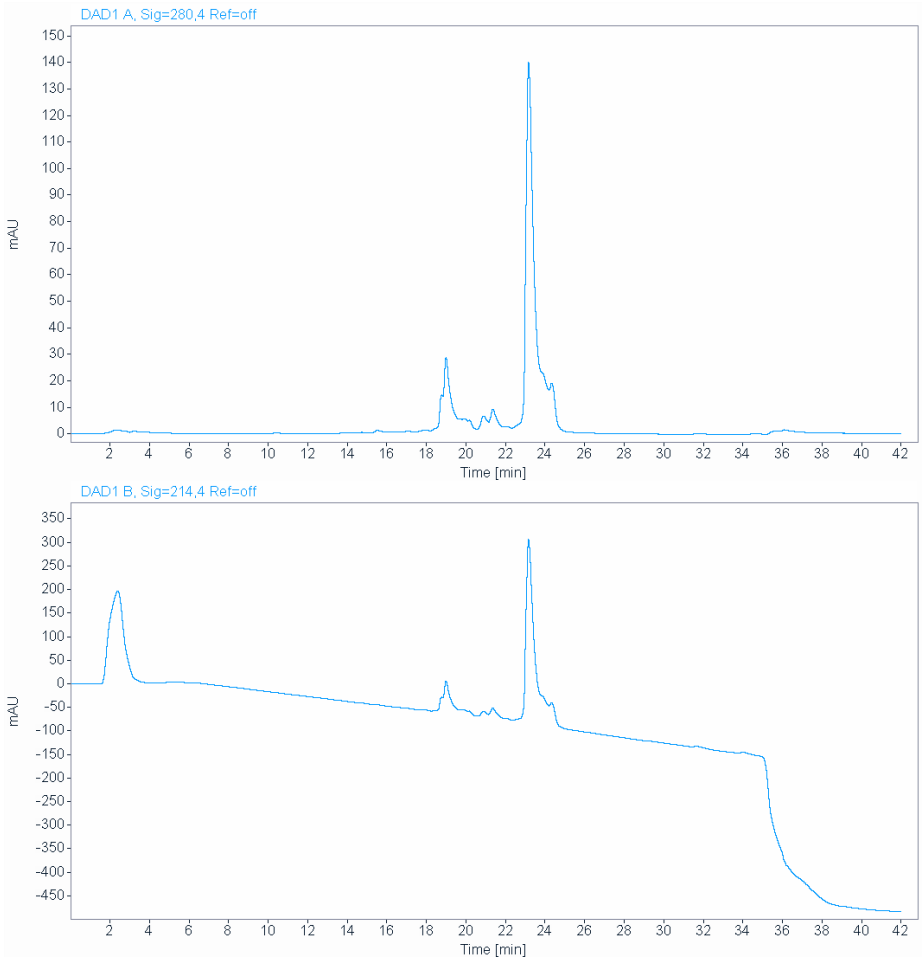

4.7 References

(1) Sen, R.; Baltimore, D. Multiple Nuclear Factors Interact with the Immunoglobulin Enhancer Sequences. *Cell* **1986**, *46*, 705–716.

(2) Verma, I. M.; Stevenson, J. K.; Schwarz, E. M.; Van Antwerp, D.; Miyamoto, S. Rel/NF-Kappa B/I Kappa B Family: Intimate Tales of Association and Dissociation. *Genes & Development* **1995**, *9*, 2723–2735.

(3) Hoesel, B.; Schmid, J. A. The Complexity of NF-κB Signaling in Inflammation and Cancer. *Mol. Cancer* **2013**, *12*, 86.

(4) Baldwin, A. S., Jr. Series Introduction: the Transcription Factor NF-κB and Human Disease. *Journal of Clinical Investigation* **2001**, *107*, 3-6.

(5) Aradhya, S.; Nelson, D. L. NF-kappaB Signaling and Human Disease. *Current Opinion in Genetics & Development* **2001**, *11*, 300–306.

(6) Yamamoto, Y.; Gaynor, R. B. Role of the NF-kB Pathway in the Pathogenesis of Human Disease States. *CMM* **2001**, *1*, 287–296.

(7) Gasparian, A. V.; Yao, Y. J.; Kowalczyk, D. M.; Slaga, T. J. Mechanisms of Constitutive NF-κB Activation in Prostate Carcinoma Cells *J. Cell Sci.* **2002**, *115,* 141-151.

(8) Gasparian, A. V.; Yao, Y. J.; Kowalczyk, D.; Lyakh, L. A.; Karseladze, A.; Slaga, T. J.; Budunova, I. V. The Role of IKK in Constitutive Activation of NF-kappaB Transcription Factor in Prostate Carcinoma Cells. *J. Cell Sci.* **2002**, *115*, 141–151.

(9) Gilmore, T. D.; Herscovitch, M. Inhibitors of NF-kappaB Signaling: 785 and Counting. *Oncogene* **2006**, *25*, 6887–6899.

(10) Feldmann, M.; Maini, R. N. TNF Defined as a Therapeutic Target for Rheumatoid Arthritis and Other Autoimmune Diseases. *Nature Medicine* **2003**, *9*, 1245-1250

(11) Rossi, A.; Kapahi, P.; Natoli, G.; Takahashi, T.; Chen, Y.; Karin, M.; Santoro, M. G. Anti-Inflammatory Cyclopentenone Prostaglandins Are Direct Inhibitors of IκB Kinase. *Nature* **2000**, *403*, 103–118.

(12) Hehner, S. P.; Hofmann, T. G.; Dröge, W.; Schmitz, M. L. The Antiinflammatory Sesquiterpene Lactone Parthenolide Inhibits NF-Kappa B by Targeting the I Kappa B Kinase Complex. *J Immunol* **1999**, *163*, 5617–5623.

(13) Traenckner, E. B.; Wilk, S.; Baeuerle, P. A. A Proteasome Inhibitor Prevents Activation of NF-Kappa B and Stabilizes a Newly Phosphorylated Form of I Kappa B-Alpha That Is Still Bound to NF-Kappa B. *EMBO J* **1994**, *13*, 5433–5441.

(14) Auphan, N.; DiDonato, J. A.; Rosette, C.; Helmberg, A.; Karin, M. Immunosuppression by Glucocorticoids: Inhibition of NF-κB Activity Through Induction of IκB Synthesis. *Science* **1995**, *270*, 286–290.

(15) Oeckinghaus, A.; Hayden, M. S.; Ghosh, S. Crosstalk in NF-κB Signaling Pathways. *Nat. Immunol.* **2011**, *12*, 695–708.

(16) Albanese, C.; Wu, K.; D'Amico, M.; Jarrett, C.; Joyce, D.; Hughes, J.; Hulit, J.; Sakamaki, T.; Fu, M.; Ben-Ze'ev, A.; Bromberg, J. F.; Lamberti, C.; Verma, U.; Gaynor, R. B.; Byers, S. W.; Pestell, R. G. IKKalpha Regulates Mitogenic Signaling Through Transcriptional Induction of Cyclin D1 via Tcf. *Mol. Biol. Cell* **2003**, *14*, 585–599.

(17) Hoshino, K.; Sugiyama, T.; Matsumoto, M.; Tanaka, T.; Saito, M.; Hemmi, H.; Ohara, O.; Akira, S.; Kaisho, T. IκB Kinase-α Is Critical for Interferon-α Production Induced by Toll-Like Receptors 7 and 9. *Nature* **2006**, *440*, 949–953.

(18) Park, K.-J.; Krishnan, V.; O'Malley, B. W.; Yamamoto, Y.; Gaynor, R. B. Formation of an IKKalpha-Dependent Transcription Complex Is Required for Estrogen Receptor-Mediated Gene Activation. *Mol Cell* **2005**, *18*, 71–82.

(19) Carayol, N.; Wang, C.-Y. IKKalpha Stabilizes Cytosolic Beta-Catenin by Inhibiting Both Canonical and Non-Canonical Degradation Pathways. *Cell. Signal.* **2006**, *18*, 1941–1946.

(20) Ruvolo, P. P. The Herculean Task of Killing Cancer Cells: Suppression of FOXO3A in Acute Leukemia Involves a Hydra of Multiple Survival Kinases. *Cell Cycle* **2012**, *11*, 1259-1259.

(21) Arkan, M. C.; Hevener, A. L.; Greten, F. R.; Maeda, S.; Li, Z.-W.; Long, J. M.; Wynshaw-Boris, A.; Poli, G.; Olefsky, J.; Karin, M. IKK-|[Beta]| Links Inflammation to Obesity-Induced Insulin Resistance. *Nature Medicine* **2005**, *11*, 191–198.

(22) Madera-Salcedo, I. K.; Cruz, S. L.; Gonzalez-Espinosa, C. Morphine Prevents Lipopolysaccharide-Induced TNF Secretion in Mast Cells Blocking IκB Kinase Activation and SNAP-23 Phosphorylation: Correlation with the Formation of a B-Arrestin/TRAF6 Complex. *J Immunol* **2013**, *191*, 3400–3409.

(23) Lin, L.; DeMartino, G. N.; Greene, W. C. Cotranslational Biogenesis of NF-kappaB P50 by the 26S Proteasome. *Cell* **1998**, *92*, 819–828.

(24) Baldwin, A. S. Control of Oncogenesis and Cancer Therapy Resistance by the Transcription Factor NF-κB. *Journal of Clinical Investigation* **2001**, *107*, 3-6.

(25) Frankland-Searby, S.; Bhaumik, S. R. The 26S Proteasome Complex: an Attractive Target for Cancer Therapy. *Biochimica et Biophysica Acta (BBA)-Reviews on Cancer*

2012, *1825*, 64-76.

(26) D'Osualdo, A.; Ferlito, F.; Prigione, I.; Obici, L. Neutrophils From Patients with TNFRSF1A Mutations Display Resistance to Tumor Necrosis Factor–Induced Apoptosis: Pathogenetic and Clinical Implications. *Arthritis & Rheumatism* **2006**, *54*, 998-1008.

(27) Noguchi, K.; Naito, M.; Oshimura, M.; Mashima, T.; Fujita, N. Chromosome 22 Complements Apoptosis in Fas-and TNF-Resistant Mutant UK110 Cells. *Oncogene* **1996**, *13*, 39-46.

(28) Ray, A.; Prefontaine, K. E. Physical Association and Functional Antagonism Between the P65 Subunit of Transcription Factor NF-Kappa B and the Glucocorticoid Receptor. *Proc Natl Acad Sci USA* **1994**, *91*, 752–756.

(29) Adcock, I. M.; Ito, K.; Barnes, P. J. Glucocorticoids: Effects on Gene Transcription. *Proc Am Thorac Soc* **2004**, *1*, 247–254.

(30) Makris, C.; Godfrey, V. L.; Krähn-Senftleben, G.; Takahashi, T.; Roberts, J. L.; Schwarz, T.; Feng, L.; Johnson, R. S.; Karin, M. Female Mice Heterozygous for IKK Gamma/NEMO Deficiencies Develop a Dermatopathy Similar to the Human X-Linked Disorder Incontinentia Pigmenti. *Mol Cell* **2000**, *5*, 969–979.

(31) May, M. J.; D'Acquisto, F.; Madge, L. A.; Glöckner, J.; Pober, J. S.; Ghosh, S. Selective Inhibition of NF-kappaB Activation by a Peptide That Blocks the Interaction of NEMO with the IkappaB Kinase Complex. *Science* **2000**, *289*, 1550–1554.

(32) Gaurnier-Hausser, A.; Patel, R.; Baldwin, A. S. A Phase I Clinical Trial of Systemically Delivered NEMO Binding Domain Peptide in Dogs with Spontaneous Activated B-Cell Like Diffuse Large B-Cell Lymphoma. *PLoS ONE* **2014**, *9*, 1-10.

(33) Rushe, M.; Silvian, L.; Bixler, S.; Chen, L. L.; Cheung, A.; Bowes, S.; Cuervo, H.; Berkowitz, S.; Zheng, T.; Guckian, K.; Pellegrini, M.; Lugovskoy, A. Structure of a NEMO/IKK-Associating Domain Reveals Architecture of the Interaction Site. *Structure* **2008**, *16*, 798–808.

(34) Fasshauer, D.; Sutton, R. B. Conserved Structural Features of the Synaptic Fusion Complex: SNARE Proteins Reclassified as Q-and R-SNAREs. *Proc Natl Acad Sci* **1998**, *95*, 15781-15786.

(35) Jochim, A. L.; Arora, P. S. Assessment of Helical Interfaces in Protein-Protein Interactions. *Mol Biosyst* **2009**, *5*, 924–926.

(36) Golden, M. S.; Cote, S. M.; Sayeg, M.; Zerbe, B. S.; Villar, E. A.; Beglov, D.; Sazinsky, S. L.; Georgiadis, R. M.; Vajda, S.; Kozakov, D.; Whitty, A. Comprehensive Experimental and Computational Analysis of Binding Energy Hot Spots at the NF-κB Essential Modulator/IKKβ Protein-Protein Interface. *J. Am. Chem. Soc.* **2013**, *135*, 6242–6256.

(37) Morrow, J. K.; Zhang, S. Computational Prediction of Protein Hot Spot Residues. *Curr. Pharm. Des.* **2012**, *18*, 1255–1265.

(38) Lise, S.; Buchan, D.; Pontil, M.; Jones, D. T. Predictions of Hot Spot Residues at Protein-Protein Interfaces Using Support Vector Machines. *PLoS ONE* **2011**, *6*, e16774.

(39) Andreana, P. R.; McLellan, J. S.; Chen, Y.; Wang, P. G. Synthesis of 2,6-Dideoxysugars via Ring-Closing Olefinic Metathesis. *Org. Lett.* **2002**, *4*, 3875–3878.

(40) Lin, Y. A.; Chalker, J. M.; Davis, B. G. Olefin Cross-Metathesis on Proteins: Investigation of Allylic Chalcogen Effects and Guiding Principles in Metathesis Partner Selection. *J. Am. Chem. Soc.* **2010**, *132*, 16805–16811.

(41) Kline, T.; Steiner, A. R.; Penta, K.; Sato, A. K.; Hallam, T. J.; Yin, G. Methods to Make Homogenous Antibody Drug Conjugates. *Pharm. Res.* **2014**.

(42) Grubbs R. H. Highly Efficient Synthesis of Covalently Cross-Linked Peptide Helices by Ring-Closing Metathesis *Angew Chem Int Ed* **1998**, *37*, 3281–3284.

(43) Karle, I. L.; Flippen-Anderson, J. L.; Uma, K.; Balaram, P. Unfolding of an Alpha-Helix in Peptide Crystals by Solvation: Conformational Fragility in a Heptapeptide. *Biopolymers* **1993**, *33*, 827–837.

(44) Blackwell, H. E.; Sadowsky, J. D.; Howard, R. J.; Sampson, J. N.; Chao, J. A.; Steinmetz, W. E.; O'Leary, D. J.; Grubbs, R. H. Ring-Closing Metathesis of Olefinic Peptides: Design, Synthesis, and Structural Characterization of Macrocyclic Helical Peptides. *J. Org. Chem.* **2001**, *66*, 5291–5302.

(45) Bernal, F.; Tyler, A. F.; Korsmeyer, S. J.; Walensky, L. D.; Verdine, G. L. Reactivation of the P53 Tumor Suppressor Pathway by a Stapled P53 Peptide. *J. Am. Chem. Soc.* **2007**, *129*, 2456–2457.

(46) Verdine, G. L.; Walensky, L. D. The Challenge of Drugging Undruggable Targets in Cancer: Lessons Learned From Targeting BCL-2 Family Members. *Clinical Cancer Research* **2007**, *13*, 7264–7270.

(47) Bautista, A. D.; Appelbaum, J. S.; Craig, C. J.; Michel, J.; Schepartz, A. Bridged Beta(3)-Peptide Inhibitors of P53-hDM2 Complexation: Correlation Between Affinity and Cell Permeability. *J. Am. Chem. Soc.* **2010**, *132*, 2904–2906.

(48) Henchey, L. K.; Kushal, S.; Dubey, R.; Chapman, R. N.; Olenyuk, B. Z.; Arora, P. S. Inhibition of Hypoxia Inducible Factor 1-Transcription Coactivator Interaction by a Hydrogen Bond Surrogate Alpha-Helix. *J. Am. Chem. Soc.* **2010**, *132*, 941–943.

(49) Khaja, K.; Robbins, P. Comparison of Functional Protein Transduction Domains Using the NEMO Binding Domain Peptide. *Pharmaceuticals 2010, Vol. 3, Pages 110-124* **2010**, *3*, 110–124.

(50) Tilstra, J.; Rehman, K. K.; Hennon, T.; Plevy, S. E.; Clemens, P.; Robbins, P. D. Protein Transduction: Identification, Characterization and Optimization. *Biochem. Soc. Trans.* **2007**, *35*, 811–815.

(51) Rehman, K. K.; Bertera, S.; Bottino, R. Protection of Islets by in SituPeptide-Mediated Transduction of the IκB Kinase Inhibitor Nemo-Binding Domain Peptide. *J Biol Chem* **2003**, *278*, 9862-9868.

(52) Asada, S.; Choi, Y.; Yamada, M.; Wang, S.-C.; Hung, M.-C.; Qin, J.; Uesugi, M. External Control of Her2 Expression and Cancer Cell Growth by Targeting a Ras-Linked Coactivator. *Proc Natl Acad Sci USA* **2002**, *99*, 12747–12752.

(53) Vassilikogiannakis, G.; Margaros, I.; Tofi, M. Olefin Metathesis: Remote Substituents Governing the Stereoselectivity of 11-Membered-Ring Formation. *Org. Lett.* **2004**, *6*, 205–208.

(54) Bird, G. H.; Bernal, F.; Pitter, K.; Walensky, L. D. Synthesis and Biophysical Characterization of Stabilized Alpha-Helices of BCL-2 Domains. *Meth Enzymol* **2008**, *446*, 369–386.

(55) Schrock, R. R.; Grubbs, R. H. *Handbook of Metathesis*; Grubbs, 2003.

(56) Wakamatsu, H.; Blechert, S. A Highly Active and Air-Stable Ruthenium Complex for Olefin Metathesis. *Angew Chem Int Ed* **2002**, *41*, 794-796.

(57) Illesinghe, J.; Guo, C. X.; Garland, R.; Ahmed, A.; van Lierop, B.; Elaridi, J.; Jackson, W. R.; Robinson, A. J. Metathesis Assisted Synthesis of Cyclic Peptides. *Chemical Communications* **2009**, *0*, 295–297.

(58) Chapman, R. N.; Arora, P. S. Optimized Synthesis of Hydrogen-Bond Surrogate Helices: Surprising Effects of Microwave Heating on the Activity of Grubbs Catalysts. *Org. Lett.* **2006**, *8*, 5825–5828.

(59) Miller, S. M.; Simon, R. J.; Ng, S. Comparison of the Proteolytic Susceptibilities of Homologous L-Amino Acid, D-Amino Acid, and N-Substituted Glycine Peptide and Peptoid Oligomers. *Drug Development Research* **1995**, *35*, 20-32.

(60) Peters, J. M. Proteasomes: Protein Degradation Machines of the Cell. *Trends in Biochemical Sciences* **1994**, *19*, 377-382.

(61) Moellering, R. E.; Cornejo, M.; Davis, T. N.; Bianco, C. D.; Aster, J. C.; Blacklow, S. C.; Kung, A. L.; Gilliland, D. G.; Verdine, G. L.; Bradner, J. E. Direct Inhibition of the NOTCH Transcription Factor Complex. *Nature* **2009**, *462*, 182–188.

(62) Majmudar, C. Y.; Wang, B.; Lum, J. K.; Håkansson, K.; Mapp, A. K. A High-Resolution Interaction Map of Three Transcriptional Activation Domains with a Key Coactivator From Photo-Cross-Linking and Multiplexed Mass Spectrometry. *Angew. Chem. Int. Ed. Engl.* **2009**, *48*, 7021–7024.

(63) Lee, S.; Braun, C. R.; Bird, G. H.; Walensky, L. D. Photoreactive Stapled Peptides to Identify and Characterize BCL-2 Family Interaction Sites by Mass Spectrometry. *Meth Enzymol* **2014**, *544*, 25–48.

(64) May, M. J.; Marienfeld, R. B.; Ghosh, S. Characterization of the IκB-Kinase NEMO Binding Domain. *J Biol Chem* **2002**, *277*, 45992–46000.

(65) Kwon, J. H.; Keates, S.; Simeonidis, S.; Grall, F.; Libermann, T. A.; Keates, A. C. ESE-1, an Enterocyte-Specific Ets Transcription Factor, Regulates MIP-3alpha Gene Expression in Caco-2 Human Colonic Epithelial Cells. *J Biol Chem* **2003**, *278*, 875–884.

(66) Kunsch, C.; Rosen, C. A. NF-Kappa B Subunit-Specific Regulation of the Interleukin-8 Promoter. *Molecular and Cellular Biology* **1993**, *13*, 6137–6146.

(67) Gill, S. C.; Hippel, Von, P. H. Calculation of Protein Extinction Coefficients From Amino Acid Sequence Data. *Analytical biochemistry* **1989**, *182*, 319-326.

(68) Højfeldt, J. W.; Cruz-Rodríguez, O.; Imaeda, Y.; Van Dyke, A. R.; Carolan, J. P.; Mapp, A. K.; Iñiguez-Lluhí, J. A. Bifunctional Ligands Allow Deliberate Extrinsic Reprogramming of the Glucocorticoid Receptor. *Molecular Endocrinology* **2014**, *28*, 249–259.

(69) Iñiguez-Lluhí, J. A.; Pearce, D. A Common Motif Within the Negative Regulatory Regions of Multiple Factors Inhibits Their Transcriptional Synergy. *Molecular and Cellular Biology* **2000**, *20*, 6040–6050.

(70) Nakayama, T.; Fujisawa, R.; Yamada, H.; Horikawa, T.; Kawasaki, H.; Hieshima, K.; Izawa, D.; Fujiie, S.; Tezuka, T.; Yoshie, O. Inducible Expression of a CC Chemokine Liver- and Activation-Regulated Chemokine (LARC)/Macrophage Inflammatory Protein (MIP)-3 Alpha/CCL20 by Epidermal Keratinocytes and Its Role in Atopic Dermatitis. *Int. Immunol.* **2001**, *13*, 95–103.

(71) Lee, S.; Kim, Y. J.; Kwon, S.; Lee, Y.; Choi, S. Y.; Park, J. Inhibitory Effects of Flavonoids on TNF-Alpha-Induced IL-8 Gene Expression in HEK 293 Cells. *BMB Rep* **2009**.

(72) Schmittgen, T. D.; Livak, K. J. Analyzing Real-Time PCR Data by the Comparative CT Method. *Nature Protocols* **2008**, *3*, 1101–1108.

(73) Livak, K. J.; Schmittgen, T. D. *Analysis of Relative Gene Expression Data Using Real-Time Quantitative PCR and the 2– ΔΔC T Method Methods 25 (4): 402–408*; Find this article online, 2001.

Chapter 5

Conclusions and Future Directions

5.1 Conclusions

Included in this dissertation, we have presented strategies for targeting large surface area, low affinity protein-protein interactions (PPIs). When classifying protein-protein interactions, we can categorize them based on affinity of interaction and surface area. Historically, the small surface area, high affinity PPIs have been the most successfully targeted using small molecules. Part of this is due to the availability of small molecule libraries targeted at other small surface area, high affinity interactions such as the interactions involved between enzymes and their ligands. This is not to say that large surface area, low affinity PPIs are undruggable. Petidomimetic strategies aimed at mimicking α-helices and β-strands, common secondary structure elements found at the interface of protein-protein interactions, have resulted in a small number of successes in the development of inhibitors of large surface area, low affinity PPIs. One of the major challenges of developing inhibitors for large surface area, low affinity PPIs is that these inhibitors often result in IC_{50}s in the low micromolar to mid micromolar range. These resulting IC_{50}s often lead to off-target effects, which can make the utility of these inhibitors challenging. One way to counter these off-target effects is by utilizing a combination approach with inhibitors targeted at the same pathway. As we demonstrated in chapter 2, combination approaches targeted at the same pathway can lead to synergistic inhibition, resulting in dose reductions and greater selectivity. The inhibitor **i1** was developed as an inhibitor of the ESX-Med23 interactions, leading to downregulation of the ESX target gene Her2 in Her2+ breast cancer cells. In the case of HNSCC, an EGFR and Her2 overexpressing

cancer, we demonstrated the ability of **i1** to enhance the activity of the EGFR/Her2 inhibitor afatinib in both cellular assays and a clinical mouse model of HNSCC.

We also developed a high-throughput assay for the discovery of new inhibitors of the VP16-ACID interaction. It has been previously demonstrated that VP16 transcriptional activity is dependent on its interaction with Med25, specifically with the ACID domain within Med25. The 80 amino acid VP16 TAD makes interactions with the ACID domain on two separate faces, denoted H1 and H2. Given, the large surface area of the VP16 TAD (>3500 Å), we sought to determine the minimal interaction of the VP16-ACID interaction. From these experiments, we were able to determine the VP16-ACID interaction is mediated by the two α-helical domains within the VP16 TAD with an affinity in the high nanomolar-low micromolar range. With these findings we were able to develop a fluorescence polarization (FP) assay targeting the minimal interaction of VP16-ACID. Based on the limited success with traditional small molecule libraries against these large surface area, low affinity interactions, we chose to use the assay to perform a pilot screen against a collection of bioactive small molecules and natural products. We hypothesized that the inclusion of natural products would produce a higher hit rate due to the access to both larger molecules and possible new 'privileged scaffolds' better suited at targeting this large surface area, low affinity PPIs.[1] The resulting pilot screen yielded natural product depside and depsidone inhibitors of the VP16-ACID interaction, validating our original hypothesis. These molecules demonstrated selective inhibition against VP16-ACID when compared to MLL-KIX, pKID-KIX, and VP16-Med15 counter screens. These molecules also demonstrated that they were able to covalently modify ACID, interacting with lysines located peripherally to the H1 and H2 binding sites on ACID. Conserved mutations of these lysines to arginines maintained affinity seen with the natural ligands, but decreased the IC_{50}s of the compounds, suggesting that these lysines were critical to the binding mechanism of these compounds. Data from these experiments demonstrated that modifications at either the H1 and H2 binding sites affects the inhibition at both the H1 and H2 site, suggesting that these molecules might possible be acting through a dual orthosteric/allosteric mechanism. Additionally, these molecules were able to inhibit ACID-mediated transcriptional events carried by the ATF6α, ERM, and RARα transcriptional activators. Together, these results demonstrate the identification and validation of Med25 ACID inhibitors. Based on the

promising results obtained, we have adapted our screen for screening the ERM-ACID interaction using the natural product extracts. Using this library of compounds has produced substantially higher hit rates. We are currently in the process of deconvoluting hits from this natural product extract screen.

Lastly, we demonstrated the development of a new inhibitor against the NF-κB activation pathway. There have been several successful inhibitors developed against the NF-κB signaling pathway, but the resulting inhibitors all have significant off-target effects, limiting their long-term use. The off-target effects that these inhibitors elicit is often due to their inhibition/activation of other signaling pathways. For example, kinase inhibitors of the NF-κB exhibit off-target effects due to the independent kinase activity of IKKα and IKKβ involved in cross talk with other pathways such as ERα and Foxo3a to name a few. Additionally, the existence of both a canonical and non-canonical NF-κB activation pathways further complicates targeting NF-κB. This prompts the need to identify points in the NF-κB signaling pathway that are unique to NF-κB. Additionally, inhibitors that target only the canonical pathways as opposed to the non-canonical pathway would be highly advantageous given the importance of the canonical pathway for the constitutive NF-κB activation found in several diseases. One such process that is highly specific to the canonical NF-κB signaling pathway, is the assembly of the IKK complex made up of a NEMO dimer, IKKα, and IKKβ. Knockdowns of NEMO were unable to activate the canonical NF-κB signaling pathway, but were able to activate the non-canonical pathways and left the kinase independent activity of IKKα and IKKβ unaffected. This demonstrates that targeting the IKK complex should provide more specific inhibitors of the canonical NF-κB signaling pathway. As we noted earlier, a recent examination of characterized PPIs has demonstrated that at the interface of these interactions, 26% of the residues are composed of α-helical structure, 24% of residues are composed of β-strand structure, and 50% of residues are made up of 'non-regular' secondary structure (loops, turns, and coils). This last category represents a tremendous opportunity for development of inhibitors since these interactions make up half of the secondary structure found at the interface of PPIs. Furthermore, most strategies have traditionally focused on targeting α-helical and β-strand secondary structures. One PPI that has been characterized as being made up of 'non-regular' structure is the NEMO-IKK interaction. A recent crystal structure of the NEMO-IKK interaction revealed a 4-helix

bundle heterotetramer composed of an N-terminal NEMO dimer complexed with the C-terminal tails of IKKα and IKKβ. Interestingly, the IKKα and IKKβ share the same NEMO-binding domain (NBD) to bind to NEMO, composed of a 6-amino acid sequence ^{737}LDWSWL^{742}, which exists as a kinked, unstructured region in the largely α-helical NEMO-IKK interaction. A cell-penetrating peptide appended to this sequence demonstrated inhibition of NF-κB activity, albeit with a modest IC_{50} (>150 μM); however, this result validates that targeting the IKK complex is a viable target for inhibitor development. Interestingly, alanine screening of IKK with its interaction with NEMO, revealed the unstructured region of IKK as the hot spot of the interaction, contrary to what is traditionally seen with extended α-helical interactions such as p53. Using this data, we utilized olefin metathesis that has been traditionally used for constrained α-helical peptides and adapted this technique to the kinked, unstructured NEMO-binding domain peptide. We achieved this by exploiting the critical D738-S740 hydrogen bond that stabilizes this kinked structure and replacing it with a metathesized olefin. By doing this, we are able to synthesize a NBD mimic that was more proteolytically stable and 8 to 10-fold more potent than the unmodified NBD peptide at inhibiting both an NF-κB driven luciferase reporter as well as endogenous NF-κB target genes MIP3α and IL-8. Furthermore, we demonstrated that the modifications that we made did not affect the ability of the NBD mimic to interact with wild-type NEMO. This was demonstrated with covalent crosslinking experiments with the NBD mimic that validated the ability of the NBD mimic to interact with NEMO in cell lysates. Together, these results suggest that olefin metathesis stabilization of the NBD peptide is a viable route for synthesizing better inhibitors of the NF-κB activation pathway. Furthermore, this result also suggests that olefin metathesis stabilization may be a viable inhibitor development strategy of other non-regular secondary structures found at the interface of PPIs in the future.

5.2 Future directions

Deconvolution and validation of hits from natural product extract screen of ERM-ACID interaction

In chapter 4 we presented the results obtained from the pilot screen against the VP16-ACID interaction that identified depside and depsidone inhibitors of Med25 ACID-

mediated transcription. Based on the encouraging results obtain from the pilot screen, we carried out a full natural product extract screen against the ERM-ACID interaction using the FP assay screen that we developed. We chose to perform the natural product extract screen against the ERM-ACID interaction due to the new research implicating ERM in cancer metastasis. [2-4] The results of the natural product screen against the ERM-ACID interaction are depicted in chapter 4. Based on the results from the natural product extract (NPE) screen, we carried out counter screens against MLL-KIX and Gal4-DNA in order to determine which NPEs were selective for ERM-ACID interaction. With the NPEs that were left after the counter screens, we selected the top 30 NPEs as determined by percent inhibition in the ERM-ACID screen. M. Beyersdorf regrew the strains from the selected NPEs in order to verify the activity of the NPEs. These NPEs were assayed against the RARα luciferase driven reporter system that was used in chapter 4. This assay is relatively high-throughput and allowed for quick assessment of inhibitory activity of regrown NPEs (Figure 5.1).

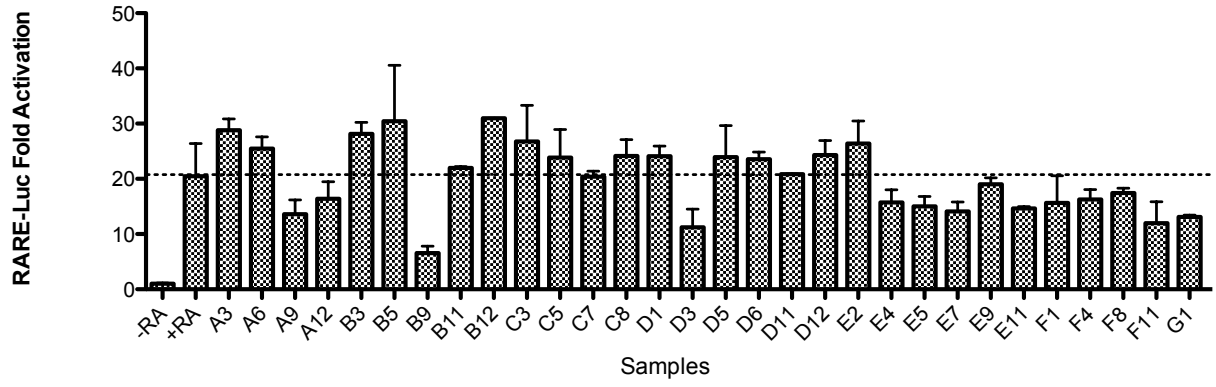

Figure 5.1 Effects of regrown NPEs against RARα luciferase reporter assay The assay was tested as a single dose (0.1% v/v). All extracts were diluted to a uniform concentration of 35 mg/mL concentration before using in assay. HeLa cells transfected with pRARE-luciferase reporter and pCMV-β-Gal were co-dosed with retinoic acid and either DMSO or compound as noted above. All DMSO levels were kept below 0.1% v/v for cellular dosings. All signals were normalized to β-Gal activity and represent the mean and standard deviation of 2 replicates.

Based on the results, we think extraxts A9, B9, D3, E7, F11, and G11 are the most promising NPEs based on inhibition seen above. These extracts are currently be deconvoluted and

will be tested for additional activity in other assays such as invasion, migration, and motility assays with ERM-dependent cell lines.

Developing an in vitro binding assay to determine inhibition constants of NBD mimics

In chapter 5, we demonstrated how a stabilized NEMO-binding domain (NBD) peptide could be synthesized using olefin metathesis. These inhibitors were 8 to 10-fold more potent than the unmodified NBD peptide, validating this stabilization strategy. Furthermore, we demonstrated that this stabilized mimic was able to interact with NEMO in cellular lysates, suggesting that the modifications do not affect binding to the native target. We are currently trying to get an *in vitro* assay developed in order to determine the inhibition constants of the NBD mimics compared to the unmodified NBD peptides. Other groups that have developed olefin metathesis stabilized α-helices have demonstrated that the binding affinity increases with the constrained analogs compared to the unmodified construct. [5-7] One of the reasons that we would like to develop an *in vitro* assay of the NEMO-IKK interaction is to determine if we observe an increase of affinity with our NBD mimics. This would suggest that pre-constraining the NBD peptide increases affinity for NEMO. Additionally, the development of an *in vitro* binding assay would provide an assay that could potentially be adapted for high-throughput screening. The identification of the NBD peptide as a hot spot for the NEMO-IKK interaction would suggest that any screen using this *in vitro* assay would provide molecules against the important region of the NEMO-IKK interaction.

5.3 Concluding remarks

Protein-protein interactions (PPIs) mediate numerous cellular processes. External and internal stimuli experienced by cells activate signaling pathways in order to respond appropriately to these stimuli. These responses are dysregulated either as a cause or consequence of disease, and therefore, small molecules that can restore normal function or inhibit aberrant function of these signaling pathways possess enormous therapeutic potential. The signaling pathways that cells use to respond to stimuli make use of numerous PPIs to turn on the necessary transcriptional activators needed to activate the appropriate target genes to respond to the stimuli. There are three general PPIs that can be

targeted to affect the activity of transcriptional activators: regulatory proteins, masking proteins, and interactions with coactivators. These PPIs can be classified into one of four classifications when considering surface area and affinity of the interaction. There have been a number of successes targeting low surface area, high affinity PPIs with small molecules; however, targeting large surface area, low affinity interactions remains challenging. One of the reasons this is challenging is because we do not possess adequate tools to target these interactions. For example, small molecule libraries that have been used to target small surface area, high affinity PPIs have had some success, but this is not entirely surprising considering the similarity between these interactions with interactions between proteins and ligands, which are highly targetable with small molecules. Here we presented three different strategies to target these large surface area, low affinity PPIs: combination strategies, screening with natural products, and stabilized peptides.

Although these interactions remain particularly challenging to target with traditional inhibitor development methods, we have presented strategies to target these types of interactions. These strategies will need to be refined over time as would be the case with any other targeting strategy, but the present strategies have provided crucial information for future development of inhibitors targeted at large surface area, low affinity PPIs.

5.4 Materials and Methods

RARα luciferase reporter assay with NPEs

The RARα luciferase reporter containing 3 tandem RARα sites (RARα-luc) was obtained from Addgene. CMV-β-Gal, and pBSSK were generously provided by Dr. Jorge Iñigues-Lluhí (The University of Michigan Pharmacology Department). All cells were maintained in 5% CO_2 at 37°C. HeLa cells were grown in Dulbecco's modified Eagle's medium (DMEM, Invitrogen) supplemented with 10% FBS. For luciferase assays, $4x10^5$ cells were seeded in a 6-well dish and allowed to adhere overnight. The media was removed and cells were transfected in Opti-Mem (Invitrogen) with 1 μg RARα-luc, 200 ng CMV-β-Gal, and 800 ng pBSSK using Lipofectamine 2000 (Life Technologies) according to manufacturer's instructions. After 4.5 h, transfection solution was removed and replaced with DMEM containing 10% FBS. At 24 h after transfection, cells were trypsinized and resuspended in DMEM supplemented with 10% FBS and seeded into a 96-well plate at a density of $8x10^3$ cells per well. After an additional 16 h, media was removed and replaced with Opti-Mem containing vehicle or NPE (0.1% v/v) as a solution in DMSO co-dosed with retinoic acid (1 μM). After cells incubated with either vehicle or compound and retinoic acid for 16 h, media was removed and cells were lysed with 60 μL of passive lysis buffer. Luciferase and β-Galactosidase activities were determined as previously described. RARα luciferase activity and response curve analysis was performed using GraphPad software.

5.5 References

(1) Evans, B. E.; Rittle, K. E.; Bock, M. G.; DiPardo, R. M.; Freidinger, R. M.; Whitter, W. L.; Lundell, G. F.; Veber, D. F.; Anderson, P. S. Methods for Drug Discovery: Development of Potent, Selective, Orally Effective Cholecystokinin Antagonists. *J Med Chem* **2002**, *31*, 2235–2246.

(2) Baert, J.-L.; Monté, D.; Musgrove, E. A.; Albagli, O.; Sutherland, R. L.; Launoit, Y. de. Expression of the PEA3 Group of ETS-Related Transcription Factors in Human Breast-Cancer Cells. *International Journal of Cancer* **1997**, *70*, 590–597.

(3) Monge, M.; Colas, E.; Doll, A.; Gonzalez, M.; Gil-Moreno, A.; Planaguma, J.; Quiles, M.; Arbos, M. A.; Garcia, A.; Castellvi, J.; Llaurado, M.; Rigau, M.; Alazzouzi, H.; Xercavins, J.; Alameda, F.; Reventos, J.; Abal, M. ERM/ETV5 Up-Regulation Plays a Role During Myometrial Infiltration Through Matrix Metalloproteinase-2 Activation in Endometrial Cancer. *Cancer Res.* **2007**, *67*, 6753–6759.

(4) Firlej, V.; Ladam, F.; Brysbaert, G.; Dumont, P.; Fuks, F.; de Launoit, Y.; Benecke, A.; Chotteau-Lelievre, A. Reduced Tumorigenesis in Mouse Mammary Cancer Cells Following Inhibition of Pea3- or Erm-Dependent Transcription. *Journal of Cell Science* **2008**, *121*, 3393–3402.

(5) Bernal, F.; Tyler, A. F.; Korsmeyer, S. J.; Walensky, L. D.; Verdine, G. L. Reactivation of the P53 Tumor Suppressor Pathway by a Stapled P53 Peptide. *J. Am. Chem. Soc.* **2007**, *129*, 2456–2457.

(6) Henchey, L. K.; Kushal, S.; Dubey, R.; Chapman, R. N.; Olenyuk, B. Z.; Arora, P. S. Inhibition of Hypoxia Inducible Factor 1-Transcription Coactivator Interaction by a Hydrogen Bond Surrogate Alpha-Helix. *J. Am. Chem. Soc.* **2010**, *132*, 941–943.

(7) Cohen, N. A.; Stewart, M. L.; Gavathiotis, E.; Tepper, J. L.; Bruekner, S. R.; Koss, B.; Opferman, J. T.; Walensky, L. D. A Competitive Stapled Peptide Screen Identifies a Selective Small Molecule That Overcomes MCL-1-Dependent Leukemia Cell Survival. *Chem. Biol.* **2012**, *19*, 1175–1186.

Appendix A

Synthesis and Biological Evaluation of Pharbinilic Acid Derivatives as Potent Inhibitors of NF-κB*

A.1 Abstract

A 7-step synthesis of pharbinilic acid, a member of the gibberellin family of natural products and the first naturally occurring allogibberic acid, is reported. An efficient decarboxylative aromatization reaction enables the synthesis of pharbinilic acid and related analogs for evaluation as modulators of NF-kB activity. Remarkably, one analog displays a 2 mM IC50 in an NF-kB activity assay and inhibits an endogenous NF-kB-regulated pathway.

A.2 Introduction

Pharbinilic acid (**1**) is a member of the rare class of allogibberic acids, isolated from the seeds of morning glory (*Pharbitis nil*) used in Korea, China and Japan as a medicinal agent.[1] Allogibberic acids were originally reported as laboratory-generated decomposition products of gibberellic acid (**2**), a phytohormone responsible for the regulation of growth and developmental processes in higher plants.[2]

---

* This work is part of a collaborative effort. J. R. Anannd synthesized, purified, and characterized all synthetic compounds. P. A. Bruno performed NF-κB reporter assay and endogenous gene expression analysis. This chapter is adapted from a published article: Annand, J. R.; Bruno, P. A.; Mapp, A. K.; Schindler, C. S. Synthesis and biological evaluation of pharbinilic acid and derivatives as NF-κB pathway inhibitors **2015**, Advance Article, DOI: 10.1039/C5CC02918J-Reproduced with permission of The Royal Society of Chemistry (RSC).

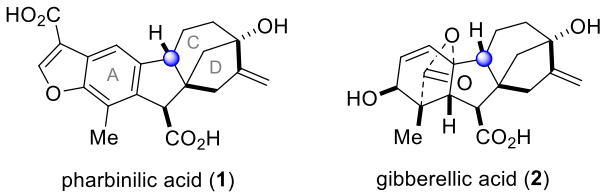

Figure A.1 Pharbinilic acid (**1**) isolated from the seeds of morning glory (*Pharbitis nil*), and gibberellic acid (**2**). The natural products share the same stereochemistry at the 5-7 ring ring juncture (blue circle).

Pharbinilic acid (**1**) represents the first naturally occurring allogibberic acid reported to date. Pharbinilic acid (**1**) was evaluated for anticancer cytotoxicity and displayed activity against A549, SK-OV-3, SK-MEL-2, and HCT-15 cell lines. Recently, gibberellic acid (**2**) and allogibberic acid (**5**) were identified by A. Koehler as modulators of the NF-κB signaling pathway.[3] Aberrant activity of the transcriptional activator NF-κB has been shown to play an important role in various cancers, inflammatory diseases and autoimmune diseases. In an effort to synthesize and identify compounds that modulate the NF-κB pathway without displaying significant cytotoxicity, we became interested in evaluating the efficacy of pharbinilic acid (**1**) and analogs to modulate NF-κB activity. Herein we report the culmination of these efforts in an efficient 7-step synthesis of pharbinilic acid (**1**) from gibberellic acid (**2**).

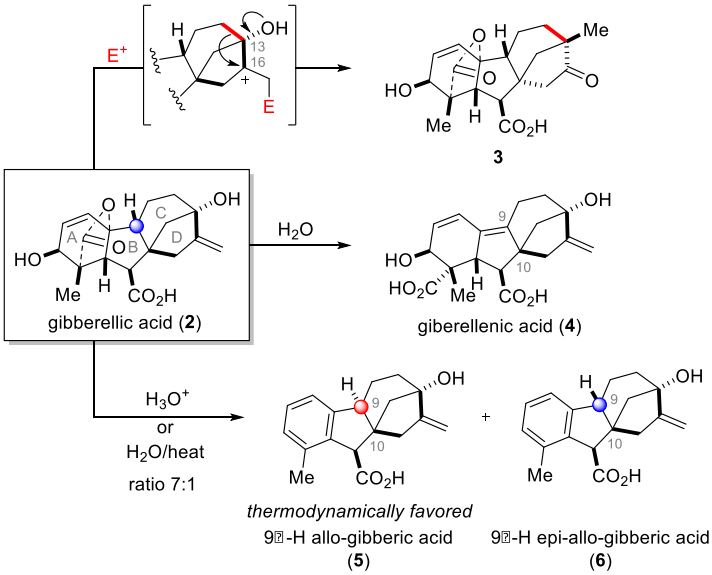

Figure A.2 Synthetic challenges associated with the inherent reactivity of gibberellic acid (**1**).

A.3 Synthesis of pharbinilic acid derivatives

Our 7-step synthetic sequence relies on commercially available gibberellic acid (**2**) [4,5] ($1.56 per 1g) which is produced industrially (50 tons per year) by the fermentation of the fungus *Gibberella fujikuroi*. [6,7] In comparison, only 6 mg of pharbinilic acid (1) were isolated from 2 kg of dried seeds of *Pharbitis nil*. Extensive studies towards the synthesis of gibberellic acid (**2**) in the 1970s revealed specific challenges associated with its highly functionalized tetracyclic core, especially the B,C,D-ring junction also present in pharbinilic acid (**1**), which E.J. Corey[8] referred to as "a singularly diabolical placement and density of functionality." The inherent reactivity of gibberellic acid (**2**) posed very specific constraints on the development of a reliable synthetic route to pharbinilic acid (**1**). Specifically, the C9-C10 cis-fused tricyclic ring system present in gibberellic acid (**2**) is known to be considerably more strained than the corresponding C9-C10 trans-fused system.[9] As a result, gibberellic acid (**2**) was found to undergo trans elimination of the lactone subunit to form gibberellenic acid (**4**) even at neutral pH. Thermal decomposition or treatment of **2** with mineral acids results in a mixture of 9a-H (**5**) and 9b-H *epi*-allogibberic acid **6** (**5/6** = 7:1). The observed epimerization at C9 in the major product **5** was shown to result as a consequence of the intermediacy of **4** and subsequent protonation to yield the thermodynamically favored C9-C10 trans fused 9a-H allogibberic acid **5**.[10] Moreover, the latent reactivity of the tertiary allylic alcohol of the C and D rings is known to be difficult to control. Exposure to various electrophiles (E+ in Figure 2) capable of reacting with the terminal alkene of **2** creates an electron-deficient C16 carbon center.[11] Hydroxy-assisted Wagner-Meerwein rearrangement of the C12-C13 bond results in the formation of a new bicyclo[3.2.1]octanone **3**. Although this rearrangement poses a potential issue in designing our synthetic strategy, we also recognized an opportunity to prepare additional analogs based on this observed reactivity. The initial isolation of pharbinilic acid (**1**) not only provided evidence that allogibberic acids do exist as genuine natural products, and not merely isolation artifacts, but more importantly determined that **1** is of the same absolute configuration as 9b-H allogibberic acid (**6**), the minor product obtained upon thermal decomposition of gibberellic acid (**2**) bearing the strained C9-C10 cis-fused tricyclic core. As a result, a successful synthetic strategy towards pharbinilic acid (**1**) is faced with two

major challenges and has to result in control of both the inherent reactivity of the 9b-H as well as the C13 tertiary allylic alcohol.

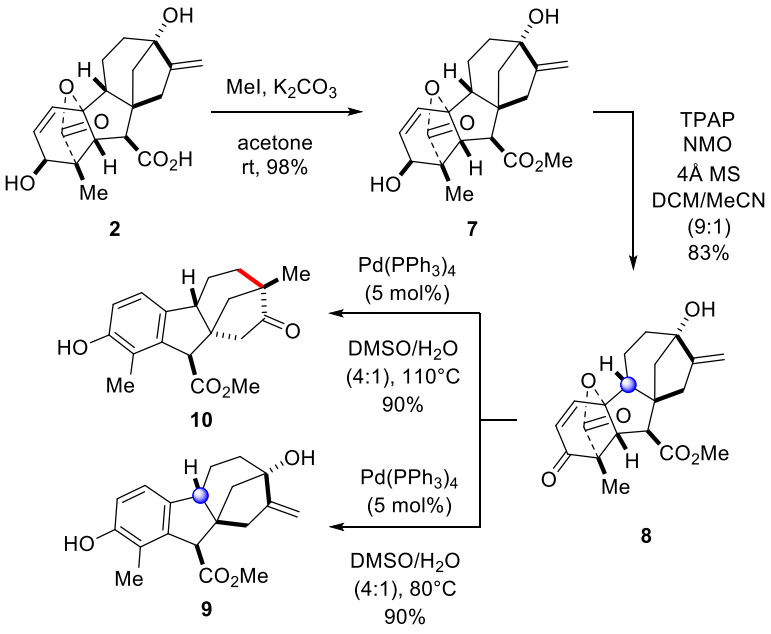

Figure A.3 Synthesis of the hydroxyl-allogibberic methyl ester (**9**).

Our synthetic strategy to pharbinilic acid (**1**) requires a mild aromatization protocol to form phenol **9** under non-aqueous conditions to avoid both epimerization of the C9b-H present in the *epi*-allogibberic acid core as well as the undesired C12-C13 rearrangement of the C and D rings. Gibberellic acid (**2**) was initially converted to its corresponding methyl ester (**7**) using methyl iodide in acetone in 98% yield. Griffith-Ley oxidation (TPAP/NMO) of the secondary alcohol proved superior over other oxidation conditions investigated (e.g. DMP, IBX, PDC) which resulted in either low yields or a complex product mixture, leading to the formation of enone **8** in 83% yield. Enone **8** was found to be very sensitive to Brønsted acids, both in aqueous and anhydrous environments. Treatment of **8** with dilute mineral acids (e.g. HCl, H2SO4) resulted in the formation of **9** along with the undesired C9a-H epimer. Changing to anhydrous organic acids (e.g. acetic acid, formic acid, *p*TsOH) circumvented the issue of epimerization; however, only the product of Wagner-Meerwein rearrangement of the C12-C13 bond without A-ring aromatization was observed. We next investigated selective transformations of the allylic lactone in **8** using transition metal catalysis. The desired rearomatization of the A ring was accomplished using Pd(PPh3)4 (5 mol%) in aqueous DMSO at 110°C, however concomitant Wagner-Meerwein

rearrangement was also observed to form ketone **10** as the sole product. Careful investigation of the reaction conditions revealed that the Wagner-Meerwein rearrangement was highly sensitive to the reaction temperature. As a result, conducting the aromatization at 80°C provided the desired phenol **9** in 90% yield.

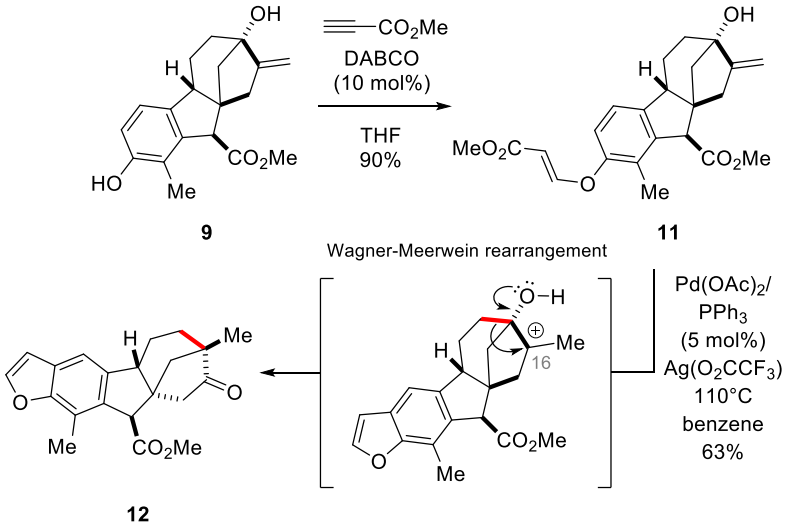

Figure A.4 Synthesis of derivatives of pharbinilic acid (**1**) via Wagner-Meerwein rearrangement of the C,D-bicyclic ring system in **10** leading to ketone **12**.

With a route to phenol **9** secured, the viability of a palladium-catalyzed oxidative cyclization approach to construct the A-ring benzofuran moiety was explored. The required 3-phenoxyacrylate **11** was readily prepared as the corresponding conjugate addition product of methylacrylate and phenol **9** in 90% yield.[12] Treatment of **11** with Pd(OAc)2/PPh3 and AgCO2CF3[13] in benzene at 110°C

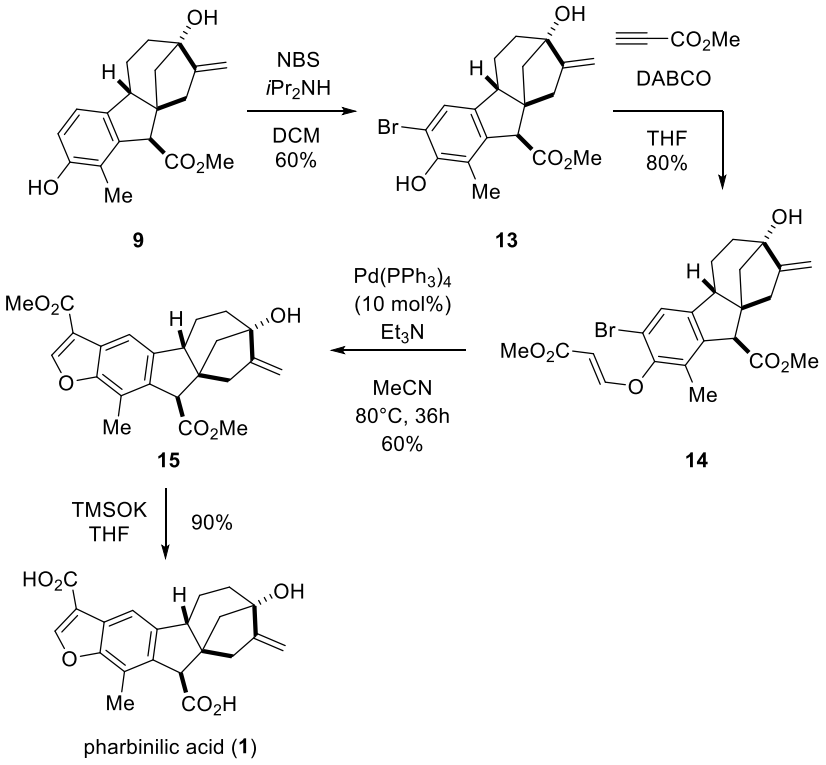

Figure A.5 Completion of the synthesis of pharbinilic acid (**1**) in seven synthetic transformations.

resulted in the formation of benzofuran **12** (63% yield) as the sole product of a Wagner-Meerwein rearrangement-decarboxylation sequence. Subsequent attempts to avoid decarboxylation during oxidative benzofuran formation centered around changing the palladium source (Pd(OAc)2, Pd(PPh3)4, PdCl2) as well as the corresponding oxidant (AgCO2CF3, PhI(OAc)2, O2) while varying the temperature from ambient temperature to 110ºC. However, none of these conditions led to the formation of the desired benzofuran methyl ester and the sole product isolated upon reaction of phenoxyacrylate **11** remained benzofuran **12**.

As we were unable to circumvent decarboxylation and/or WM rearrangement from **10**, we revised our strategy to rely on bromophenol **13** to enable a intramolecular Heck reaction to form the benzofuran, avoiding the use of Lewis acidic additives that may have contributed to the undesired WM rearrangement and/or decarboxylation. Bromination[14] of **10** (NBS, *i*Pr2NH, 60% yield) followed by conjugate addition with methyl propiolate (DABCO, THF) provided **14** in 80% yield. Heck annulation[15] of phenoxyacrylate **14** proceeded at 80ºC, preventing the undesired rearrangement/decarboxylation side

products, and afforded the pharbinilic bismethyl ester **15** in 60% overall yield. Saponification was best carried out under anhydrous conditions (KOTMS, THF) to provide the desired natural product, **1**, in 19% overall yield in seven total synthetic transformations starting from commercially available gibberellic acid **2**.

A.4 Effects of synthesized derivatives against an NF-kB reporter assay

Due to the report of giberellic acid and related structures as NF-kB inhibitors,[16] we examined the activity of **1** and analogs (**7-9**, **11-13**, **15**) in an NF-kB reporter gene assay. In this experiment, HeLa cells bearing a luciferase reporter plasmid driven by NF-kB were treated with each compound for 1 h followed by IL-1b stimulation of NF-kB activity. Two results are of particular note. While pharbilinic acid (**1**) was not active in this assay, conversion of the two carboxylic acid moieties to methyl esters as in **15** significantly enhanced activity, with an IC50 of 69 mM (Table 1). Additionally, enone **8** was the most active of the group, with significant inhibition observed even at 2 mM concentrations. The efficacy of **8** as a modulator of endogenous NF-kB was further assessed through examination of a native NF-kB-regulated gene, MIP3α. [17,18] As shown in Figure 4, analogous levels of inhibition were observed. Further cellular studies are currently underway to characterize the mode of action of these molecules and their effects in other cellular models of NF-kB pathways.

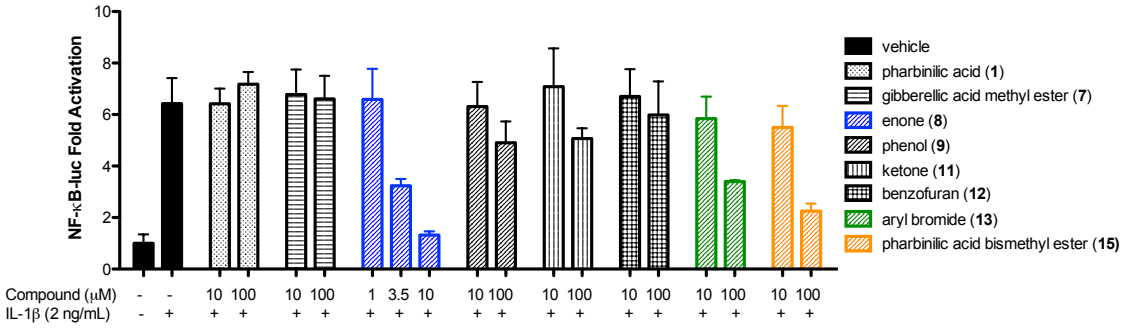

Figure A.6 Synthetic analogs of 1 and 2 inhibit NF-kB-driven transcription in cells. HeLa cells transfected with a NF-kB-driven luciferase reported plasmid and a CMV-driven b-galactosidase reporter were dosed with compounds 1, 7-9, 11-13, and 15. After 1 h, th addition of IL-1b stimulated NF-kB activity, in accordance with standard protocols (see SI for details). The fold activation shown is the luciferase activity of each experiment normalized to b-galactosidase activity. All data is represented as the mean and S.D. of 4 technical replicates.

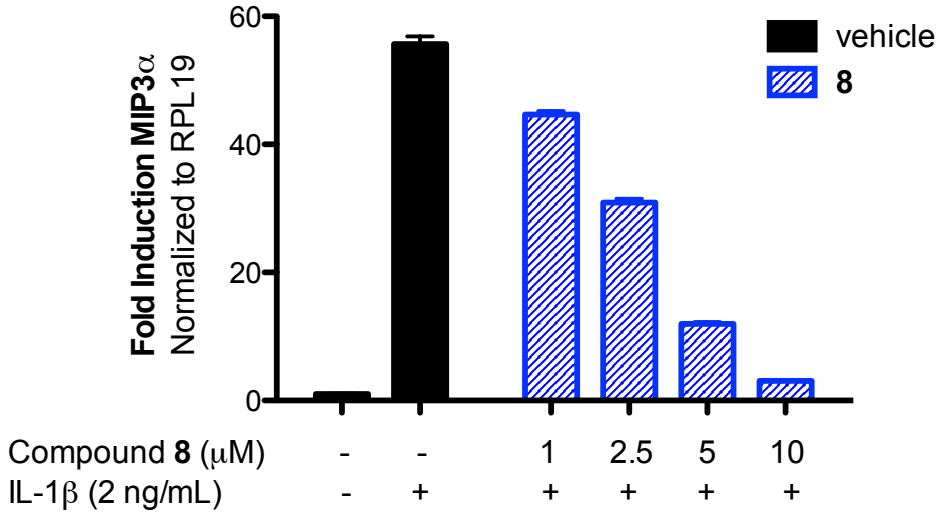

Figure A.7 Inhibition of MIP3a gene expression. Compound 8 was tested for its ability to inhibit IL-1b stimulated MIP3a gene expression in HeLa cells. All data is presented as the mean CT and S.D. of 3 replicates

In summary, we have developed a robust and concise synthesis to the first naturally occurring allogibberic acid, pharbinilic acid (**1**), which is tailored to the inherent reactivity associated with the gibberellins to proceed under mild reaction conditions without observing any epimerization of the C9b-H or Wagner-Meerwein rearrangement of the C12-C13 bond. Additionally, we have looked at the inhibitory effects of these compounds against NF-kB activity, identifying compound **8** as a potent inhibitor. The flexible and concise synthetic strategy will enable a full structure-activity relationship study of this class of NF-kB inhibitors, leading to chemical probes against this centrally important transcription factor.

A.5 Materials and methods

All synthetic protocols, characterization, spectra, and cell protocols are as noted in: Annand, J. R.; Bruno, P. A.; Mapp, A. K.; Schindler, C. S. Synthesis and biological evaluation of pharbinilic acid and derivatives as NF-κB pathway inhibitors **2015**, Advance Article, DOI: 10.1039/C5CC02918J

A.6 References

(1) Kim, K. H.; Choi, S. U.; Son, M. W.; Choi, S. Z.; Clardy, J.; Lee, K. R. Pharbinilic Acid, an Allogibberic Acid From Morning Glory (Pharbitis Nil). *J. Nat. Prod.* **2013**, *76*, 1376–1379.

(2) Krishnamoorthy, H. N. *Gibberellins and Plant Growth.*; Wiley Eastern Limited.: New York, 1975.

(3) Koehler, A. N. Methods for Modulating Nf-Kb Using Gibberellins. WO2010062372A3, 2009.

(4) Huigens, R. W.; Morrison, K. C.; Hicklin, R. W.; Flood, T. A.; Richter, M. F.; Hergenrother, P. J. A Ring-Distortion Strategy to Construct Stereochemically Complex and Structurally Diverse Compounds From Natural Products. *Nat Chem* **2013**, *5*, 195–202.

(5) Morrison, K. C.; Hergenrother, P. J. Natural Products as Starting Points for the Synthesis of Complex and Diverse Compounds. *Nat Prod Rep* **2014**, *31*, 6–14.

(6) Darken, M. A.; Jensen, A. L.; Shu, P. Production of Gibberellic Acid by Fermentation. *Applied Microbiology* **1959**, *7*, 301–303.

(7) Rodrigues, C.; Vandenberghe, L. P. de S.; de Oliveira, J.; Soccol, C. R. New Perspectives of Gibberellic Acid Production: a Review. *Crit. Rev. Biotechnol.* **2012**, *32*, 263–273.

(8) Corey, E. J.; Danheiser, R. L. Stereospecific Total Synthesis of Gibberellic Acid. a Key Tricyclic Intermediate. *J. Am. Chem. Soc.* **1978**, *100*, 8031.

(9) Martin, S. F.; Lindberg, T. *Strategies and Tactics in Organic Synthesis, Vol. 2Academic*; San diego, 1989.

(10) Pryce, R. J. New Intermediates in the Aqueous Decomposition of Gibberellic Acid. *Journal of the Chemical Society, Perkin Transactions 1* **1974**, *0*, 1179–1184.

(11) Grove, J. F.; T. P. C. Mulholland. 605. Gibberellic Acid. Part XII. the Stereochemistry of Allogibberic Acid. *J. Chem. Soc.* **1960**, 3007.

(12) Fan, M. J.; Li, G. Q.; Li, L. H.; Yang, S. D.; Liang, Y. M. DABCO-Catalyzed Reaction of Phenols or 1, 2-Diphenols with Activated Alkynes Leading to the Formation of Alkenoic Acid Esters or 1, 3-Dioxole Derivatives. *Synthesis* **2006**, *14*, 2286–2292.

(13) Li, Y.; Xie, Y.; Zhang, R.; Jin, K.; Wang, X.; Duan, C. Copper-Catalyzed Direct Oxidative C-H Amination of Benzoxazoles with Formamides or Secondary Amines Under Mild Conditions. *J. Org. Chem.* **2011**, *76*, 5444–5449.

(14) Velder, J.; Robert, T.; Weidner, I.; Neudörfl, J. M.; Lex, J.; Schmalz, H. G. Modular Synthesis of Chiral Phosphine-Phosphite-Ligands From Phenolic Precursors: a New Approach to Bidentate Chelate Ligands Exploiting a P --> O to P --> C Migration Rearrangement. *Advanced Synthesis & Catalysis* **2008**, *350*, 1309–1315.

(15) Onyango, E. O.; Fu, L.; Gribble, G. W. Synthesis of a Furano Abietane Cyano Enone—a New Scaffold for Biological Exploration. *Tetrahedron Letters* **2014**, *55*, 4636–4638.

(16) Ghosh, S.; Hayden, M. S. New Regulators of NF-kappaB in Inflammation. *Nat. Rev. Immunol.* **2008**, *8*, 837–848.

(17) Kwon, J. H.; Keates, S.; Simeonidis, S.; Grall, F.; Libermann, T. A.; Keates, A. C. ESE-1, an Enterocyte-Specific Ets Transcription Factor, Regulates MIP-3alpha Gene Expression in Caco-2 Human Colonic Epithelial Cells. *J Biol Chem* **2003**, *278*, 875–884.

(18) Nakayama, T.; Fujisawa, R.; Yamada, H.; Horikawa, T.; Kawasaki, H.; Hieshima, K.; Izawa, D.; Fujiie, S.; Tezuka, T.; Yoshie, O. Inducible Expression of a CC Chemokine Liver- and Activation-Regulated Chemokine (LARC)/Macrophage Inflammatory Protein (MIP)-3 Alpha/CCL20 by Epidermal Keratinocytes and Its Role in Atopic Dermatitis. *Int. Immunol.* **2001**, *13*, 95–103.